Chasing time

CHASING TIME

Characterisation and application of precision temporal measurements
with silicon pixel detectors

Robbert Erik Geertsema

CHASING TIME

Characterisation and application of precision temporal measurements
with silicon pixel detectors

PROEFSCHRIFT

ter verkrijging van de graad van doctor aan de Universiteit Maastricht,
op gezag van de Rector Magnificus, prof. dr. Pamela Habibović,
volgens het besluit van het College van Decanen,
in het openbaar te verdedigen
op Woensdag 10 januari 2024 om 13:00 uur

door

Robbert Erik Geertsema

Promotor
  Prof. dr. M.H.M. Merk

Copromotoren
  Dr. K. Akiba, Nikhef, Amsterdam
  Dr. H.L. Snoek, Nikhef, Amsterdam

Beoordelingscommissie
  Prof. dr. ir. C.J.G. Onderwater (voorzitter)
  Prof. dr. R.M.A. Heeren
  Prof. dr. S. Hild
  Dr. D. Hynds, Oxford University
  Dr. M. Wu, Radboud University

"It's a dangerous business, going out of your door. You step into the Road, and if you don't keep your feet, there is no knowing where you might be swept off to."

– J.R.R. Tolkien, *The Lord of the Rings*

❧ Contents ❧

CHAPTER 1

❧

INTRODUCTION TO HIGH ENERGY PHYSICS EXPERIMENTS AND THEIR DETECTORS

SILICON PIXEL DETECTORS are central elements in modern-day high energy particle physics experiments due to their high efficiency and good resolution for the tracking of charged particles. Silicon strip detectors have been used since the early 1980s [1, 2] to achieve precise position measurements in dedicated beam telescopes. In the late 1990s, silicon pixel detectors were first exploited in high energy physics; at CERN initially implemented in the WA97 [3] and DELPHI [4] experiments. The development of silicon sensor technology and detector integration has continued throughout the years after their first implementation. Challenges that arose for the application of silicon sensors in high energy particle physics experiments were achieving high position resolution while remaining radiation hard. For the first time in many decades, we are facing the challenge of improving a new measurement technique in silicon sensors: temporal measurements. Measuring the so-called *time-of-arrival* of charged particles would be of added value in the next generation of high energy physics experiments. This addition of *temporal information* is crucial to meet the required performance in upgraded or novel accelerator complexes. This dissertation focuses on the development and characterisation of the temporal measurement with silicon pixel sensors and detectors operating at the *Large Hadron Collider* (LHC), as well as the use of this temporal information in real-time event selection in the LHCb experiment at the LHC.

CURRENT DAY ACCELERATORS

Since many particles of interest in particle physics are highly unstable, we can only study them indirectly via their decay products after they are produced at collisions between particles with sufficient energy. The first accelerators date back to the late 1800s, using for example cathode ray tubes in the discovery of X-rays [5] as well the electron [6]. After these electrostatic field based accelerators a switch was made to time-varying accelerators, of which the first concept was proposed in the form of a *linear accelerator* in 1924 by Gustav Ising [7]. The first linear accelerator, a *klystron*, was constructed in 1937 [8]. However, the first time-varying accelerator built was not a linear accelerator but a *cyclotron*, conceptualised by Ernest Lawrence in 1929 and constructed in 1930 [7]. From that point on, different types of particle accelerators emerged.

The largest and most energetic particle accelerator that currently exists is the Large Hadron Collider (LHC) located at the European Organization for Nuclear Research (CERN). Constructed between 1998 and 2008 and first operated in 2009, the LHC is a *circular collider* and contains two adjacent parallel proton beamlines that collide head-on at different interaction points. When the LHC first operated, each beamline contained an energy of 3.5 TeV, which has been upgraded throughout the years to the current energy of 7.8 TeV per beam. At four points around the LHC ring, the two beams are crossed such that proton-proton collisions occur. Dedicated detectors have been constructed around these interaction points: ATLAS, ALICE, CMS and LHCb.

The particle beams in the LHC consist of closely spaced bunches containing a large number of protons (1.15×10^{11}). When these two beams cross each other, collisions occur between the protons of the two beams. The rate R of these physics processes depends on the process cross-section σ, the bunch crossing frequency f, the number of particles in each bunch of the two beams, N_1 and N_2, and the overlapping transversal area size A of the beams:

$$R = f \cdot \frac{N_1 N_2}{A} \cdot \sigma = \mathcal{L} \cdot \sigma. \tag{1.1}$$

Here $\mathcal{L}$ is defined as the luminosity and is a property of the collider. To study rare physics processes with a small cross-section σ, the luminosity of these accelerators is required to be high to yield a sufficiently high rate R. One of the options implemented at LHC to achieve this is to have a bunch crossing rate of 40 MHz, which sets strict limits on the detector requirements on radiation damage, speed, and data collection rate.

LHCb and its silicon detectors

The experiments of the early days of particle physics, such as the cathode rays that were used to discover the electron, are small compared to the large and complex detector systems currently used around the interaction points of the LHC. These current experiments contain multiple subsystems designed for the detection of specific particles. Silicon detectors are present in all four main LHC experiments and are used in their tracking systems. Silicon detectors have proven their use and capability as part of precision tracking systems and are usually impractical and too expensive for the outer part of the detectors. Therefore, the experiments implement layers of high-precision silicon sensors (pixelated and strip detectors) as part of their inner tracking system.
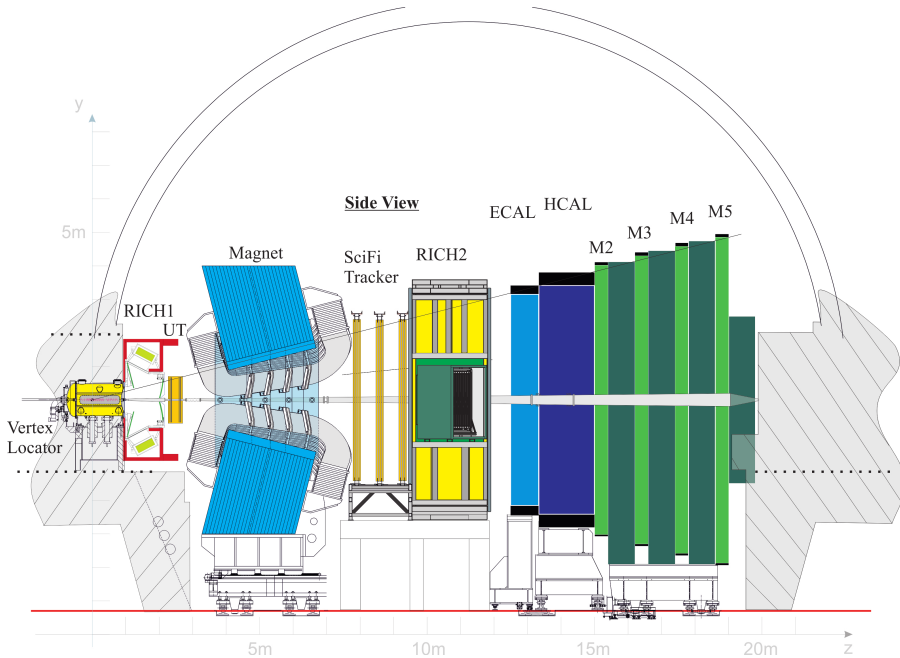
Figure 1.1: An illustration of the LHCb detector after the first upgrade (2022). The different subdetectors are indicated in various colours, as well as the outline of the cavern (grey lines and striped grey area) and the magnet (blue). The proton-proton interactions take place in the VELO, around $z = 0$. Figure taken from [9].

One of the four experiments at the LHC is the LHCb (LHC beauty), shown in fig. 1.1. This experiment is located at interaction point 8 at the LHC and consists of a forward single-arm spectrometer. In other words, it focuses its particle detection in the forward region close to the beam pipe. Due to a high particle production rate in the forward region, the detector operates at a reduced collision rate compared to the maximum that the LHC can produce. Figure 1.1 depicts the

various subdetectors that make up the LHCb detector. The proton-proton collisions happen around $z = 0$, inside the volume of the *Vertex Locator* (VELO). The VELO is a silicon pixel based tracker, the subject of this dissertation. Two other detectors that are part of the LHCb tracking system are the *Upstream Tracker* (UT - silicon based) and the *Scintillating fibre* (SciFi - fibre based) tracker. The remaining detectors include *particle identification* (PID) systems, *RICH1* (Ring-imaging Cherenkov detector) and *RICH2*, the measurement of the energy of particles via the *Electromagnetic Calorimeter* (ECAL) and *Hadron Calorimeter* (HCAL), and identification of muons in the four muon chambers (MX).

The LHCb detector is designed to study Charge-Parity (CP)-symmetry violation and rare decays of particles including the b- and c-quark. Over the years, the field of subjects in LHCb gradually extended, resulting in a physics study in 2011 [10] proposing an upgrade of the detector (and an increase in its received instantaneous luminosity) with a wider physics case. This letter of intent was the starting point of the upgrade that the LHCb detector underwent between 2019 and 2022, which is currently referred to as Upgrade 1. In 2018 an extended physics case for a subsequent upgrade of the whole detector was explored [11], which marked the start of Upgrade 2, and is the starting point of the research discussed in this dissertation. The proposed upgrade of the detector allows increasing the number of collisions per bunch crossing by over a factor of six compared to current nominal conditions. The Upgrade 2 of the LHCb is currently under consideration, in line with the planned upgrade of the LHC - the High Luminosity LHC (HL-LHC). Research and development have already started for Upgrade 2 and currently investigates novel technology implementations in the various subdetector systems. One of the novel technologies proposed for the VELO is the addition of temporal information, which utilises a time-of-arrival measurement on each hit. This addition helps to resolve the high density of particles related to the increased number of proton-proton collisions, and the goal is to utilise the per-hit temporal information in both tracking and vertexing in LHCb. The first developments of the subdetectors towards Upgrade 2 are detailed in [12].

LHCb's Upgrade 2 prospect

The instantaneous luminosity that LHCb will receive during Upgrade 2 directly translates into an increased rate of events that are studied at LHCb. This, in turn, allows to improve the accuracy of measurements on CP violating and rare decay processes, as well as improving measurements on lepton universality tests. The physics prospects and sensitivities of LHCb are detailed in [11]. The increased luminosity will extend LHCb's physics program beyond what is possible with the Upgrade 1 detector.

The VELO is central in LHCb's physics program due to its vertexing performance, and it is essential to maintain or improve the current Upgrade 1 performance in the higher multiplicity environment of the high-luminosity LHC. This poses novel challenges for the VELO, among which are the high non-uniform radiation damage as well as the high track density in the forward direction. To deal with the higher number of proton-proton collisions during the Upgrade 2 operation, the VELO is currently planning to implement per-hit temporal information in all its detectors.

SCOPE OF THE DISSERTATION

This dissertation reports on the possible implementation of temporal information in the VELO Upgrade 2, and delves into the physics of silicon sensors and their time-of-arrival measurement. The latter encompasses the development of novel pixel sensors using dedicated systems and the development of particle beam and optical based characterisation systems.

Simulations will be presented highlighting the impact of the addition of temporal information to the performance of the VELO, discussed in chapter 2. The time resolution indicated by these studies is indicative of the resolution that needs to be achieved in the next several years of development, and sets a goal for the research performed on silicon sensors in this dissertation.

The theoretical aspects of silicon sensors, from the formation of the *pn-junction* to the effect of radiation damage in silicon and the generation of the current signal induced by charged particles, are discussed in chapter 3. The aspects of processing and digitising the induced signals in the silicon sensor are discussed in chapter 4. Additionally, two *Application-Specific Integrated Circuits* (ASICs) and their dedicated readout systems are discussed and explained.

Two beam telescopes, dedicated systems to characterise detectors in a particle beam environment, are discussed in chapter 5. One system is based on Timepix3 ASICs and one is based on Timepix4 ASICs. The construction, and the first results obtained with the Timepix4 based telescope, are also discussed in chapter 5 in the form of a paper for which I performed part of the analysis and took part in the data taking. I am the author of the section about the temporal performance, and contributed to the text of the remainder of the paper. Characterisation studies of silicon sensors using the Timepix3 based telescope in view of the Upgrade 1 of the VELO are presented. Both the charge collection properties and the temporal properties of various designs of silicon sensors have been studied to decide the design incorporated in the VELO, and two papers published in view of these studies are discussed in chapter 6. In these papers, the data analysis regarding the studies with particles perpendicular to the sensors was performed by me. I am also the author of the text contained within these sections.

A second, optical based, type of characterisation system is discussed in chapter 7. This chapter contains a paper that discusses a two-photon absorption (TPA) system constructed and commissioned at Nikhef as well as presenting the first results using two-photon absorption in silicon sensors on Timepix3 ASICs, measuring both the charge collection and temporal properties. I performed all measurements and data analysis contained within this paper, and I am the author of the text. The first result with a $100\,\mu$m silicon sensor on a Timepix4 ASIC is discussed separately from the paper in this chapter, and finds an improved time resolution over the results with Timepix3 ASICs. However, further developments can still be implemented to improve the measured time resolution, and suggestions are made on implementing these improvements.

CHAPTER 2

❦

THE IMPACT OF TIMING INFORMATION FOR THE LHCB UPGRADE 2 VELO

T HE NEXT MAJOR UPGRADE of the LHCb detector, and more specifically the upgrade of the Vertex Locator (VELO) of LHCb, is under consideration and is scheduled to take place during *Long Shutdown 4* (LS4). The LS4 is a 2-year stop of the LHC planned, at the time of writing, to start in 2033, during which there is time to perform work on the detector in the LHCb cavern. With its ability to withstand and record more interactions per second, this upgrade allows the LHCb Collaboration to extend its physics capabilities beyond what is currently feasible. At this stage, intentions have been spoken out to pursue Upgrade 2 (U2) [13]. The baseline scenario includes an increase of the instantaneous luminosity to 1.5×10^{34} cm^{-2}s^{-1} - around six times more than Upgrade 1 (U1) - and to collect data corresponding to an integrated luminosity of 50 fb^{-1} per year, for a total of six years [13]. This luminosity implies an average of 42 visible collisions (referred to as pile-up) per bunch crossing compared to on average 7 visible collisions during Upgrade 1. The expected beam conditions in LHCb are that the collisions are distributed along the collision axis with a spatial *Root Mean Square* (RMS) of 44.7 mm and a temporal RMS of 186 ps [13].

One of the challenges for the VELO, due to the increased luminosity, is the increased irradiation and resulting damage to the sensor. The precise nature of radiation damage will be discussed in chapter 3. It is important to realise that a higher particle flux results in faster degradation of the detectors. Hence, moving the detector closer to the interaction point or increasing the instantaneous luminosity will result in more radiation damage per unit time. The track density per

event at the hottest spot within the VELO is estimated by [13]

$$\text{track density} = 39 \times \left(\frac{R}{\text{cm}} \right) \text{ tracks per cm}^2 \text{ per event}, \qquad (2.1)$$

where R is the distance of the sensor to the beam. This expression yields the relation between the expected hit rate and hence the radiation damage as a function of the radial distance from the collision axis.

The consequence of data taking at larger instantaneous luminosity and pile-up is an increased difficulty to separate the individual proton-proton collisions, which are called *Primary Vertices* (PVs), and to associate *Secondary Vertices* (SVs) with their primary origin vertex. With the spatial resolution of the current detector, the more densely populated collision region will result in spatially overlapping collisions after reconstruction. The addition of temporal information to the detected hits will help resolve this problem and relies on the fact that the primary vertices do not coincide in time. An example of how temporal information can aid the VELO in mitigating pile-up is shown in fig. 2.1. These figures depict a typical bunch crossing that is expected during the VELO Upgrade 2. The dots indicate the position of the primary vertices, and the lines indicate the trajectories (*tracks*) of the particles emanating from these primary vertices. The colour of the vertices and tracks indicates the temporal information: the relative time at which they occur. The bottom plot shows the entire bunch crossing, with no selection in time, while the middle and top plots show two smaller time windows within the bunch crossing. These last two plots show only the primary vertices and tracks that are present in the smaller time window and indicate how the temporal information can aid in pile-up suppression. A common misconception is that primary vertices and their decay products that occur outside of the temporal window are perhaps discarded, but in fact, the temporal window is used as a rolling shutter throughout the event, whereas track matching algorithms only consider primary vertices close in time. The general idea is that the more precise the temporal information is, the better pile-up can be resolved.

Simulations have been performed to study which time resolution is required for the VELO to mitigate the detrimental effects of pile-up. These simulations test the standalone primary vertex reconstruction and the physics performance for various event selection algorithms for different simulated time resolutions of the detector. The remainder of this chapter is divided as follows: in section 2.1 the design of the VELO Upgrade 1 and the scenarios that are currently considered for the VELO are discussed, in section 2.4 the simulation setup is explained and in section 2.5 results from the simulation are shown and discussed.
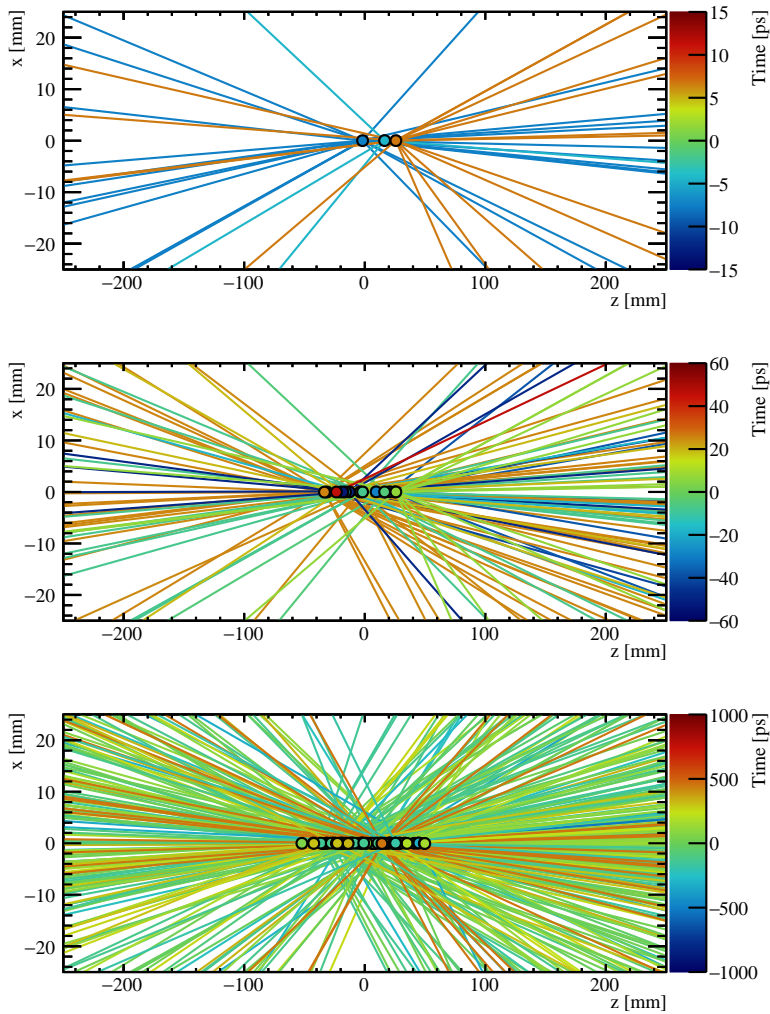
Figure 2.1: Three figures indicating the impact of temporal information on pile-up suppression for the VELO. The dots in the figures are the primary vertices and the lines indicate the particle trajectories originating from these primary vertices. The colours indicate the timestamp associated with the vertices and tracks. A typical proton-proton collision is shown, with on average 42 visible collisions. By including temporal information, and selecting a smaller window in time, the effective pile-up is artificially reduced, visible by a reduction of coloured vertices and tracks. The bottom figure shows the full proton-proton collision, the middle figure shows a time slice of 120 ps and the top figure shows a time slice of 30 ps.

2.1 Upgrade 2 VELO detector design scenarios

The VELO is designed and optimised as the *inner tracker* for the LHCb experiment. As a dedicated experiment for b- and c-quark physics, the LHCb experiment is instrumented in the forward direction, with the acceptance of the VELO limited to the region: $2 < \eta < 5$ ($13 < \theta < 269$ mrad). Track reconstruction, therefore, is also mainly focussed in the forward direction. Some tracks, however, are also reconstructed in the backward and radial direction to reconstruct the position of the primary vertices. The reconstruction efficiency of these tracks is not as critical as for those in the forward direction. The detector layout is designed with a requirement of four hits as a minimum for a track to be reconstructed.
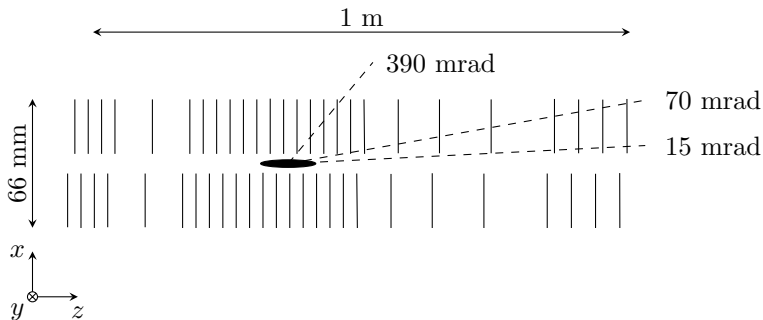
Figure 2.2: The spacing and layout of the individual modules of the VELO. The vertical black lines indicate the modules, and the black circle indicates the position of the interaction region. The dashed lines and the related angles indicate the approximate acceptance of the VELO. Figure adapted from [14].
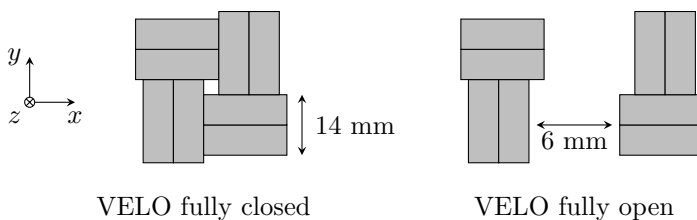
Figure 2.3: Side view of the detection material on each module. The VELO is shown in a closed (radially fully covered) and open position. The grey rectangles indicate the silicon sensors. Figure adapted from [14].

The VELO Upgrade 1 design consists of detection planes perpendicular to the beam axis. The spacing between the individual planes is optimised to ensure that the largest acceptance is covered with the four-hit track requirement. The resulting layout of the VELO is shown in fig. 2.2. The detector has 26 layers, which consist of two halves that approach the beamline from opposing sides. The

innermost point of the sensors is 5.1 mm away from the beam. The detector that makes up one-half of a detection layer, referred to as a module, is shown in fig. 2.4. The detection region extends around 3 cm from the module's innermost part and covers the beam axis radially (see fig. 2.3). The LHC beam vacuum is separated from the vacuum in which the modules operate by a thin aluminium box called the RF-foil. The side of this box which faces the beam has corrugations that match the modules' positions in z and minimises the amount of material traversed by particles within LHCb's acceptance [15]. This foil is made out of thin corrugated aluminium (not indicated in these figures). The design of the VELO Upgrade 1 detector is implemented as a reference scenario to the Upgrade 2 simulations presented in this chapter. The studies performed in this chapter mainly focus on the addition of temporal information to the VELO and the implication of this on the reconstruction performance. In these studies, the Upgrade 2 scenario refers to the Upgrade 1 detector geometry including temporal information while operating with the beam conditions that are currently considered for the Upgrade 2 detector.
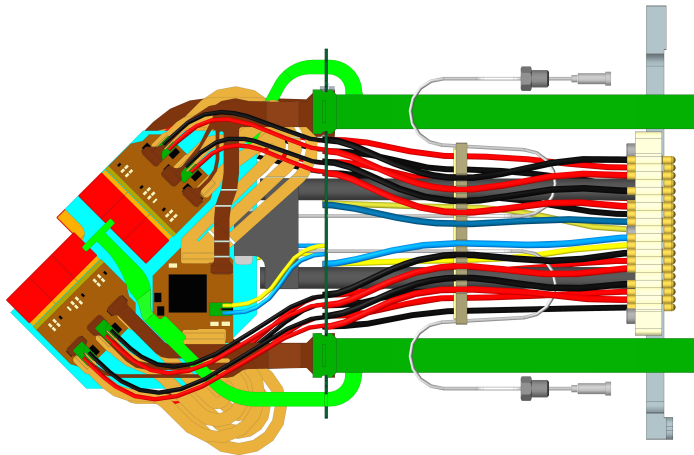
Figure 2.4: An illustration showing an individual module of the Upgrade 1 detector. The red squares indicate the hybrid pixel detectors and are offset to the detectors on the other side of the module for optimal coverage. The module overall is around 30 cm in length. Illustration taken from [16].

The layout of the Upgrade 1 VELO was optimised for the environment it is currently facing, with one of the major changes over its predecessor being a decreased inner radius from 8 to 5.1 mm. Since the conditions that the Upgrade 2 VELO will be facing are very different compared to the conditions for Upgrade 1, the layout and design of the detector are to be further studied before settling on a final design.

The increased pile-up density and the need to distinguish secondary heavy flavour decay vertices steer possible Upgrade 2 detector designs. The main challenge comes from the increased instantaneous luminosity, which directly affects the data transmission rate and track reconstruction performance as well as the accumulated radiation damage in the long term. The latter imposes strict requirements optimising the detector's inner radius versus the detector's lifetime and replacement frequency. In [13], two possible scenarios for the detector design of the VELO are considered. In this section, the aspects of these two scenarios will be further discussed. These two designs serve to guide the discussion on the final design and impact of the VELO.

The specifics of each of the two scenarios are mainly driven by the precision on the *impact parameter* (IP), the closest distance a track approaches its production vertex. This resolution can be expressed as [17]:

$$
\begin{aligned}
\sigma_{\mathrm{IP}}^2 = & \frac{\Delta_{01}^2 \left(\sigma_1^2 + \sigma_2^2\right)}{\Delta_{12}^2} \\
& + \frac{r_{\mathrm{foil}}^2}{p_T^2 \sqrt{2}} \left[0.0136 \sqrt{\frac{x_{\mathrm{foil}}}{X_0}} \left(1 + 0.038 \ln \frac{x_{\mathrm{foil}}}{X_0}\right)\right] \\
& + \frac{r_1^2}{p_T^2 \sqrt{2}} \left[0.0136 \sqrt{\frac{x_1}{X_0}} \left(1 + 0.038 \ln \frac{x_1}{X_0}\right)\right].
\end{aligned}
\tag{2.2}
$$

Here σ_1 and σ_2 are the uncertainties (hit resolution) on the first and second measurement points, respectively and depend on the detection technology and pixel size. The Δ_{ij} terms represent the distance between point i and point j. A convention is used where 0 is the point of origin, 1 and 2 are the first and second measurement points and *foil* refers to the RF-foil. Furthermore, r_i is the radius of layer i, x_i is the thickness of layer i, and X_0 is the radiation length. The first term represents the resolution of the track measurement based on the first two planes, the second term represents the scattering contribution from the material of the RF-foil and the third term represents the scattering contribution from the material of the first detection plane. From this formula, it can be seen that an increased spacing between the first and second measurement (Δ_{12}) will increase the precision of the impact parameter measurement. Similarly, moving the detector closer to the interaction region, reducing r_1, also results in an increased precision of this measurement. The latter, however, results in a more considerable amount of radiation damage, which degrades the operation of the detector. The contribution of the foil is the multiple scattering that particles experience when traversing material, resulting in a deviation in their direction and directly worsening the track reconstruction precision when extrapolating the measured track to its origin. This degradation of the track reconstruction precision also translates into

a degradation in the impact parameter resolution. Therefore, moving the RF-foil further out will result in a larger impact parameter uncertainty. These aspects should be considered when comparing the different detector designs since these imply different limitations such as a potential yearly replacement of the whole detector. Here, two opposite scenarios are highlighted for further studies: so-called scenarios A and B. The final design will most likely be a compromise between these two study cases.

- **Scenario A**: this scenario considers an identical geometrical layout to Upgrade 1, and therefore has an inner radius of 5.1 mm and an identical RF-foil shape. It also considers the same hit resolution (pitch of 55 μm) and therefore implies the same impact parameter resolution. This scenario, however, suffers from intense irradiation and may require a yearly detector replacement due to the annual accumulated fluence of 1.0×10^{16} 1 MeV n_{eq}/cm^2. Another challenge for this scenario is the very high hit rate, and therefore data rate, directly related to the increased instantaneous luminosity.

- **Scenario B**: this scenario considers a VELO that is moved out to an inner radius of 12.5 mm leading to a worsened impact parameter resolution due to the larger extrapolation arm. To compensate, it requires a significantly lighter (or complete removal of the) RF-foil to maintain a similar impact parameter resolution. This can be seen from the second and third term in eq. (2.2), which indicates that, to keep a constant combined contribution from the material of the first plane and the foil, the radius of the first hit can be increased if the material of the RF-foil (radiation length) is reduced. This scenario is chosen such that the particle fluence in the detector is similar to that of the Upgrade 1 detector, which implies that a similar technology can be used in the Upgrade 2 detector as was used in the Upgrade 1 detector. The increased radius, however, requires a better hit resolution to keep the impact parameter resolution the same as in the Upgrade 1 detector. This can be achieved by reducing the pixel pitch from 55 μm to 42 μm.

In this chapter, the implementation of temporal information is studied, focusing on a single scenario: scenario A.

2.2 Time resolution required for the VELO Upgrade 2

To understand which time resolution is required in scenario A, the reconstruction efficiency of primary vertices is studied for a luminosity of 1.0×10^{34} cm$^{-2}s^{-1}$ and 1.5×10^{34} cm$^{-2}s^{-1}$, both with 2400 colliding bunches. This results in an average of 42 visible interactions per bunch crossing (referred to as pile-up). The region in which collisions occur is approximately 15 μm wide (perpendicular to the beam) and approximately 44 mm long, with the interactions occurring over a length of

180 ps in time. All events used in this study are minimum bias events. In fig. 2.5 the reconstruction efficiency of primary vertices is shown as a function of the hit resolution. The dotted line indicates the primary vertex reconstruction efficiency for the Upgrade 1 detector, which does not include any temporal information. The efficiency of the two Upgrade 2 scenarios is found to decrease monotonously when the time resolution is decreased, while only showing a slight reduction in performance between 1.5×10^{34} cm^{-2}s^{-1} and 1.0×10^{34} cm^{-2}s^{-1}. The addition of time information in the primary vertex reconstruction algorithm decreases the possibility of misreconstructing a vertex caused by randomly combining two tracks that come close to each other. These results show that the performance of the Upgrade 1 condition is achieved if a single hit time resolution of at least 50 ps is implemented in the Upgrade 2 scenario. A worse time resolution results in an increase of random combinations, and therefore reduces the efficiency. From this study, the required single hit time resolution is set at 50 ps for the additional studies shown in this chapter.
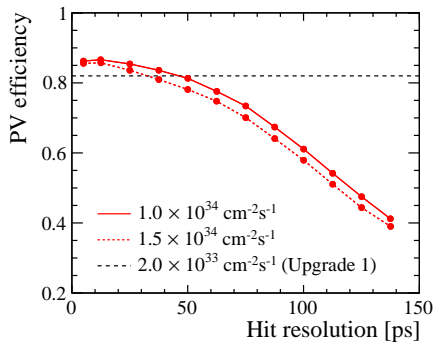
Figure 2.5: The primary vertex reconstruction efficiency as a function of hit time resolution. The black dashed line indicates the Upgrade 1 beam conditions and does not use temporal information. The solid and dotted red lines indicate two luminosity values for the Upgrade 2 beam conditions, and both include temporal information in the primary vertex reconstruction. Figure adapted from [13].

Subsequently, the impact of adding 50 ps per hit temporal information is studied for the primary vertex reconstruction efficiency as a function of the number of reconstructed tracks originating from the primary vertex, shown in fig. 2.6. The black line indicates the expected performance of the detector with Upgrade 1 beam conditions, and the blue and red lines indicate the performance of the detector under Upgrade 2 beam conditions with (red) and without (blue) the use of 50 ps temporal information per hit. One can see that the efficiency is significantly reduced when no temporal information is included, while the efficiency is recovered to the level of performance of the detector with the lower pile-up (Upgrade 1 beam conditions). Therefore, a proper primary vertex reconstruction requires the inclu-

sion of temporal information to maintain efficient primary vertex reconstruction in the high pile-up environment.
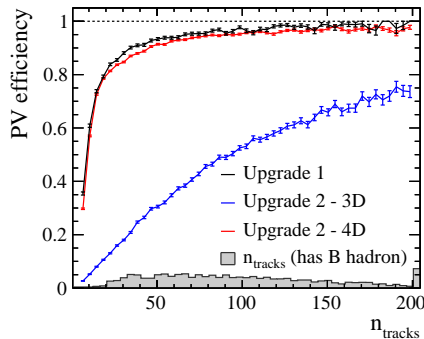
Figure 2.6: The primary vertex reconstruction efficiency as a function of the number of tracks emerging from the primary vertex. The black line indicates the performance of the Upgrade 1 detector, and the blue and red lines indicate two scenarios for Upgrade 2: without temporal information (blue) and with temporal information (red). Figure adapted from [13].

The impact of the addition of temporal information in the Upgrade 2 scenario and the ability to maintain the performance of currently employed parameters in physics analyses should be further investigated. A limited selection is discussed in section 2.5.

2.3 PARAMETERS FOR LHCB ANALYSES

In this section, we study several quantities that are typically used in LHCb analyses and discuss how their performance is affected by an increased pile-up. As a benchmark decay channel for B-physics, $B_s^0 \to D_s^- \pi^+$ is used, where the D_s^- meson further decays into two kaons and a pion. The B_s^0 meson is produced at the collision point of the two colliding protons, called the primary vertex. Particles originating from a primary vertex are called *prompt tracks*. After the B_s^0 meson travels a short distance of several millimetres, dictated by an exponential decay, it decays into the D_s meson and the pion. The position of this decay is called the secondary vertex. The D_s meson subsequently decays further until only stable kaons and pions remain. The particles originating from the secondary vertices are called *displaced tracks* as they typically do not point back to the primary vertex. The schematic overview of the $B_s^0 \to D_s^- \pi^+$ decay channel is shown in fig. 2.7.

To reconstruct the decay structure depicted in fig. 2.7, different tracks need to be combined to reconstruct the D_s^- meson, and subsequently to reconstruct the B_s^0 meson. In the selection process, prompt tracks must be distinguished from displaced tracks. This is an important aspect of selecting candidates of interest
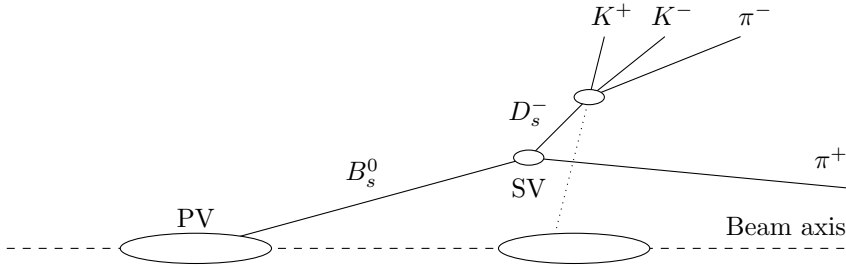
Figure 2.7: A schematic indication of a $B_s^0 \rightarrow D_s^- \pi^+$ decay. The black lines indicate the trajectories of the particles and the dotted line indicates that the K^- meson directly points to a non-associated primary vertex, which therefore might wrongly be reconstructed as a prompt particle.

in the trigger of LHCb. A variable that can be used to select these tracks is the impact parameter. The impact parameter is the distance between the extrapolated track and the closest primary vertex to this extrapolation. The impact parameter has proven to be a powerful discrimination parameter with the original VELO detector as well as the Upgrade 1 VELO. However, when the pile-up is further increased, the extrapolated tracks from secondary particles will randomly coincide with a unrelated primary vertex. This is indicated in fig. 2.7 by the dotted line pointing from the secondary vertex to a second primary vertex unrelated to the depicted decay.

In practice, the impact parameter requirement is applied by the unitless IP_{χ^2}. The IP_{χ^2} parameter is defined as the impact parameter distance divided by the total uncertainty and considers both the extrapolated uncertainty on the track and the uncertainty on the position of the primary vertex. For a given track, the IP_{χ^2} is determined for all reconstructed primary vertices in an event, and the lowest value is used as the discriminating value.

The impact of higher pile-up can be suppressed by employing the temporal information from detector hits in the VELO. When temporal information is included in the same decay, now shown in fig. 2.8 with the associated timestamps, a distinction between the timestamp of the displaced track and that of the non-associated primary vertex can be made. One can see that all components of the decay have a similar timestamp, whereas the unrelated primary vertex that at first would have been associated, does not match in time. Using temporal information, the correct primary vertex is now selected for all displaced tracks. One can even argue that, when an infinite precision can be achieved on both the momentum and temporal measurement, the track to primary vertex association can be based solely on the matching of timestamps of particles and vertices. In reality, the complications that arise from the need for momentum information in the earliest

stage of reconstruction make it impracticable, if not impossible, to execute a fully time-based association.
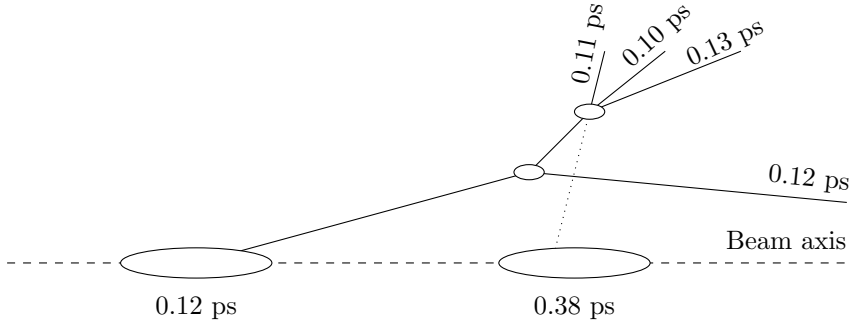
Figure 2.8: The same decay as fig. 2.7, but the associated timestamps, corrected for their time of flight, are indicated. One can see that all timestamps of the decay are similar, while the one from the non-associated primary vertex is different and can therefore be excluded.

The depiction of a decay as a stationary event, such as one often depicts in diagrams, is not truly correct at the timescales that we are considering. One should, and needs to, consider the time of flight and the propagation of the decay throughout all four dimensions: spatial and temporal. As these are related using the particle's velocity, it is crucial to know the velocity accurately. Since there is a large variety of velocities, the spread originating from a simple assumption, such as a common speed (for example the educated guess of the speed of light), quickly dominates over the resolution of the temporal measurement and will dilute the temporal information to the extent that it cannot be used to regain performance.

The relation between the position and time of a particle also implies that, in general, we cannot speak of a timestamp of a track without defining where on the track the timestamp is measured or extrapolated to. Since the distance between a track and the different primary vertices in an event is different, the track's timestamp needs to be corrected to compensate for the time of flight before a comparison between the timestamp of a track and a primary vertex can be made.

The addition of temporal information to regain physics performance will impact parameters used throughout analyses in LHCb. In the remainder of this chapter, we will highlight the impact on a subset of these parameters: the discriminating power of displaced tracks and the decay time resolution.

2.4   SIMULATION SETUP

For the timing study simulations, events of the type $B_s^0 \to D_s^- (\to K^- K^+ \pi^-)\, \pi^+$ (and its charge-conjugate) are used with the expected increase in instantaneous luminosity as well as other settings of the beam parameters for the Upgrade 2 beam conditions, which are taken from [18], and corresponds to a luminosity of 1.5×10^{34} cm$^{-2}s^{-1}$. The standard LHCb simulation package (Gauss v53r1 [19]) is used to generate the events with the inputs described before. The interactions of the final state particles with the detector material and the detector digitisation response are simulated with the GEANT4 toolkit [20] as described in [21]. This simulation yields all true timestamps and locations of all particle and material interactions, which in turn are smeared based on their time and spatial resolution according to the parameters under study.

To simulate an accurate representation of the implications of the primary vertex reconstruction, the spatial and temporal resolution of the primary vertices were taken directly from Monte Carlo and have been smeared based on the number of prompt tracks in the VELO acceptance. This method is used since the resolutions depend on the number of tracks used to reconstruct a primary vertex, as shown in fig. 2.9. This figure shows the x, z and time resolution of reconstructed primary vertices as a function of the number of tracks in the primary vertex. The black line indicates the resolution under the Upgrade 1 conditions, and the red line indicates the resolution for the Upgrade 2 conditions where temporal information is included to assign tracks to the vertex. The slight difference between the two curves is due to the difference in beam scenarios between the Upgrade 1 conditions and the Upgrade 2 scenario that is considered. To simulate the effect of merging primary vertices in the Upgrade 2 scenario which does not include temporal information, 25% of the primary vertices are merged with a second primary vertex and a larger spatial uncertainty of 1 mm is assigned to this merged primary vertex. After these studies were performed, a dedicated 4D (using spatial and temporal information) tracking algorithm was developed. This new tracking algorithm will allow studies to have a more accurate representation of the primary vertex reconstruction.

2.5   SIMULATION RESULTS

To understand the consequences of a 50 ps single hit resolution, two aspects have been studied. Firstly, the ability to discriminate between particles from the primary vertex and particles from secondary vertices in section 2.5.1, and secondly, the decay time resolution of a B_s meson in section 2.5.2. Both are expected to have reduced performance in an environment with an increased combinatorial background due to the increased track and vertex density. As a baseline, the Upgrade 1 performance is taken and compared to the performance of the Upgrade 2 scenario with and without temporal information. Finally, the impact of changing the acceptance of the VELO detector will be discussed in section 2.5.3.
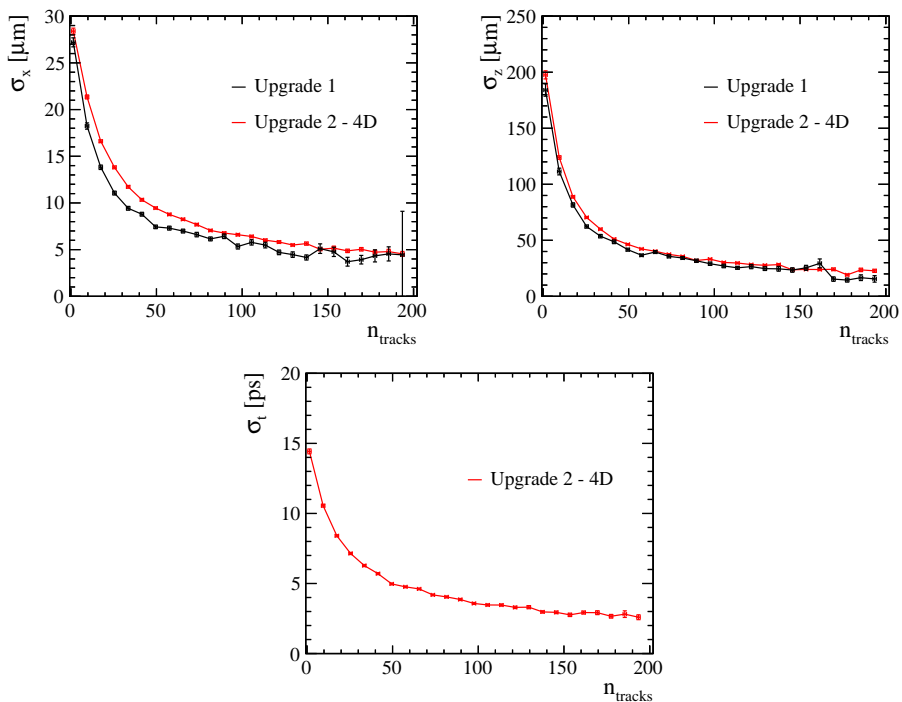
Figure 2.9: The resolution of the reconstructed primary vertices perpendicular (parallel) to the beam axis is shown on the top left (top right) and the time resolution is shown on the bottom. The black line indicates the resolution for the Upgrade 1 conditions, and the red line indicates the resolution for the Upgrade 2 scenario where temporal information is included in the primary vertex reconstruction. Figures adapted from [13].

2.5.1   THE IMPACT OF TIMING INFORMATION ON THE DISCRIMINATING POWER

As discussed in section 2.3, one of the most important parameters that aid in discriminating between prompt and displaced particles is the impact parameter, and more specifically the impact parameter significance (IP_{χ^2}). A *ROC curve* (Receiver Operating Characteristic curve) is used to quantify the impact of the increased instantaneous luminosity on finding displaced tracks. The tracks are selected based on their IP_{χ^2}, where for each value of IP_{χ^2} the number of displaced tracks that have a higher IP_{χ^2} than the threshold are counted and divided by the total amount of displaced tracks in the dataset (y-axis). At the same time the number of prompt tracks with an IP_{χ^2} higher than the threshold is divided by the total number of prompt tracks in the dataset (x-axis). These two values are plotted against each other, and this sequence is repeated for a range of IP_{χ^2}

values. When temporal information is included in the reconstruction, only the IP$_{\chi^2}$ is included when the track passes the primary vertex within 3σ in time.
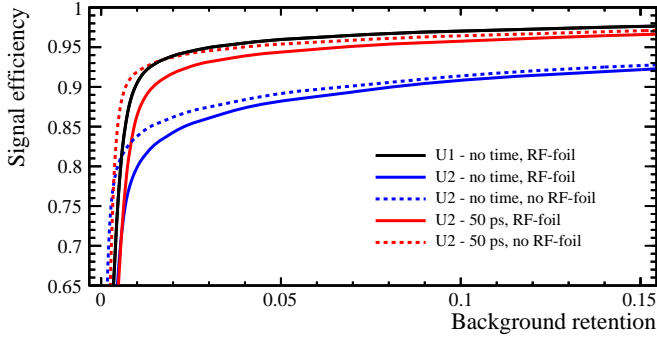
Figure 2.10: The ROC curve indicating the discrimination power of the IP$_{\chi^2}$ to distinguish displaced from prompt tracks. The black line indicates the current Upgrade 1 performance, and the other line styles and colours indicate different scenarios that are considered for Upgrade 2. Besides the addition of temporal information, the effect of the RF-foil is also shown by including (solid line) or removing (dashed line) the RF-foil. Figure adapted from [13].

This procedure yields the ROC curve shown in fig. 2.10, which shows the effectiveness of the IP$_{\chi^2}$ as a discrimination tool to find displaced tracks for five different scenarios. The tracks have been fitted using a simplified Kalman filter, and only tracks with a momentum of at least $2\,\mathrm{GeV}/c$ in the LHCb acceptance are included, similar to the current set of requirements for the reconstruction. The solid black line indicates the performance in the Upgrade 1 beam conditions, while the other four dashed/dotted lines indicate different detector designs under the Upgrade 2 beam conditions. Within the Upgrade 2 scenarios, two separate cases are considered: with or without the RF-foil and with or without using temporal information. Considering the Upgrade 2 scenario in which the RF-foil is included, the performance drops significantly without temporal information and is almost completely recovered by adding a temporal measurement with a resolution of $50\,\mathrm{ps}$ time resolution per hit. The performance is further recovered by removing the amount of passive material coming from the RF-foil, since this decreases the multiple scattering before the first measurement of the track. From this result, the conclusion is drawn that including timing information with a $50\,\mathrm{ps}$ per hit time resolution in the VELO allows maintaining a good performance even under the high pile-up conditions of high luminosity running, irrespective of the in- or exclusion of the RF-foil.

2.5.2 THE IMPACT OF TIMING INFORMATION ON THE DECAY TIME RESOLUTION

By precisely reconstructing the creation and decay position of a particle, the travelled distance is determined. Combining this distance with the momentum measurement, the particle decay time can be calculated. In this study, the D_s meson origination from a B_s meson is used to study the decay time resolution of the D_s meson using the previously used decay channel.

To reconstruct the D_s meson, two oppositely charged kaons and one charged pion are combined if the distance of closest approach of the trajectories (tracks) is maximally 0.1 mm. Only tracks are considered that have an impact parameter of more than 0.1 mm, are within the LHCb acceptance, have a momentum of at least 5 GeV/c and have at least a transverse momentum of at least 200 MeV/c. Only primary vertices are considered for the impact parameter determination that fall within 3σ in time if temporal information is included, otherwise all primary vertices are considered. In the higher pile-up environment, there is a larger probability for random combinations, and therefore a degradation of the decay time resolution is expected. Similarly to the implementation of temporal information in the calculation of the impact parameter, the decay tracks must be within 3σ in time. The reconstructed vertex of these three particles is used as the decay point of the D_s meson.

The reconstructed D_s meson is used to find a second pion, which satisfies the requirements mentioned before, that comes close to the reconstructed flight path of the D_s meson. If the distance between them, called the *Distance Of Closest Approach* (DOCA), is less than 0.1 mm, the combination of the D_s meson and the pion is reconstructed as the B_s meson. This point is used as the production point of the D_s meson and the distance between the production and decay points is calculated. From this distance, the reconstructed decay time is derived using the true momentum of the particle and compared to the true decay time that was given by the simulation. The residual between these two values for the three scenarios considered is shown in fig. 2.11. This figure also presents the fitted width σ of a Gaussian function, as well as the calculated RMS to quantify the distribution's tails. The fitted width of the distribution is found to stay similar in all scenarios, while the RMS shows a significant degradation under the high pile-up conditions of the Upgrade 2 beam conditions. This degradation is again mostly recovered when the temporal information is included, however, the tails of the distribution are still slightly more prominent compared to the Upgrade 1 conditions. This result indicates that implementing a 50 ps hit time resolution significantly reduces the impact of the higher pile-up on the performance of the VELO.
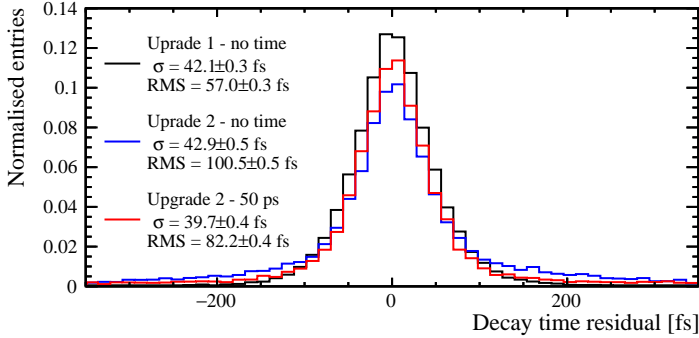
Figure 2.11: The decay time residual of the reconstructed decay time of a D_s meson. The black line indicates the Upgrade 1 performance and the blue (red) line indicates the performance in the Upgrade 2 conditions without (with) temporal information. The values indicated in the legend are the width of a Gaussian distribution fitted to the distribution (σ) and the RMS of the full distribution.

2.5.3 THE IMPACT OF THE ACCEPTANCE OF THE VELO

The reconstruction probability of a D_s meson is studied for the case of a reduced small angle acceptance of the VELO. As discussed before, reducing the acceptance and keeping the overall VELO the same length means that the sensors can be positioned further away from the beamline, and thus from the interaction point. This has both detrimental and beneficial effects. The benefit is the drastically lower radiation damage further away from the beamline. At the same time, the major downside is a degradation of the impact parameter resolution (eq. (2.2)) as well as a reduction in acceptance, the latter is studied here by considering the loss of tracks in the high pseudorapidity area: $\eta > 4.7$.

In the high pseudorapidity region, the pointing resolution of the tracks is significantly worse than the resolution of the reconstructed primary vertices along the beamline, which makes it generally difficult to assign these tracks to the correct primary vertex (illustrated in fig. 2.12). In this illustration, two primary vertices are indicated alongside three different tracks. The oval shape of the primary vertices depicts the uncertainty of their reconstructed positions, which in the beam direction is much larger compared to the direction perpendicular to the beam direction due to the forward acceptance of LHCb. Track 1 and 2, indicated in this figure, show two different tracks at a low pseudorapidity: one prompt track and one displaced track. The impact parameter for these two tracks is a clear discriminating variable to select the displaced track out of these two. The third track indicated is in the high pseudorapidity range and potentially is a displaced track from one of the primary vertices. However, due to the small angle to the beam axis, the extrapolated track has a large probability of randomly intersecting

an unrelated primary vertex, resulting in a badly measured impact parameter. This in turn dilutes the discriminating power of the impact parameter at high pseudorapidity, and thus the statistical gain by including this region in analyses might be minimal.

The addition of temporal information can however aid in regaining this discrimination power. By comparing the particle's timestamp to that of the primary vertices, unrelated vertices can partially be excluded. Therefore, the addition of temporal information can aid in the discrimination power in the high pseudorapidity region. This performance improvement however only aids to a certain extent, since at very small angles close to the beamline, even after selecting the primary vertices that fall within 3σ in time, the number of random vertices lining up is simply too large.
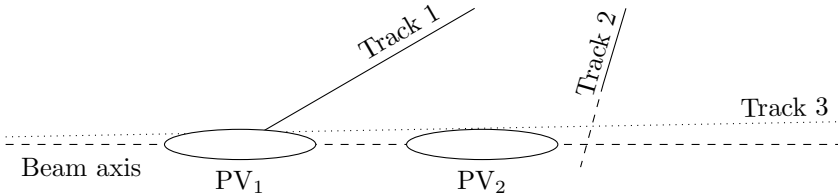
Figure 2.12: In this figure two different primary vertices are indicated and labelled accordingly, as well as three different particle tracks. Track 1 is a prompt track originating from PV_1, track 2 is a displaced track from PV_2, and track 3 does not originate from either PV_1 or PV_2. However, the extrapolated track passes close by the two primary vertices.

To understand the impact of the high rapidity region on a typical analysis, the decay products of a $D_s(KK\pi)$ meson, originating from a B_s meson are studied via a counting study in different pseudorapidity regions. The same requirements set for the decay resolution study are applied here, as well as assuming a perfect particle identification process. The selection of the decay product is made using the pseudorapidity of the decay products, effectively making the forward acceptance of the VELO slightly smaller, otherwise using the layout of the Upgrade 1 VELO.

The number of reconstructed D_s mesons which have (part of) their decay products in $4.7 > \eta > 5.0$ (with respect to $2 > \eta > 4.7$) and $4.85 > \eta > 5.0$ (with respect to $2 > \eta > 4.85$) are counted to differentiate between the performance in the low and high pseudorapidity regions. The D_s meson is reconstructed if two oppositely charged kaons and a pion, all with an impact parameter of at least $0.1\,\mathrm{mm}$, have a DOCA of less than $0.1\,\mathrm{mm}$. This D_s meson is considered part of the signal if the two kaons and the pion truly originated from the D_s meson, and are considered background if at least one of the three decay products is not related to the D_s meson. The background case can also exist where three unrelated particles

randomly approach each other, while they do not originate from a D_s meson, which leads to an additional D_s meson that is wrongly reconstructed. In the case of the addition of temporal information in the Upgrade 2 scenario, only primary vertices that fall in 3σ temporal windows with the decay product are considered for the determination of the impact parameter. Similarly, the timestamp of all three decay products at the point of closest approach (the secondary vertex) should fall within a 3σ temporal window of each other.

The results from this counting study are shown in table 2.1 through table 2.6 and contain the results of the Upgrade 1 scenario and the Upgrade 2 conditions with and without temporal information (assuming a 50 ps hit resolution). The maximum amount of signal is higher in the Upgrade 1 conditions because a larger data sample was used, therefore, the absolute numbers cannot be compared directly between Upgrade 1 and Upgrade 2. To compare the different scenarios, the signal-to-background ratio (S/B) is indicated.

These results show a significant degradation of the signal-to-background ratio when more decay products are present in the high pseudorapidity region, independent of the scenario. A similar trend is present when moving from Upgrade 1 to Upgrade 2 without temporal information, where there is a significant loss in signal-to-background ratio. This loss in signal-to-background ratio is fully recovered when including temporal information, indicating that the addition of temporal information is successful in suppressing background events as well as improving the discriminating power of the impact parameter. Besides the difference in signal-to-background ratio in the high pseudorapidity region, one can also see that the absolute number of signal events that have at least one track in this region is relatively small, around 10%. Therefore, the impact of this region on the total statistics is minimal. What also should be noted is that, contrary to the other scenarios, the addition of temporal information in the case of at least two tracks in the highest pseudorapidity, $\eta > 4.85$, does not fully recover the performance. This is most likely due to the very small angle to the beamline, which dilutes the power of temporal information.

The relative contribution of this high pseudorapidity region in combination with the significantly lower signal to background ratio in this region (from around 6 to 2), for both the $\eta > 4.7$ and $\eta > 4.85$ case, gives the motivation to decrease the acceptance of the VELO from $2 > \eta > 5$ to $2 > \eta > 4.7$ based on this decay channel. Different physics channels should be studied to ensure that none of them extensively use data from this region, as well as to understand how the impact of this change in the VELO propagates to the other subdetectors in order to fully understand the impact of such a change in the layout of the VELO.

In summary, this study indicates that the high pseudorapidity range does not contribute in statistical gain in a high particle multiplication scenario. Therefore, if the acceptance of the VELO could be reduced, this indicates that placing the detector at a larger minimum radius, leading to a lower radiation damage requirement, could allow the development of a cheaper overall detector, and perhaps ease the fast-timing requirements. This, in turn, allows a broader selection of sensor and ASIC technologies that can be considered for the VELO, since radiation tolerance is often the limiting factor.

Table 2.1: All tracks in $2 < \eta < 4.7$

	Signal	Background	S/B
U1	19707	3128	6.30
U2	14104	13364	1.06
U2 time	14041	2170	6.47

Table 2.2: All tracks in $2 < \eta < 4.85$

	Signal	Background	S/B
U1	20546	3587	5.73
U2	14623	14134	1.03
U2 time	14537	2408	6.04

Table 2.3: ≥ 1 track in $4.7 < \eta < 5$

	Signal	Background	S/B
U1	1727	976	1.77
U2	1017	2179	0.47
U2 time	1016	508	2.00

Table 2.4: ≥ 1 track in $4.85 < \eta < 5$

	Signal	Background	S/B
U1	803	461	1.74
U2	464	1116	0.42
U2 time	483	239	2.02

Table 2.5: ≥ 2 track in $4.7 < \eta < 5$

	Signal	Background	S/B
U1	500	160	3.13
U2	271	217	1.25
U2 time	262	62	4.23

Table 2.6: ≥ 2 track in $4.85 < \eta < 5$

	Signal	Background	S/B
U1	126	29	4.34
U2	64	52	1.23
U2 time	57	21	2.71

2

2.6   Summary

In this chapter the implications of the increased instantaneous luminosity and the subsequent higher pile-up expected for the next upgrade of LHCb are discussed, and more specifically for the VELO Upgrade 2. A possible solution to mitigate the detrimental effects of this increase is the addition of temporal information on a per-hit basis. The required time resolution for such an implementation in the VELO is studied in this chapter, along with the implication for some of the quantities used in the physics analysis. We determined from simulation that a 50 ps per hit resolution results in a similar performance as the Upgrade 1 detector. The additional pile-up results in a larger combinatorial background for all quantities studied, and is fully mitigated by adding temporal information. The impact of the higher instantaneous luminosity on track finding and data rate is not studied in this work but should be investigated in parallel to the development of the detector in order to cope with the Upgrade 2 scenario.

The required 50 ps hit time resolution sets a stringent goal for the detector development in the coming years. Therefore, both the sensor resolution and the electronics performance should be significantly improved from the present resolution as shown in chapter 5 and chapter 7. The remaining chapters focus on the physics principles (chapter 3) and technology (chapter 4) behind the current state-of-the-art silicon detectors employed in high energy physics as well as discussing different characterisation techniques that are used in the development of these detectors.

Chapter 3

Silicon particle detectors

I N THE CURRENT AGE of high energy physics, silicon tracking detectors have become a central component of many high energy physics experiments. Previous tracking detectors, ranging from photosensitive plates, cloud and bubble chambers, and multi-wire proportional chambers (MWPC), are limited in both their detection speed and reconstruction time, but also in their position resolution. The introduction of silicon sensors as particle trackers has been crucial for state-of-the-art high energy physics experiments. They are therefore envisioned to be part of the next generation of high energy physics experiments. However, there is also room for further improvement in multiple aspects of these detectors such as the readout speed, and position and time resolution. In fact, these aspects need to be improved to be able to provide sufficient information to deploy silicon tracking detectors for the next generation of experiments.

Over the last few years, the high energy physics research and development community has focused on achieving fast-timing tracking detectors that operate at high rates, have excellent spatial resolution and withstand high radiation levels. In this chapter, the fundamental principles behind silicon particle detectors are reviewed, along with the implications of long-term operation in these experiments. We start with an introduction to the principles of semiconductors and pn-junctions and how they are deployed to detect highly energetic particles and photons. Among others, the time resolution and charge collection mechanisms are discussed. Subsequently, we discuss how highly energetic particles can damage these silicon detectors and the implication of this on the operation of silicon detectors.

3.1 BAND STRUCTURE OF SILICON

Silicon tracking detectors are based on the principle of semiconductor particle detectors, particularly the band structure and density of states in semiconductors.

In general, materials can be classified into three types: insulators, conductors, and semiconductors. Semiconductors are characterised by the existence of a relatively small energy bandgap within the band structure of the material. This band structure dictates which energy states charge carriers within the material can occupy as a function of their wavevector k. In case there is a clear band where, for a specific energy, no states are allowed, the material is characterised as either a semiconductor or insulator depending on the size of the bandgap, while the absence of this gap classifies the material as a conductor. For semiconductors, this energy bandgap is in the order of electronvolts, which corresponds to the energy of thermal fluctuations at room temperature as well as to the energy of optical photons. Therefore, processes that can excite an electron from the valence band to the conduction band can easily occur. The three material types are illustrated in fig. 3.1.

A further distinction can be made for semiconductors: intrinsic and extrinsic. An intrinsic semiconductor is a material that can be classified as a semiconductor without the addition of additional foreign atoms. For an extrinsic semiconductor, the pure material can not be classified as a semiconductor, but after adding foreign atoms in the material, it becomes a semiconductor.
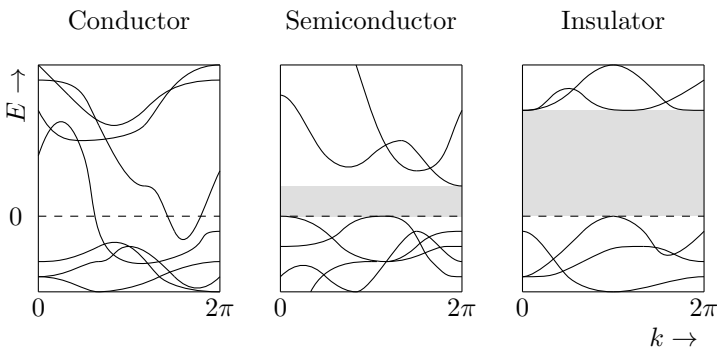
Figure 3.1: Illustration of an example banddiagram of a conductor, semiconductor, and an insulator. The energy band where no states are allowed in the semiconductor and the insulator is called the (energy) bandgap, and is indicated by the shadowed region.

The characteristics of a solid-state material can be derived from its density of states. This describes the number of available states per unit volume and per unit energy. For a normal material (three dimensions), the allowed states in k-space,

or sometimes also called momentum space, are quantised [22] in *cubes* of length π/L, where L is the length of the cube of material in normal space. Therefore, each cube in momentum space has a volume of $\left(\frac{2\pi}{L}\right)^3$. Due to the Pauli exclusion principle [23], only two electrons can occupy the same momentum space cell at the same time. Therefore the total amount of electrons that are present in all momentum space is given by

$$N = 2\frac{V_{\text{solid}}}{(2\pi/L)^3} = 2 \cdot \left(\frac{L}{2\pi}\right)^3 \cdot \frac{4}{3}\pi k^3. \tag{3.1}$$

Here V_{solid} is equal to the volume in momentum space of a sphere with radius k, and subsequently k denotes the wavevector (or momentum). From this expression for the number of electrons, the density per unit energy can be determined

$$\frac{\mathrm{d}N}{\mathrm{d}E} = \frac{\mathrm{d}N}{\mathrm{d}k}\frac{\mathrm{d}k}{\mathrm{d}E} = \left(\frac{L}{\pi}\right)^3 \pi k^2 \frac{\mathrm{d}k}{\mathrm{d}E}. \tag{3.2}$$

The energy as a function of wavevector for electrons is given by $E(k) = \frac{\hbar^2 k^2}{2m^*}$ [22], where $m^* \equiv m^*_{e/h}$ represents the effective mass of an electron/hole. From this it follows that $\frac{\mathrm{d}k}{\mathrm{d}E} = \frac{m^*}{\hbar^2 k}$, and $k = \sqrt{2m^* E}/\hbar$. Combining these relations with eq. (3.2) yields the density of states per unit volume and per unit energy

$$g(E_{\text{eff}})dE_{\text{eff}} = \frac{1}{L^3}\frac{\mathrm{d}N}{\mathrm{d}E_{\text{eff}}} = \frac{1}{2\pi^2}\left(\frac{2m^*_{e/h}}{\hbar^2}\right)^{3/2} E_{\text{eff}}^{1/2} dE_{\text{eff}}. \tag{3.3}$$

Here E_{eff} denotes the effective energy, which is $E - E_c$ in the conduction band and $E_v - E$ in the valence band, and essentially is the energy difference between the energy state and either the conduction or valence band. A more detailed derivation of the density of states per unit volume and per unit energy can be found in [22].

The energy states are not filled randomly but in a specific order. At low temperatures (near $T = 0\,\text{K}$) the lowest energy states are filled first, while higher energy states are only filled when there is no lower energy state available. The highest level that is filled in this situation is referred to as the Fermi level. However, when the temperature is non-zero, this transition between filled and non-filled sites becomes more gradual instead of abrupt. This behaviour can be described by the Fermi-Dirac distribution [24]:

$$f(E) = \frac{1}{1 + e^{(E-E_f)/k_b T}}, \tag{3.4}$$

where k_b is the Boltzmann constant. From the density of states (eq. (3.3)) and the distribution of electrons (eq. (3.4)), the carrier density can be calculated, which describes the number of electrons at each energy level within the band. For

the conduction band, the carrier density is given by the density of states $g_c(E)$ multiplied by the probability distribution to find an electron at that energy [22]

$$n(E) = g_c(E) f(E). \tag{3.5}$$

This probability function for the conduction band is illustrated in fig. 3.2. The black line indicates the density of states in the conduction band $(g_c(E))$, the orange line indicates the Fermi-Dirac distribution and the red area indicates the charge density $n(E)$. The carrier density per unit energy yields the total number of charge carriers. To calculate the total number of carriers within the conduction band, the carrier distribution is integrated from the lowest energy E_c to the highest energy of the conduction band. However, because $\lim_{E \to \infty} f(E) = 0$, the upper limit of the integral can be set to infinity. The total number of electrons in the conduction band follows from combining eq. (3.3), eq. (3.4) and eq. (3.5) and is given by [22]

$$n = \int_{E_c}^{\infty} n(E)dE = \int_{E_c}^{\infty} \frac{1}{2\pi^2} \left(\frac{2m_e^*}{\hbar^2} \right)^{3/2} \sqrt{E - E_c} \, \frac{1}{1 + e^{(E - E_f)/k_b T}} dE. \tag{3.6}$$

This integral cannot be solved analytically. However, a numerical solution can be found for each energy. Similarly, the number of holes can be found for the valence band [22]

$$p = \int_{-\infty}^{E_v} g_v(E) \left[1 - f(E) \right] dE \tag{3.7}$$

$$= \int_{-\infty}^{E_v} \frac{1}{2\pi^2} \left(\frac{2m_h^*}{\hbar^2} \right)^{3/2} \sqrt{E_v - E} \, \frac{1}{1 + e^{(E - E_f)/k_b T}} dE. \tag{3.8}$$

The expression for both n and p can be simplified in the non-degenerate limit. This limit assumes that the Fermi level is at least $3k_b T$ (≈ 0.08 eV at $300\,\mathrm{K}$ - compared to a bandgap of generally > 1 eV) from both bands. In this limit, the Fermi-Dirac distribution can be replaced by a simpler exponential function [25], and thus the carrier density can be expressed as

$$n \approx \int_{E_c}^{\infty} \frac{1}{2\pi^2} \left(\frac{2m_e^*}{\hbar^2} \right)^{3/2} \sqrt{E - E_c} \, e^{(E_f - E)/k_b T} dE \tag{3.9}$$

$$\approx N_c \, e^{-\frac{E_c - E_f}{k_b T}}, \tag{3.10}$$

and

$$p \approx \int_{-\infty}^{E_v} \frac{1}{2\pi^2} \left(\frac{2m_h^*}{\hbar^2} \right)^{3/2} \sqrt{E_v - E} \, e^{(E_f - E)/k_b T} dE \tag{3.11}$$

$$\approx N_v e^{-\frac{E_f - E_v}{k_b T}}. \tag{3.12}$$

Here N_c and N_v represent the effective density of states in the conduction and valence band. They can be approximated as

$$N_c = 2 \left(\frac{2\pi m_e^* k_b T}{h^2} \right)^{3/2} \tag{3.13}$$

$$N_v = 2 \left(\frac{2\pi m_h^* k_b T}{h^2} \right)^{3/2}. \tag{3.14}$$

For the situation where the Fermi level lies between the conduction and valence band, the density of electrons and holes in the valence and conduction band is shown in fig. 3.3. A more in-depth derivation of these carrier densities can be found in [26].
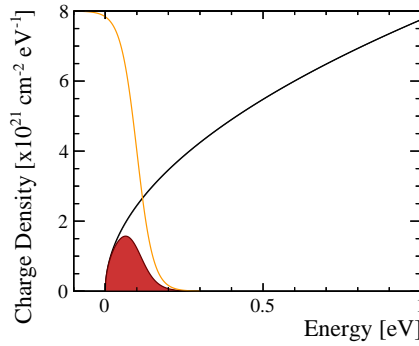
Figure 3.2: The conduction band for a material that has the conduction band energy E_c at $0\,\mathrm{eV}$. The black line indicates the band $g_c(E)$, the orange line indicates the Fermi-Dirac distribution $f(E)$, and the red area indicates the charge density $n(E)$.

The model discussed in this case is simplified. For more complex materials, multiple bands will be present, as well as a dependency on the momenta of the electrons (the wavevector k). The bandstructure of materials is frequently depicted using a *banddiagram*, which depicts the allowed energy levels as a function of the momenta of the charge carriers. Such a banddiagram can be measured using angle-resolved photoemission spectroscopy (ARPES), in which photons are used to eject electrons from the material. Both the wavevector and the energy of these electrons are measured, from which the distribution of the bands can be determined. An example banddiagram of silicon is shown in fig. 3.4. The different letters in this figure indicate specific points in the *Brillouin zone* of silicon.

Figure 3.3: The valence and conduction band for a material that has the Fermi level at $0.6\,\mathrm{eV}$, $E_v=0\,\mathrm{eV}$, and $E_c=1.1\,\mathrm{eV}$. The difference in the width of the two bands is due to the different mobility of electrons and holes. The black line indicates $g_{v/c}(E)$, the orange line indicates the Fermi-Dirac distribution $f(E)$, the blue area indicates the charge density $p(E)$, and the red area indicates the charge density $n(E)$.
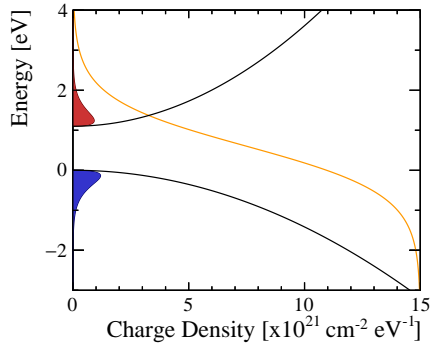
3.2   PN-JUNCTION

The conductive properties of silicon can be altered by *doping* the material, allowing a more versatile application of silicon. During this process, a number of atoms that have a different number of valence electrons is introduced into the crystalline lattice. This number of atoms is much larger than the intrinsic carrier concentrations n and p. Thus the total carrier concentration is often expressed as solely the number of charge carriers added by doping.

In principle, doping and the subsequent creation of a pn-junction can be applied in any semiconductor. In practice, however, achieving high enough quality and purity of a semiconductor to use it as a pn-junction is difficult. Silicon, however, has been used for decades and the knowledge of the creation of a high purity *wafer* has been perfected over this time. Therefore, silicon is at the moment the best choice for high-purity and quality pn-junctions in high energy physics. However, different materials have been used in smaller experiments such as cadmium-tellurite [28], gallium-arsenide [29] and new materials such as diamond and silicon-carbide are currently a focus of research as a possible replacement for silicon. The research in this dissertation, however, focuses on silicon detectors (pn-junction) and will therefore be used in this chapter as the main material under consideration.

Silicon has four valence electrons that bind the silicon atom to its four closest neighbours. If a foreign atom with an additional valence electron is introduced in the lattice, this electron will not be bound to the neighbouring atoms in the
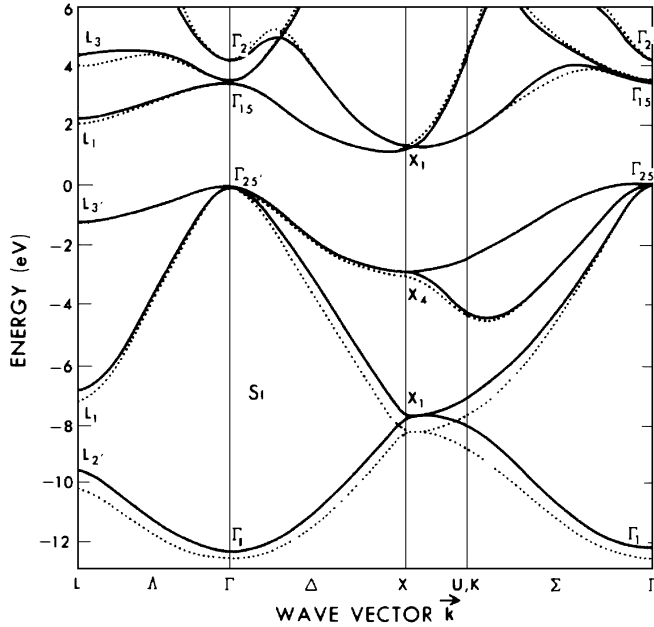
Figure 3.4: This figure depicts the band diagram of silicon. These bands show the allowed energy levels for charge carriers at different momenta. The bandgap of silicon is also visible between an energy of 0 eV and 1.12 eV. The x-axis depicts different positions within the Brillouin zone, indicated by the letters, and the indices indicate a numbering of bands. Figure taken from [27].

lattice (fig. 3.5 left). Therefore, this electron can be excited into the conduction band with just a small amount of energy. The single energy state that is created by introducing this atom, lies within the bandgap but close to the conduction band, resulting in a higher Fermi level. Since this type of doping introduces an additional electron, the atom is called donor, and the silicon is now called *n-type*. A common atom to dope n-type silicon is phosphorus.

An atom with three valence electrons can also be introduced into the lattice (fig. 3.5 right). In this case, not all bonds to the neighbours can be filled. This missing bond can be filled by a neighbouring valence electron or by recombination. This absence of an electron is also referred to as a *hole*, and thus the dopant atom is referred to as an acceptor, creating *p-type* silicon. The presence of these non-filled bonds creates states that lie in the bandgap close to the valence band, resulting in a shift of the Fermi level towards the valence band. Boron atoms are commonly used to dope p-type silicon. Typically, the concentration of these doping atoms is low, ranging from one dopant for every 100 million silicon atoms to one dopant for every 1000 silicon atoms.
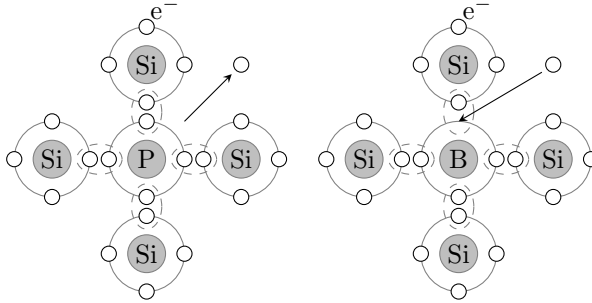
Figure 3.5: Left (Right) schematically shows how a phosphorus (boron) atom introduces an additional electron (hole) in the lattice. The four neighbouring silicon atoms are shown as well.

By connecting p-type silicon with n-type silicon, a pn-junction will develop at the interface. Since the concentration of electrons and holes differ between the two types, due to their different dopant types, the electrons at the interface will diffuse from the n-type side to the p-type side and the holes will diffuse from the p-type side to the n-type side. The minority carriers, the electrons in p-type and holes in n-type, will recombine with the majority carriers, which results in a current over the junction. Since both types of silicon are initially neutrally charged, this deficit of majority carriers results in a region of negative space charge on the p-type side and positive space charge on the n-type side of the junction. This difference in space charge leads to a build-up of an electric field over the junction, creating a drift current over the junction. Since the drift and diffusion current have the opposite sign, they cancel when the pn-junction is at thermal equilibrium. When this equilibrium is reached, the Fermi level is constant throughout the junction. However, since the Fermi level is closer to the conduction band for n-type silicon, and closer to the valence band for p-type silicon, the potential on either side is different to ensure that the Fermi level is constant (see fig. 3.6). The potential difference between the two sides of the pn-junction is referred to as the *built-in voltage* V_{bi}, and is given by [30]

$$V_{bi} = \frac{k_b T}{q} \ln\left(\frac{N_a N_d}{n_i^2}\right), \qquad (3.15)$$

where N_a and N_d are the acceptor and donor doping concentrations respectively, n_i the intrinsic carrier concentration (which generally is around the same magnitude or smaller as the doping concentration), k_b is the Boltzmann constant, T the temperature, and q the elementary charge.

The *depletion zone* of a pn-junction is defined as the region in which no free charge carriers are present. The width of this depletion zone, defined perpendicular

to the junction interface, due to the built-in voltage is [30]

$$w = \sqrt{\frac{2\varepsilon_0 \varepsilon_{Si} V_{bi}}{q} \left(\frac{1}{N_a} + \frac{1}{N_d}\right)}. \tag{3.16}$$

Here ε_0 is the permittivity of a vacuum, and ε_{Si} is the permittivity of silicon.

An external voltage can be applied over the pn-junction. If a positive potential difference larger than V_{bi} is applied to the p-type side, it allows a current to flow through the junction. This mode of operation is called forward bias. However, if a negative potential difference is applied to the p-type side, it does not allow any current to flow except a small leakage current, generally referred to as *dark current*. In the forward bias case, the applied voltage counteracts the built-in voltage, lowering the width of the depletion zone, resulting in more charge carriers diffusing over the pn-junction. This allows a net current to flow over the junction and indicates the typical usage of diodes in most electronic circuits. When a reverse bias is applied, the potential difference over the junction is enlarged, resulting in a larger depletion zone. The width of the depletion zone can be expressed similarly to that of the built-in depletion zone since only the applied voltage is changed under the presence of an external voltage: $V_{bi} \to V_{bi} + V_{ext}$, yielding

$$w = \sqrt{\frac{2\varepsilon_0 \varepsilon_{Si} \left(V_{bi} + V_{ext}\right)}{q} \left(\frac{1}{N_a} + \frac{1}{N_d}\right)} \approx \sqrt{\frac{2\varepsilon_0 \varepsilon_{Si} V_{ext}}{q} \left(\frac{1}{N_a} + \frac{1}{N_d}\right)}. \tag{3.17}$$

In practice, the applied external voltages are much larger than the built-in voltage, and this component to the depletion zone is often neglected.

The continued diffusion of the electrons and holes with an external field through the junction gives rise to a net current. The diffusion currents (known as the electron and hole current) across the junction are given by [30]:

$$J_{n/p} = q D_{n/p} \frac{n_i^2}{N_{d/a} L_{n/p}} \left(e^{qV/k_b T} - 1\right). \tag{3.18}$$

Here $L_{n/p}$ is the diffusion length, and $D_{n/p}$ are the diffusion constants.

Since the two currents have the opposite direction and opposite sign, they can be linearly added to find the total current in the junction:

$$J = J_n + J_p = J_0 \left(e^{qV/k_b T} - 1\right) \tag{3.19}$$

$$J_0 \equiv q n_i^2 \left(\frac{D_n}{N_a L_n} + \frac{D_p}{N_d L_p}\right). \tag{3.20}$$

This result is known as the Shockley equation and describes the current-voltage characteristics of a pn-junction under both forward and reverse bias.
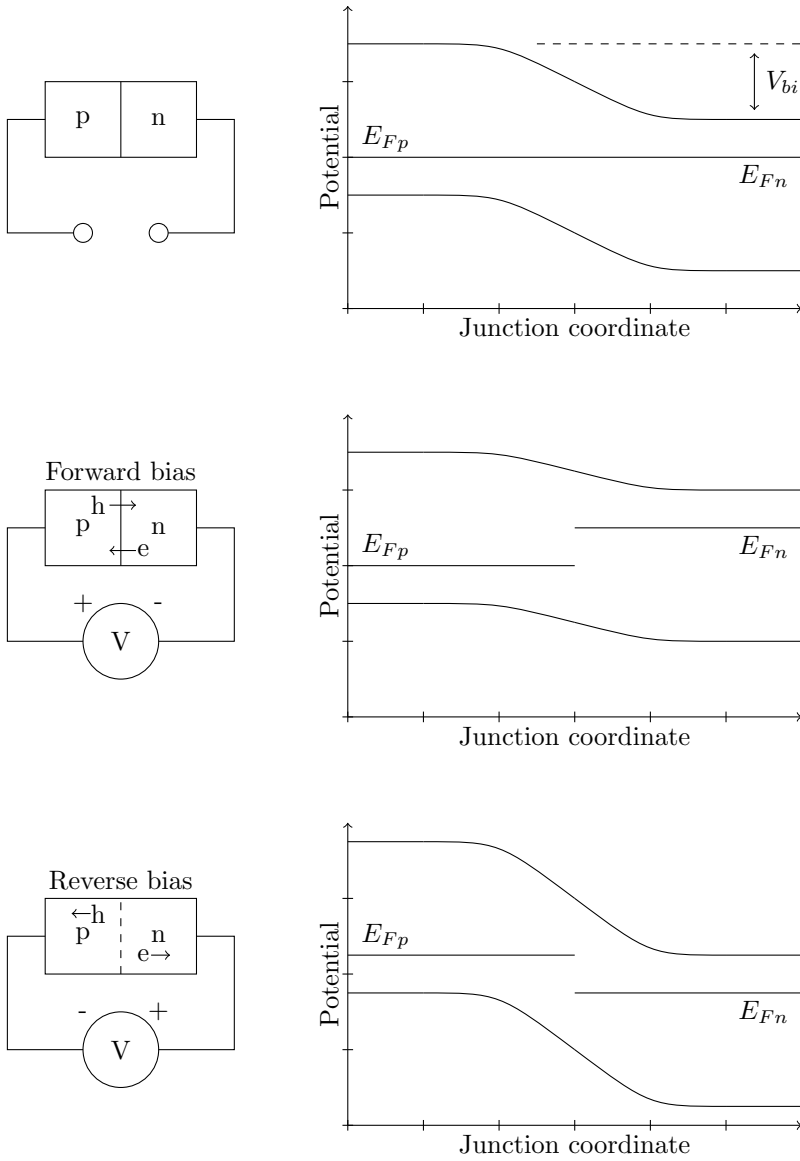
Figure 3.6: Overview of the Fermi level, and the valence and conduction bands in the presence of no external bias (top), forward bias (middle), and reverse bias (bottom). Figure adapted from [30].

3.3 SILICON AS A DETECTION MEDIUM

The previous sections describe how a volume in silicon can be depleted of free charge carriers to detect any externally created electrons and holes. Subsequently, we can focus on how a (highly energetic) particle interacts with silicon to create these charge carriers.

Electrons present in the valence band can be excited to higher energy states, and end up in the conduction band. This excitation can occur by various processes through electromagnetic interactions. Photons or charged particles can interact with these electrons in the valence band, and excite them to the conduction band, resulting in the creation of an *electron-hole pair*. By applying an external voltage to the silicon, the detection volume can be depleted of free charge carriers. Since the detection volume is empty of any charge carriers, any additional electron-hole pairs created by a traversing particle can be detected.

Traditionally, pixelated silicon detectors consist of a bulk of either p- or n-type silicon (see fig. 3.7), with respectively either an n- or p-type *implant* (with the exception that n-type bulk can be combined with an n-type implant). Both p^+ and n^+ refer to the relative amount of doping, in some cases p^{++} and n^{++} are used to indicate higher doping levels. The implant is connected to processing and readout electronics. This implant is first connected to a metal layer, which in turn is connected to the *Under Bump Metallization* (UBM), which later connects to bump bonds in the processing steps. There is a non-conductive silicon-oxide layer between the implants on which a passivation is deposited to better shield the sensor from the external environment.

If the bulk consists of p-type (n-type) material, this detector design is referred to as p-on-n (n-on-p) and if both the bulk and the implant consist of n-type silicon, it is referred to as n-on-n. The main difference is the type of charge carrier that drifts towards the implant, holes for p-on-n and electrons for n-on-p. This difference can have substantial consequences for the speed and operation of the detector in more complex sensor designs such as Low Gain Avalanche Diodes (LGADs) [31] and 3D sensors [32]. These modified and more complex sensor designs are briefly described later in this chapter.

Generally, semiconductor sensors can detect either charged particles or photons. There are small differences between the interaction of highly energetic charged particles and (near-)optical photons which are discussed in this section since both will be used throughout this dissertation to characterise silicon sensors. Silicon is a so-called indirect semiconductor: the top of the valence band is at a different position within the Brillouin zone than the bottom of the conduction band. This means that there is a momentum mismatch between states in the top of the valence band and the bottom of the conduction band. For an electron
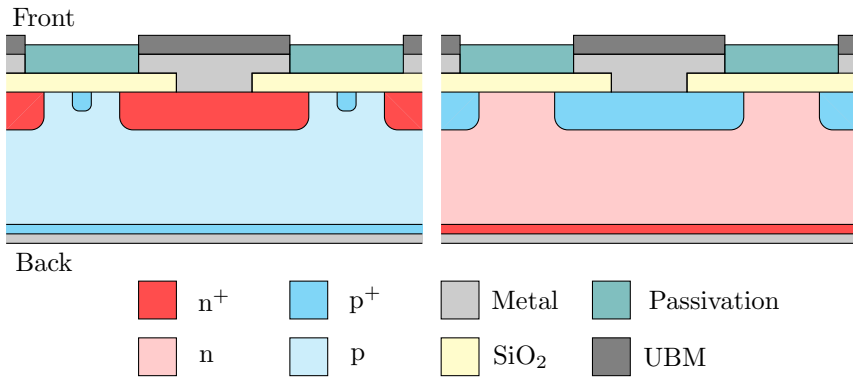
Figure 3.7: Diagram of the cross section view of a planar silicon sensor. A typical n-on-p sensor is shown on the left and a typical p-on-n sensor is shown on the right. The small p^+ areas are called p-stops and are there to guide the field lines to the implants. The metal is there to connect the Under Bump Metallization (UBM) to the implant and the UBM is there to in turn connect the implant to the readout electronics (not illustrated here).

with an energy larger than the bandgap energy to make this excitation, it is crucial to have a change in momentum since no energy states exist with low enough energy in the conduction band with the same momentum. This is illustrated in fig. 3.8. However, there do exist states in the conduction band with low energy, however, these have a different momentum. Therefore, the excitation is possible if an additional amount of momentum (Δk in the illustration) is transmitted to the electron, which is generally taken from *phonons*, lattice vibrations, present in the crystalline lattice. Therefore, the excitations by optical photons are highly temperature dependent [33] since more vibrations, and thus phonons, are present for higher temperatures. On the other hand, for excitations generated by traversing highly energetic charged particles, the energy transfer to liberate a single electron-hole pair is much higher. The average energy transferred in such an interaction is 3.6 eV, which is known as the *mean pair-creation energy* in silicon. This excitation, therefore, does not require a pre-existing phonon from the lattice, while the processes through which the excitations are produced are different between the photon and particle interactions, in both cases, electron-hole pairs are created and can be detected in a similar fashion. A more in-depth explanation of energy loss in silicon by charged particles is given in the next subsection using the Bethe-Bloch equation.

3.3.1   Bethe-Bloch equation: energy loss in materials

Energy loss of charged particles in a material is a complex subject, and only the main aspects are summarised here. A full detailed explanation can be found in [34].
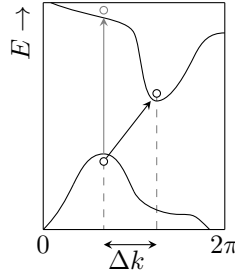
Figure 3.8: Illustration of the excitation of an electron in an indirect semiconductor. To allow the excitation to happen, an additional amount of energy and momentum are needed (black circle and arrow). If no momentum is added to the electron, more energy is needed to allow an excitation to occur, this is indicated by the grey arrow and circle.

When a charged particle traverses a material, the particle interacts with the material via several mechanisms and transfers energy to the material. This interaction is described by the *Bethe-Bloch* equation. This equation gives the rate of energy loss in a material (expressed in units of MeV g^{-1} cm^2). This rate is also referred to as the stopping power. For a particle with a velocity of $0.1 \leq \beta\gamma \leq 1000$ the energy loss is approximated by [34]

$$-\left\langle \frac{\mathrm{d}E}{\mathrm{d}x} \right\rangle = Kz^2 \frac{Z}{A} \frac{1}{\beta^2} \left[\frac{1}{2} \ln\left(\frac{2m_e c^2 \beta^2 \gamma^2 T_{max}}{I^2} \right) - \beta^2 - \frac{\delta\left(\beta\gamma\right)}{2} \right]. \qquad (3.21)$$

The various parameters are related to both the properties of the particle and the material: I is the mean excitation energy, Z is the atomic number, A is the atomic mass of the material, $\delta\left(\beta\gamma\right)$ is the density effect correction, T_{max} is the maximum energy transfer to an electron in a single interaction, and K is the coefficient for $\mathrm{d}E/\mathrm{d}x$ and is $K = 4\pi N_A r_e m_e c^2$. Here N_A is Avogadro's number, r_e is the classical electron radius, m_e is the electron mass, and c is the speed of light. The energy transfer process requires a minimum amount of energy to be transferred, implying a lower cutoff, while the upper limit is given by momentum conservation between in- and outgoing states.

The stopping power for four different particles in silicon is shown in fig. 3.9. The various lines indicated in this figure show the dominating effects in regions. Often for detectors operating at the LHC, the measured particles are approximately *minimum ionising particles* (MIP) and have an energy range where the stopping power is minimal.

The energy deposition of a particle in a material is a stochastic process. The energy loss probability function $f(\Delta; \beta\gamma, x)$ associated with this energy loss function (eq. (3.21)) for a given interaction length, often the material thickness, is
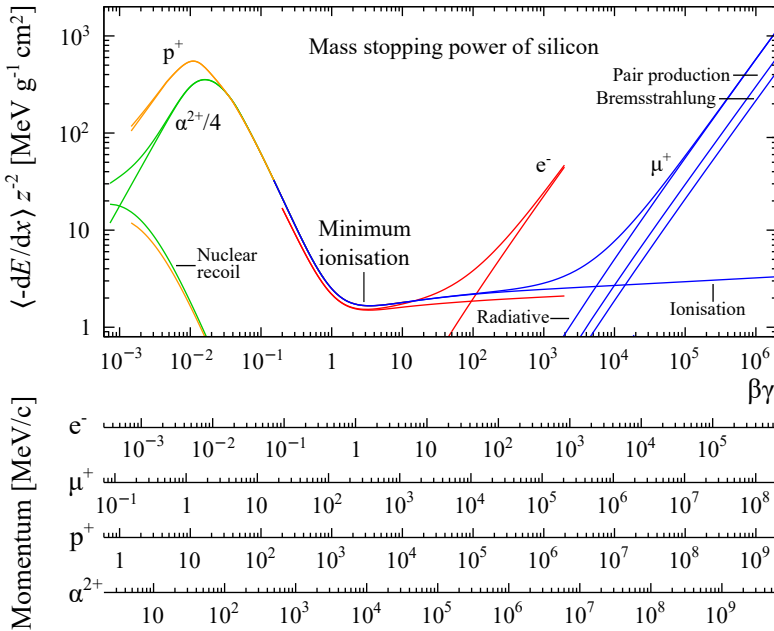
Figure 3.9: The mass stopping power of silicon as a function of the velocity of electrons [35], muons [36], protons [37], and alpha particles [38] (normalised to the charge number squared). The different effects that dominate in the different regions of the momenta spectrum are indicated. The stopping power is highest when the particles have either low or high momentum. The region around a $\beta\gamma$ of 3 is known as minimum ionising.

described by a highly-skewed Landau-Vavilov distribution [39]. This function can be approximated as a convolution of a Laundau [40] distribution with a Gaussian distribution, known as a *Langaus*. Since the tail of this distribution is substantial, the moments of the distribution are not defined. Therefore, the energy most likely deposited is not referred to as the mean, but the Most Probable Value (MPV), also known as the mode of the distribution. The MPV, Δ_p, is given by [41]

$$\Delta_p = \xi \left[\ln \left(\frac{2mc^2\beta^2\gamma^2}{I} \right) + \ln \left(\frac{\xi}{I} \right) + j - \beta^2 - \delta\left(\beta\gamma\right) \right], \qquad (3.22)$$

where $\xi = \frac{K}{2}\left\langle\frac{Z}{A}\right\rangle\left(\frac{x}{\beta^2}\right)$ (in MeV), and $j = 0.200$ [39]. What should also be noted, since it is not directly visible from this expression, is that the MPV of the Langaus is directly proportional to the thickness of the sensor. A more detailed explanation of the processes that occur and the corresponding formulas for the passage of particles through matter can be found in [34].

RADIATION LENGTH

Another quantity related to the energy deposition in a material is the *radiation length X_0*. The radiation length is defined as the mean distance that it takes for a highly energetic electron to lose all but 1/e of its initial energy, where it is assumed that this energy loss is solely due to bremsstrahlung.

3.3.2 SHOCKLEY–RAMO THEOREM

So far we have discussed how particles can create charge carriers in silicon, and how many will be created. Furthermore, we discussed that these charge carriers drift towards their corresponding implant by the potential that is externally applied. Next, we will discuss how this movement will translate to a current that can be measured or detected, and how this influences the time resolution of the detector.

Electrons and holes that are liberated in the bulk drift towards their corresponding implant. The movement of these charge carriers within the sensor induces a current on both the back and front implant of the sensor. This effect is described by the *Shockley–Ramo theorem* [42].

To be able to calculate the induced current on the readout electrode, the concept of a *weighting field*, $\vec{\mathbf{E}}_w$, is introduced. The weighting field is constructed as the effective electric field by setting the collection electrode, generally the segmented readout electrode, at unit potential, and all other electrodes at zero potential. The weighting field is a geometrical property of the detector and is often numerically approximated via dedicated software simulations. The resulting electric field is defined as the weighting field and depends on all dimensions of the pixels, such as thickness, pitch, and implant size. A theoretical description of the weighting field for arbitrary pixel dimensions as well as implant width is given in [43]. An example of the weighting field for two sensors with different thicknesses is shown in fig. 3.10. As can be seen in this figure, the weighting field peaks around the readout electrode, and thus charge carriers at the back of the sensor do (almost) not contribute to the induced signal. Only when these charge carriers are drifting close to the readout electrode will they induce a significant signal on the implant.

The induced current of a charge q, moving with a velocity $\vec{\mathbf{v}}$ on the collection implant, is given by

$$I = q\vec{\mathbf{v}} \cdot \vec{\mathbf{E}}_w. \tag{3.23}$$

This is called the Shockley–Ramo theorem and was initially developed to describe the response of vacuum tubes. It was later proven that this theorem also holds for charges moving in the space charge region of a semiconductor [44, 45].
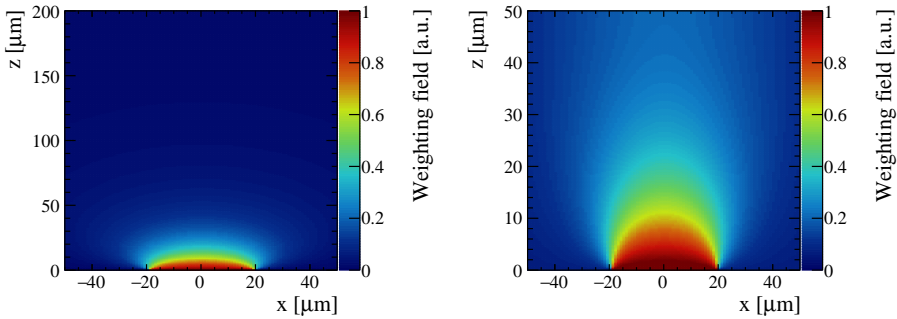
Figure 3.10: Left (Right): Weighting field for a 200 µm (50 µm) sensor. The size of both implants, centred on $x = 0$, is 39 µm. The volume of the pixel with the highest weighting field is located close to the segmented readout electrode (implant).

Since both types of charge carriers (electron and holes) contribute to the induced signal on the segmented readout electrode, the current on this electrode can be expressed as

$$I_{tot} = q \sum_{i=1}^{N_{e/h}} \left(\vec{\mathbf{v}_{\mathbf{e,i}}} + \vec{\mathbf{v}_{\mathbf{h,i}}} \right) \cdot \vec{\mathbf{E}}_w, \tag{3.24}$$

where $N_{e/h}$ is the number of electron-hole pairs generated, and $\vec{\mathbf{v}_{\mathbf{e,i}}}$ and $\vec{\mathbf{v}_{\mathbf{e,i}}}$ is the velocity of the ith electron and hole respectively. Since the mobility of holes is approximately three times lower than that of electrons [46], the two contributions have different time scales. The contribution of the electrons generally peaks quickly after the generation of the charge carriers, while the contribution from the holes is stretched out over a longer timescale. This effect is illustrated in fig. 3.11, in which the simulated current of a typical n-on-p sensor is shown. In this figure, the contribution of both types of charge carriers is indicated schematically.

3.3.3   TIME RESOLUTION OF SILICON SENSORS

So far, we have described the different aspects of detecting a (highly energetic) particle in silicon. These different aspects, however, also influence the final time resolution of the detector and could be tuned to achieve a better time resolution. Therefore, it is essential to understand which aspects play a role, in order to understand and improve the time resolution.

The time resolution of silicon detectors is a combination of the contribution of multiple aspects of these detectors. The time resolution, σ_t, can be approximately broken down by [47]

$$\sigma_t^2 = \left(\frac{N}{dV/dt} \right)^2 + \left(\left[\frac{t_r V_{th}}{S} \right]_{\text{RMS}} \right)^2 + \left(\frac{\text{TDC}_{\text{bin}}}{\sqrt{12}} \right)^2. \tag{3.25}$$
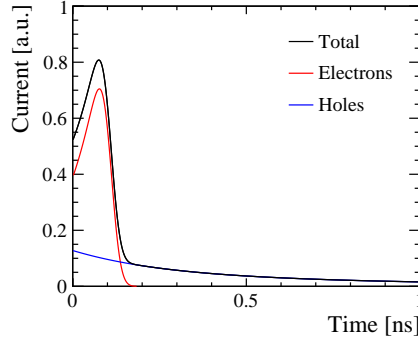
Figure 3.11: Simulated induced current on the segmented readout side of a pixel with a pitch of $55\,\mu m$ and a depth of $200\,\mu m$. Charge is deposited $15\,\mu m$ away from the segmented readout electrode with a Gaussian distribution. The electron contribution is the initial spike of the signal, while the remaining signal is induced by the holes moving away from the implant. The red (blue) line indicates the electron (hole) contribution. The black line indicates the total signal.

- The first component in this equation reflects the signal-to-noise level of the signal. Here N is the noise on the voltage level, and dV/dt is the slope of the rising edge of the signal. The rise time of this signal is not affected by a change in the magnitude of the signal, and thus we can see that a larger signal will directly decrease this term, yielding a better time resolution. Similarly, a smaller noise N will improve the time resolution.

- The second component is summarising the contribution of timewalk to the time resolution. Since the magnitude of the signal can differ based on the number of liberated charge carriers, it can take different lengths of time before the signal crossed the threshold V_{th}. The risetime of the preamplifier is given by t_r and also influences this contribution to the total time resolution. From this term, we can see that increasing the signal size or decreasing the preamplifier risetime will decrease the magnitude of this contribution to the total time resolution.

- The third component represents the contribution from the Time-to-Digital converter (TDC). This component is directly determined by the size of the TDC bins and corresponds to the uncertainty of a uniform distribution with the width of the TDC bin.

On the sensor side, both the contribution from noise and that of the slope of the rising edge of the signal, dV/dt, are influenced by the design parameters of the sensor, such as pixel pitch and thickness. The slope of the signal can be affected by changing the weighting field of the sensor since the induced current, the signal, is directly related to the weighting field. Charge carriers that traverse through the

higher gradient region of the weighting field will therefore induce a larger current, resulting in a larger dV/dt, and therefore a better signal-to-noise ratio.

The type of charge carrier that is collected, impacts the time resolution. Since the mobility of holes is approximately three times lower than that of electrons, the velocity is also lower for the same electric field. Hence, the collection of holes will also result in a dV/dt approximately three times lower than collecting electrons. Therefore, electron collecting (n-on-p) devices are generally considered to provide a better time resolution than hole collection sensors (p-on-n).

Drift velocity

The temporal properties can be improved by increasing the electric field, which directly translates to a velocity increase of the charge carriers, yielding a better signal-to-noise ratio.

There however is a limit to this, from both a practical and a theoretical perspective. When high bias voltages are applied, an electric discharge can occur from the back of the sensor to the ASIC, resulting in a broken detector. Therefore, in air without any precautions, typically not more than 250 V is applied to prevent these sparks. Another practical limitation is the breakdown of the sensor at around 3×10^5 V/cm. When a higher field is applied, electron multiplication can occur, resulting in a sudden increase in leakage current damaging the sensor.

Another limitation comes from the so-called *saturation velocity*. As the energy of electrons and holes increases when the electric field is increased, it starts to strongly act on the lattice and directly transmits energy to the lattice in the form of *optical phonons* [48], which are out-of-phase movements of atoms in the lattice. This energy transfer decreases the velocity of the charge carriers, resulting in an upper limit of the drift velocity. The saturation velocity is determined experimentally, and an example is shown in fig. 3.12. This figure shows the drift velocity for electrons and holes at different temperatures as a function of the electric field. For low electric field strengths, the drift velocity increases linearly with the electric field, however, at higher values a saturation is visible which is called the saturation velocity. It is important to note that radiation damage generates more effective acceptors and donors, leading to a decrease in the mobility of charge carriers [49].

A different factor contributing to the drift velocity is that the mobility of electrons and holes in doped silicon can be drastically lower for high doping concentration ($N > 10^{16}$ cm^{-3}). Experiments have shown that the electron mobility varies depending on the donor concentration [51, 52], and the hole mobility depends on the acceptor concentration [52]. Both mobilities decrease when the doping concentration increases. Since the highly doped region around the implants is thin, the decrease in mobility in practice does not affect the resolution of current silicon sensors.
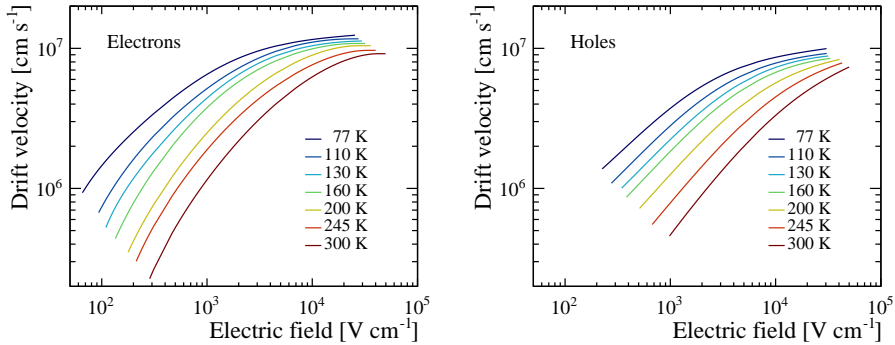
Figure 3.12: Drift velocity for electrons (left) and holes (right) at different temperatures as a function of the applied electric field. At high electric fields, the drift velocity of both types of charge carriers saturates. Data taken from [50].

ALTERNATIVE SENSOR DESIGNS

As we have seen in the previous sections, design choices and practicalities of specific sensor designs can drastically influence the final temporal performance. Therefore, different sensor concepts have emerged in the past few decades. Historically, only thick planar sensors existed since this was what the industry provided. However, some limitations have become evident during the development of these thick silicon sensors. The time resolution is mainly limited due to the inherently large drift distances that the charge carriers need to traverse to the high part of the weighting field. A possible solution to this problem is to decrease the thickness of the sensors. This, however, introduces a new limit: decreased charge, since the interaction length of particles with the detector is also reduced. Therefore, the signal-to-noise ratio for these thin planar sensors is worse compared to thick planar sensors.

To cope with the limited interplay of the radiation length X_0 and signal, Low Gain Avalanche Diodes (LGAD - fig. 3.13 left) have been developed. These sensors incorporate a highly doped layer on top of the segmented readout electrode. This layer results in localised high electric fields which lead to charge multiplication [31]. Therefore, a thin detector can achieve a better signal-to-noise ratio while still having less material compared to thick planar sensors. LGADs however, are inherently more vulnerable to radiation damage since the doping concentration is lowered quickly [53]. This effect is discussed later on and is currently the limiting factor for this type of sensor.

Another novel development in the field of silicon particle detectors is 3D sensors [32] (fig. 3.13 right), which consist of doped regions that reach into the bulk of the sensor as pillars or walls. These sensors benefit from a large signal formation and a better time resolution due to, on average, smaller drift distances, but have the downside of having a lower fill factor due to the pillars and walls.

There is ongoing research to find the ideal sensor technology that can achieve the optimal time resolution for each specific application. The final sensor choice for different experiments and different applications depends on many variables, as we have discussed, and thus there is not one *does is all* sensor.

Front

Back

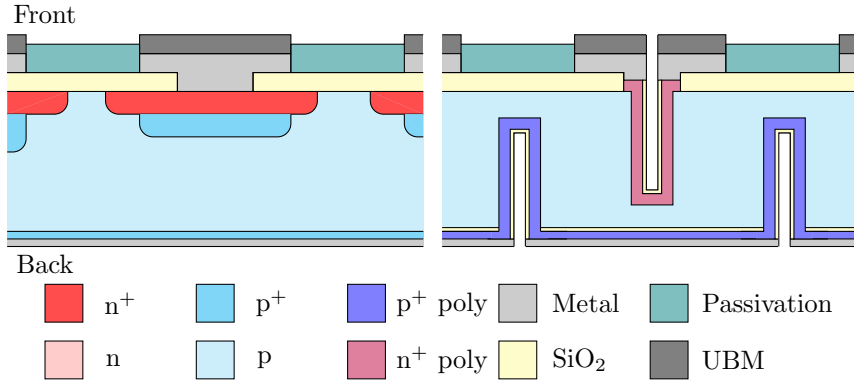|	n$^+$		p$^+$		p$^+$ poly		Metal		Passivation
	n		p		n$^+$ poly		SiO$_2$		UBM

Figure 3.13: An illustration of a LGAD (3D) sensor on the left (right). The poly stands for polycrystalline silicon. The 3D sensor design shown here is typical for a sensor produced by Centro Nacional de Microelectrónica (CNM).

3.4   Radiation damage in silicon

The density of particles is extremely high close to the interaction point at the experiments at CERN. For the experiments, it is essential to have detectors close to these interaction points to optimise for vertexing and the impact parameter resolution. When highly energetic particles traverse these detectors, there is a small chance that they will damage the detector, which is called radiation damage. The inner trackers, such as the VELO [12], must cope with a large amount of radiation and subsequent damage over the lifetime of the experiments. This damage leads to the performance degradation of the silicon detector and directly affects measurable quantities such as an increase in leakage current, bulk resistivity and free charge carrier trapping in the sensor.

This damage can occur in the main part of the silicon sensor, the so-called bulk, or on the surface at the silicon/silicon-oxide interface. The bulk is the volume in which the electron-hole pairs are created. The radiation damage to these two different areas, bulk versus surface, is often discussed separately. The damage to the bulk influences many parameters of the sensor, while the surface damage mainly affects the leakage current as well as the characteristics of the electronics.

In the following subsections, the different aspects of radiation damage in silicon sensors are discussed as well as the implications of these changes to the operation of the detector, such as the impact on the spatial and time resolution. A more detailed overview of all aspects of radiation damage in silicon sensors can be found in [54].

3.4.1 CREATION OF DEFECTS

When a particle interacts with the silicon bulk, it can not only generate electron-hole pairs, but it can also directly interact with the silicon lattice (referred to as the bulk). When this happens, a silicon atom can be knocked out of its initial position within the lattice and is displaced, referred to as *bulk damage*. Such a displacement is called a *primary knock-on atom* (PKA). The displaced atom forms an interstitial, called a *Frenkel-pair*, or can react with impurity atoms in the lattice. This displacement only occurs when the transferred energy to the atom is above the threshold energy of $E_d = 25$ eV [55].
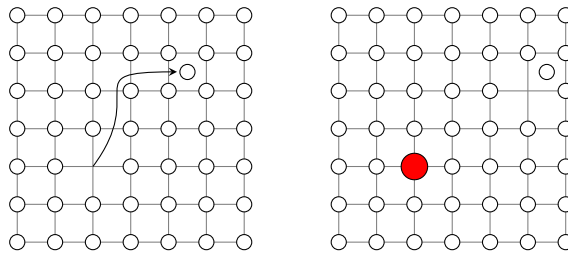

Figure 3.14: Diagram of a primary knock-on atom leaving a vacancy and creating an interstitial on the left, and an impurity atom (red) and a Frenkel pair on the right.

Alternatively, the energy transferred in the collisions can be much larger, such as with nuclear reactions caused by a traversing hadron. In this case, the PKA will move through the lattice, and lose its recoil energy E_R by interactions with the atoms in the lattice such as through ionisation or further displacement of secondary atoms. These secondary effects are called point defects. When nearly all energy of the PKA is lost through these interactions, the non-ionising interactions dominate and thus form dense regions of defects. These regions are called *defect clusters*. Depending on the energy and type of particle, a different combination of point defects and defect clusters is created.

The different types of interactions result in different types of damage caused by different types of particles and energies. Figure 3.15 shows a simulation of the number of vacancies created by three respective types of particles [56], illustrating the different amounts of damage in the silicon lattice. The vacancies are an absence of a silicon atom, which was removed from the original position via the process described above. The left plot shows the number of vacancies in a 1 µm

depth of the lattice created by 10 MeV protons with a total fluence of 10^{14} cm^{-2}. The middle plot shows the vacancies created by the same fluence of 24 GeV/c protons, and the right plot shows this for 1 MeV neutrons. One can see the different vacancies clustering for the different types of radiation. Neutrons tend to produce vacancy clusters with few localised point defects, while the 10 MeV protons create a uniform distribution of point defects with few clusters. These clusters are generally produced by collisions with a high momentum transfer and thus are not common in irradiation with low momentum particles (< 1 MeV). On the other hand, one can see that the 24 GeV/c protons produce both point defects and clusters of vacancies.
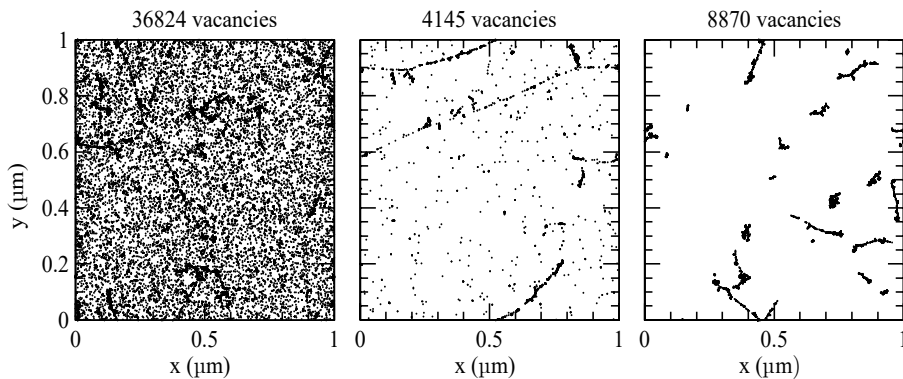

Figure 3.15: Spatial distribution of vacancies produced by 10 MeV protons (left), 24 GeV/c protons (middle), and 1 MeV neutrons (right) respectively. The vacancies shown here correspond to a slab with a thickness of 1 μm and a fluence of 10^{14} cm^{-2}. Figure taken from [56], and is obtained with simulations.

Besides damage to the bulk, the surface region is also sensitive to radiation damage. This damage is referred to as *surface damage*, and consists of all defects in the oxide layer (often SiO$_2$) and the interface between silicon and the oxide. This damage, however, occurs mostly on, and impacts, the electronic side of the detector: the ASIC. Since this effect is of interest to the electronics industry, this damage has been better understood and can to a certain extent be controlled by design choices and the manufacturing process [57]. The effect of surface damage to silicon sensors mainly manifests itself as charge accumulation at the interface. This decreases the resistance between readout electrodes and can lead to charge sharing between neighbouring pixels [57].

POINT DEFECTS

Induced vacancies and interstitials can react with either each other or with other impurities inside the silicon lattice. Some of these defects can be electrically active and give rise to states in the bandgap. These states can hold electrons or holes that are generated in the bulk and are therefore referred to as traps. The energy

of the trap (E_t) is related to either the conduction (E_c) or valence band (E_v) energy. Since these defects create energy states within the bandgap, they can aid in the excitation of electrons from the valence to the conduction band. Therefore, thermal excitations are more common, and as a consequence the leakage current also increases.

A distinction is made between acceptors, donors, and amphoteric levels. *Acceptors* are defects that are negatively charged when occupied with an electron, while *donors* are defects that are neutral when occupied with an electron. If defects have two levels, and thus can acts as donors or acceptors, they are called *amphoteric defects*.

Further, the location of the Fermi level determines the charge of the defect. If the Fermi level is located above the defect level, acceptors are negatively charged and donors are neutral, while if the Fermi level is below the defect level acceptors are neutral and donors are positively charged.

NIEL SCALING OF RADIATION DAMAGE

The composition of radiation environments is diverse; a scaling model is needed to compare the different types of irradiation. The amount of radiation damage is often expressed as a function of *neutron equivalent per square centimetre at 1 MeV* (1 MeV n_{eq} cm^{-2}), where the damage created by radiation is scaled to a standard value which is taken as the damage that a 1 MeV neutron causes in the material. This procedure is known as the *Non-Ionizing-Energy-Loss* (NIEL) scaling hypothesis.

The NIEL scaling hypothesis assumes that radiation damage induces changes in the properties of silicon linearly with the NIEL. The total fluence Φ is given by

$$\Phi = \int_{E_{min}}^{E_{max}} \mathrm{d}E \; \phi(E). \tag{3.26}$$

The energy spectrum is assumed to be $\phi(E)$, and is integrated over the energy range E_{min} to E_{max} with E as the energy of the impinging particles. To scale this fluence to the 1 MeV neutron equivalent, the hardness factor κ is used. The factor κ is calculated as

$$\kappa = \frac{\int \mathrm{d}E \; \phi(E) D(E)}{\Phi \; D(1\,\mathrm{MeV})}, \tag{3.27}$$

where $D(E)$ is the displacement damage cross section, and $D(1\,\mathrm{MeV})$ is the damage cross section for irradiation with 1 MeV neutrons, and is 95 MeV mb [58]. The scaled fluence Φ_{eq} is calculated as

$$\Phi_{eq} = \kappa \cdot \Phi. \tag{3.28}$$

The different scaling factors for common types of particles and energies can be seen in fig. 3.16. This figure shows the relative damage for four different particles: protons, neutrons, electrons, and pions. For high energy physics at the LHC, the particles that cause damage generally range from 10 MeV to hundreds of GeV, where the relative damage caused by the different particle species is within the same order.
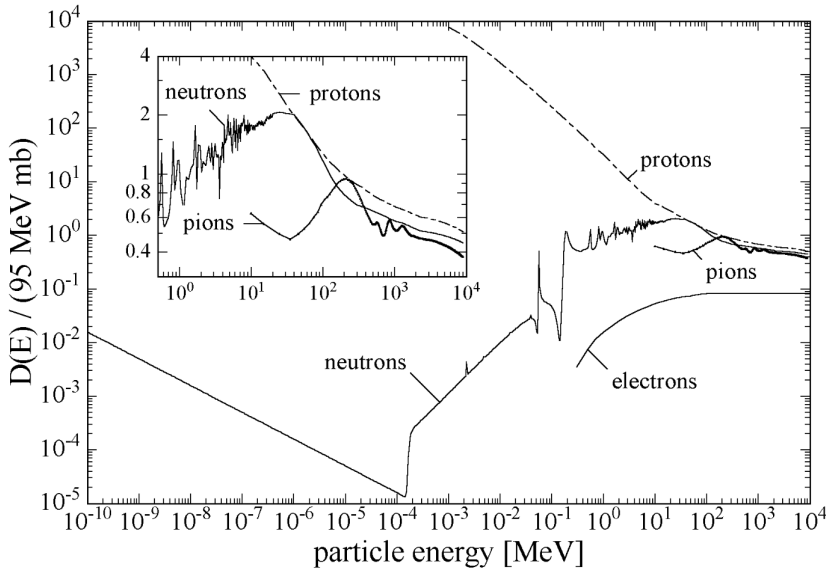

Figure 3.16: Displacement damage function $D(E)$ scaled to 95 MeV mb for different types of particles. Figure taken from [59].

Donor and acceptor removal

The boron and phosphorus atoms that are present in the silicon as dopants can be removed from their acceptor and donor states by radiation damage. Donor removal is studied for n-type silicon [60, 61], and the effect of acceptor removal [53] is important to understand for p-type silicon, especially in novel sensor techniques such as LGADs. For LGADs in particular, the acceptor removal is problematic, since the gain layer is created using heavily doped p-type silicon. With acceptor removal, the electric field that at first was high enough to achieve electron multiplication is decreased to lower values, and the gain mechanism is suppressed.

Recent studies have shown that infusion of other types of atoms in the lattice, such as carbon, can partially prevent the gain suppression in highly irradiated LGADs [62]. Radiation hardness up to 2.5×10^{15} 1 MeV n_{eq} cm^{-2} has recently been proven, but this is currently still an order of magnitude lower compared to radiation hard planar sensors.

ANNEALING

A method to partially mitigate the effects of radiation damage is called annealing. This method for example could be used during the downtime of the detector to partially regain the Charge Collection Efficiency (CCE).

Radiation-induced defects in the crystalline lattice can migrate through the lattice aided by thermal energy. The rate of this migration depends heavily on the temperature, and thus mobility of the defects, as well as on reactions with other defects in the lattice. Raising the temperature to allow higher mobility of these defects is called *annealing*. Annealing that mitigates defects is named *beneficial*, while annealing for too long will degrade the performance again, and is named *reverse annealing*. Figure 3.17 shows the difference in effective doping concentration N_{eff} (the irradiation induced change in the effective doping concentration) as a function of annealing time. A lower ΔN_{eff} means essentially less degradation of the performance. As can be seen in this figure, after around 100 minutes of annealing at 60° C, the beneficial annealing stops and the reverse annealing dominates.

Irradiated detector samples are stored at around -20° C, and need to be cooled to at least this temperature during operation to avoid unintentional annealing. This needs to be considered during the design of tracking detectors in the LHC, as any unintentional heating during for example downtime of the experiments can lead to reduced performance of the silicon sensors.

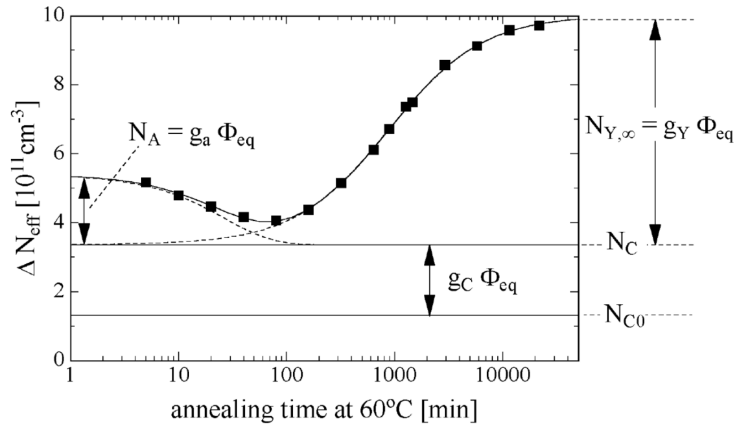Figure 3.17: Change in effective doping concentration as a function of annealing time at 60° C. The lowest effective doping concentration is achieved after around 100 minutes of annealing. Figure taken from [59].

3.4.2 OPERATIONAL EFFECTS OF SILICON SENSORS

After having reviewed the mechanism of radiation damage in silicon sensors, we can subsequently address the implications of radiation damage in detectors and

experiments. Several effects due to radiation damage limit the operation of these detectors, such as a decrease in collected charge, type inversion, and the double junction effect. These three points will be discussed in this section.

Charge collection efficiency

One of the major impacts of radiation damage to the operation is the percentage of charge carriers that will still contribute to the induced charge, often expressed as the *Charge Collection Efficiency* (CCE). This efficiency can drop below 50%, and have a major impact on the operation of the silicon detector.

The energy states within the bandgap that are produced by point defects can also trap free electrons and holes for a short period of time called the trapping time $\tau_{e/h}$. The capture probability can be expressed using the effective trap concentration N_t, the capture cross-section σ, and the thermal velocity of the charge carriers v_{th} [63]:

$$\frac{1}{\tau} = \sigma v_{th} N_t. \tag{3.29}$$

Since this trapping time can be large in comparison to the drift time, the delay introduced by the trap can be large enough such that it falls outside the collection time of the electronics, effectively lowering the collected charge. For heavily irradiated sensors, the number of traps becomes one of the limiting factors for its operation, resulting in a substantial loss of induced charge. Trapping rates increase linearly with radiation damage and are inversely proportional to temperature [64]. When the signal degrades, the signal-to-noise ratio also becomes smaller, leading to a worse time resolution and a worse charge and spatial measurement.

Type inversion

The initial positive space charge region formed by the pn-junction is counteracted by the formation of a negative space charge region induced by radiation damage. The net space charge decreases as the amount of radiation damage increases. For n-type silicon this decrease in space charge will eventually cause a flip in the sign of the space charge, effectively becoming p-type. This flipping point is known as the *Space Charge Sign Inversion* (SCSI). This SCSI does not occur for p-type silicon since the space charge before radiation damage is already negative.

Since the depletion voltage depends linearly on the absolute value of the space charge, the depletion voltage for an n-type detector will first decrease since the space charge magnitude initially decreases [65]. What should be noted for these n-type detectors is that due to SCSI, the sign of the bias voltage will need to be flipped when the detector goes through SCSI. The voltage required to deplete the bulk also depends linearly on the space charge. Therefore, higher voltages are required to deplete radiation-damaged sensors.

DOUBLE JUNCTION EFFECT

In the early 2000s, a side effect of radiation damage was discovered that leads to possible mitigation of the lowering of collected charge as an effect of radiation damage. An increase in the collected charge with respect to the non-irradiated detector was observed [66, 67] for heavily irradiated planar sensors from around 1×10^{15} 1 MeV n_{eq} cm^{-2}. This increase of charge is contributed to the *double junction* effect, which is caused by a change in the distribution of hole and electron current components after irradiation. The electron current j_n and hole current j_p have a linear dependence on the depth inside the detector. The electron current is largest close to the n$^+$ contact, and j_p is largest close to the p$^+$ contact. Since defects are uniformly distributed throughout the depth, more positive charge will be accumulated at the p$^+$ contact, and more negative charge will be accumulated at the n$^+$ contact. This difference in the distribution of free charge carriers will lead to a non-uniform electric field throughout the detector's depth. This in turn leads to an electric field that has two peaks: near both contacts a peak. An illustration of this field is shown in fig. 3.18. This sudden increase in the electric field near the segmented readout implant can lead to localised charge multiplication. Therefore, an increase in the collected charge might be observed for highly irradiated planar sensors.

This radiation-induced charge multiplication has been thought to aid the charge collection efficiency for highly irradiated sensors since a larger signal directly increases this efficiency. The time resolution of the sensor is also a function of the signal size, and a larger signal might lead to a better time resolution. However, as will be discussed in section 6.2, an improvement of the time resolution in sensors that display this double junction effect is not yet observed.

3.5 DESIGN IMPLICATIONS FOR SENSOR TECHNOLOGIES

So far we have discussed how silicon sensors can be used to detect (highly energetic) particles, measuring both their spatial position and arrival time, and what the implications of radiation damage on these sensors are. We have also discussed that new sensor technologies have emerged in the past decade that aim to address the shortcomings of planar sensor technology. The first change in the field was a shift towards developing more radiation tolerant sensors, as well as thinner sensors. However, new experiments at the high luminosity LHC and beyond require even higher radiation tolerance, with the additional requirement on temporal performance. This has led to another paradigm switch in sensor design. There is now a need to develop sensors that are even more radiation resistant, and besides this, also have a good time resolution.

Currently, there are four crucial aspects for silicon tracking detectors: position resolution, time resolution, radiation hardness, and material budget. These four
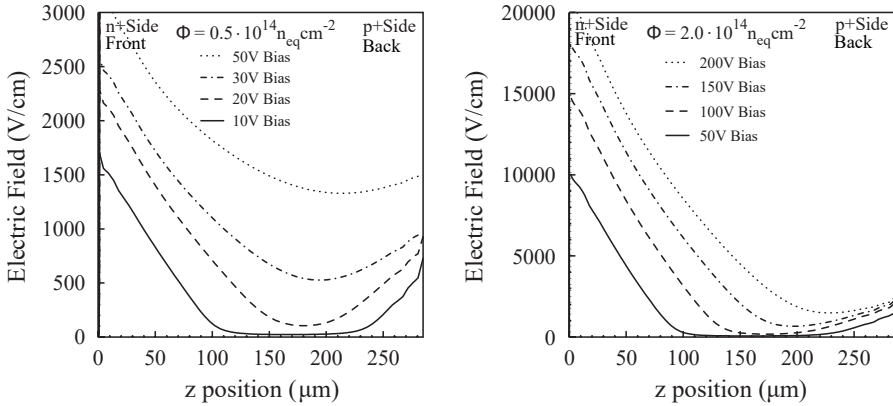
Figure 3.18: The simulated electric field as a function of depth in a 300 μm sensor after a fluence of 0.5×10^{14} 1 MeV n_{eq} cm^{-2} (left) and 2.0×10^{14} 1 MeV n_{eq} cm^{-2} (right). A peaked electric field can be observed close to the front of the sensor that increases rapidly with fluence. This electric field gives rise to charge multiplication in the volume close to the electrodes. Figure taken from [66].

requirements must be achieved with the lowest possible power consumption. The power constraint appears in the sensor discussion indirectly, as it among others affects the operational temperature. This is not thoroughly discussed further, but nevertheless, it is important to note that using more power in the electronics improves the time resolution [68]. The position resolution can be improved by reducing the pixel pitch, which in turn will lower the capacitance of the pixel. This leads to a lower noise rate, improving the time resolution. As can be expected, there is no sensor technique that *does it all*, and generally a sensor technique improves three out of the four aspects, while worsening the fourth.

After this overview of the main aspects of silicon sensors, we reflect on the strong points and applications of the different sensor technologies that have been discussed. Historically, due to their availability in the industry, thick (~ 300 μm) p-on-n planar sensors have been used. These have proven to suit initial applications in tracking detectors in the past few decades, but have been found not to withstand the increase in radiation damage (and having type inversion after irradiation), and they fail to provide a sufficient time resolution for future experiments at the LHC. However, for experiments that do not require a high rate and radiation damage, they might still be a perfect match since the costs are low compared to newer techniques.

We have also seen a turn to slightly thinner n-on-p sensors as a natural next step of thick planar sensors, which can withstand up to around 10^{16} 1 MeV n_{eq} cm^{-2}, but still do not offer the best time resolution. To mitigate this, both LGAD and

3D sensor designs have seen an increase in use. LGADs have proven that $\mathcal{O}(10\ \text{ps})$ of time resolution is reachable, but generally have a worse position resolution since the implant and interpad distances are relatively large. In addition, a non-uniform fluence profile results in a difficult operation, as the bias voltage needs to increase quickly with radiation damage. However, in case these sensors can be applied at larger distances from the interaction point, they may be a suitable choice. For instance, in the Atlas High Granularity Timing Detector (HGTD) [69] or the CMS MIP Timing Detector (MTD) [70]. The non-uniform fluence profile and the small pitch required for the VELO imply that LGADs are a poor choice of sensor technology to implement for the VELO.

The 3D sensors techniques have also achieved a time resolution of $\mathcal{O}(10\ \text{ps})$ using a sensor without charge multiplication. However, they do require thicker sensors in order to achieve this time resolution, increasing the sensor material budget of experiments. The radiation hardness of 3D sensors exceeds that of LGADs and can most likely cope with the non-uniform irradiation profile over a sensor, however, this is still to be demonstrated. One of the disadvantages of this sensor technology is the fact that less charge can be generated right on top and below the columns, leading to a lower fill factor compared to planar sensors. 3D technology is considered one of the possible options for future upgrades of tracking detectors, and is already planned to be used in the ATLAS Insertable B-Layer (IBL) [71].

Another recent development in sensor and electronic design are Monolithic Active Pixel Sensors (MAPS). These sensors contain both the sensitive silicon volume and the electronics in the same piece of silicon. This design choice allows for low noise and low material budget, and does not require bump-bonding of the sensor to the ASIC. However, current developments in radiation hardness and time resolution have not yet achieved the same performance that other sensor techniques have achieved.

Besides these three main developments in sensor technologies, the older planar designs are also still under consideration since they have been under development for several decades, and have thus far been proven to be one of the most radiation resistant sensor technologies along with 3D sensors. The time resolution is generally observed to be worse compared to the newer sensor technologies due to their inherently lower signal-to-noise. However, for some tracking detectors, such as the VELO, these sensors could still be considered to be a feasible option to implement.

Finally, it is important to realise that there is a wide amount of R&D on different sensor materials such as diamond and silicon carbide. So far these sensor materials have proven that they can achieve similar performance on a small scale, but no large-scale implementation has been achieved to date. Therefore, this dissertation focuses on silicon as a detection material.

CHAPTER 4

❧

READOUT SYSTEMS FOR PIXEL DETECTORS

T HE SIGNAL generated by a particle in a pn-junction needs to be transformed for readout and further processing. In bubble chambers in the past, pictures were taken and processed to reconstruct the information in which we are interested: where and when did a particle interact with the detection medium. This processing step is more complicated for silicon pixel detectors and is discussed in this chapter.

4.1 DETECTOR READOUT PRINCIPLES

The signal current generated by electron-hole pairs that drift in the detection medium towards the implants is described by the Shockley–Ramo theorem. The collection time τ of the electron-hole pairs generally is around $\mathcal{O}(5\,\text{ns})$. These generated currents, however, are too small to be processed by conventional electronics and thus need to be amplified. In most high-energy physics applications, this signal is amplified using a preamplifier, turning the current signal into a voltage signal as well. An example of a preamplifier is a *Charge Sensitive Preamplifier* (CSP), which in essence integrates the signal current from the sensor, and generates a voltage signal with an amplitude that is proportional to the incoming input charge. When a current source is put in parallel to the CSP, the charge build up at the capacitor will be discharged at a constant rate, and subsequently, the voltage after the CSP will decrease at a constant rate. The incoming input charge will then be proportional to the length of the voltage pulse after the CSP. Commonly the Krummenacher feedback circuit [72] is used to achieve the discharge of the integrated current signal. This yields the possibility of measuring the total signal charge by measuring the length of the signal, commonly referred to as the Time-over-Threshold (ToT). The threshold is applied to avoid being sensitive to noise

spikes. An illustration of the signal along with the (partially) processed analogue signal is shown in fig. 4.1.
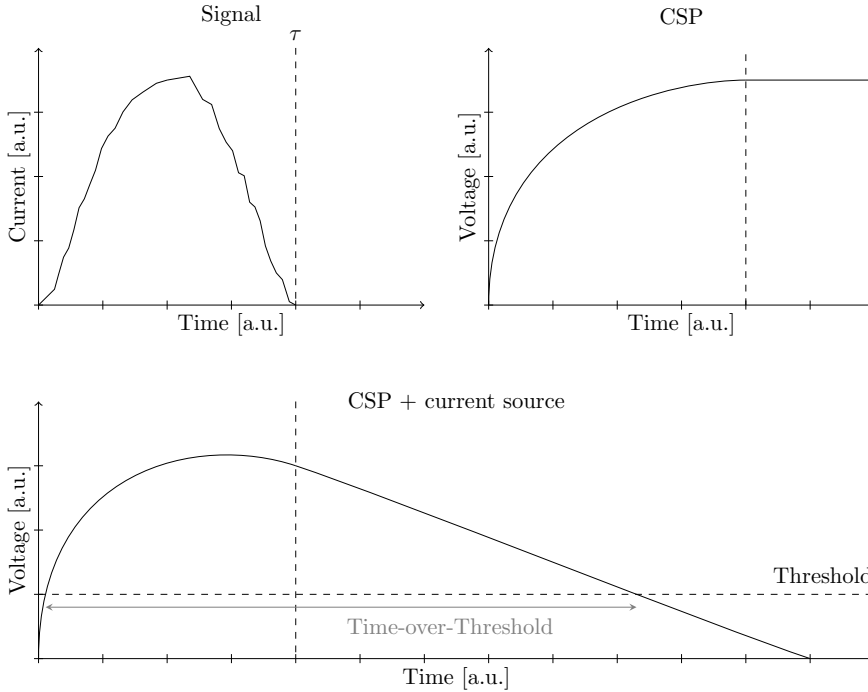

Figure 4.1: Top left: schematic representation of the current signal created by the drift of the charge carriers in the sensor. Here τ is the time it takes to collect all charge from the sensor. Top right: the analogue signal after processing the signal in a charge-sensitive preamplifier (CSP). Bottom: the analogue signal after processing the signal with a CSP in parallel with a current source that actively lowers the voltage.

The easiest method to read out a silicon particle detector is to connect a single segmented readout electrode to a preamplifier and record the amplified voltage signal. However, when this method is expanded to more pixels, one runs into problems, both in terms of cabling and data bandwidth. Therefore, Application Specific Integrated Circuits (ASIC) are employed. These circuits often contain a dedicated preamplifier for each pixel, in combination with logic that digitises the signal. In this fashion, the whole ASIC, and thus thousands to millions of pixels can be read out in sequence. In the final application of silicon pixel detectors, ASICs are used to process the signal from the detection medium, while at small scale, such as in R&D facilities often single elements are still amplified and read out using an oscilloscope.

Two different categories of pixel detectors are *monolithic* and *hybrid* pixel detectors (see fig. 4.2). A hybrid detector consists of a sensor that is *bump bonded* to an ASIC, while for monolithic detectors the sensor and electronics are fully integrated in the silicon volume. Monolithic detectors are also commonly known as Monolithic Active Pixel Sensors (MAPS). The bump bonds in hybrid detectors make the electrical connection between the sensor and the ASIC. Hybrid pixel detectors have been developed first. In recent years monolithic pixel detectors have made improvements in their technology and started to come closer to the temporal performance of hybrid detectors. In this dissertation, we will focus on hybrid pixel detectors.
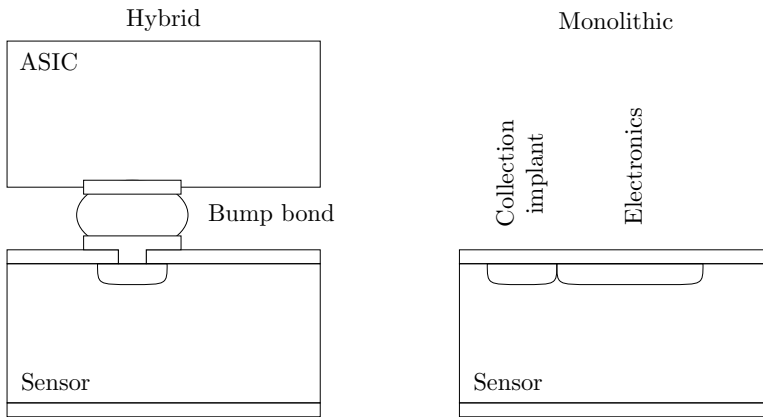
Figure 4.2: Illustration of a hybrid (left) and a monolithic (right) detector. The main difference is the inclusion of the electronics in the detection silicon. For the monolithic detector, the collection implant is shown next to the electronics that are embedded in the sensor.

The silicon pixel detectors studied in this dissertation are connected to two different ASICs from the Medipix family of chips [73]: Timepix3 and Timepix4. These ASICs are described in section 4.2.1 and section 4.2.2 respectively. In section 4.3 their dedicated readout is discussed.

4.2 MEDIPIX FAMILY OF ASICS

Since the first introduction of large area (photon-counting) hybrid pixel detectors in the WA97 experiment [3], it has been demonstrated that there is a large potential for these detectors in high energy physics experiments. The development of dedicated pixelated photon-counting hybrid pixel detectors started and led to the foundation of the Medipix collaboration [74]. In 1997 this collaboration produced its first ASIC: the Medipix [75]. This chip was mainly aimed for medical applications (such as X-ray imaging). It consisted of 64×64 pixels, each measuring $170\,\mu m \times 170\,\mu m$, and used a node size of $1\,\mu m$.

Developments in commercial sub-micron CMOS-processing and fine pitch bump bonding technologies led to the Medipix2 ASIC [76] in 1999. This chip has pixels with dimensions of $55\,\mu m \times 55\,\mu m$. This downscaling with respect to the first Medipix chip was mostly enabled by the decrease in node size to 250 nm. In 2006, the Timepix chip [77] based on this Medipix2 ASIC was developed. This chip does not rely on the photon-counting mode but can measure the Time-of-Arrival (ToA) in 10 ns bins or the ToT of hits depending on the mode. Further advances in CMOS-processing and ASIC design allowed for further improvements and led to the creation of the Medipix3 ASIC [78] in 2010 with a node size of 130 nm. This chip has four different thresholds and features a charge summing mode (CSM) that sums the charge of neighbouring pixels. In 2014 a successor of the Timepix was developed: Timepix3 [79], which has both a more precise ToA (1.56 ns bins) and ToT measurement. Another improvement is the ability to measure both ToA and ToT simultaneously. In 2016 the Medipix4 collaboration was established, planning to develop two new chips, the Medipix4 and Timepix4. The Timepix4 [80] was released in 2021, which has a further improved ToA and ToT measurement with ToA bins of 195 ps and a ToT granularity of 1.56 ns. The Medipix4 ASIC is expected to be released within a few years. Both ASICs produced by the Medipix4 collaboration are prepared for through-silicon via (TSV) and thus can be tiled on all four sides, contrary to all previous generation chips that had an inactive periphery on one side of the chip. This allows ASICs to be placed adjacently with minimal dead area penalty for wire bonding and leads to the possibility of large-scale tiling of chips without loss in coverage.

In the next sections, we focus further on the details of the Timepix3 and Timepix4 ASIC along with their implemented measurement techniques.

4.2.1 THE TIMEPIX3 ASIC

The Timepix3 is a data-driven ASIC that can measure both the Time-of-Arrival (ToA) and the Time-over-Threshold (ToT) simultaneously and consists of a pixel matrix of 256×256 pixels with a pitch of $55\,\mu m \times 55\,\mu m$. On one side of the pixel matrix, there is an insensitive area referred to as the periphery. This area extends beyond the pixel matrix and contains clock distribution, data routing, and other circuits [79]. The Timepix3 can operate in three different modes: event-counting, time-of-arrival only, and time-of-arrival and charge simultaneously. The first mode is reminiscent of the origins of the Medipix collaboration and is implemented for contingency. The ASIC can simultaneously measure the total time the voltage in a pixel was above the threshold in a defined time interval when operated in this mode. This integrates the ToT of all hits and is called the *integrated Time-over-Threshold* (iToT). In the second mode, the time-of-arrival of individual hits is measured. The third mode, as the name suggests, records the time-of-arrival and time-over-threshold for each hit.

Super-pixel: Building block: Pixel matrix:
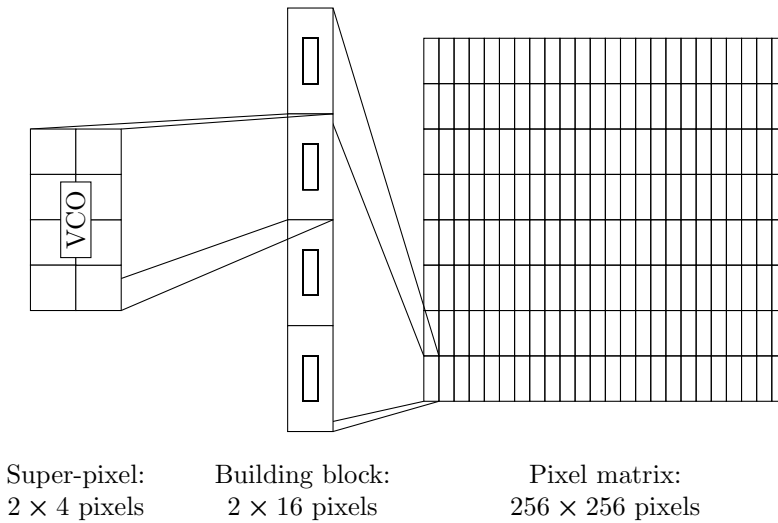2×4 pixels 2×16 pixels 256×256 pixels

Figure 4.3: A schematic view of the different groupings in the pixel matrix of Timepix3. As indicated, a single VCO is shared by all pixels in the super-pixel. In turn, four super-pixels share some common clock buffering. These super-pixel groups make up the full matrix.

Each pixel in the matrix contains its own analogue circuitry, consisting of a charge-sensitive preamplifier with Krummenacher feedback [72] and has leakage current compensation. In addition to the preamplifier, there is also a local threshold adjustment and a discriminator. Besides the analogue circuitry, each pixel also contains a digital part which includes a ToT counter as well as a coarse and a fine time counter. Each group of 2×4 pixels, referred to as a super-pixel, shares additional common logic and a local start-stop voltage-controlled ring oscillator (VCO). This VCO generates a 640 MHz clock that is used for fine timestamping in bins of 1.56 ns. The VCO will start when a pixel is above the threshold and will stop as soon as the first rising edge of the slow clock (40 MHz) is seen. This, however, means that if two pixels are hit within the same 25 ns period the second hit encounters an already running oscillator. Since the start-up time of each pixel within the super-pixel varies slightly due to differences in the length of the traces to the VCO, and thus varies in capacitance, the time resolution of such the ASIC will degrade. Therefore, it is essential to measure and characterise these pixel-to-pixel differences to reach the optimal temporal performance of the ASIC. This encompasses the correction of each hit based on the predetermined offsets and characteristics of the various clocks as well as their distribution that have been determined beforehand by the characterisation. Furthermore, each vertical group of four super-pixels are grouped and share clock buffering. Each vertically placed column of building blocks is called a *double column* and shares some End-

of-Column (EoC) logic at the periphery. This grouping structure is indicated in fig. 4.3. An overview of the analogue and digital logic in the pixels and super-pixels is shown in fig. 4.4.

ToA and ToT measurement

The Time-over-Threshold (ToT) measurement is performed with the 40 MHz clock and the Time-of-Arrival (ToA) measurement with both the 40 MHz and the 640 MHz VCO. The coarse timestamp is collected from a counter that keeps track of the number of 40 MHz cycles that passed. When a hit arrives, and the voltage after the preamplifier crosses the threshold, the value of this counter is latched and stored in the digital part of the pixel. At the same time a signal is sent to the VCO, which subsequently will start running after a short start-up time. This short start-up time results in a small ToA mismeasurement, but only for a hit that starts the VCO. For hits arriving shortly thereafter within the same super-pixel, the VCO is already running and hence this start-up time causes a mismeasurement. After starting the VCO, the pixel starts counting the number of 640 MHz cycles that have passed until the first rising edge of the 40 MHz clock. At that moment this count is read out along with the coarse timestamp from the 40 MHz clock that was latched. At the same time, the VCO will stop running. These two measurements combined yield the final ToA with a bin size of 1.56 ns. A different counter will keep running, counting the number of 40 MHz cycles until the signal returned below the threshold yielding the ToT. An illustration of a Timepix3 measurement is shown in fig. 4.5 in which two different signals are shown.

An important effect that arises when measuring different signal sizes is also indicated in fig. 4.5. Each amplifier design has a specific rise time. This rise time indicates the time it takes for the voltage signal to rise from the baseline to the maximum value. Since the rise time of a preamplifier is independent of the signal amplitude, the time it takes for signals with different signal heights to cross the predetermined threshold value depends on the signal amplitude. This effect is referred to as timewalk and can be characterised by a delay as a function of signal amplitude and hence ToT. Since the charge deposition in the detection medium is a stochastic process, there will be different delays and thus timewalk will affect the time resolution of the detector. The characterisation can be used to correct the time-of-arrival of each hit based on the ToT measurement to mitigate timewalk effects.
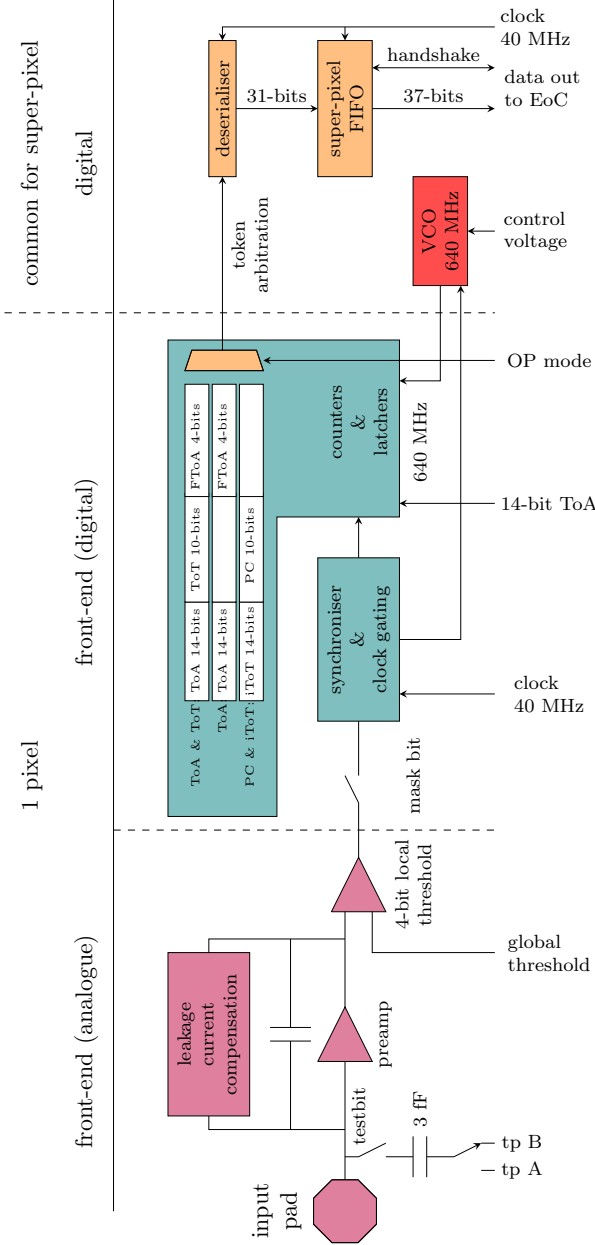
Figure 4.4: Schematic diagram of a single pixel circuitry in Timepix3. The separations are indicated by the dashed lines. The components that are shared by the super-pixel are indicated on the right-hand side. All components are labelled accordingly, and the different operation selection modes are shown as well in the centre block. Figure is adapted from [79].
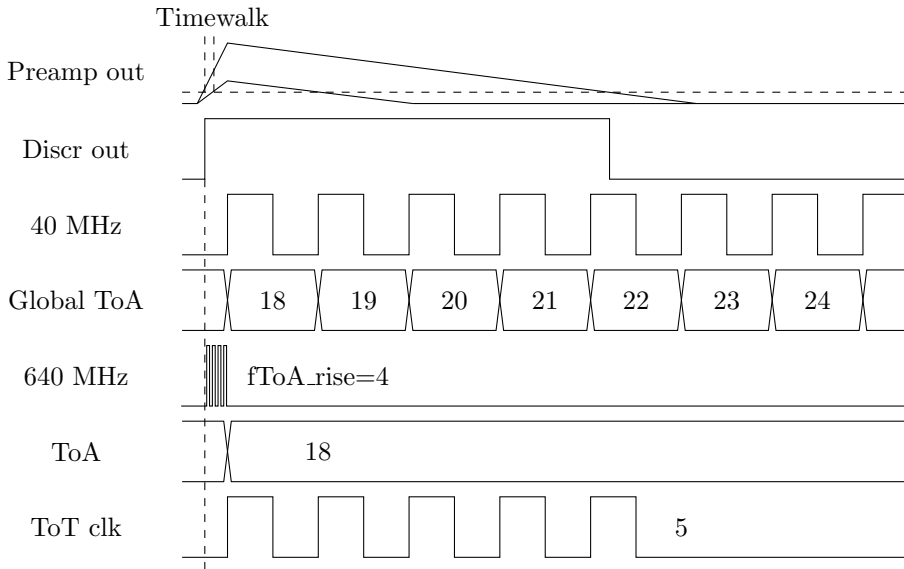
Figure 4.5: An illustration of the different clocks and the measurement technique of Timepix3. The preamplifier signal shows two different amplitude signals. The difference in the time when the signal crosses the threshold (dashed line) is different based on the charge of the hit, this effect is known as timewalk. The large signal is used as an example to show how the ToA and ToT values are determined. Figure adapted from [79].

It is important to note that the VCO frequency can be tuned by changing the control voltage supplied to the oscillator. This control voltage is generated at the periphery from a main VCO and subsequently distributed throughout the pixel matrix. During this distribution process, slight drops in voltage can occur, especially close to the edges of the distribution network. Therefore, the frequency of the VCOs close to these edges runs slightly slower, resulting in on average larger TDC bins.

The ToA and the ToT information is passed on to the super-pixel logic, shared by eight pixels. This logic, however, can only be accessed by a single pixel at a time. Once a pixel is allowed from the super-pixel logic to propagate its information, the data are moved into a deserialiser and written into a buffer for readout. Since the data are almost instantly moved into this buffer, the pixels have a dead-time of only 475 ns. Each super-pixel in turn accesses the column bus using a round-robin token scheme, via which the data are further propagated towards the End-of-Column (EoC) block, which is positioned at the periphery. Each double column has its own dedicated EoC block.

4.2.2 THE TIMEPIX4 ASIC

The Timepix4 ASIC [80] is the successor of the Timepix3 ASIC and is similar in many respects. It has two operating modes: photon counting and data-driven mode. The photon counting mode, in a similar fashion to Timepix3 measures the number of times the threshold is passed in a certain time interval, and the data-driven mode measures the ToA and ToT of each hit separately and directly pushes the data off the chip. The Timepix4 ASIC is also mated with sensors that consist of pixels with a pitch of $55\,\mu m \times 55\,\mu m$ each. However, the pixel size in the ASIC has been slightly decreased to make space to move the peripheries underneath the sensor. To ensure the matching with a $55\,\mu m$ pitch, the top layer of the ASIC is a readout layer that has bump bonding pads with a $55\,\mu m$ pitch in both directions, such that the electronic pixel can be offset from the sensor pixel. The pixel matrix of Timepix4 has been increased to 448 columns by 512 rows which is grouped in two matrices of 448×256 pixels with a dimension of $55\,\mu m \times 51.4\,\mu m$ each. The top two metal layers connect the bump pads to the ASIC pixel inputs. This routing adds a small capacitance to the input capacitance of each pixel. The capacitance is matched for each pixel separately to ensure a uniform response of the matrix.

The small downscaling of the electronic pixels leaves around $460\,\mu m$ available for the two side peripheries, and around $920\,\mu m$ for the centre periphery. This additional area is used for the peripheral circuitry, the in- and output, and the Through Silicon Via (TSV) structures. The two side peripheries also have wire bond extenders to allow the use of traditional wire bonding instead of TSV to connect the ASIC to a PCB. These side peripheries can be diced off, in case the communication is performed via the TSV, resulting in an ASIC that can be placed adjacently to itself with minimal dead area penalty for wire bonding. The Timepix4 ASIC global sizes and positions are illustrated in fig. 4.6.

Similarly to Timepix3, the analogue front-end consists of a charge-sensitive amplifier with leakage current compensation based on the Krummenacher circuit and a nominal risetime of $10\,ns$ [80]. A user-programmable feedback capacitance is implemented. A MOS gate capacitance can be enabled to program the chip in an adaptive gain mode, which only works if the signals are positive. This allows users to have a broader range in which charge can be measured, allowing a broader application range. In parallel, a 3 fF capacitor can also be enabled to decrease the gain of the amplifier to operate in the low gain mode, similarly implemented to allow a broader range of applications. A schematic illustration is shown in fig. 4.9.
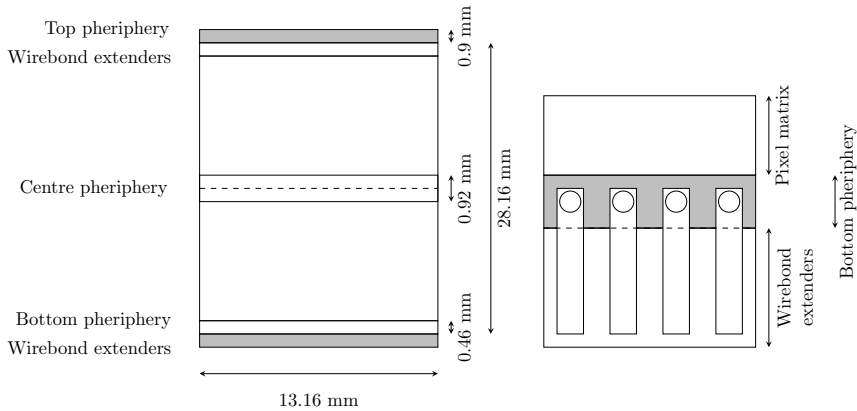
Figure 4.6: A diagram indicating the different positions and sizes of the Timepix4 ASIC on the left, and an enlarged view of the bottom periphery and wirebond extenders on the right. The three different peripheries are indicated, as well as the wirebond extenders. The dashed line in the right illustration, over the wirebond extenders, indicates the dice line where the ASIC can be diced off if TSVs are used.

DATA-DRIVEN READOUT

Just as in Timepix3, the pixels are grouped in super-pixel of two by four pixels with a shared VCO. When the discriminator of one of the pixels of the super-pixel is active, this will start the VCO. The VCO contains four inverter stages, in essence making three additional copies of the original 640 MHz clock, all shifted $\pi/2$ in phase with respect to each other (fig. 4.7). When the signal crosses the discriminator threshold, the state of the four inverters is recorded and is used to determine the 2-bit ultra-fine Time-of-Arrival start (ufToA_start). At the same time, a counter that counts the number of rising edges of the original 640 MHz is started. The VCO is stopped on the next rising edge of the 40 MHz clock, and the state of the four inverters is recorded, this time providing the ultra-fine Time-of-Arrival stop (ufToA_stop). The difference between the ufToA_start and ufToA_stop yields the ultra-fine Time-of-Arrival (ufToA). This method gives TDC bins of 195 ps, while not requiring a gigahertz clock. At the same moment when the ufToA_stop is determined, the content of the 16-bit ToA counter is latched along with the value of the 640 MHz counter, which gives the fine Time-of-Arrival (fToA_rise). At this point, a counter keeps track of the number of rising edges of the 40 MHz to determine the Time-over-Threshold (ToT), and the pileup value is determined. This pileup value is 0 if it is the first hit in the super-pixel of the 40 MHz clock cycle, and 1 if it is not the first hit. This value can be used to determine if the timestamp for example needs to be corrected for a difference in the start-up time of the VCO for each hit. This process is illustrated in fig. 4.8.
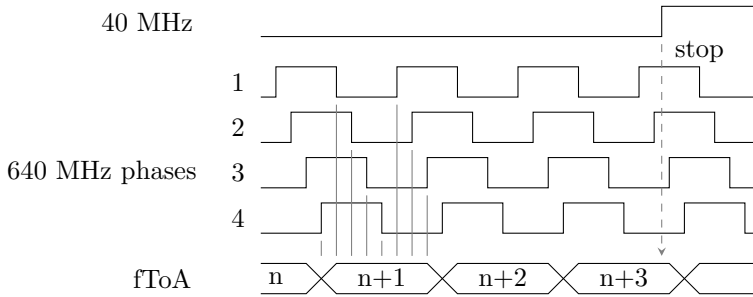
Figure 4.7: A diagram of the ufToA measurements, and the four 640 MHz clocks that are used to generate eight different bins. The vertical grey lines indicate the eight different bins. Figure adapted from [81].

When the signal falls below the threshold again, the ToT counter is latched and the VCO is restarted. It increments the fToA_fall counter until the next rising edge of the 40 MHz clock. The ability to also measure the fToA_fall enables extending the ToT with a more precise measurement compared to Timepix3 (25 ns vs 1.56 ns). This could yield a more accurate energy measurement, which can be of interest for application in particle identification and can lead to a more precise timewalk calibration. After this stage, the row address is appended to the data packet. This packet is passed along towards the end-of-column (EoC), where it receives the double-column address, totalling a 64-bit packet per hit.

The pixels must request permission to transfer the data from the pixel to the EoC. A priority encoder is used to determine in which order the pixels get permission. Such an encoder is a circuit or algorithm that outputs the binary value of the highest priority input that is active [82]. At each periphery, a packet processor aggregates the data packets. From here, a router multiplexes the data onto the available fast serial links. The speed of these links can be programmed between 40 Mbps and 10 Gbps.

To reach the temporal precision Timepix4 aims for, it is crucial to have an accurate copy of the VCO at each super-pixel. Therefore, there are major design changes compared to Timepix3. Each double column of Timepix4 is divided into 16 smaller groups, called super-pixel groups, consisting each of four super-pixels. This group is called the super-pixel group (SPG). Each SPG contains two adjustable delay buffers (ADBs). One of these ADBs is used to propagate the clock up the double column, while the second one is used to propagate the clock downwards again. At the EoC there is a controller that ensures that the delay between the input and return of the clock after it has propagated through each SPG twice (round trip) is exactly 25 ns. The control can increase or decrease the delay to the ADBs and contains 14 coarse delay elements and 15 fine delay elements. The
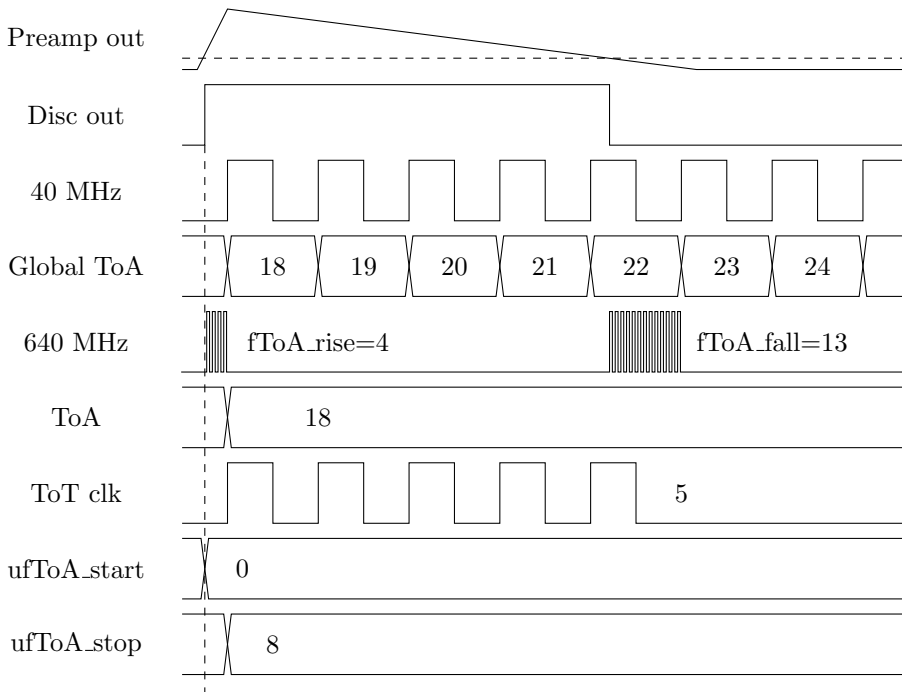
Figure 4.8: A diagram of the different clocks and the measurement technique of Timepix4 in data-driven mode. The signal is indicated by the line shown in the preamp out row, and the horizontal dashed line represents the threshold. Figure adapted from [80].

step size of the fine delay is 4 ps. In case one of the ADBs is malfunctioning, the possibility of disabling this ADB is also implemented in the ASIC. Relying on these ADBs for the clock distribution yields a more stable clock distribution with respect to Timepix3.

The Timepix4 ASIC also has so-called digital pixels. The first super-pixel row on each side of the ASIC can be enabled to register an external input instead of the signal from the pixels. Four external signals can be timestamped with the same precision as the signals generated by particles in the silicon sensor using these digital pixels.

Different versions of Timepix4 ASIC

The first engineering run of the Timepix4, submitted in the fourth quarter of 2019 and now referred to as *Timepix4v0*, was found to contain a few bugs. One of the main issues was that the VCO behaved differently than expected. Therefore, the control voltage that was needed to achieve the 640 MHz was outside the voltage range. When the control voltage of the VCO was turned down to its lowest value,

the VCO was operating at approximately 840 MHz. This means the fToA ranges from 0 to 20 instead of 0 to 15. Since the fToA bit contains five bits, the dynamic range was still enough to operate the ASIC without a loss of information. Besides the problem with the VCO frequency, there was a problem with the 640 MHz clock in the edge peripheries as well as excess noise in the pixels above the peripheries.

A resubmission of the ASIC was made in the third quarter of 2020 and addressed the problem with the 640 MHz in the edge peripheries as well as the excess noise. This submission also contained test structures on the wafer to test various designs of the VCO in order to resolve that problem in a future resubmission. This second version is referred to as *Timepix4v1* and was the first version of the chip that was used in sensor studies.

In the second quarter of 2021, a second resubmission of the ASIC was made that solved the problem of the VCO running too fast, and proved to have addressed this issue. This version is referred to as *Timepix4v2* and is envisioned to be the last alternation of the chip. Tests with the Timepix4v2 have proven that the VCO is indeed capable of running at the design value of 640 MHz.
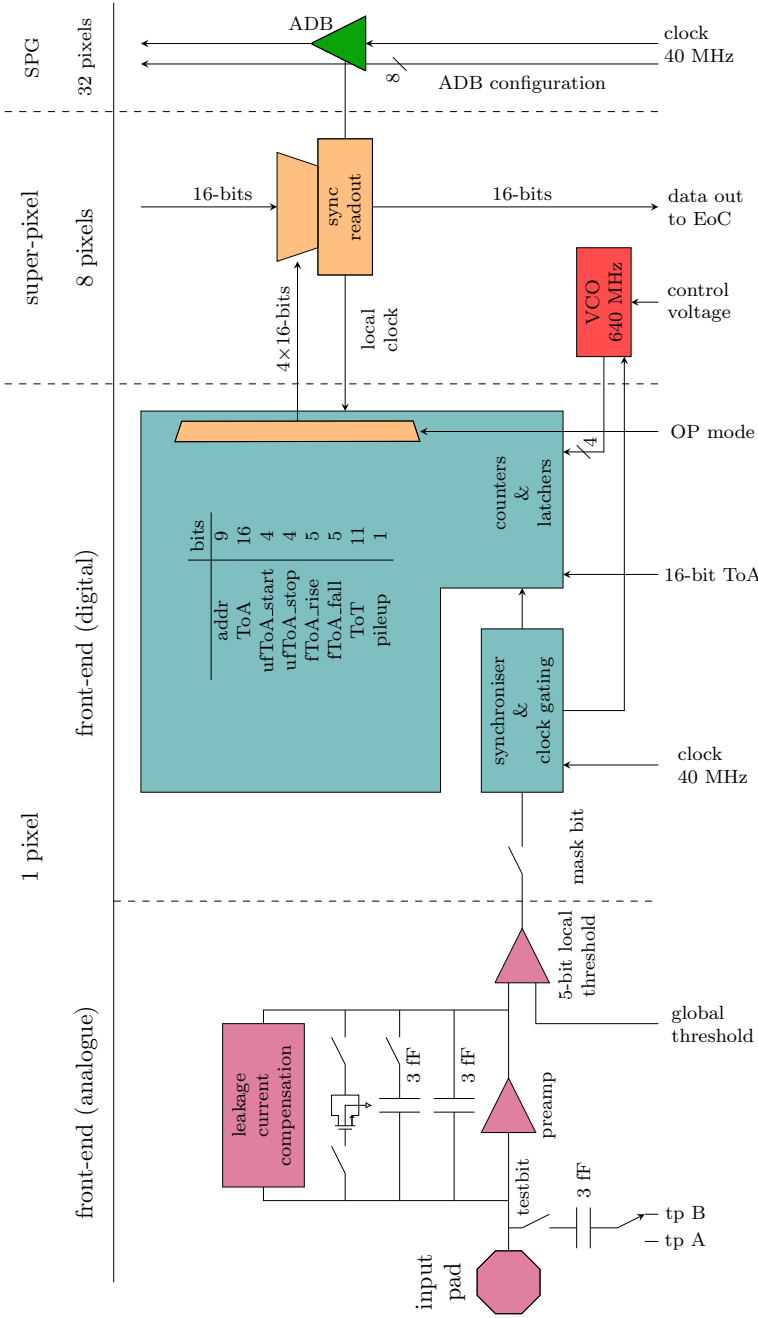
Figure 4.9: Schematic diagram of a single pixel circuitry in Timepix4. The separations are indicated by the dashed lines. The components that are shared by the super-pixel or every 32 pixels are indicated on the right-hand side. All components are marked accordingly and the different operation modes are shown in the centre block. Figure is adapted from [80].

4.3 DEDICATED READOUT FOR TIMEPIX ASICS

The ASICs that have been described here need dedicated electronics to process the output signals. Generally, ASICs will be glued onto a dedicated PCB, which, in turn, can be connected to a dedicated readout board. These PCBs and readout boards are specifically designed for each ASIC. However, the components used on these boards often consist of an FPGA, memory, and a connection to interface with the next part of the readout chain (such as ethernet or optical communication). For Timepix3, one of the readout boards that is available is the SPIDR [83, 84] (Speedy PIxel Detector Readout) that is developed at Nikhef. A successor of the SPIDR is also developed to read out the Timepix4 ASIC, named SPIDR4. These two readout boards are discussed in the following paragraphs and are used for the work contained in this dissertation.

4.3.1 THE SPIDR READOUT BOARDS

The SPIDR [83, 84] is based on the Xilinx Virtex 7-series FPGAs. Two different versions of the system were developed. The first version of the SPIDR is based on the VC707 development board, which is widely available as an *off-the-shelf* system and can be used to read out up to two Timepix3 ASICs in parallel. The second version is a custom system developed by Nikhef, named the Compact-SPIDR.

The Compact-SPIDR is smaller compared to the SPIDR, as the name already suggests. Since this Compact-SPIDR is developed specifically to read out ASICs, it contains functionality dedicated to reading out a pixel chip, such as dedicated power lines and sensors [83].

The SPIDR has the ability to timestamp an external signal. This timestamping relies on the common 40 MHz clock shared between the Timepix3 and the VC707. A Phase-Locked Loop (PLL) generates a 320 MHz clock from this common clock and provides six copies shifted by $\pi/3$ in phase, respectively. Registering the state of these six clocks when a trigger signal arrives, allows the trigger to be timestamped in bins of 260 ps. The Compact-SPIDR however cannot timestamp these external trigger inputs.

In contrast to SPIDR, the SPIDR4 was directly developed via a custom readout board. Therefore, it has been optimised for the readout of Timepix4, with dedicated power lines and sensors. Since Timepix4 already has digital pixels that can timestamp external signals, there is no possibility to timestamp via the SPIDR4. The readout of the SPIDR4 goes either over a single 10 Gbit/s Ethernet connection or using dedicated Samtec[1] FireFly devices that allow up to 16 lanes of optical 10 Gbit/s readout.

---

[1] Samtec, Inc., 520 Park East Boulevard, New Albany, Indiana United States of America

4.4   Summary

As discussed in this chapter, the signals produced by sensors are further processed and digitised by the ASIC. These ASICs in turn are read out by dedicated readout boards which are designed with high data throughput in mind. The readout boards in turn send the data to dedicated data acquisition computers which store the data for analysis at a later stage.

In the case of multi-detector experiments, such as beam telescopes, this involves the association of hits on different planes into tracks. To evaluate the temporal and spatial resolutions of prototype detectors, the information is combined and the predicted position and timestamp can be compared to the measurement of the prototype. This is explained in detail in chapters 6 and 7, where the testbeam and lab analysis results are presented.

CHAPTER 5

❧

BEAM TELESCOPES

THE CHARACTERISATION of any detector that provides spatial and temporal measurements requires the precise knowledge of when and where a particle traverses the sensing material. Several measurement techniques have been developed in order to either obtain this information or to control the position and time of the creation of the charge carriers. Examples of this are charged particle tracking devices (commonly known as beam telescopes), micro-focussed X-ray beams, and collimated optical or particle beams. The micro-focussed X-ray beams and highly collimated beams are examples of precisely controlling when and where the charge carriers are liberated, while beam telescopes can reconstruct and extrapolate the time and position of the trajectories of particles. Two of these measurement techniques have been used in this dissertation to study the behaviour and characteristics of silicon sensors: beam telescopes and (near-)optical focused beams.

In the previous chapters, we have discussed how a charged particle can be detected in a single sensor and its signal subsequently read out via dedicated electronics boards. This chapter discusses how multiple detection planes are combined into a beam telescope. We will focus on the two specific beam telescopes used for detector studies in this dissertation, based on Timepix3 ASICs and Timepix4 ASICs, respectively.

Beam telescopes consist of multiple detector planes used to reconstruct the trajectories of traversing particles. In literature, these devices are also called (beam) hodoscopes, coming from the Greek *hodos* for path, and *skopos* for an observer. However, this term eventually became less used, and researchers started to use the term *beam telescope*. Hodoscopes, or beam telescopes, have proven their use already for many decades. By being able to measure the position of particles at different positions along its trajectory, the path, also referred to as the *track* of

the particle, can be determined and either inter- or extrapolated to the position of a Device-Under-Test (DUT). This way, the position and time measurement of the DUT can be compared to the predicted values from the beam telescope. This allows to evaluate properties of the DUT such as its hit efficiency or spatial and time resolution.

This chapter focuses on the Timepix3 telescope [85, 86] and the Timepix4 telescope. The latter device is still under development. The main goal of these two telescopes is to provide a testbed for sensor and ASIC characterisation for the LHCb VELO project. The Timepix3 telescope has been used for the sensor and ASIC development of the VELO Upgrade 1 [87, 88], and the Timepix4 telescope is envisioned to play a similar role in this development for the VELO Upgrade 2 [13]. Both of these telescopes are operated in a beamline located at the North Area of CERN, where the beam dump of the SPS is used to create a beamline consisting of a mixed 180 GeV/c hadron beam (protons, pions, and kaons) used among others for detector research.

The main difference between the two telescopes is the time resolution. After several years of analysis and optimization, the track time resolution for the eight plane based Timepix3 telescope is estimated at 276 ± 4 ps [86]. The Timepix4 telescope is expected to reach a resolution below 100 ps based on the silicon detector planes. This difference can be mainly attributed to the developments in ASIC technology.

The focus for the VELO Upgrade 1 was on the spatial resolution - the VeloPix [89] (the ASIC implemented in the VELO Upgrade 1) has 25 ns TDC bins. Therefore, the temporal characterisation of sensors for the VELO Upgrade 1 was of lesser importance and the main focus was to achieve a spatial resolution at the DUT to enable intra-pixel studies. Based on the lessons learnt with the Timepix3 telescope, the layout and configuration of the Timepix4 telescope are slightly modified, as is discussed below.

This chapter is divided as follows. In section 5.1 we discuss the Timepix3 telescope along with some performance matrices. In section 5.2 we discuss the Timepix4 telescope and improvements that can be implemented to achieve better operation in the future.

5.1   The Timepix3 telescope

The Timepix3 telescope [85] was constructed in 2013 and finally decommissioned in 2021. It consisted of two arms each containing four planes of Timepix3 ASICs, in total including eight detector planes. Each Timepix3 ASIC is connected to a planar 300 μm p-on-n sensor. The planes are each titled 9° degrees in both axis with respect to the beam to improve the spatial resolution. By tilting the sensors, the charge sharing between neighbouring pixels is enhanced resulting in a more

accurate measurement using a charge-weighted position measurement based on the lateral charge spread within the silicon sensor. A DUT can be placed between the two arms and can be rotated and moved laterally with respect to the beam. A more detailed description of this telescope can be found in [85]. The schematic layout is shown in fig. 5.1 and the mechanical design of the telescope is shown in fig. 5.2. As a time reference system, two scintillators have been included which are connected to the trigger inputs of the SPIDRs via an amplifier and *Constant Fraction Discriminator* (CFD), to prevent timewalk on the scintillator signal.
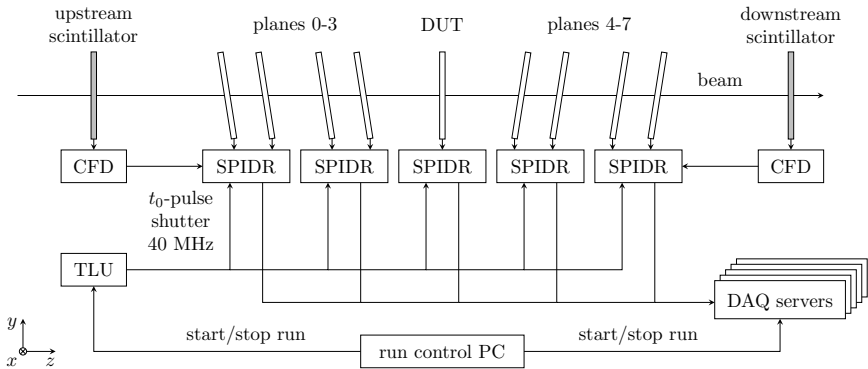

Figure 5.1: A schematic illustration of the Timepix3 telescope. The planes and the DUT are indicated along with the scintillators. The different signal paths are indicated by arrows and are labelled accordingly. Figure adapted from [86]

Each set of two planes is connected to a single SPIDR that is in turn connected to both a central *run control computer*, and a dedicated data acquisition (DAQ) server. The Timepix3 ASICs are all connected to a central *Telescope Logic Unit* (TLU). This TLU distributes a common 40 MHz clock, a t_0-pulse that resets the counters of all ASICs at the same moment to create a common start, and a shutter signal. This shutter signal ensures that all planes start and stop measuring at the same time. The TLU in turn is controlled via the run control computer.

The Timepix3 telescope achieved a spatial resolution at the z position of the DUT of $1.69 \pm 0.16\,\mu\mathrm{m}$ (in x and y), and an initial time resolution of about 350 ps solely based on the timestamps of the eight Timepix3 planes, excluding the use of the scintillators. After correcting for timewalk effects in the tilted planes, pixel-to-pixel variations in the VCO frequency and VCO startup time, a time resolution of 276 ± 4 ps [86] is achieved based on only the Timepix3 planes, which is slightly worse than what is expected based on the time resolutions of the individual telescope planes. The remaining contributions to the time resolution are thought to be due to variations in the time offsets between telescope planes and triggers [86].
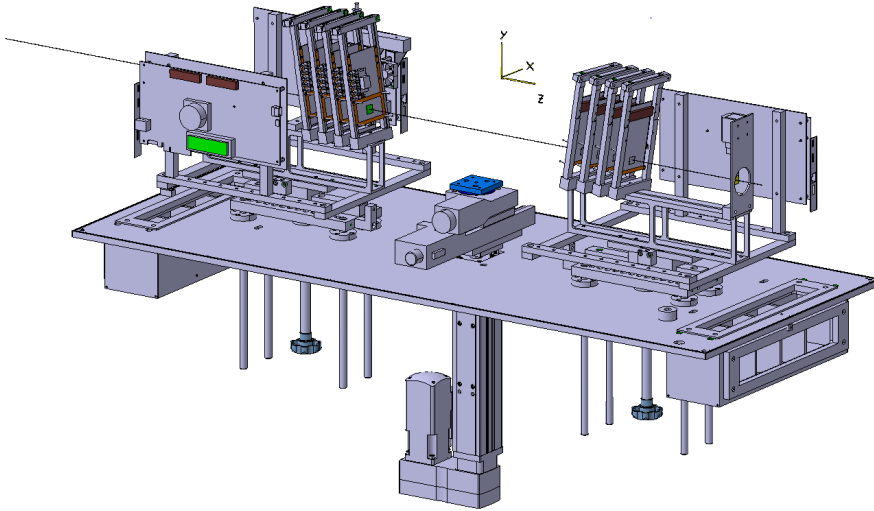
Figure 5.2: A drawing of the mechanical layout of the Timepix3 telescope. The two arms of the telescope are visible, along with the four detector planes per arm. The axis system and the path of the particle beam (solid black line traversing the two arms) are also indicated. The scintillators are not shown in this drawing. Figure taken from [85].

A dedicated software package *Kepler* [85] has been developed that provides the alignment of the telescope as well as the tracking and association of hits on the DUT to tracks. This package is based on the *Gaudi* [90] event processing framework, and is similar in flow to the software used by the LHCb collaboration.

5.2   THE TIMEPIX4 TELESCOPE

With the release of the next generation ASIC in the Timepix family, a new telescope based on the Timepix4 ASIC is constructed. This telescope aims to develop a platform to test novel sensors and ASICs for application in fast-timing and position-sensitive detectors. The most significant improvement expected from this change of ASIC is an improvement of the time resolution of the telescope. Four 100 μm n-on-p planes are placed perpendicular to the beam to accommodate the precise time resolution, since thin planes placed perpendicular to the beam achieve a better time resolution than the thick (tilted) planes. The other four planes remain planar 300 μm n-on-p sensors tilted at an angle of 9° with respect to the beam. The loss of four tilted planes compared to the Timepix3 telescope will result in a slightly worse pointing resolution at the DUT position. However, the addition of four dedicated timing planes will improve the temporal resolution significantly. The telescope tracks are expected to have a time resolution of just below 100 ps based solely on the detector planes. To be able to study devices with this

telescope that have a better time resolution such as LGADs, a *MicroChannel Plate PhotoMultiplier Tube* (MCP-PMT) in combination with a PicoTDC, a 64 channel TDC with 3 ps bin size, is employed that can be synchronised using the TLU. This combination is expected to yield a time resolution in the order of 20 ps, but will not be able to cope with the same beam rate as the Timepix4 planes can. Therefore, the temporal information is envisioned to come solely from the Timepix4 hits in high-rate applications, while the more precise temporal information can be used in low-rate applications.

The similarity of the Timepix4 telescope to that of the Timepix3 telescope allowed to extend the previous software framework, *Kepler*, to include the processing of Timepix4 and PicoTDC data. However, the control software for the telescope needed to be redesigned since the control of SPIDR4 is different from that of SPIDR, as well as the addition of the PicoTDC into the control software and additional peripherals.

In contrast, some significant changes have been applied in the Timepix4 telescope with respect to the Timepix3 telescope. Whereas the Timepix3 telescope employed two *high voltage* (HV) supplies as the bias supply of the telescope sensors, each plane in the Timepix4 telescope will be supplied by separate HV channels to be able to characterise every sensor separately and determine the optimal operation conditions such as the bias voltage of each plane. Moreover, all ASICs will be cooled directly via a titanium-printed cooling block in which chilled glycol circulates that is connected to the ASIC (or PCB). The two arms are also subdivided into two smaller enclosures that are both flushed with dry air to prevent condensation.

The initial configuration of the Timepix4 telescope is similar to that of the Timepix3 telescope, but the outer four tilted 300 μm sensors planes have been replaced with four perpendicular 100 μm sensors, as indicated in fig. 5.3. The mechanics of the arms are constructed such that changing the layout of the planes can be performed without constructing new enclosures. Simulations are being carried out to optimise the layout for the two arms, after which the telescope can be adapted correspondingly.

5.2.1 VERSIONS OF THE TIMEPIX4 TELESCOPE

Since the release of the Timepix4 ASIC, three configurations of the telescope have been implemented, reflecting the availability of both ASICs and sensors throughout the construction period of the telescope.

- The first configuration was implemented for a beamtest period in October 2021. It consisted of four planes of Timepix4v1 ASICs, two perpendicular 100 μm n-on-p and two tilted 300 μm n-on-p sensors, constructing essentially one arm of the final configuration of the telescope. Due to the limited avail-
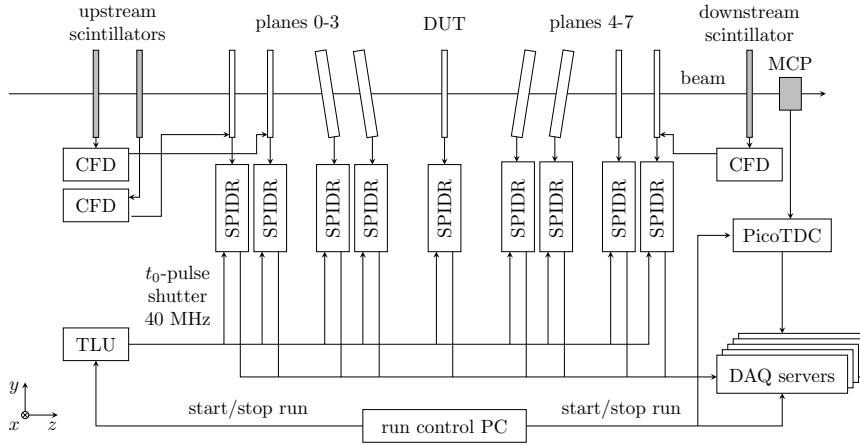
Figure 5.3: A schematic illustration of the Timepix4 telescope. The planes and the DUT are indicated along with the scintillators and MCP. The different signal paths are indicated by arrows and are labelled accordingly. The solid line through the scintillators and planes indicates the beam path.

ability of Timepix4v1 ASICs that were bump bonded to sensors at that time, this configuration was limited to only these four planes. However, it proved to be a valuable test object for future configurations of the telescope. The results from this configuration have been analysed and the findings summarised in the paper reproduced in section 5.3. The results contain voltage and bias scans for both the position and time resolution of the individual planes. This served as a proof of principle to scan the operating conditions and find the optimal settings for the final telescope. A picture of this telescope is shown in fig. 5.4 where, on top, four SPIDR4s can be seen and two upstream scintillators in front of the enclosure (left-hand side of the picture).

- The second configuration was implemented for a beamtest period in June 2022, and consisted, due to limited availability of Timepix4v2 ASICs, of a combination of four Timepix4v1 ASICs and four Timepix4v2 ASICs. The arm from the previous configuration was used, and a second one was constructed containing four Timepix4v2 ASICs, again with two perpendicular $100\,\mu m$ n-on-p and two tilted $300\,\mu m$ n-on-p sensors.

- A third configuration was implemented for a beamtest period in October 2022, completely with Timepix4v2 ASICs, however during the operation of this telescope it was found out that not all ASICs were operational, and thus the telescope was used with seven planes (three perpendicular $100\,\mu m$ n-on-p and four tilted $300\,\mu m$ n-on-p sensors). Eight planes is still the minimal planned configuration for the next beam campaign.
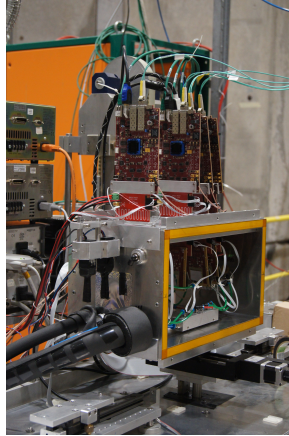
Figure 5.4: Picture of the first configuration of the Timepix4 telescope which was constructed in October 2021. The four SPIDRs can be seen on top of the enclosure, as well as two scintillators (black) in front of the enclosure. The four Timepix4 planes can be seen inside the enclosure.

In the remainder of this section, we focus further on the final concept of the telescope. As mentioned before, the Timepix4 telescope is influenced by the Timepix3 telescope, and thus similarities are inherent. The expected eight plane layout of the Timepix4 telescope is shown in fig. 5.3, which incorporates the missing plane from the October 2022 beamtest period. The main difference is the change from tilted 300 μm planes to 100 μm planes as a timing reference (first and last two planes). In addition, a third scintillator and a new timing reference system based on an MCP-PMT and PicoTDC were added. Once this telescope is commissioned, the planes will be characterised for their temporal performance and spatial resolution. Based on these scans, the optimal operation conditions will be determined. It is also envisioned that newer types of sensors will be bump-bonded to Timepix4 ASICs, and subsequently could be added to the telescope, such as 3D or LGAD sensors. These sensors could replace the planar 100 μm n-on-p sensors that are currently used for timing.

With a fully functional Timepix4 telescope, the sensors that need to be characterised and tested for the Upgrade 2 of the LHCb VELO can be tested, both with the high-rate capability, with a temporal reference resolution of just below 100 ps, and at low-rate capability with a more precise temporal reference resolution of around 20 ps based on the MCP-PMT.

5.3   Reconstruction of charged tracks with Timepix4 ASICs

This section contains a paper that describes the first version of the telescope. This telescope consisted of a single arm with four Timepix4v1 ASICs. The paper also contains the analysis and results of both the spatial and temporal performance of the individual planes for different operating conditions. These consist of bias voltage and threshold scans.

This paper titled *"Reconstruction of charged tracks with Timepix4 ASICs"* is published in JINST [91].

Reconstruction of charged tracks with Timepix4 ASICs

**K. Akiba,[a,*] M. van Beuzekom,[a] V. van Beveren,[a] W. Byczynski,[b,c] V. Coco,[b] P. Collins,[b]
E. Dall'Occo,[d] R. Dumps,[b] T. Evans,[e] R. Geertsema,[a] E.L. Gkougkousis,[b] M.M. Halvorsen,[b]
B. van der Heijden,[a] K. Heijhoff,[a] E. Lemos Cid,[f] T. Pajero,[g] D. Rolf[b,d] and H. Schindler[b]**

[a]*Nikhef,*
 Science Park 105, 1098 XG Amsterdam, the Netherlands

[b]*CERN,*
 1211 Geneve, Switzerland

[c]*Tadeusz Kosciuszko Cracow University of Technology,*
 Cracow, Poland

[d]*TU Dortmund,*
 Otto-Hahn-Strasse 4, 44227 Dortmund, Germany

[e]*Department of Physics and Astronomy, University of Manchester,*
 Manchester, United Kingdom

[f]*Instituto Galego de Fisica de Altas Enerxias (IGFAE), Universidade de Santiago de Compostela,*
 Santiago de Compostela, Spain

[g]*Department of Physics, University of Oxford,*
 Denys Wilkinson Bldg., Keble Road, Oxford, OX1 3RH, United Kingdom

 E-mail: kazu.akiba@nikhef.nl

ABSTRACT: The spatial and temporal performance of a four-plane system composed of silicon sensors bump-bonded to Timepix4 ASICs is assessed with a 180 GeV/c mixed hadron beam at the CERN SPS and reported in detail. Particle tracks are reconstructed using time-space measurements from the four detector planes, two 100 μm planes perpendicular to the beam and two 300 μm sensors under an angle of 9°. The spatial hit resolution is assessed to be (15.5 ± 0.5) μm and (4.5 ± 0.3) μm for 100 μm and 300 μm thick sensors, respectively. The timestamps from the detectors are also measured with fine precision, yielding time resolutions of (452 ± 10) ps, (420 ± 10) ps, (639 ± 10) ps, (631 ± 10) ps for the two 100 μm and two 300 μm thick sensors respectively. These measurements are combined to a track time resolution of (340 ± 5) ps. The design of the detector system is described together with its data acquisition system, operational infrastructure, and dedicated software.

KEYWORDS: Hybrid detectors; Particle tracking detectors (Solid-state detectors); Solid state detectors; Timing detectors

---

*Corresponding author.

Contents

5

1 Introduction

Future experiments in high energy physics will require timing measurements of the order of 10 ps in addition to the state-of-the-art spatial measurements. The main motivation is to cope with the high occupancy at hadron colliders operating at a high number of collisions per bunch crossing, by separating tracks from different quasi-simultaneous collisions [1]. The Timepix Application Specific Integrated Circuit (ASIC) family has previously been employed in the reconstruction of charged particle trajectories [2–5], in particular as an R&D platform for sensors, ASICs and other detector components used for the upgrades of the LHCb experiment. Timepix4 [6] is a novel ASIC designed for performing both temporal and spatial measurements with 195 ps bin width and $55 \times 55\,\mu m^2$ pixel size. Its timing precision enables the use of spatial and temporal information in a 4D-tracking approach, which is essential in the R&D efforts for the next generation of experiments.

In this paper the design of a single arm four-plane telescope based on the Timepix4v1 ASIC is described together with the data acquisition system, operational infrastructure and dedicated software. This is a first step towards a two arm telescope with at least eight planes with the final version of Timepix4 ASIC [6], targeting a spatial resolution of $2\,\mu m$ or better and a temporal resolution of $O(30)$ ps. Finally, the spatial and temporal performances are assessed using a 180 GeV/c mixed hadron beam at the SPS H8 beam line facility [7].
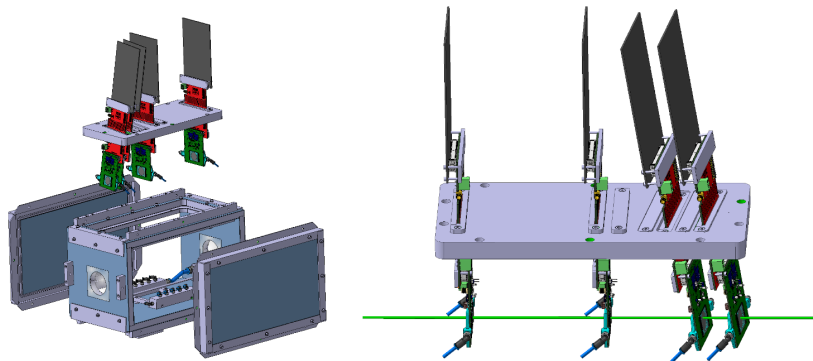
Figure 1. Mechanical design of the telescope-like arrangement of four measuring planes. The sensors are placed in a light-tight nitrogen environment, separated from the outside by flanges placed at predefined positions. The green solid cylinder line cutting through the planes represents the traversing beam.

2   Hardware description

The telescope consists of a single arm with four detector planes as illustrated in figure 1. A global right-handed coordinate frame is defined with the z axis in the direction of the beam and the y axis pointing upwards. This convention is adopted throughout this paper.

The detectors are mounted inside a custom hermetic enclosure to provide a cold, light-tight and humidity free environment. The top cover of this box was machined with slots to allow the insertion of detector planes with the use of matching flanges. The individual flanges are composed of matching half-moons which are attached to the detector boards for insertion in the slots. The positions of the telescope planes along the z axis are determined by predefined slots on the top cover, and are 0, 150, 250 and 290 mm. The slots are machined to achieve different angles of the sensor planes with respect to the z axis. The two upstream sensors are perpendicular to the z axis to achieve a better temporal resolution. The other two sensors are angled at 9° with respect to the x and y axes in order to improve the spatial resolution [8]. For the majority of the data collection period, the first two slots were instrumented with 100 μm thick sensors (with identifiers N30 and N29), while 300 μm thick sensors (identified by N23 and N28) occupied the downstream slots. In the following sections, this is referred to as the default configuration. A limited data set was also acquired with an alternative configuration, where one 100 μm sensor (N29) was placed in an angled slot and a 300 μm sensor (N23) in the perpendicular slot. The base of the telescope box is mounted on a remote controlled motion stage, which allows the entire telescope to be moved along the x and y axes, to align the telescope with respect to the beam.

2.1   Timepix4 ASIC

Timepix4 is a readout ASIC capable of simultaneous time-of-arrival (ToA) and time-over-threshold (ToT) measurements [6]. The ASIC has a pixel matrix of 448×512 square pixels of 55 μm pitch. Hence, the total active area of the detector assemblies is around $24.6 \times 28.2 \, \text{mm}^2$. The ToA of each particle hit above a predefined and programmable threshold is measured by a time-to-digital

converter (TDC) with a nominal bin width of 195 ps. Each group of 2×4 pixels, referred to as a superpixel, shares a Voltage Controlled Oscillator (VCO), which provides the 640 MHz reference clock for the pixel TDCs. Four versions of this clock are generated, and equally shifted in phase. By registering the state of all four clocks, the TDC bin of 195 ps is achieved. For this beam test, the first submission of the Timepix4 was used, which presents a flaw in the design of the VCO, causing it to oscillate about 25% too fast. For the same reason, the control voltage that is generated by the periphery Phase-Locked Loops (PLLs) could not be used, and hence the oscillation frequency was not stabilised, which degrades the time resolution. The ToT measurements used in the analyses presented in this paper are performed with a 25 ns bin width.

The Timepix4 ASIC is divided into two halves, denoted top and bottom, in order to increase readout speeds by placing serialisers on both sides. The data can be read out by up to 16 serialisers capable of running at a maximum bandwidth of 10 Gbit/s each, to be capable of reading out a maximum hit rate of 3.6 Mhits/mm^2/s. During the beam test, only one serialiser per side was used, and the combined link speed was set to 2×2.56 Gbit/s, thereby limiting the bandwidth to order 100 Mhits/s, which is still about two orders of magnitude larger than the typical rate required for the H8 beam line.

2.2 Sensors

Planar n-on-p (electron collecting) silicon sensor technology is used in this system. The sensors are composed of p-type silicon bulk with n^+-type implants, and were manufactured by ADVACAM.[1] The back side is a uniform p^+ implant which is subsequently metallised to allow for the application of a reverse bias voltage to the sensor. The front side is segmented with 448×512 approximately 39 μm square n^+ implants, separated by a uniform p-spray, and covered with under-bump metallisation which allows the pixels sensors to be bonded with solder bumps to the ASICs. The 300 μm sensors are fully depleted at a reverse bias voltage of approximately 50 V with a leakage current of around 15 nA at room temperature, and they could be operated up to 150 V without breakdown. The 100 μm thick sensors are fully depleted at around 10 V with a leakage current of about 5 nA at room temperature. One of the two thin sensors presents breakdown below 50 V, while the other could be reliably biased up to about 200 V. Two I-V characteristic curves of the 300 μm and 100 μm thick sensors are show in figure 2.

2.3 Cooling

Cooling of the planes is provided by a cooling block directly attached to the detector board, with a small surface overlap with the ASICs. The cooling blocks are made of 3D printed titanium with hollow cavities which allow liquid glycol to circulate through. The fluid is distributed in parallel to each of the planes. The cooling blocks have a circular cut-out to minimise the amount of material traversed by incident particles. The interface between the detector board and its cooling block was improved by attaching a high thermal conductivity sheet. The cooling fluid is pumped through the cooling block by an off-the-shelf chiller.

2.4 Scintillators

The timing measurements are complemented by three plastic (EJ200[2]) scintillators mounted onto the telescope box. Two are placed upstream of the pixel sensors and spaced approximately 2 cm apart

---

[1]Advacam, Tietotie 3, 02150 Espoo, Finland.

[2]ELJEN technology, 1300 W. Broadway, Sweetwater, TX 79556, U.S.A.
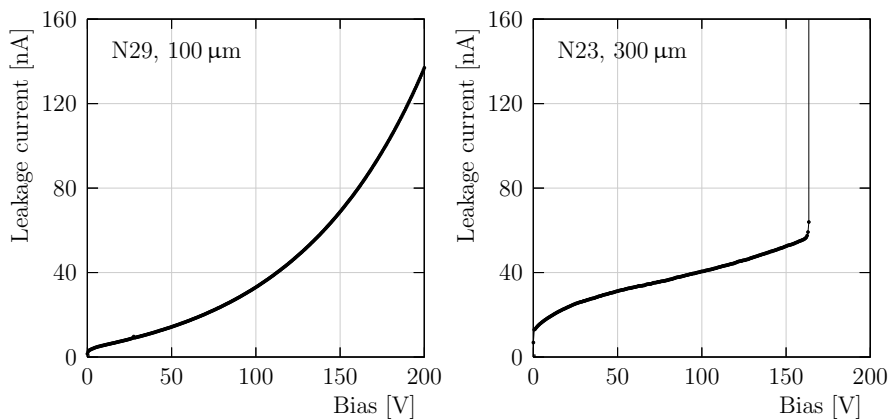
Figure 2. Left (right): I-V characteristic curve for N29 (100 μm) and N23 (300 μm) sensors. The sensors N23, N28, N30 breakdown at 160 V, 140 V and 50 V respectively, while N29 did not breakdown up to 200 V, which was the limit of the measuring range.

from each other, while the third is placed at the downstream side. The scintillators are instrumented with HPK[3] Photo Multiplier Tubes (PMTs) and their signals are processed by ORTEC-584 constant fraction discriminators (CFD) to minimise the contribution of timewalk to the electronics jitter. Each CFD output is fed back to a different Timepix4 plane where it is timestamped with a TDC of the same precision as that of the pixels. The synchronisation between the ASICs was found to be insufficiently stable to combine the three timestamps. The individual scintillators are all determined to have a resolution of around 100 ps, therefore the one most upstream was arbitrarily chosen to provide the reference time measurement.

3   Data acquisition

The Timepix4 ASICs are configured and read out with a custom developed system called SPIDR4, which is based on a Xilinx Zynq 7000 FPGA, provides the slow control interface to the Timepix4 via the on-chip ARM processor, which receives configuration commands via a 1 Gbit copper ethernet link. Regarding the slow control, all SPIDR4 systems are connected to the same computer, which runs four instances of the slow control application, one for each SPIDR4 plus Timepix4. Each instance of the DAQ (Data Acquisition) application is controlled by its corresponding slow control application. The main DAQ interface to the telescope is managed through a run-control application, which also directs all of the slow control instances.

The pixel data from Timepix4 consists of a 64 bit word for each hit. This hit data is transmitted from the chip to the FPGA using a serial 64/66 standard encoding scheme to allow for clock recovery and transmission line balancing. The distance between Timepix4 chip and FPGA is about 25 cm; the distance could be increased to about one meter, via commercially available FMC cables. The Timepix4 is operated with only one 2.56 Gbit/s serial link per half of the chip, as the track rates at this test beam

---

[3]Hamamatsu Photonics K.K., 325-6, Sunayama-cho, Naka-ku, Hamamatsu City, Shizuoka Pref., 430-8587, Japan.

were relatively low, typically below a million per second. The data from both links of each Timepix4 device are descrambled by the FPGA in SPIDR4 and packed into UDP datagrams, which are transmitted via an optical 10 Gbit ethernet connection to the DAQ computers, one for each SPIDR4. The main task of the DAQ application is to write the data to local disk, and no significant data processing is performed.

3.1 Software

A software application based on the GAUDI event processing framework [9], KEPLER, has been developed for the reconstruction and analysis of data recorded with Timepix telescopes [2]. The core functionality of the software, which is to provide reconstructed and aligned tracks in a variety of formats to end users, remains largely unchanged. The main new feature in KEPLER is the implementation of a decoder for the Timepix4 data format. In addition, large improvements to the CPU performance of the reconstruction have been achieved by simplifying the intermediate data structures used by the software and modernisation of the code base.

3.2 Data quality monitoring

A new graphical user interface is implemented to control the execution of KEPLER and to monitor the quality of the collected data in real time, implemented using the QT5 toolkit. The communication between the interface and the KEPLER server is established through the Distributed Information Management (DIM) protocol [10]. The monitored information mostly consists of histograms of quantities such as the spatial and ToT distributions of the hits in each plane, as well as properties related to the clusters or tracks. In addition the number of errors in the configuration of the ASICs and in the data communication are displayed.

4 Experiment control system and monitoring

A dedicated experiment control system is implemented to remotely operate motion stages and power supplies, as well as to monitor the environmental conditions of the telescope. The system implementation is divided in the following way: the operation of High Voltage and the monitoring of bias currents (HV control); the operation of the motion stage (motion control); the monitoring of temperature and humidity. A block diagram representation of the system is given in figure 3. The WinCC Open Architecture (OA) software suite (WinCC OA[4]) is used to implement the control system, which also provides alarm and logging capabilities. The communication between WinCC OA and the hardware is established with a custom server based on the DIM protocol and the Open Platform Communications Unified Architecture (OPC UA).

The HV-control operates two Keithley 2410 Source Meters[5] that provide independent bias voltages to the 100 μm and 300 μm thick sensor planes in the default configuration. The translation of the telescope along the x and y axes is performed by PI[6] motion stages with a repeatability of 2 μm.

The temperatures of each plane, as well as the temperature and humidity within the telescope enclosure, are monitored with four-wire Pt100 and HIH4000 sensors,[7] connected via an Embedded

---

[4]SIMATIC WinCC Open Architecture Portal https://www.winccoa.com/.

[5]Tektronix, Inc. 14150 SW Karl Braun Drive, Beaverton, OR 97077, U.S.A.

[6]Physik Instrumente (PI) GmbH & Co. KG Auf der Roemerstrasse 1 76228, Karlsruhe, Germany.
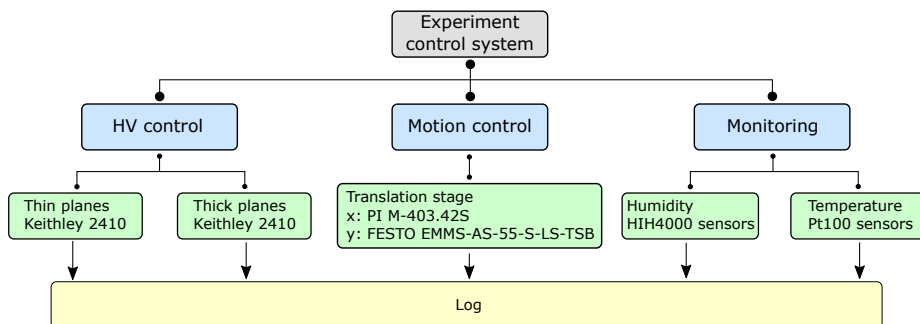
[7]Honeywell, Charlotte, NC, U.S.A.

Figure 3. Schematic overview of the experiment control system.

Local Monitor Board (ELMB). The monitored values for each component are logged in order to enable studies of the telescope performance as a function of environmental conditions. In addition, the logging of operational settings such as the bias voltage complements the information manually recorded in the logbook of the testbeam.

5 Spatial resolution and efficiency

Clusters are reconstructed by grouping nearby hits that are within 100 ns from each other. This window was selected to ensure that no two tracks overlap in time with the beam rate at SPS, and ensures that all hits with a large timewalk can also be assigned to the correct cluster. The timestamp of the cluster is assigned as the earliest time measurement in the group of hits [3]. The cluster position is calculated as the ToT-weighted average of the position of the hits constituting the cluster. Particle tracks are reconstructed requiring a cluster in each plane and their trajectories determined using a straight line fit. The clusters are required to be within a 100 ns time interval allowing a low background and high-efficiency track reconstruction given the particle rate at the SPS was less than 2×10^5 particles/s. The positions and orientations of the planes with respect to each other are determined using the Millepede algorithm [11], using a set of around 12,000 tracks. The alignment procedure is repeated several times, with progressively more stringent requirements on the χ^2 of the tracks in each iteration.

The residual is defined as the difference between the position of a cluster, and the extrapolated position of the track to the given plane. The residual is said to be *unbiased* if the cluster on the plane of interest is excluded from the track fit. The unbiased residuals are determined in the ASIC coordinate system where the x and y axes correspond to the directions of increasing column and row numbers, respectively. The resulting distributions are shown in figure 4. The spatial resolution of each plane is defined as the RMS of the unbiased residuals. Clusters outside of a central interval containing 99% of the distribution are discarded before calculating the RMS, which is then referred to as the truncated RMS. The x residuals for the nominal data-taking conditions are shown in figure 4. The truncated RMS is found, with negligible uncertainty, to be 33.2 μm, 16.6 μm, 7.2 μm and 8.7 μm for N30, N29, N23 and N28, respectively. The residual distribution is given by the convolution of the intrinsic resolution of the detector and the resolution of the track projection. The latter is the dominant contribution to the residual on the first plane due to the long extrapolation distance, and is
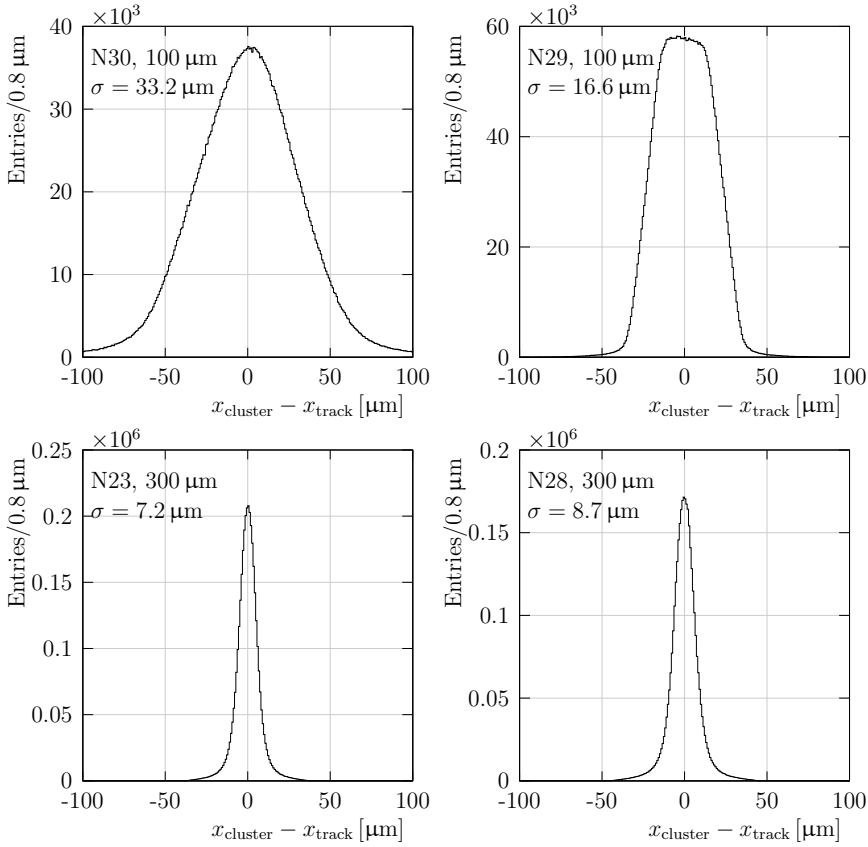
Figure 4. Distributions of *x* residuals for the clusters of each plane. The residual is defined as the difference between the cluster position and the intercept of the associated track.

estimated to be around 30 μm from the track fit. The majority of clusters consists of a single hit for the 100 μm planes placed perpendicular to the beam, which results in a worse resolution with respect to the angled planes. This can be seen from the characteristic top-hat distribution of N29 shown in the top right of figure 4. The intrinsic resolution of the planes at their operating tilt is estimated from simulation, assuming that the resolution is equal in each direction and identical for planes with the same thickness and tilt. The resolutions are found to be (15.5 ± 0.5) μm for N30 and N29 and (4.5 ± 0.3) μm for N23 and N28, in agreement with the values found for tilted 300 μm sensors bonded to Timepix3 [2].

The resolution degrades significantly with increasing operating threshold, as the measurement small charges becomes progressively lost, deteriorating the interpixel positon determination. This effect is shown in figure 5. Conversely, the resolution is found to be largely independent of the applied bias voltage.
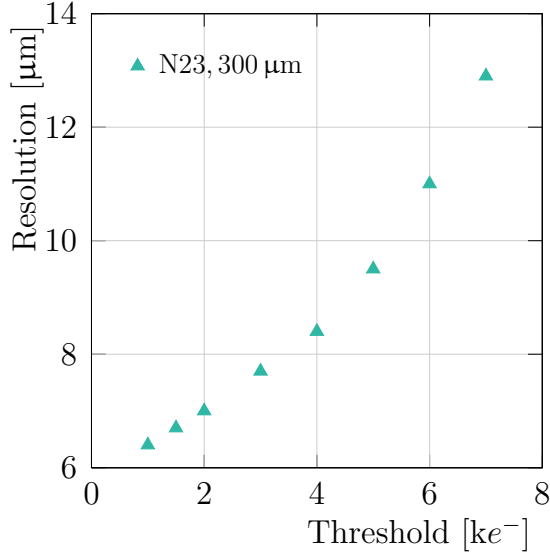
Figure 5. Resolution for the central 300 μm plane as a function of threshold.

The single-plane efficiency is measured for each plane by reconstructing tracks from the other three planes and by searching for a cluster within 150 μm and 100 ns in space and time, respectively. The efficiencies are found to be $(92.0 \pm 5.0)\%$, $(99.4 \pm 0.2)\%$, $(99.1 \pm 0.4)\%$ and $(98.2 \pm 0.3)\%$ for planes N30, N29, N23 and N28, respectively. The uncertainties are assigned using run-to-run variations throughout the data taking period. The smaller efficiency and larger variation for plane N30 is due to a large number (around 10%) of malfunctioning columns.

6   Temporal performance

In this section, the temporal performance of each of the four Timepix4 planes is assessed. The time-to-threshold (TtT) is defined as the difference between the timestamp of the earliest hit in a cluster and the reference time. The time-to-threshold is analogous to the residuals for the spatial measurements, which yields the main figure-of-merit used in this section, the temporal resolution, defined as the RMS of the time-to-threshold distribution. The timestamps are corrected for timewalk and per-pixel time offsets. After applying these corrections, the resolution is studied as a function of bias and threshold.

Timewalk correction.   It is important to correct for timewalk for low-amplitude signals, such as from the 100 μm sensors or for hits that share charge with other pixels in the same cluster in the 300 μm planes. The timewalk correction is performed based on the ToT of each hit, instead of the measured charge, since an accurate charge calibration procedure has not been developed for Timepix4 yet.
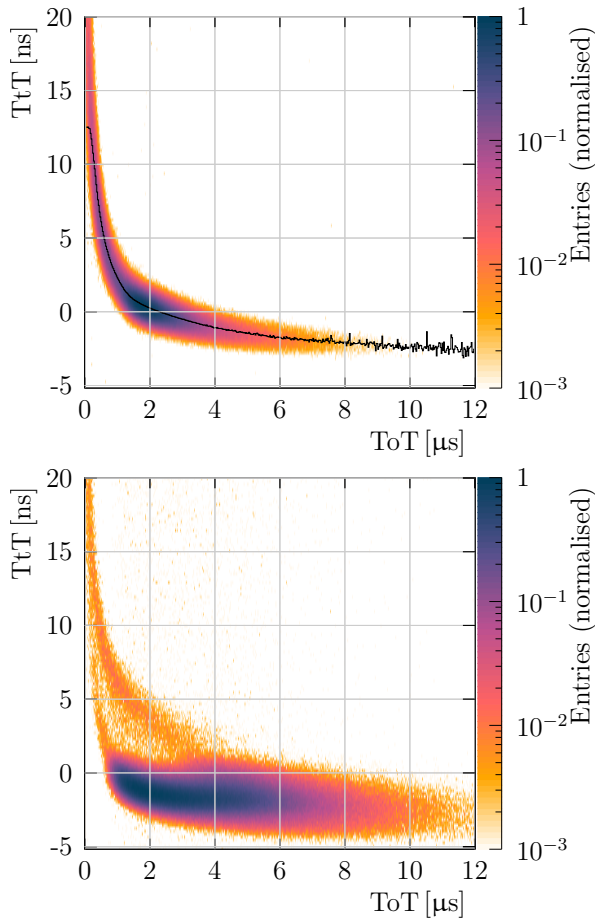
Figure 6. Top (bottom): typical timewalk distribution for a 100 μm (300 μm) plane biased at 50 V (130 V). Since the 300 μm plane is tilted, the typical timewalk distribution shows multiple bands. The black line indicates the average of the distribution.

Two different timewalk correction methods are employed, depending on the angle of the sensor with respect to the beam, as described in [3]. For the perpendicular (100 μm) sensors, the timewalk correction is performed exclusively using the ToT of hits. A lookup table that contains the average TtT for each value of ToT is created per plane. An example timewalk distribution for N29 (100 μm) is shown in figure 6 (top), where the line indicates the values in the lookup table. For the tilted (300 μm) sensors, the correction needs to account for timewalk and drift times, since the charge carriers can be liberated at different distances to the pixel implants [3].

The timewalk distribution for a tilted sensor is shown in figure 6 (bottom). Multiple bands can be seen in the distribution, indicating the necessity of a correction that additionally accounts for
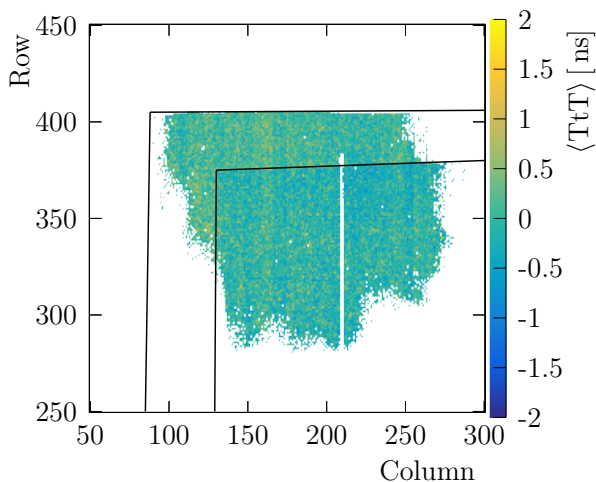
Figure 7. Measured average TtT of individual pixels of N29. The lines indicate the regions covered by each scintillator. The absence of the vertical line of data is due to partially malfunctioning columns.

the intrapixel track position at each plane. This method is described in detail in ref. [3]. Since this correction depends on drift velocity and threshold, the lookup table is determined for each set of operational settings.

Per-pixel corrections. A correction is required to account for per-pixel time offsets due to differences in VCO start time and VCO frequency variations. The average TtT is determined for each pixel to account for these differences. Corrections for differences of the TDC bin sizes are not implemented due to the limited size of the data samples.

Figure 7 shows the average TtT of the pixels of N29 (100 μm), where the lines indicate the regions covered by the two upstream scintillators. The timestamps are corrected for timewalk before the average is determined for each pixel. The distribution of the average TtT of these pixels shows a large variation with an RMS of 315 ps. This effect is corrected by subtracting the average TtT of the pixel from the timestamp.

Time resolution. The four planes of the telescope are characterised as a function of the bias voltages and threshold. The temporal resolution is determined after both timewalk and per-pixel time offset corrections have been applied. Figure 8 shows the TtT distribution, before any correction (filled histogram), after the timewalk correction (hashed), and after both timewalk and per-pixel delay corrections (solid line). The time resolution is improved from (783 ± 24) ps to (439 ± 10) ps, implying that a total contribution of 648 ps has been removed.

The resolution changes as a function of operational settings such as bias voltage and threshold. Scans over these parameters are shown in figure 9, where the left and right figures show bias and threshold scan, respectively. For all planes the time resolution shows improvement for higher bias voltages. The two tilted 300 μm sensors have a resolution that is significantly worse than that of

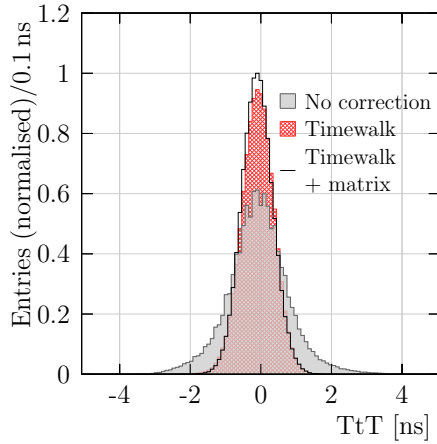**Figure 8**. TtT distribution of all pixels of N29 ($100\,\mu$m) biased at $50\,$V and a threshold of $1000\,e^-$. The filled histogram indicates the uncorrected TtT distribution, the hashed represents this distribution after the timewalk correction, and the solid line displays this distribution after both a timewalk and per-pixel time offset correction.
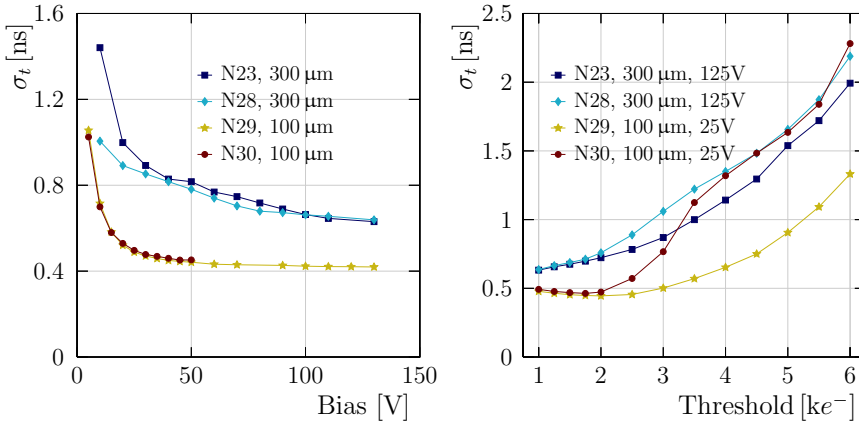

Figure 9. Left (right): time resolution of the four telescope planes as a function of the bias voltage (threshold). The four planes are indicated by the different markers.

the $100\,\mu$m sensors. The main cause is the more complex timewalk correction in addition to higher variations in the Ramo-Shockley weighting field, in comparison to the $100\,\mu$m sensors.

As shown in figure 9 (right) the time resolution slightly improves as a function of threshold for the two $100\,\mu$m sensors, reaching the best resolution around the value of $2000\,e^-$. This effect is counterintuitive but well described in ref. [6]. The two tilted $300\,\mu$m sensors do not show a local minimum. This is probably due to the larger variations in the time corrections. Plane N30 achieves

its best resolution at 50 V, and the other planes at 130 V, all at a threshold of $1000\,e^-$. Their time resolutions are (452 ± 10) ps, (420 ± 10) ps, (639 ± 10) ps, and (631 ± 10) ps for N30, N29, N38, N23, respectively. The uncertainty is estimated from run-to-run variations. The resolution of the detectors saturates around 50 V for the $100\,\mu$m sensors and around 130 V for the $300\,\mu$m sensors, and an improvement by increasing the bias voltage further is not expected.

The track time is determined by taking the uncertainty-weighted average of the individual measurements. To achieve the best track time resolution the planes should be biased at the highest operational high voltages. The resolution is determined in a configuration where the two thin planes are biased at 50 V and the other planes at 130 V, while the threshold is $1000\,e^-$ for all planes. The achieved track resolution is (340 ± 5) ps. The result of the combination of single plane measurements to a track is worse than what is expected from the naïve calculation using the separate resolutions. This is due to correlations between the time measurements, which can lead to a significantly worse resolution [3], and drift in the synchronisation between the planes.

7 Conclusions

A system composed of four Timepix4 detectors is used to reconstruct high energy hadrons from the CERN SPS H8 beam line. The overall spatial resolution is assessed for each of the detector planes by projecting the reconstructed tracks using the other three planes. The resolutions in the default configuration are estimated to be $(15.5 \pm 0.5)\,\mu$m and $(4.5 \pm 0.3)\,\mu$m for $100\,\mu$m and $300\,\mu$m thick sensors, respectively, after subtracting the expected contribution from the track extrapolation.

The timestamps from the detector are corrected for timewalk and per-pixel time offsets, finally yielding individual time resolutions of (452 ± 10) ps, (420 ± 10) ps, (639 ± 10) ps, and (631 ± 10) ps for N30 (perpendicular $100\,\mu$m), N29 (perpendicular $100\,\mu$m), N28 (tilted $300\,\mu$m), and N23 (tilted $300\,\mu$m), respectively, when compared to the measurements from the reference scintillators. These resolutions have been achieved at a threshold of $1000\,e^-$ and 50 V bias for N30, and 130 V for the other planes. These measurements can be combined to a track time resolution of (340 ± 5) ps.

---

[8]https://ep-rnd.web.cern.ch/.

References

[1] LHCb VELO group, *Considerations for the VELO detector at the LHCb Upgrade II*, Tech. Rep., LHCb-PUB-2022-001, CERN, Geneva (2022).

[2] K. Akiba et al., *LHCb VELO Timepix3 Telescope*, 2019 *JINST* **14** P05026 [arXiv:1902.09755].

[3] K. Heijhoff et al., *Timing performance of the LHCb VELO Timepix3 Telescope*, 2020 *JINST* **15** P09035 [arXiv:2008.04801].

[4] K. Heijhoff et al., *Timing measurements with a 3D silicon sensor on Timepix3 in a 180 hadron beam*, 2021 *JINST* **16** P08009 [arXiv:2105.11800].

[5] E. Dall'Occo et al., *Temporal characterisation of silicon sensors on Timepix3 ASICs*, 2021 *JINST* **16** P07035 [arXiv:2102.06088].

[6] X. Llopart et al., *Timepix4, a large area pixel detector readout chip which can be tiled on 4 sides providing sub-200 ps timestamp binning*, 2022 *JINST* **17** C01044.

[7] CERN Engineering Department, *The H8 Secondary Beam Line of EHN1/SPS*, https://sba.web.cern.ch/sba/BeamsAndAreas/H8/H8_presentation.html.

[8] E. Buchanan et al., *Spatial resolution and efficiency of prototype sensors for the LHCb VELO Upgrade*, 2022 *JINST* **17** P06038 [arXiv:2201.12130].

[9] M. Clemencic, H. Degaudenzi, P. Mato, S. Binet, W. Lavrijsen, C. Leggett et al., *Recent developments in the LHCb software framework Gaudi*, *J. Phys. Conf. Ser.* **219** (2010) 042006.

[10] C. Gaspar, M. Dönszelmann and P. Charpentier, *DIM, a portable, light weight package for information publishing, data transfer and inter-process communication*, *Comput. Phys. Commun.* **140** (2001) 102.

[11] V. Blobel, *Software alignment for tracking detectors*, *Nucl. Instrum. Meth. A* **566** (2006) 5.

5

CHAPTER 6

$\maltese$

RESULTS USING BEAM TELESCOPES

The TIMEPIX3 TELESCOPE provided a crucial testbed for the characterisation and development of the sensors and ASICs for the LHCb VELO Upgrade 1. During the year 2014 through 2018, various sensor designs have been tested to decide which sensors can be used for the upgraded detector. Three different sensor types and designs from two different manufacturers have been fully characterised. All sensors were bump bonded to the Timepix3 ASIC on which the VeloPix [89] - the ASIC used in the VELO Upgrade 1 - is based. These ASICs in turn were connected to SPIDRs which were used as a readout board. The combination of the sensor with the ASIC is called an assembly. Multiple assemblies were mounted in the telescope and tested for several parameters. In the VELO Upgrade 1 context, three papers were published with results gathered using the Timepix3 telescope containing the findings of the charge collection efficiency [92], spatial resolution [93], and the temporal characteristics [94]. The findings from the latter were not incorporated for the decision of sensor design for Upgrade 1, since the VeloPix ASIC only supports binning in 25 ns TDC bins (corresponding to the interval between bunch crossings in the LHC) but are of great interest in view of the implementation of temporal information in Upgrade 2.

In this chapter two papers are reproduced that summarise the findings of the charge collection properties and the temporal characteristics studied with the Timepix3 telescope.

6.1   Charge collection properties of prototype sensors for the LHCb VELO upgrade

This section contains a paper that describes the charge collection properties of various prototype sensors for the LHCb VELO Upgrade 1 which were studied using the Timepix3 Telescope.

This paper titled *"Charge collection properties of prototype sensors for the LHCb VELO upgrade"* is published in JINST [92].

Charge collection properties of prototype sensors for the LHCb VELO upgrade

R. Geertsema,[a,1] K. Akiba,[a] M. van Beuzekom,[a] E. Buchanan,[b] C. Burr,[c] W. Byczynski,[c,d] P. Collins,[c] E. Dall'Occo,[a,e] T. Evans,[c,f] V. Franco Lima,[g] K. Heijhoff,[a] P. Kopciewicz,[h] F. Marinho,[i] E. Price,[b] B. Rachwal,[h] S. Richards,[b] D. Saunders,[b] H. Schindler,[c] H. Snoek,[a] T. Szumlak,[h] P. Tsopelas,[a,j] J. Velthuis[b] and M.R.J. Williams[k]

[a] *Nikhef, Science Park 105, 1098 XG Amsterdam, the Netherlands*

[b] *University of Bristol, Beacon House,
Queens Road, BS8 1QU, Bristol, United Kingdom*

[c] *CERN, 1211 Geneve, Switzerland*

[d] *Tadeusz Kosciuszko Cracow University of Technology, Cracow, Poland*

[e] *Now at TU Dortmund,
Otto-Hahn-Straße 4, 44227 Dortmund, Germany*

[f] *University of Oxford, Particle Physics Department,
Denys Wilkinson Bldg., Keble Road, Oxford OX1 3RH, United Kingdom*

[g] *Oliver Lodge Laboratory, University of Liverpool,
Liverpool, L69 7ZE, United Kingdom*

[h] *AGH University of Science and Technology, Faculty of Physics and
Applied Computer Science, Kraków, Poland*

[i] *Federal University of São Carlos,
Rodovia Anhanguera, km 174, 13604-900 Aranas, Brazil*

[j] *Now at Spectricon, Science and Technology Park of Crete, Heraklion, Greece*

[k] *School of Physics and Astronomy, University of Edinburgh,
Edinburgh, United Kingdom*

E-mail: r.geertsema@nikhef.nl

ABSTRACT: An extensive sensor testing campaign is presented, dedicated to measuring the charge collection properties of prototype candidates for the Vertex Locator (VELO) detector for the upgraded LHCb experiment. The charge collection is measured with sensors exposed to fluences of up to 8×10^{15} 1 MeV n_{eq} cm^{-2}, as well as with nonirradiated prototypes. The results are discussed, including the influence of different levels of irradiation and bias voltage on the charge collection properties. Charge multiplication is observed on some sensors that were nonuniformly irradiated with 24 GeV protons, to the highest fluence levels. An analysis of the charge collection near the

---

[1]Corresponding author

guard ring region is also presented, revealing significant differences between the sensor prototypes. All tested sensor variants succeed in collecting the minimum required charge of 6000 electrons after the exposure to the maximum fluence.

6

Contents

1 Introduction

The Vertex Locator (VELO) [1] is the silicon vertex detector surrounding the interaction region of the LHCb experiment [2]. Throughout LHC Runs 1 and 2, the VELO was based on silicon strip sensors. The VELO will be upgraded to a hybrid pixel system for Runs 3 and 4. The detector is designed to withstand a maximum fluence of 8×10^{15} 1 MeV n_{eq} cm^{-2}, corresponding to the amount expected after an integrated luminosity of 50 fb^{-1} [3] over the 8-year lifetime of the upgraded experiment. The charge collection properties of the prototype sensors prior to, and after irradiation up to maximum fluence are reported in this paper.

An extensive R&D programme was launched to obtain sensors able to meet the challenging requirements for radiation hardness of the VELO upgrade. One of the crucial sensor requirements is that the amount of charge collected for a high energy charged particle is more than 6000 e$^-$ after the detector is exposed to the maximum fluence. This ensures that the signal is sufficiently above the expected highest threshold of 1000 e$^-$, even if the charge is shared amongst several pixels. Furthermore, it was essential to evaluate the performance at the edge of the sensor, since this is the region closest to the interaction point and hence with the highest occupancy during the operations of the detector.

The prototype sensors have been characterised using readily available Timepix3 ASICs [4]. The Timepix3 ASIC has a data-driven readout which provides a 10 bit Time-over-Threshold (ToT) measurement, and a timestamp with ∼ 1.56 ns precision.

In this paper, the performance of several different prototypes is discussed, comparing results of irradiated and nonirradiated samples. The different sensor designs are described in section 2. The experimental setup is outlined in section 3, with a detailed description of the charge calibration method in section 3.2. The irradiation programme is detailed in section 4. The charge collection results for different bias voltages are discussed in section 5.1. During the evaluation programme, radiation induced charge multiplication was observed and results are described in section 5.2. The edge performance is presented in section 5.3, followed by the conclusion in section 6.

2   Sensor prototype designs

A VELO upgrade assembly consists of a single sensor bump-bonded to three ASICs, and is referred to as a triple-chip assembly. However, for the charge collection studies, single ASIC assemblies have also been used, since it makes the irradiation and testing in the lab or in the beam more affordable. The size of the sensors for the VELO upgrade is approximately 42.5×14.1 mm^2, consisting of three groups of 256×256 pixels. The pixels have a 55 μm pitch, except for those in the interchip region, which are elongated in order to have complete coverage between the ASICs. The elongated pixels are either 110 or 137.5 μm depending on the round of production.

For the first round of prototyping, sensors have been produced by two vendors, Hamamatsu Photonics K. K. (HPK)[1] and Micron Semiconductor Ltd.[2] The HPK sensors have been produced with n$^+$-type implants separated by p$^+$-stop implants on a 200 ± 20 μm thick float-zone p-doped silicon substrate (resistivity of 3–8 kΩ cm). The back of the sensor consists of a thin p$^+$-doped layer and is fully metallised. Two different guard ring designs with distances of 450 and 600 μm from the edge of the sensor to the edge of pixel matrix have been evaluated. This distance is often referred to as Pixel-To-Edge (PTE). The pixel implants are either 35 or 39 μm squares with rounded corners. The Micron prototypes have been produced with 36 μm wide n$^+$-type implants with rounded corners and p$^+$-spray isolation. Two different types of substrates have been used: 200 μm p-type (> 5 kΩ cm) and 150 μm n-type (> 1.5 kΩ cm). The latter is double sided processed with guard rings on the backside of the sensor partially implanted underneath the edge pixels (see figure 1). The back of these sensors consist of a thin p$^+$-doped layer and the back for the p-type substrate is fully metallised, while for the n-type substrate the back is metallised in a grid structure. For these sensors there are two PTE variants with corresponding distances of 250 μm and 450 μm. The n$^+$-p-p$^+$ (n$^+$-n-p$^+$) sensors are from now on referred to as n-on-p (n-on-n) sensors.

The operational voltage needed to yield a signal of at least 6000 e$^-$ after the highest fluence is expected to be 1000 V [3]. For n-on-p sensors the operation above a certain voltage can generate an electrical discharge between the sensor and the ASIC if the assembly is placed in a gaseous environment. The n-on-n sensor design does not suffer from electrical discharge at voltages below 1000 V since these sensors are processed on both sides allowing for guard rings on each side of the sensor. This lowers the potential on the side closer to the ASIC. In order to prevent discharges in n-on-p sensors, these sensors either received a C-type parylene coating[3] prior to irradiation or are operated in vacuum.

---

[1]Hamamatsu Photonics K. K., 325-6, Sunayama-cho, Naka-ku, Hamamatsu City, Shizuoka, 430-8587, Japan.

[2]Micron Semiconductor Ltd, 1 Royal Buildings, Marlborough Road, Lancing BN158UN, United Kingdom.

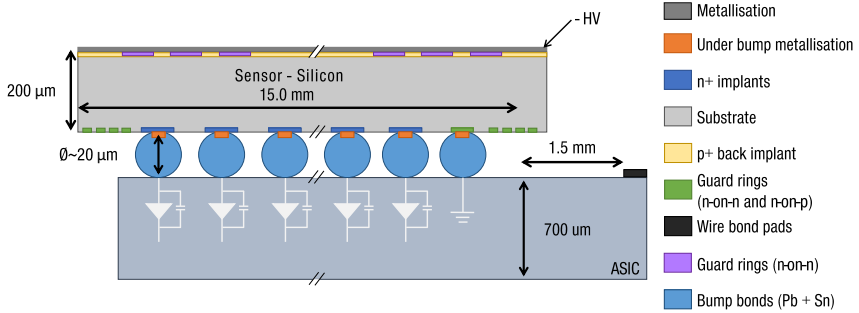[3]Comelec SA, La Chaux-de-Fonds, Switzerland.

Figure 1. A cross section of the sensor connected to the ASIC. The different implants are indicated with different colors. Both the design of the n-on-p and n-on-n sensors are shown in this diagram, since the only difference is the guard rings on the back of the sensor.

3   Experimental setup and calibration

3.1   The Timepix3 telescope at CERN SPS

An extensive testbeam programme has been carried out at the SPS H8 beamline at CERN to characterise the sensors at high rate. The beam is a mixed charged hadron beam ($\sim$ 67% protons, $\sim$ 30% pions) at 180 GeV/c.

The Timepix3 telescope [5] is a high rate, data-driven beam telescope, composed of two arms of four planes each. Each plane is equipped with a 300 μm p-on-n silicon sensor that is bump bonded to a Timepix3 ASIC. The centre of the telescope is reserved for the Device Under Test (DUT). The DUT area is equipped with remotely controlled motion stages able to translate in x and y directions (orthogonal to the beam axis) and rotate about the y axis. A vacuum box can also be installed on the central stage to facilitate testing of irradiated devices at high voltage. The cooling block connected to the ASIC can be cooled down to temperatures of -35 °C, which keeps the sensors below -20 °C. The temperature of the cold box is measured with a Pt100, which is converted to the corresponding sensor temperature using a calibration curve. This calibration curve is determined before the testbeam in a dedicated lab setup. In this setup a Pt100 was glued to the sensor itself and another Pt100 was glued to the cold box in order to measure the sensor temperature for different cold box temperatures. The pointing resolution at the DUT position is about 1.6 μm, enabling intrapixel studies of the DUT. The typical temporal resolution on a track using only the Timepix3 timestamps is about 350 ps.

3.2   Front-end calibration

The recorded Time-over-Threshold (ToT) values are converted to a corresponding number of electrons via a charge calibration procedure. The measured ToT for a given injected charge varies from pixel to pixel due to variations in the discharge current across the pixel matrix. The relation between ToT and charge for each pixel can be determined by injecting testpulses with known charge into the preamplifier. The injected charge depends on the voltage difference of two internal voltage DACs

Table 1. Characteristics of the facilities used in the irradiation programme.

Facility	Particles	Cooling	Scanning	Intensity [10^{12} s^{-1} cm^{-2}]	Hardness Factor
Karlsruhe	23 MeV protons	yes	yes	25	2.20 ± 0.40 [10]
IRRAD	24 GeV protons	yes	no	0.02	0.62 ± 0.04 [10]
Ljubljana	reactor neutrons	no	no	3.05	0.90 ± 0.03 [11]

whose value can be measured externally, and on the capacitance of the test capacitor which varies only slightly across the ASIC.

A calibration curve is determined separately for each pixel [6]. The test pulse calibration method was validated for one of the assemblies by comparing it to the characteristic lines from an ^{241}Am source and agreed to within 4% [7], and was also cross-checked using X-rays with several energies from the LNLS synchrotron in Brazil.

4   Irradiation programme

The fluence that the VELO upgrade will receive is estimated using simulations of proton collisions at 14 TeV [3]. The hadronic collisions produce a nonuniform fluence exposure over each sensor. The maximum integrated fluence expected at the most irradiated sensor position is 8×10^{15} 1 MeV n$_{eq}$ cm^{-2}. The difference in fluence over a single sensor due to this nonuniform irradiation can be as large as a factor 120.

Three different types of irradiation are used in the studies presented in this paper. Sensors received uniform neutron irradiation at the TRIGA MARK II reactor at JSI [8] in Ljubliana, Slovenia, of half, and of maximum fluence. The IRRAD facility at CERN [9] provides a 24 GeV proton beam that is approximately normally distributed, hence yielding a nonuniform fluence profile. Forschungszentrum Karlsruhe Cyclotron at Karlsruhe (KIT) can provide a 23 MeV proton beam with a small cross section which can be scanned over the sensor in order to approximate the nonuniform radiation profile of the upgraded VELO. The fluences provided by JSI, IRRAD, and KIT are known with an accuracy of ±10%, ±10%, and ±20%, respectively. Table 1 shows a summary of the properties of the three facilities.

4.1   IRRAD profile

After irradiation, the residual activation of the assemblies is obtained by measuring the distribution of hits in the sensor when not exposed to the beam. The hits are caused by the radioactivity induced in the assembly and thus their rate is proportional to the fluence. The radiation profile can then be determined from the activation map, modelled using a two-dimensional Gaussian distribution [12]. The activation profile is then normalised to match the fluence measured by an aluminium foil that was placed alongside the assemblies during irradiation. The foil was later subdivided in six regions, examined for activation through γ-ray spectroscopy. The reconstructed fluence profile of a single-chip assembly is shown in figure 2. The corresponding fluence measured with the aluminium foil is overlaid for each region, where the measured proton fluence has been converted in neutron equivalent unit using a hardness factor of 0.62 ± 0.04 [10]. The reconstructed fluence profile is found to be consistent with the measured charge collection profile.
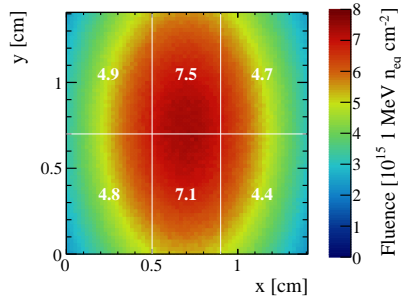
Figure 2. The reconstructed fluence profile from irradiation at IRRAD. The dosimetry results, converted to neutron equivalent fluence, for the six regions are indicated by the white numbers ($\times 10^{15}$ 1 MeV n_{eq} cm^{-2}).

5   Results with beam

The prototype sensors were characterised using the Timepix3 telescope in beam tests using the SPS at CERN. Only DUT clusters associated to a telescope track are selected in order to mitigate background hits from internal radioactivity and noise. Clusters are matched to a track if they are within a space (time) region of $110 \times 110\ \mu m^2$ (100 ns) from the value predicted by the telescope. The cluster size is limited to four pixels since larger clusters are usually due to nuclear interactions (with a much larger energy deposition) or δ-rays.

A fit is performed to the cluster charge distribution, which can be described by a convolution of Landau and Gaussian distributions, in order to determine the Most Probable Value (MPV) of the Landau. The standard deviation of the MPV distribution over the chip is quoted as the uncertainty on the MPV, and is determined for this assembly to be around $350\,e^-$, corresponding to about 2% of the MPV, which is much larger than the statistical estimate from the fit. This uncertainty is determined with a single nonirradiated $200\,\mu m$ n-on-p assembly and, since it is dominated by ASIC effects, it is considered representative of all other prototypes. The uncertainty on the absolute calibration is determined to be 4%, as discussed in section 3.2.

This section is organised as follows. In section 5.1 the charge distribution is studied for both nonirradiated and uniformly irradiated sensors operated at different bias voltages and placed perpendicular to the beam. It is followed by section 5.2 in which the charge distribution as a function of fluence for nonuniformly irradiated sensors also placed perpendicular to the beam is discussed. Finally, the performance at the edge of the sensors is discussed in section 5.3, in which different angles of the sensor with respect to the beam are used. For figures in which devices of different types are shown together, a colour code is used: green for HPK n-on-p, blue for Micron n-on-p, and purple for Micron n-on-n. An overview of the assemblies is given in appendix A.

5.1   Bias studies

Nonirradiated assemblies.   Assemblies were tested in the SPS beam at the same time as the irradiation campaign, thus not all of the assemblies could be studied prior to being irradiated; therefore, a representative subset of assemblies was tested prior to being irradiated in order to make comparisons with the results post irradiation.
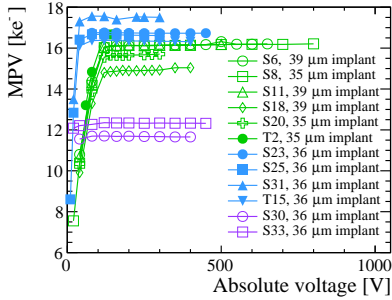
Figure 3. MPV of the cluster charge (for clusters associated to a telescope track) as function of bias voltage for nonirradiated assemblies, measured in beam tests. The uncertainties are not indicated in the plot, see the text for a detailed explanation.
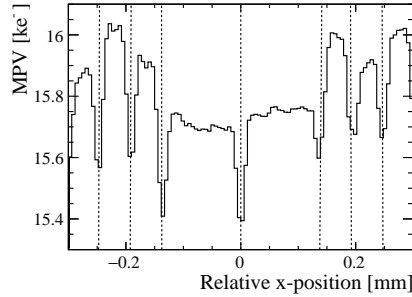
Figure 4. The MPV for different positions around the inter-chip region between two ASIC on T23 before irradiation. The middle of the interchip region is indicated as the zero point on the x-axis. The vertical dashed lines indicate the pixel column borders.

Figure 3 shows the MPV as a function of bias voltage for several nonirradiated assemblies. For the HPK sensors, indicated by the green curves, the MPV of the collected charge saturates between 100 and 110 V and shows no dependence on the implant size. The MPV of the Micron sensors, indicated by the blue curves (n-on-p) and purple curves (n-on-n), reaches a plateau at less than 40 V. The difference in MPV for the Micron sensors is due the different thicknesses of the two types, 200 µm and 150 µm for n-on-p and n-on-n sensors, respectively. The small differences in MPV between sensors of the same type are due to wafer-to-wafer variations in thickness up to 10%, and variation in the testpulse capacitance due to process variations of about 5% (one sigma).

The main difference other than the area between the single-chip and triple-chip assemblies is the presence of elongated pixels located in the region in between the chips. It is important that the response of the inter-chip region is similar to the rest of the sensor. This region is investigated for the HPK n-on-p triple-chip assembly T23 before irradiation. The MPV of the interchip region of HPK triple-chip assembly T23 is shown in figure 4, where the middle between chips is defined as zero. Three characteristics can be observed: the dips between columns; the variation from column-to-column (the narrow flat regions); and the slightly lower MPV of the interchip region (wider flat regions). The dips between columns are due to threshold effects, and the variation from column-to-column is due to the charge calibration. The MPV is slightly lower for the two elongated columns compared to the other columns in the figure. However, this difference still falls within the total variation of the MPV over the columns, which is found to be $300\,e^-$ using the same method as for the total variation over the pixel matrix. Therefore, it is concluded that the interchip region collects all charge.

Irradiated assemblies. The MPV as a function of bias voltage after irradiation to full fluence at JSI is shown in figure 5. All of the assemblies follow the same trend, with the MPV increasing linearly from about $2500\,e^-$ at 200 V to about $8000\,e^-$ at 1000 V. The leakage current at bias voltages higher than 600 V for S24 was larger than the leakage current compensation in the ASIC,
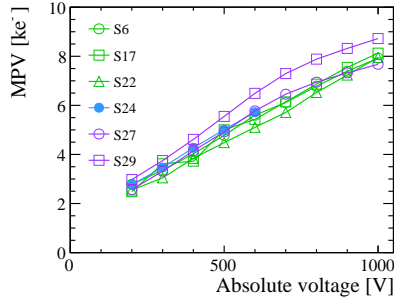
104

Figure 5. MPV as function of bias voltage after uniform irradiation at JSI Ljubljana to 8×10^{15} 1 MeV n_{eq} cm^{-2}, without additional controlled annealing. The uncertainties are not indicated in the plot, see the text for a detailed explanation.
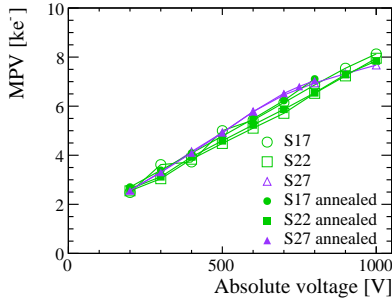

Figure 6. MPV as function of bias voltage after uniform irradiation at JSI to 8×10^{15} 1 MeV n_{eq} cm^{-2}, before and after annealing for 80 min. at 60°C.

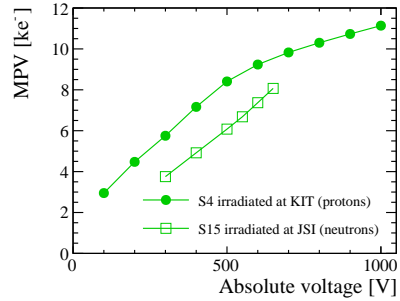**Figure 7.** MPV as function of bias voltage after uniform irradiation to 4×10^{15} 1 MeV n_{eq} cm^{-2}, without additional controlled annealing.

resulting in changes in the charge calibration per pixel. Hence these points are excluded from this figure.

The measurements shown in figure 5 were performed before any controlled annealing. A subset of the assemblies were tested again with beam after having been annealed for 80 minutes at 60 °C. As can be seen in figure 6, the results before and after annealing are in agreement. The leakage current at bias voltage of 900 V for S17 after annealing was larger than the leakage current compensation in the ASIC, resulting in changes in the charge calibration per pixel. The sensors were kept at room temperature for 11 days after irradiation, after which they were cooled at -15 °C, beside the aforementioned additional controlled annealing.

Several assemblies have been irradiated with either reactor neutrons or protons. As described in reference [13], the damage to silicon from neutron irradiation is different to the damage from proton irradiation. Figure 7 shows the MPV as a function of bias voltage for two HPK single-chip assemblies after uniform irradiation to a fluence of 4×10^{15} 1 MeV n_{eq} cm^{-2} at KIT (assembly S4 — proton
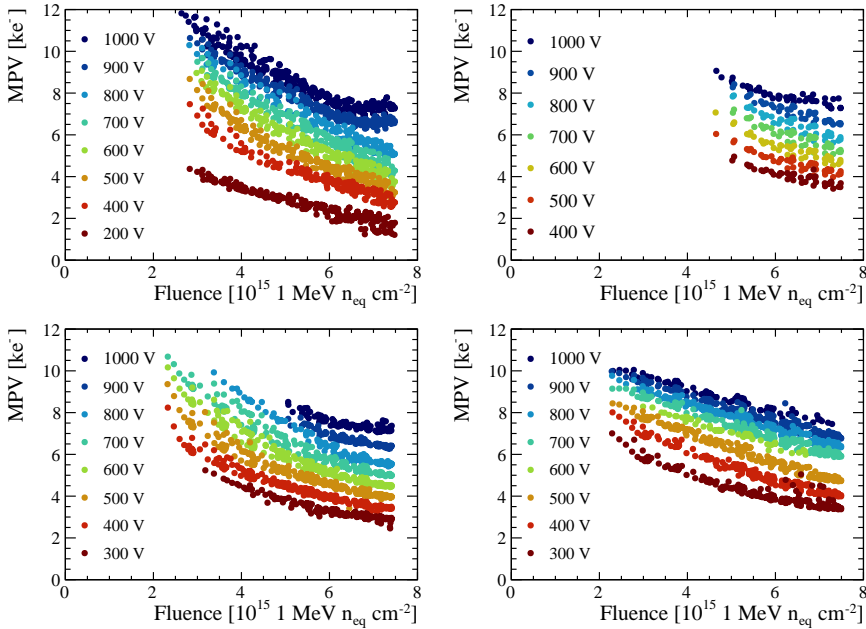
Figure 8. MPV as function of fluence at different bias voltages, after irradiation at IRRAD. Top left: HPK assembly S8 with 35 μm implant width. Top right: HPK assembly S11 with 39 μm implant width. Bottom left: Micron n-on-p assembly S25. Bottom right: Micron n-on-n assembly S30.

irradiation) and JSI (assembly S15 — neutron irradiation). The curve for S15 does not extend up to 1000 V because the assembly sparked, as it was not parylene coated and thus measurements were performed only up to 675 V in a CO_2 atmosphere.

5.2   Charge multiplication

As reported in several previous studies [14–16], charge multiplication in planar silicon sensors is expected at fluences above 5×10^{15} 1 MeV n_{eq} cm^{-2} but typically in considerably larger pitches than presented here.

Figure 8 shows the MPV as a function of the fluence at different bias voltages and figure 9 the MPV as a function of the voltage at different fluence levels. Both figures present the results after irradiation at IRRAD. Charge multiplication is observed in all sensors where the bias voltage can reach 1000 V, except for the Micron n-on-n assembly. This effect emerges at a fluence of about 6.5×10^{15} 1 MeV n_{eq} cm^{-2} and increases with bias voltage. The difference in the n-on-p and n-on-n sensors that leads to the presence (absence) in charge multiplication is not known.

Charge multiplication is expected to occur in regions with a high electric field. These positions are close to the pixel implant, and thus the amount of charge multiplication could depend on the intrapixel position. Figure 10 shows the MPV for different intrapixel positions of assembly S8 after irradiation at IRRAD up to maximum fluence at a bias of 1000 V. For this figure, clusters
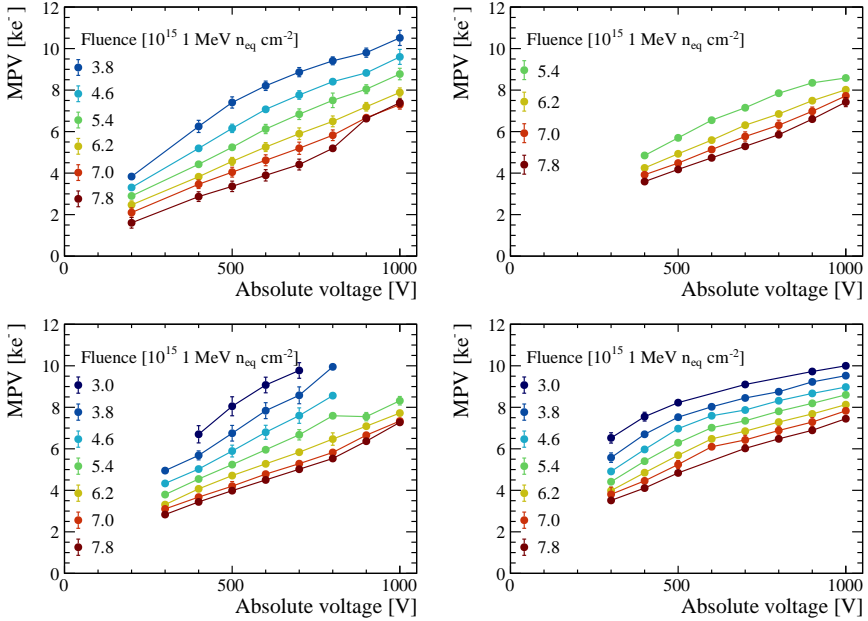
Figure 9. MPV as function of bias voltage at different fluence levels, after irradiation at IRRAD. Top left: HPK assembly S8 with 35 μm implant width. Top right: HPK assembly S11 with 39 μm implant width. Bottom left: Micron n-on-p assembly S25. Bottom right: Micron n-on-n assembly S30.

are selected in the regions of the sensor that were exposed to fluences in the range of 7.3 to 7.9×10^{15} 1 MeV n_{eq} cm^{-2}. As a comparison, the intrapixel MPV for S8 before irradiation is shown in figure 11. Diagonal bands can be seen near the corners of the pixel; here the MPV is lower than in the corner itself. This is due to charge sharing with neighbouring pixels. A detailed explanation is given in appendix B.

For the IRRAD assemblies, the intrapixel MPV study is performed for different fluence values up to maximum fluence. By comparing a slice of 5.5 μm along the middle of the pixel ($y = 27.5$ μm) of the intrapixel cluster charge distribution at different fluence levels, the position within the pixel where charge multiplication occurs can be determined, as is shown in figure 12. The MPV decreases with fluence up to 7×10^{15} 1 MeV n_{eq} cm^{-2}. At this point the MPV begins to increase with fluence, which is a clear indication that charge multiplication is occurring. The small drop from the middle to the edge of the pixel is due to charge sharing effects. The charge collected relative to that of the lowest fluence bin is shown in figure 13 in order to demonstrate where in the pixel the charge multiplication occurs. It can be concluded that charge multiplication occurs uniformly over the centre of the pixel, while towards the edge of the pixels charge multiplication seems to be lower.

5.3 Edge performance

The performance of the sensors at the edge, near the guard ring region, is investigated by illuminating these areas with the beam. Results are shown for one corner of the sensor, but it has been verified
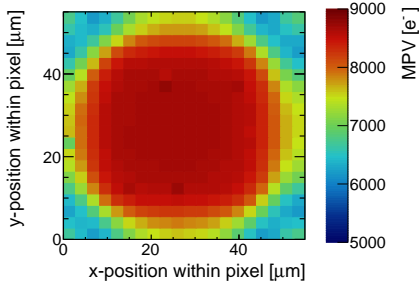
Figure 10. The MPV of the cluster charge distribution within a pixel for S8 at 1000 V after irradiation at IRRAD. Only clusters in the region of the sensor exposed to fluences in the range 7.3 to 7.9×10^{15} 1 MeV n_{eq} cm^{-2} are selected.
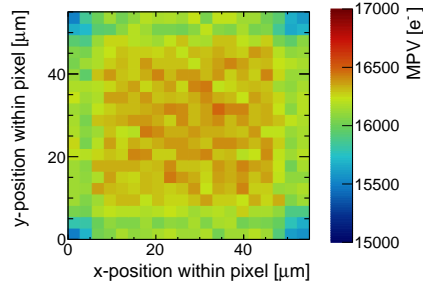

Figure 11. The MPV of the cluster charge distribution within a pixel for S8 at 800 V before irradiation.
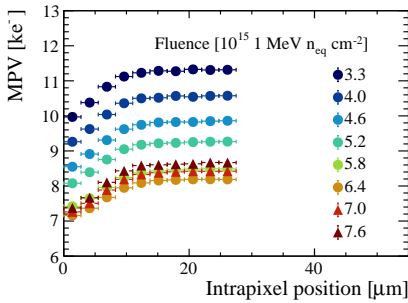

Figure 12. Intrapixel cluster charge MPV (for $y = 27.5\,\mu$m) for different fluence values of S8 at an operating voltage of 1000 V.
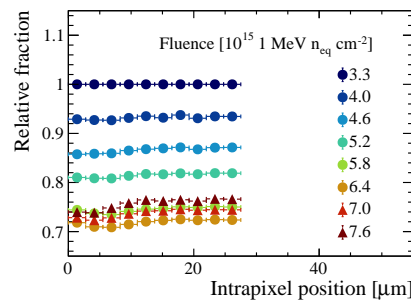
Figure 13. The relative fraction of the intrapixel charge in comparison to the lowest fluence for the cross-section of the pixel at $y = 27.5\,\mu$m.

that the other corners behave the same. Nonirradiated sensors are operated at a bias where they are above the depletion voltage estimated from charge saturation measurements. The results are shown for single chip sensors, but all prototypes tested exhibit consistent behaviour at the edge between single and triple sensors as well as between different types of irradiation.

The performance at the edge of the pixel matrix is quantified by measuring the cluster charge as a function of the track intercept position. The expected behaviour is to collect charge from tracks traversing the pixel matrix, but not from tracks passing through the guard ring area apart from a small amount of diffused charge. The MPV as a function of the track distance from the edge in the *x* direction (corresponding to increasing column numbers) can be seen in figure 14 for all the tested nonirradiated assemblies. The uncertainty assigned to the MPV is statistical only. The solid line represents the edge of the pixel matrix and the dashed lines the borders between pixels. Two prototype variants exhibit an undesired behavior. All of the 200 μm Micron n-on-p

sensors accumulate charge in the last pixel from tracks traversing the sensor beyond the edge of the pixel matrix, while the 150 μm Micron n-on-n (250 μm PTE backside guard rings) sensor does not collect the full charge in the last pixel. None of the HPK sensors show this behaviour apart from some expected charge diffusion at the boundary between the guard ring and the edge pixel.
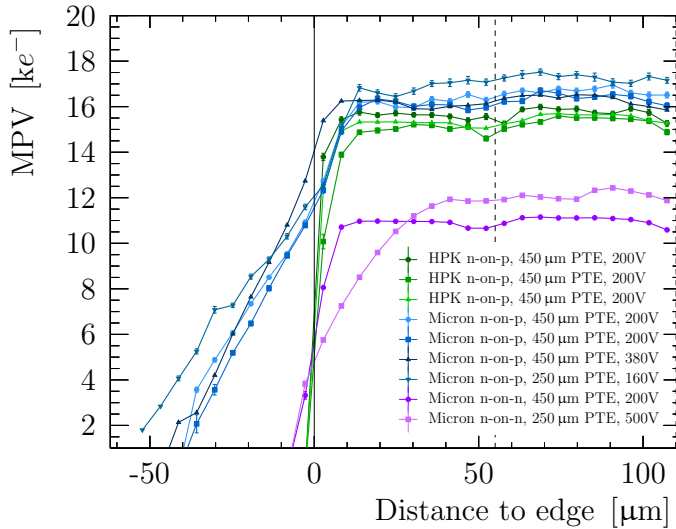

Figure 14. Cluster charge MPV as a function of the distance of the track intercept from the edge of the pixel matrix for all the nonirradiated assemblies tested. The solid line represents the border of the pixel matrix and the dashed lines the borders between pixels.

The simplest geometrical model that can explain the observed edge effect for Micron n-on-p and Micron n-on-n sensors is a tilted border between the charge collection region of the guard rings and that of the pixels. This is illustrated in figure 15 for Micron n-on-p sensors, where the charge distribution as a function of the track intercept position, x, is studied at three different angles: -12°, 0° and +12°. In the schemes, the black arrow represents the particle trajectory nearest to the physical edge where the deposited charge is fully collected, with the red cross showing the corresponding measured position of the intercept between the track and the sensor, and the shaded area indicating the charge collection region of the guard rings. At -12° the slope of the charge deposit is present and extends far beyond the edge of the matrix. The charge is fully collected by the pixel implants up to the point indicated by the red cross. Beyond that point the first pixel starts to pick up charge from the guard ring region (represented in grey). At +12° the slope in the charge deposit almost disappears. The charge is either fully collected by the pixel implant or fully collected by the guard rings. This model explains why in the case of Micron n-on-p sensors charge is collected from the guard ring region at the pixel side. Analogously, angled measurements with Micron n-on-n sensors show that the border is tilted in the opposite direction, such that charge from the outermost pixel

is lost to the guard rings at the backplane side [12]. The tilted border hypothesis could be verified by a TCAD[4] simulation, but this was not pursued because the details of the guard ring design is proprietary information.
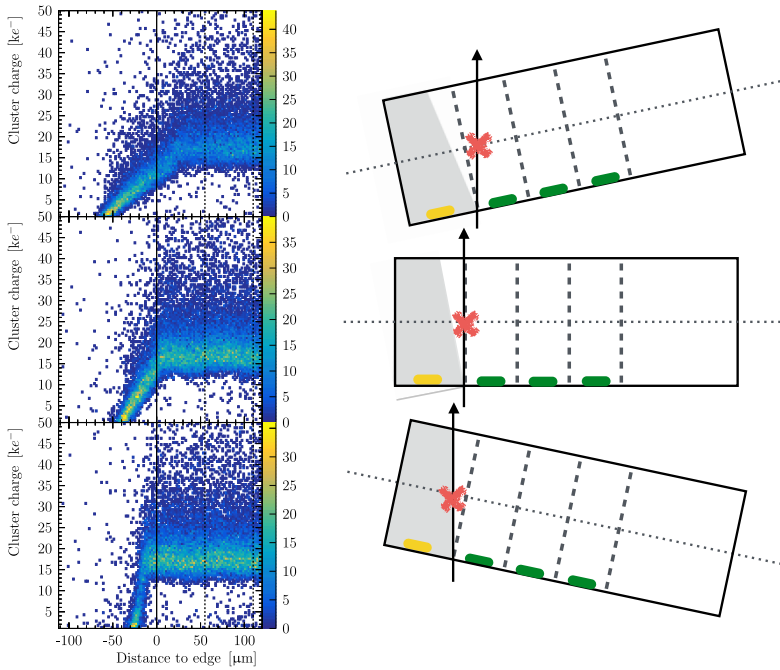
Figure 15. Cluster charge as a function of the distance of the track intercept from the edge (left) and related sketch (right) for a 200 μm thick Micron n-on-p sensor with 450 μm guard rings operated at 380 V. The sensor is rotated with respect to the beam by $-12°$ (top), $0°$ (middle) and $+12°$ (bottom).

For Micron n-on-p sensors, the observed edge effect leads to an approximately 30% excess of hits in the first column of the pixel matrix with the sensor biased above depletion voltage and traversing tracks at normal incidence. The second column of the pixel matrix also shows an excess of hits, leading to the conclusion that the distortion of the electric field is such that the second column collects charge from tracks going through the first column. A similar effect has been observed for active-edge silicon sensors in ref. [17]. The excess of hits decreases with increasing operation voltage due to the stronger electric field, and it is also observed to decrease when tracks are at an angle with respect to the sensor. An excess of hits in the first column and row of the pixel matrix is also observed in a lab experiment using a ^{90}Sr source, verifying the beam test findings. Data have been collected operating the sensor at different voltages and the observed hit excess dependence has the same trend as the one obtained from testbeam data.

---

[4]Technology Computer Aided Design.

The MPV profiles for irradiated sensors are shown in figure 16 as a function of the distance to the edge in the x direction. After irradiation by either protons or neutrons with fluences ranging from 2 to 8×10^{15} 1 MeV n_{eq} cm^{-2}, the behaviour at the edge is comparable among the different prototype variants. The linear charge deposit extending beyond the edge observed in nonirradiated Micron n-on-p sensors is strongly reduced after irradiation. This can be explained by the fact that the sensors are not fully depleted even at the highest operational voltage used in the tests.
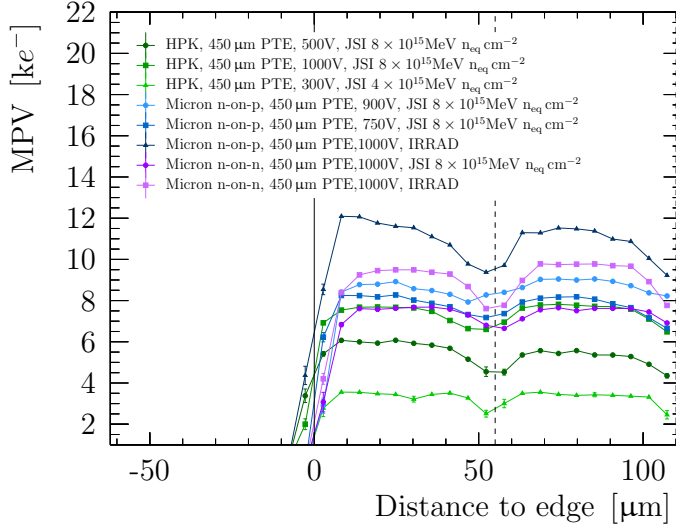
Figure 16. MPV of the cluster charge as a function of the distance to the edge of the associated track intercept for all the assemblies uniformly irradiated at JSI and nonuniformly irradiated at IRRAD. The solid line represents the border of the pixel matrix and the dashed lines the borders between pixels.

6 Conclusions and outlook

An extensive testing campaign has been performed for the VELO upgrade, investigating several planar silicon sensor designs from two different vendors: HPK and Micron. In this paper, a study of the charge collection before and after irradiation up to 8×10^{15} 1 MeV n_{eq} cm^{-2} of these sensors is presented. Irradiation of the sensors was performed at JSI with neutrons and at IRRAD and KIT with protons. The MPV as a function of bias voltage is determined before irradiation, and shows saturation at 16 ke$^-$, 17 ke$^-$, and 12 ke$^-$ for HPK n-on-p, Micron n-on-p, and Micron n-on-n, respectively. After irradiation, the MPV decreases significantly and shows a linear dependence on the bias voltage. At a bias voltage of 1000 V, the MPV is around 8 ke$^-$, indicating that the sensor achieves the requirement of collecting more than 6 ke$^-$ after irradiation to the maximum expected fluence for the VELO upgrade.

During the campaign charge multiplication was observed for both the HPK and Micron n-on-p sensors, while no charge multiplication is observed for the Micron n-on-n sensors. Charge multiplication is observed uniformly over the centre of the pixel, while it seems less near the edge.

Two classes of tested prototypes exhibited unexpected behaviour at the edge prior to irradiation. In the case of Micron n-on-p sensors, charge is gained from the guard ring region at the pixel implant side, while in the case of the Micron n-on-n sensors with 250 μm PTE, charge from the outermost pixels is lost to the guard ring area. In view of the VELO upgrade the observed edge effect is critical, since it would increase the occupancy in the part of the sensor where it is already the highest. Moreover, it leads to a loss of spatial resolution for the first measured point.

The studies presented in this paper were decisive in the choice to adopt the 200 μm thick HPK n-on-p sensors with 39 μm implant width and 450 μm guard ring size for the VELO upgrade.

Acknowledgments

6

A List of assemblies

The details of the assemblies that are tested during this analysis are summarised here. Two different types of substrates (n-on-p and n-on-n) are used from two different vendors. Further differences between individual assemblies are indicated in the table below.

Table 2. Assemblies tested during the charge collection property studies. Single-chip assemblies are indicated by an S in their ID, while triple-chip assemblies are indicated by a T.

ID	Vendor	Thickness [μm]	Type	Edge width [μm]	Implant [μm]	Irradiation facility	Peak fluence [10^{15} 1 MeV n_{eq} cm^{-2}]
S4	HPK	200	n-on-p	600	39	KIT	4
S6	HPK	200	n-on-p	450	39	JSI	8
S8	HPK	200	n-on-p	450	35	IRRAD	8
S11	HPK	200	n-on-p	450	39	IRRAD	8
S15	HPK	200	n-on-p	450	35	JSI	4
S17	HPK	200	n-on-p	450	39	JSI	8
S18	HPK	200	n-on-p	450	39	—	—
S20	HPK	200	n-on-p	450	35	—	—
S22	HPK	200	n-on-p	450	35	JSI	8
S23	Micron	200	n-on-p	450	36	JSI	8
S24	Micron	200	n-on-p	450	36	JSI	8
S25	Micron	200	n-on-p	450	36	IRRAD	8
S27	Micron	150	n-on-n	450	36	JSI	8
S29	Micron	150	n-on-n	450	36	JSI	8
S30	Micron	150	n-on-n	450	36	IRRAD	8
S31	Micron	200	n-on-p	250	36	—	—
S33	Micron	150	n-on-n	250	36	—	—
T2	HPK	200	n-on-p	450	35	KIT	4
T15	Micron	200	n-on-p	450	36	KIT	8
T23	HPK	200	n-on-p	450	39	—	—

B Shape of the intrapixel cluster charge distribution

The MPV distribution within a single pixel shows an peculiar feature: a diagonal region near the corner is observed to have a lower MPV than both the centre and the corners of the pixel, as is shown in figure 17. For this figure, the four corners of pixel have been 'folded' into one in order to maximise the effective size of data sample.

The MPV distribution as a function of the intrapixel position is split by the size of the cluster in order to study the origin of this structure, as is shown in figure 18, where the fraction of clusters of each size is also indicated. From the intrapixel position of the different cluster sizes it can be seen that the contribution to the band is mainly from clusters of size two or three, while the contribution to the corner is mainly from four-hit clusters. Because for four hit clusters all three neighbouring pixels must also measure a hit, there is no possibility to have undetected charge due to the signal in the neighbouring pixels being below the detection threshold. Conversely, for the other cluster sizes, there is the possibility that a neighbouring pixel collected some of the charge, but that it did not pass the detection threshold. If this occurs, the measured cluster charge is incomplete. For a single

pixel cluster up to three contributions could be missing. This inefficiency is unlikely to occur for hits in the middle of the pixel due to the limited size of the charge cloud, while it is more likely to happen to hits near the corners.

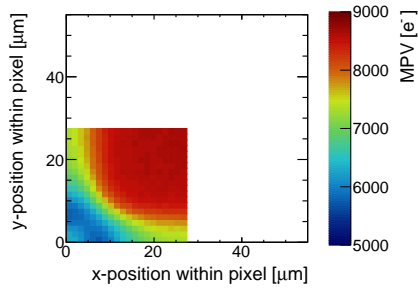**Figure 17.** The MPV of the cluster charge distribution within a pixel for S8 at 1000 V after irradiation at IRRAD. Only clusters in the fluence range of 7.3 to 7.9×10^{15} 1 MeV n_{eq} cm^{-2} are selected.
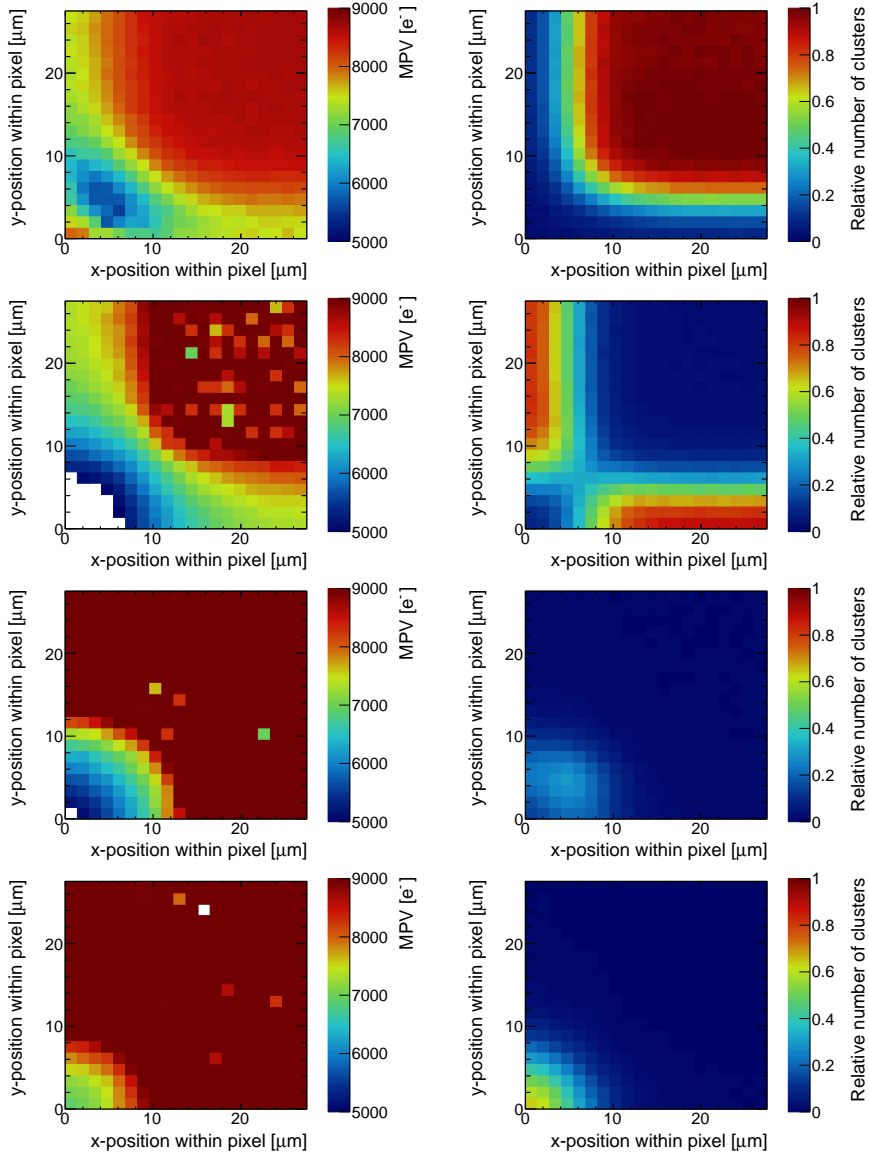
Figure 18. MPV for different intrapixel clusters positions (left) and the relative number of clusters (right) for cluster size one (first row), two (second row), three (third row), and four (last row).

References

[1] R. Aaij et al., *Performance of the LHCb Vertex Locator*, 2014 *JINST* **9** P09007 [`arXiv:1405.7808`].

[2] LHCb collaboration, *The LHCb Detector at the LHC*, 2008 *JINST* **3** S08005.

[3] LHCb collaboration, *LHCb VELO Upgrade Technical Design Report*, Tech. Rep. CERN-LHCC-2013-021. LHCB-TDR-013 (Nov, 2013).

[4] T. Poikela et al., *Timepix3: a 65k channel hybrid pixel readout chip with simultaneous ToA/ToT and sparse readout*, 2014 *JINST* **9** C05013.

[5] K. Akiba et al., *LHCb VELO Timepix3 Telescope*, 2019 *JINST* **14** P05026 [`arXiv:1902.09755`].

[6] J. Jakubek et al., *Pixel detectors for imaging with heavy charged particles*, *Nucl. Instrum. Meth. A* **591** (2008) 155.

[7] M. Vicente Barreto Pinto, *Caracterização do TimePix3 e de sensores resistentes à radiação para upgrade do VELO*, MSc. thesis, UFRJ, Rio de Janeiro, Brazil (2016), CERN-THESIS-2016-008.

[8] L. Snoj, G. Žerovnik and A. Trkov, *Computational analysis of irradiation facilities at the JSI TRIGA reactor*, *Appl. Radiat. Isot.* **70** (2012) 483.

[9] B. Gkotse, M. Glaser, M. Moll and F. Ravotti, *IRRAD: The New 24GeV/c Proton Irradiation Facility at CERN*, AIDA-2020-CONF-2016-006.

[10] P. Allport et al., *Experimental Determination of Proton Hardness Factors at Several Irradiation Facilities*, 2019 *JINST* **14** P12004 [`arXiv:1908.03049`].

[11] G. Kramberger, *Signal development in irradiated silicon detectors*, Ph.D. thesis, Ljubljana University, Slovenia (2001) CERN-THESIS-2001-038.

[12] E. Dall'Occo, *Search for heavy neutrinos and characterisation of silicon sensors for the VELO upgrade*, Ph.D. thesis, Nikhef, Amsterdam (2020).

[13] V. Cindro et al., *Radiation damage in p-type silicon irradiated with neutrons and protons*, *Nucl. Instrum. Meth. A* **599** (2009) 60.

[14] I. Mandic, V. Cindro, G. Kramberger and M. Mikus, *Measurement of anomalously high charge collection efficiency in n+p strip detectors irradiated by up to $10^{16} n_{eq}/cm^2$*, *Nucl. Instrum. Meth. A* **603** (2009) 263.

[15] J. Lange, J. Becker, E. Fretwurst, R. Klanner and G. Lindström, *Properties of a radiation-induced charge multiplication region in epitaxial silicon diodes*, *Nucl. Instrum. Meth. A* **622** (2010) 49 [`arXiv:1007.4735`].

[16] M. Mikuž et al., *Study of anomalous charge collection efficiency in heavily irradiated silicon strip detectors*, *Nucl. Instrum. Meth. A* **636** (2011) S50.

[17] K. Akiba et al., *Probing active-edge silicon sensors using a high precision telescope*, *Nucl. Instrum. Meth. A* **777** (2015) 110.

6.2 TEMPORAL CHARACTERISATION OF SILICON SENSORS ON TIMEPIX3 ASICS

This section contains a paper that describes the temporal characterisation that was performed on different prototype sensors of the LHCb VELO Upgrade 1. It contains both the analysis of particles that interacted on normal incidence of the sensor, as well as the so-called *grazing angle*, in which the sensor is placed almost parallel to the beam to measure the characteristics at different depths in the sensor. One of the major findings in this paper is that the time resolution degrades with radiation damage. It was also concluded that it is not regained when radiation induced charge multiplication occurs.

This paper titled *"Temporal characterisation of silicon sensors on Timepix3 ASICs"* is published in JINST [94].

6

*J*inst

Temporal characterisation of silicon sensors on Timepix3 ASICs

E. Dall'Occo,[a,1,*] **K. Akiba,**[a] **M. van Beuzekom,**[a] **E. Buchanan,**[b] **P. Collins,**[c] **T. Evans,**[c] **V. Franco Lima,**[d] **R. Geertsema,**[a] **H. Schindler,**[c] **H. Snoek**[a] **and P. Tsopelas**[a,2]

[a]*Nikhef, Science Park 105, 1098 XG Amsterdam, The Netherlands*

[b]*University of Bristol, Beacon House, Queens Road, BS8 1QU, Bristol, U.K.*

[c]*CERN, 1211 Geneve, Switzerland*

[d]*Oliver Lodge Laboratory, University of Liverpool, Liverpool, L69 7ZE, U.K.*

E-mail: `elena.dallocco@cern.ch`

Abstract: The timing performance of silicon sensors bump-bonded to Timepix3 ASICs is investigated, prior to and after different types of irradiation up to 8×10^{15} 1 MeV n_{eq} cm^{-2}. The sensors have been tested with a beam of charged particles in two different configurations, perpendicular to and almost parallel to the incident beam. The second approach, known as the grazing angles method, is shown to be a powerful method to investigate not only the charge collection, but also the time-to-threshold properties as a function of the depth at which the charges are liberated.

6

---

[*]Corresponding author.

[1]Now at TU Dortmund, Otto-Hahn-Straße 4, 44227 Dortmund, Germany

[2]Now at Spectricon, Science and Technology Park of Crete, Heraklion, Greece

Contents

1 Introduction

Understanding the timing capabilities of silicon sensors is fundamental for operation in a high rate environment such as the LHC. In view of the upgrade of the LHCb VErtex LOcator (VELO) [1] a wide range of prototype sensors have been tested in a beam of charged particles in order to assess their suitability. The upgraded VELO is a hybrid silicon pixel detector capable of 40 MHz readout, which surrounds the proton-proton collision region and is dedicated to the tracking and reconstruction of primary and secondary vertices. The main challenge for the operation of the sensors is the high and nonuniform radiation exposure, with a maximum fluence of 8×10^{15} 1 MeV n_{eq} cm^{-2}, expected at the closest point to the proton-proton collision after 50 fb^{-1} of integrated luminosity. Hence, the prototype sensors have been tested before and after different irradiation types and fluences.

This paper presents an investigation of the temporal properties of different sensor prototypes. The timing performance is determined using a particle beam with two complementary methods: at normal incidence and with a grazing angle [2, 3] approach. The grazing angle method consists of analysing particle tracks that traverse the sensor almost parallel to its surface, such that the depth that a charge is deposited at can be inferred from the position of the corresponding hit within a cluster. The depletion depth of planar sensors can be precisely determined using the grazing angle technique [4]. It has also been applied in charge diffusion studies in silicon [5] and to perform intrinsic spatial resolution studies [6]. In this paper, the grazing angle technique has been further developed to study the time properties of the sensors as a function of depth. A complementary technique for studying sensor properties as a function of depth is the transient current technique (TCT) [7–9], which provides a characterisation and visualisation of the electric field distribution.

Two main figures-of-merit are used to quantify the timing performance: the time from when the charge is liberated to when the signal crosses the threshold on average, referred to as time-to-threshold, and the width of the time-to-threshold distribution, referred to as the temporal resolution.

This paper is organised as follows. In section 2.1 the sensor prototypes are described, followed by the experimental setup in section 2.2. In section 2.3 the time-to-threshold measurement method is discussed. The results for nonirradiated, uniformly neutron irradiated and nonuniformly proton irradiated sensors are presented in sections 3 and 4 for sensors placed perpendicularly to the beam and at grazing angles, respectively. The conclusions are drawn in section 5.

2   Methodology

2.1   Detector assemblies under study

The prototype assemblies tested are hybrid pixel detectors, composed of sensors with 256×256 pixels of 55 μm pitch bump-bonded to Timepix3 ASICs [10]. The assemblies are glued to a 635 μm thick AlN ceramic board and wire-bonded to a custom made Kapton-copper hybrid, also glued to the ceramic substrate, subsequently read out by a SPIDR system [11].

The prototype sensors were produced by two different manufacturers, Hamamatsu Photonics K. K. (HPK)[1] and Micron Semiconductor Ltd.[2] The prototype sensors have different design features, such as pixel implant size, sensor thickness, bulk type, pixel-to-edge (PTE) distance. The main characteristics of the assemblies are summarised in table 1. The details of individual assemblies and their identification numbers, which will be used in the following, can be found in appendix A.

The Timepix3 ASIC can simultaneously measure the threshold crossing time, denoted by Time-of-Arrival (ToA), and the time the signal is above threshold, denoted by Time-over-Threshold (ToT). The former is registered with a Time-to-Digital Converter (TDC) with a bin width of 1.56 ns. The latter is related to the energy deposited and is converted into equivalent units of collected electrons

---

[1] Hamamatsu Photonics K. K., 325-6, Sunayama-cho, Naka-ku, Hamamatsu City, Shizuoka, 430-8587, Japan.

[2] Micron Semiconductor Ltd, 1 Royal Buildings, Marlborough Road, Lancing BN158UN, U.K.

Table 1. Prototype assemblies.

Vendor	Type	Thickness	PTE	Implant width
HPK	n-on-p	200 μm	450, 600 μm	35, 39 μm
Micron	n-on-p	200 μm	450 μm	36 μm
Micron	n-on-n	150 μm	250, 450 μm	36 μm

via a charge calibration process, as described in reference [12]. More details on the Timepix3 ASIC can be found in table 2. The threshold is set at $1000\,e^-$ to ensure the data is free from noise.

Table 2. Characteristics of the Timepix3 ASIC.

Technology	130 nm CMOS
Peaking time	< 25 ns
Noise	80–100 e^-
TDC bin width	1.56 ns

Several assemblies were irradiated up to the maximum fluence of 8×10^{15} 1 MeV n_{eq} cm^{-2}, with some exposed to 24 GeV/c protons at IRRAD and others to neutrons at the JSI reactor in Ljubljana. The uncertainty on the fluence at both facilities is estimated to be of the order of 10%. The main characteristics of the two facilities have been summarised in table 3. During the shipping from the irradiation facilities the sensors were kept at room temperature for 11 days, while in between measurements they were stored in a freezer at a temperature of $-15\,°C$ to reduce possible annealing effects. Both types of irradiation have been investigated as the damage to the sensor is different [15] and the actual radiation environment of the detector will be a mixture of the two. A nonuniform irradiation profile is used at IRRAD to emulate the expected conditions of the upgraded VELO. The irradiation profile is reconstructed combining the activation map of the assembly and the measurement provided by the dosimetry survey. This method is thoroughly described in reference [16]. The reconstructed fluence profile is shown in figure 1.

Table 3. Characteristics of the facilities used for the irradiation programme.

Facility	Particles	Cooling	Scanning	Intensity [10^{12} s^{-1} cm^{-2}]	Hardness factor
IRRAD	24 GeV protons	Yes	No	0.02	0.62 ± 0.04 [13]
Ljubljana	Reactor neutrons	No	No	3.05	0.90 ± 0.03 [14]
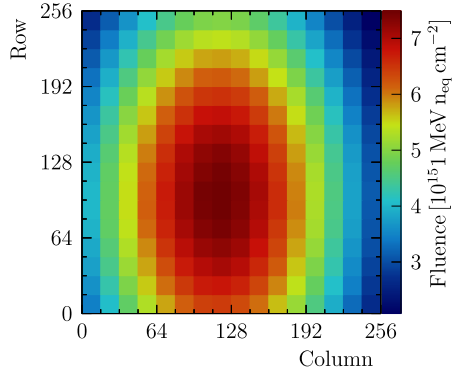
Figure 1. Reconstructed fluence profile.

2.2   Test beam campaign

An extensive test beam programme has been carried out at the SPS H8 beamline at CERN to characterise the sensors. The beam is a mixed charged hadron beam ($\sim 67\%$ protons, $\sim 30\%$ pions) at $180\,\mathrm{GeV}/c$. The trajectories of particles are reconstructed with the Timepix3 telescope [12], a high rate, data-driven beam telescope, composed of two arms of four planes each. Each plane is instrumented with a $300\,\mu\mathrm{m}$ p-on-n silicon sensor bump-bonded to a Timepix3 ASIC. The centre of the telescope is reserved for the Device Under Test (DUT). The DUT area is equipped with remotely controlled motion stages able to translate the DUT in x and y directions (orthogonal to the beam axis) and to rotate it about the y axis. A vacuum box can also be installed on the central stage to facilitate testing of irradiated devices at high voltage. The DUT can be cooled down to temperatures of about $-20\,°\mathrm{C}$.

The pointing resolution at the DUT position is about $1.6\,\mu\mathrm{m}$, enabling intrapixel studies of the sensor. The typical temporal resolution on a track using only timestamps of the telescope Timepix3 planes is about $350\,\mathrm{ps}$. In the grazing angle configuration, an excellent temporal resolution is useful as clusters can be associated to tracks only using the timing information, which avoids the complexities of performing the association with only one spatial dimension.

2.3   Time-to-threshold measurement

The time-to-threshold (TtT) of a hit is obtained by subtracting the track time provided by the telescope from the hit time measured in the DUT. There is a constant offset between the track and DUT hit times due to time-of-flight and differences in cable length between the DUT and the telescope planes, and hence only relative differences in the time-to-threshold are meaningful. The most probable value of the time-to-threshold is determined by fitting the distribution with a

Cruijff [17] function, a Gaussian function with different left-right widths and non-Gaussian tails

$$
f(x; x_0, \sigma_L, \sigma_R, \alpha_L, \alpha_R) =
\begin{cases}
\exp\left(-\dfrac{(x - x_0)^2}{2(\sigma_L^2 + \alpha_L(x - x_0)^2)}\right), & \text{if } x < x_0, \\[3mm]
\exp\left(-\dfrac{(x - x_0)^2}{2(\sigma_R^2 + \alpha_R(x - x_0)^2)}\right), & \text{if } x > x_0,
\end{cases}
\tag{2.1}
$$

where x_0 is the mean, $\sigma_{L,R}$ is the left-right width and $\alpha_{L,R}$ parametrises the left-right tail. The right width is in general larger than the left width due to timewalk. An example of the fit to the time-to-threshold distribution is shown in figure 2. Unless otherwise stated, the quoted resolution corresponds to the right width of the Cruijff function. The measured resolution is the sum in quadrature of the intrinsic resolution of the DUT and the resolution of the telescope, of 350 ps [12]. The resolution of the DUT can be described by a combination of three terms [18]

$$
\sigma_t^2 = \left(\left[\frac{t_r V_{th}}{S}\right]_{RMS}\right)^2 + \left(\frac{t_r}{S/N}\right)^2 + \left(\frac{TDC_{bin}}{\sqrt{12}}\right)^2,
\tag{2.2}
$$

where the first component is the contribution from timewalk, the second component is the contribution from jitter, and the last component is the contribution from TDC binning. Here t_r is the rise time of the signal at the output of the amplifier, V_{th} is the threshold of the discriminator, S is the amplitude of the signal, N is the noise of the front-end, and TDC_{bin} is the TDC bin width. The contribution due to Landau fluctuations is estimated to be lower than 50 ps for both nonirradiated and irradiated sensors, and hence negligible compared to the other terms. The additional contribution from different time offsets within the pixel matrix is consistent between all ASICs [19] and thus is neglected.
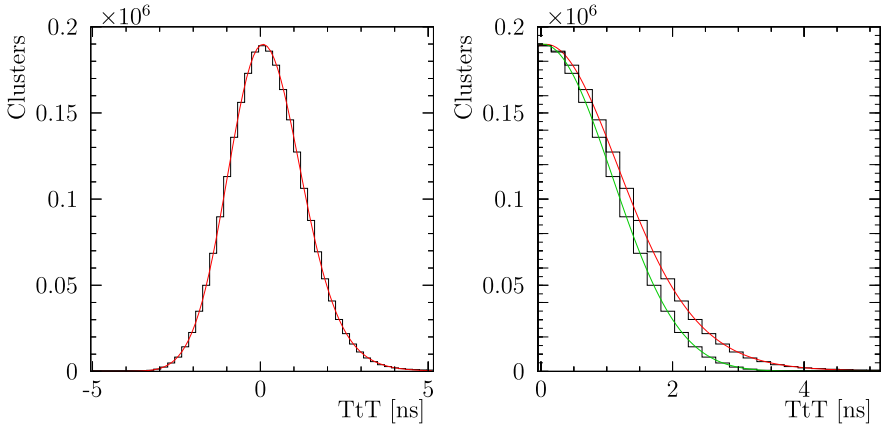

Figure 2. Example of a typical time-to-threshold (TtT) distribution for a sensor irradiated to full fluence after timewalk correction (left), and the same distribution mirrored around the *y*-axis (right), where the right-hand side is indicated in red and the left-hand side in green.

In order to understand the charge collection time, the effects of the sensor must be disentangled from those of the ASIC. It is particularly important to correct for timewalk after irradiation due to the degraded charge collection. For studies at normal incidence, the timewalk curve is determined per pixel by injecting a test pulse with known charge in the pixel front-end. Conversely, the grazing angle method has the advantage that the timewalk curve can be determined directly from the testbeam data, by selecting only charges liberated at small depth, up to about 25 µm from the pixel electrodes, in order to reduce the effect of the sensor to a negligible level. The timewalk curve obtained with this method is found to be compatible with that obtained from test pulse data for a subset of the assemblies, an example of which is shown in appendix B.

The timewalk curve is parameterised as

$$t(q) = \frac{A}{q - q_0} + C,$$ (2.3)

where t is the time-to-threshold, q is the charge, q_0 the charge corresponding to the onset of the asymptote, A the slope and C the offset. The inverse function is used to correct the measured time-to-threshold of each hit. Unless otherwise specified, the results shown are corrected for timewalk.

3 Results at perpendicular incidence

In this section, the time response of the different sensor designs is studied prior to and after irradiation, with some prototypes exposed to uniform and others to nonuniform irradiation profiles. The prototypes are placed perpendicular to the incident beam, thus the charge is liberated along the thickness of the sensor allowing for a direct measurement of the resolution per pixel.

3.1 Nonirradiated sensors

Five assemblies have been tested prior to irradiation in order to disentangle sensor effects from those caused by radiation damage. For these sensors, the resolution and the time-to-threshold are shown as a function of the operating voltage in figure 3. The resolution for all the sensor types improves with increasing voltage and saturates at around 0.8 ns. At the highest voltages, the resolution is dominated by contributions from the ASIC, with comparable contributions from jitter, TDC binning and different time offsets within the pixel matrix [19]. Therefore the resolution saturates at lower voltage than the time-to-threshold. The time-to-threshold of the signal decreases with the operation voltage indicating that the electric field is increasing and the charge carriers do not reach their saturation velocity until a voltage of around 1000 V. All types of sensors achieve a similar temporal resolution and time-to-threshold at high voltage, while a small difference arises between the different types at lower voltages.

3.2 Uniformly irradiated sensors

The resolution for irradiated sensors is expected to be worse due to an increased jitter in the signal. After irradiation the amount of charge collected decreases, degrading the signal-to-noise ratio and
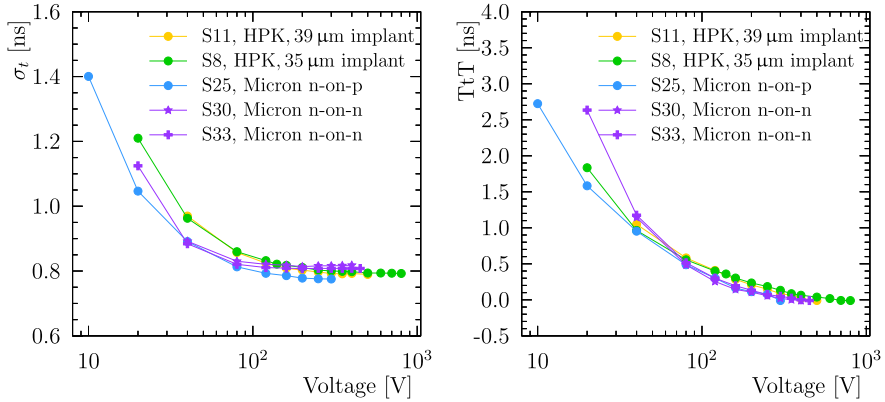
Figure 3. Resolution (left) and time-to-threshold (right) as a function of operating voltage for different nonirradiated sensors.

thus the resolution. The mobility of the charge carriers also decreases due to radiation damage [20, 21], further degrading the time resolution.

The resolution for sensors irradiated to 8×10^{15} 1 MeV n_{eq} cm^{-2} are shown in figure 4 (left). All the sensors show the same trend, with the resolution improving as the applied bias increases. This can mainly be attributed to the change in signal amplitude, which increases linearly with applied bias from 200 to 1000 V [22] with no evidence of saturation. The resolution is also not seen to saturate at 1000 V, indicating that better timing performance could potentially be achieved by further increasing the bias voltage. Figure 4 (right) shows that the time-to-threshold trend as a function of voltage is similar between the different types of sensor after irradiation. The time-to-threshold is worse than prior to irradiation, especially at a bias voltage below 400 V.

It can be concluded that after irradiation to the maximum fluence, the sensors would need to be operated with a voltage of at least 1000 V to optimise the resolution. Such a high voltage also mitigates the effect of timewalk, which is beneficial for the operations of the detector by reducing the probability that hits are recorded in the subsequent bunch crossing.

3.3 Nonuniformly irradiated sensors

The resolution is studied as a function of fluence using a nonuniformly irradiated sensor. Figure 5 shows the resolution and time-to-threshold of a HPK sensor for two different operating voltages, 500 V and 1000 V, with similar trends observed for intermediate voltages. The resolution degrades with increasing fluence. While increasing the voltage improves the resolution in all cases, as was already noted in figure 4 (left), the performance achieved prior to irradiation is never attained. The time-to-threshold for the two different operating voltages is comparable, as was already observed in figure 4 (right).

The variation of the resolution within a pixel for different fluences is investigated in order to understand if the observed degradation is localised. The square pixel symmetry is exploited
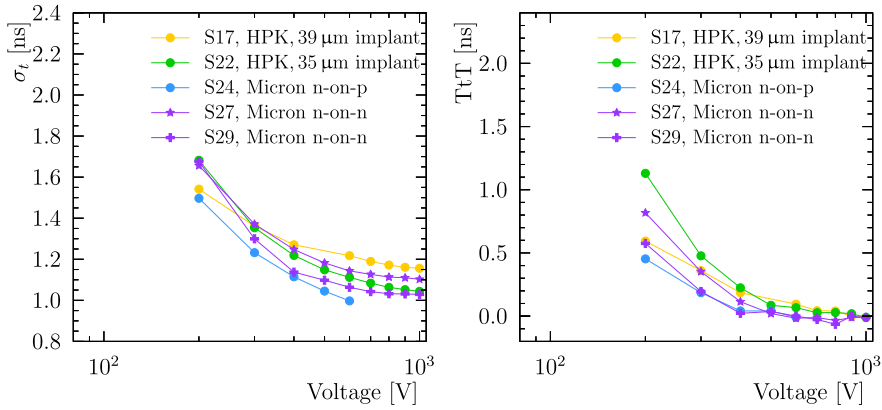
Figure 4. Resolution (left) and time-to-threshold (right) as a function of operating voltage for sensors irradiated to full fluence at JSI.
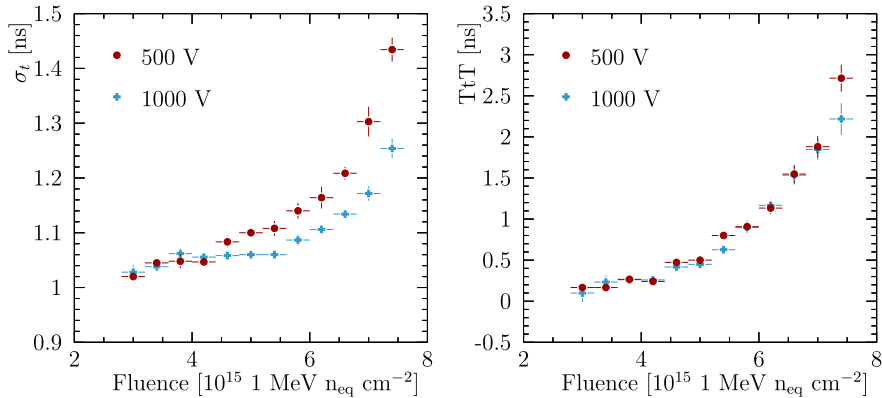
Figure 5. Resolution (left) and time-to-threshold (right) as a function of fluence for different operating voltages for a 200 μm nonuniformly irradiated HPK n-on-p sensor (S8).

by combining the data from four quadrants into one in order to maximise the effective sample size for the intrapixel study. The resolution and the time-to-threshold of a slice of 5 μm centred at $y = 27.5$ μm of the pixel, where the origin is the lower left corner, is shown in figure 6. The resolution is uniform over the pixel for all fluence levels at an operating voltage of 1000 V.

Charge multiplication is observed for this sensor, as reported in reference [22]. The Most Probable Value (MPV) of the collected charge is presented in figure 6 in order to evaluate interplay of the timewalk and high fluence effects. At the highest fluences, 7.0 and 7.6×10^{15} 1 MeV n_{eq} cm^{-2}, the signal is larger than the immediate lower fluence bin, 6.4×10^{15} 1 MeV n_{eq} cm^{-2}. Despite a
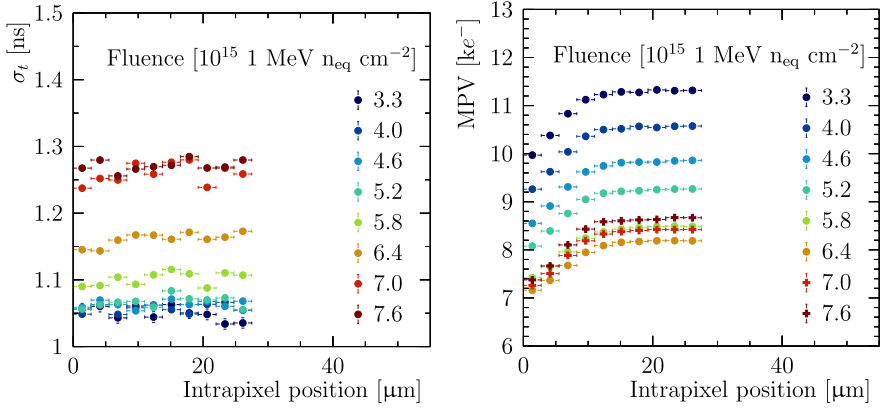
Figure 6. Resolution (left) and MPV of the cluster charge (right) for a slice of 5 μm centred at $y = 27.5$ μm of the pixel as a function of intrapixel position for different fluences for a 200 μm nonuniformly irradiated HPK n-on-p sensor (S8) operated at 1000 V. The uncertainties are statistical only.

higher signal due to charge multiplication, no improvement is observed in the resolution, being dominated by the ASIC contributions, nor time-to-threshold.

4 Results at grazing angles

The grazing angle technique is used to study the time-to-threshold as a function of the depth at which the charge is deposited in the sensor. The charge collection as a function of depth is also measured, providing complementary information to understand the time dependent properties of the sensors. Firstly, the data selection and grazing angle method are described in section 4.1, followed by the results for nonirradiated sensors in section 4.2, and uniformly neutron irradiated sensors and nonuniformly proton irradiated sensors in sections 4.3 and 4.4, respectively.

4.1 Data selection

In the grazing angle setup, the sensor is placed almost parallel to the beam such that the incident particle traverses multiple adjacent pixels, as illustrated in figure 7.

Only clusters on the DUT that are associated to tracks reconstructed by the telescope are used. A cluster is considered associated to a track if the time difference between the two is less than 10 ns, where the time of the cluster is defined as the earliest timestamp amongst its constituent pixel hits. Given the average rate at the CERN SPS of 2M tracks for a spill of 4.5 s, the time cut is sufficient to perform the cluster-track association, expecting two tracks in the same time window in less than 0.5% of the cases. Clusters are removed from the analysis in the case where the corresponding track could be associated to multiple clusters. The cluster is required to span only one pixel row in order to remove particle tracks with delta-ray emissions or secondary particle production, as illustrated in figure 7 (right), discarding about half of the data. A gap of up to three contiguous

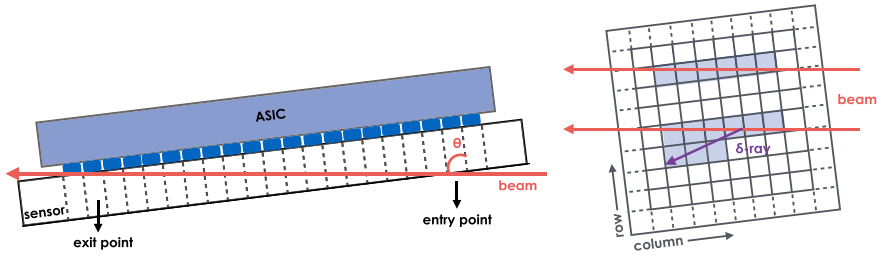**Figure 7.** Illustration of the grazing angle setup. Top view of the sensor (left): the entry and exit point of the track are indicated, as well as the angle θ of the track with respect to the sensor. Front view of the sensor (right): two different types of track are represented, with and without the emission of a δ-ray.

empty pixels is allowed within the cluster to account for signals in dead or masked pixels, or with charge lower than the threshold in the case of irradiated sensors. The entry and exit point of the track is required to be further than three pixels from the edge of the pixel matrix to ensure that the full cluster is within the sensitive volume. The cluster length, which is given by the number of adjacent columns, depends on the incident angle θ. The expected cluster length is

$$N\left(\theta\right) = \frac{\tan \theta \times \lambda}{55 \ \mu m},\tag{4.1}$$

where N is the number of pixels forming the cluster and λ is the active depth of the sensor. The measured cluster length for a given angle is distributed around the expected value. A fit to the cluster length distribution is performed with a Gaussian distribution and clusters with length larger than one standard deviation from the fitted mean are rejected, removing about 40% of the data.

Data sets have been acquired at four angles: 83, 85, 87, 89 degrees. The active depth of the sensor for nonirradiated and uniformly irradiated sensors is determined by performing a fit to the average cluster length using equation (4.1), where $\theta = \alpha + \epsilon$ with α fixed to the chosen angle and ϵ allowed to vary to account for a possible offset. The angle offset is found to be of the order of 0.05 degrees.

As illustrated in figure 7, the depth $d(i)$, defined as the distance from the charge deposit to the pixel implant, can be parameterised by the hit position of the pixel i within the cluster by inverting equation (4.1):

$$d(i) = \frac{55 \ \mu m \times i}{\tan \theta}.\tag{4.2}$$

Using this relationship, the time needed for the induced signal to cross the threshold (time-to-threshold) is investigated as a function of the depth. A depth of $0 \ \mu m$ corresponds to the pixel electrode side, while the full depth, $150 \ \mu m$ or $200 \ \mu m$ depending on the sensor, corresponds to the sensor back side. The following plots are obtained with the sensor placed at a $85°$ angle with respect to the beam, giving a depth step of $55 \ \mu m \times \cos(85°) \approx 4.8 \ \mu m$, unless otherwise stated. The uncertainty on the measured depth due to the uncertainty on the angle offset and a possible missing hit at the beginning or end of the cluster is found to have a negligible impact on the charge and time-to-threshold distributions.

The charge collected is measured by performing a fit to the hit charge distribution at a given depth. Two sources of systematic uncertainty on the MPV are considered, charge calibration and digitisation. The systematic uncertainty on the charge calibration has two components: due to the imperfect knowledge of the injected charge and the statistical uncertainty from the test pulse procedure. The former is assigned to be 4% of the measured charge, according to reference [23]. The latter is obtained by generating pseudoexperiments to evaluate how the correlated uncertainties of the calibration curve parameters affect the MPV and yields $30\,e^-$ for a nonirradiated sensor and $50\,e^-$ for a sensor irradiated at full fluence, where the uncertainty is larger in the irradiated case due to the smaller charge collected. The digitisation uncertainty is assigned to account for the discrete values of ToT. This uncertainty is estimated as $40\,e^-$ for hit charges higher than $\sim 2500\,e^-$, but rapidly increases for lower charges. The effect of this systematic uncertainty on the MPV of the charge distribution is determined using pseudoexperiments and results in $20\,e^-$ and $50\,e^-$ for a nonirradiated sensor and for a sensor irradiated at full fluence, respectively.

4.2 Nonirradiated sensors

The results for nonirradiated sensors are shown in figure 8 for HPK n-on-p (top), Micron n-on-p (middle) and Micron n-on-n (bottom) sensors, in terms of charge collected (left) and time-to-threshold (right) as a function of depth for different bias voltages. It can be seen that the three families of sensors exhibit the same trend for both the charge collected and time-to-threshold profiles. For a nonirradiated sensor and bias voltage above depletion, the MPV of the charge collected is constant and equal to the charge expected for the full thickness of the sensor. The time needed to cross the threshold is less than 5 ns. The depletion voltage is found to be 120 V and 40 V for HPK and Micron n-on-p, respectively. Below the depletion voltages the charge drops linearly, starting at the border between depleted and nondepleted volume up to a depth of about 20 µm from the border. This is an effect due to diffusion known as charge migration [24, 25]. No hits are registered below $2000\,e^-$, despite being significantly far from the threshold, due to a time requirement of 100 ns imposed in the clustering process. The increase in time-to-threshold with depth can be mainly attributed to the nonuniformity of the weighting field, which increases towards the pixel electrodes, and hence most of the signal is induced while drifting near the electrodes. Since the sensor is nonirradiated and the collected charge is higher than $3000\,e^-$, the timewalk has a negligible effect. Partially depleted sensors have an additional contribution to the time-to-threshold from charges migrating from the nondepleted region due to diffusion.

4.3 Sensors irradiated to full fluence

The trends of the charge collected and time-to-threshold as a function of depth for uniformly irradiated sensors, as illustrated in figure 9 for HPK n-on-p, are quite different from the behaviour observed for nonirradiated devices. Firstly, there is an overall signal reduction due to charge trapping, which is not fully recovered by an increase in bias voltage. Not all the charge liberated at a given depth is collected and this decreases with distance from the electrodes because charge needs to travel over a longer distance and hence has a larger probability to be trapped [15]. The charge at each bias voltage shows a slight decrease close to the electrodes. This is due to two different effects: the lower field between the neighbouring pixel implants and hole trapping, since

129

Figure 8. Charge collected (left) and time-to-threshold (right) as a function of depth for a 200 μm thick nonirradiated HPK n-on-p sensor (S6, top), a 200 μm thick nonirradiated Micron n-on-p sensor (S23, middle) and a 150 μm thick nonirradiated Micron n-on-n sensor (S34, bottom). A depth of 0 μm corresponds to the pixel electrodes side while 200 μm (top and middle) or 150 μm (bottom) corresponds to the backside. For the MPVs, the error bars indicate the systematic uncertainties on the measurements, while for the time-to-threshold, the error bars indicate the statistical uncertainty.
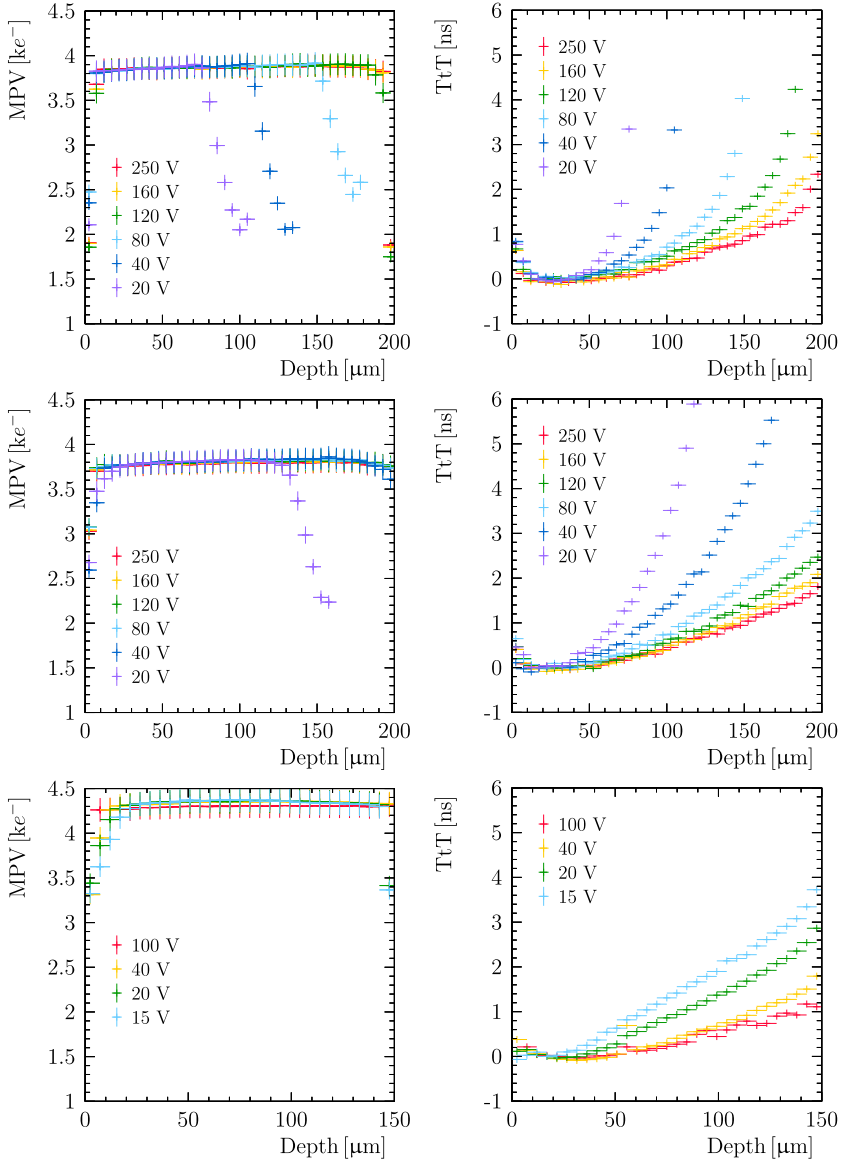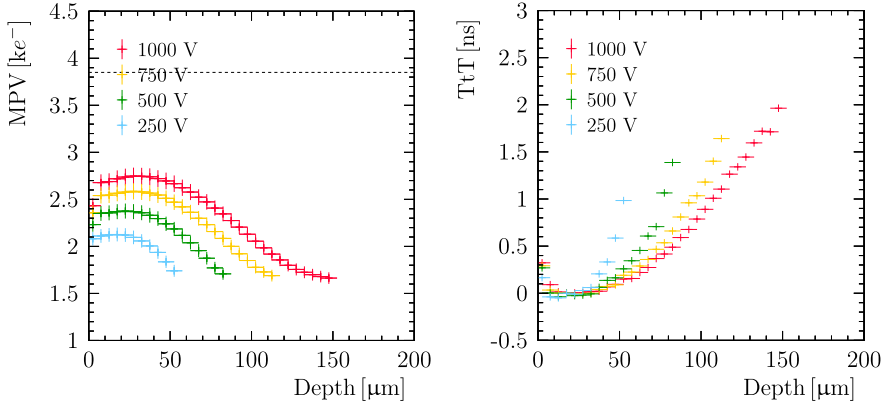
Figure 9. Charge collected (left) and time-to-threshold (right) as a function of depth for a 200 µm thick HPK n-on-p sensor (S22). The dashed line indicates the charge collected by a nonirradiated sensor of the same type. The sensor is uniformly irradiated to 8×10^{15} 1 MeV n_{eq} cm^{-2}. For the MPVs, the error bars indicate the systematic uncertainties on the measurements, while for the TtT, the error bars indicate the statistical uncertainty.

for charges liberated close to the electrodes the current is mainly induced by the motion of holes. Secondly, most of the charge from the nondepleted volume recombines before it could be collected. This can be attributed to charge trapping and slow drift in combination with the integration time of the front-end. The time for the integration of the signal is limited, hence the discharge can start while still in the process of integrating; this is especially relevant for a small amount of charge. A possible effect of a doubly peaked electric field according to the double junction model for highly irradiated sensors [15, 26] is not observed. This can be attributed to a combination of the small amount of charge and the low weighting field at the backside of the sensor.

The percentage of charge loss due to irradiation per depth is illustrated in figure 10 for the different types of sensors and different types of irradiation, where for the sensors nonuniformly irradiated at IRRAD the region with average fluence of 7.6×10^{15} 1 MeV n_{eq} cm^{-2} is selected. The percentage of charge lost varies with depth between about 25% close to the electrodes and 60% at the border of the active region. These values are compatible with what is reported in literature for similar fluences [27]. The charge loss increases with depth up to the active volume of the sensor after irradiation, while nothing is collected from the nondepleted volume. Only Micron n-on-n sensors (150 µm thick) reach full depletion. A different behaviour is observed between proton and neutron irradiation, with a steeper dependence on depth in the case of protons.

The time-to-threshold after timewalk correction increases with depth, up to 2 ns, independent of the voltage applied. The different sensors show the same trend in time-to-threshold as a function of depth, as can be seen in figure 11 (left). The resolution as a function of depth is shown in figure 11 (right) and is found to be constant up to around 90 µm depth. At this point, the right-sided resolution increases due to residual timewalk. Timewalk corrections are large for these assemblies and therefore the results prior to correction are described in detail in appendix B.
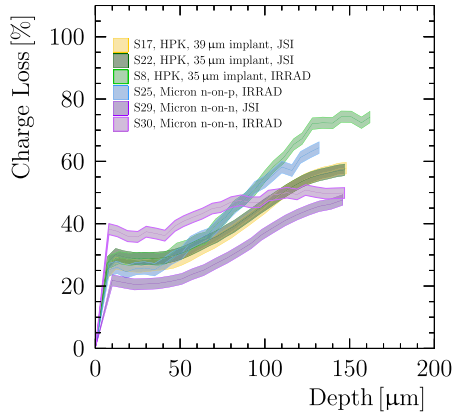
Figure 10. Percentage of charge loss as a function of depth for a HPK n-on-p and a Micron n-on-p sensors and for different radiation types.
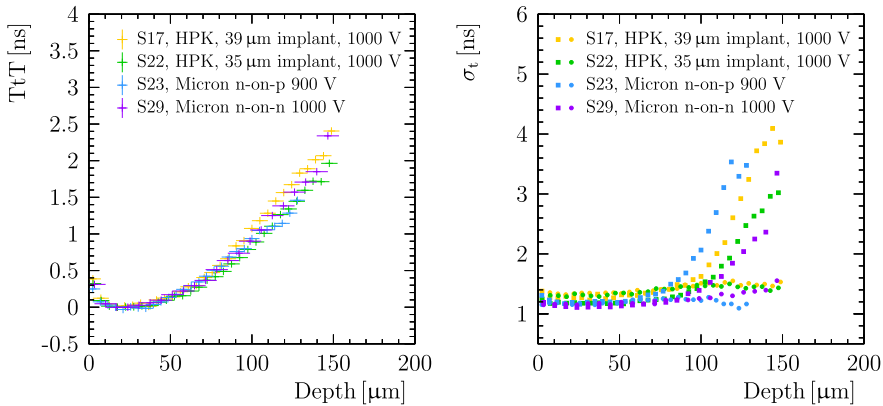
Figure 11. Time-to-threshold (left) and resolution (right) as a function of depth for uniformly irradiated sensors. The circle and square markers indicate the left and right-sided resolution, respectively.

4.4   Nonuniformly irradiated sensors

The assemblies presented in this section were irradiated nonuniformly, following the shape of the illumination by the proton beam as shown in figure 1. All the assemblies have been tested without additional controlled annealing, with the exception of the Micron n-on-n sensor that underwent controlled annealing for 80 minutes at 60 °C.

The charge collection and time-to-threshold for charges liberated at different depths in the bulk of the sensors are studied as a function of fluence at different operation voltages in figures 12 and 13
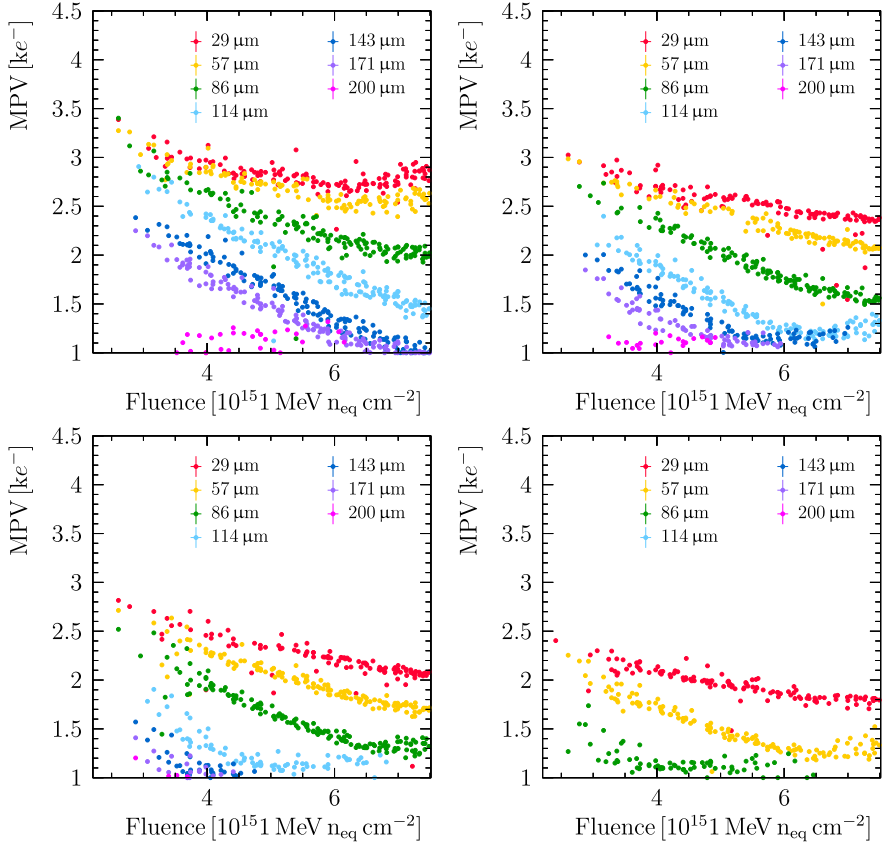
Figure 12. Charge collected as a function of fluence from different depths for a 200 μm HPK n-on-p sensor (S8) operated at 1000 V (top left), at 750 V (top right), at 500 V (bottom left) and at 250 V (bottom right).

for a HPK n-on-p sensor. The charge is collected only up to $\sim 90\,\mu$m depth from the electrodes for low voltages, around 250 V, and decreases as a function of fluence. Increasing the bias voltage, the charge is collected from deeper in the sensor, up to $\sim 170\,\mu$m depth at 1000 V. At the highest voltage tested, the spread in time-to-threshold with depth is about 1 ns at low fluences and about 6 ns at 8×10^{15} 1 MeV n_{eq} cm^{-2}, with charge collected more slowly from deeper in the sensor. At a given depth and fluence charge is collected more slowly as the voltage is decreased. Larger data sets would be needed to determine any changes in the resolution of the sensor.

At depths smaller than 80 μm, there is a sizeable deviation from the trend for the highest fluence region. This effect, observed only at 1000 V bias, is recognised as the so-called charge multiplication or avalanche effect [28–30]. The charge multiplication happens close to the pixel electrodes where the electric field is highest. If charges are liberated in the high field volume,

133
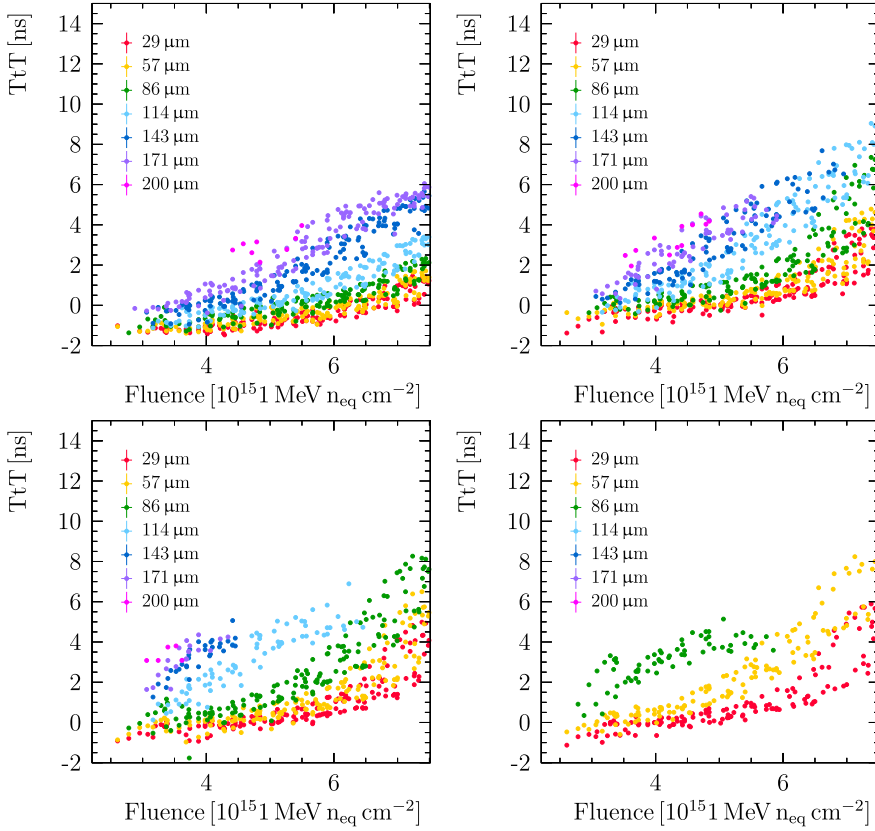
Figure 13. Time-to-threshold as a function of fluence from different depths for a 200 μm HPK n-on-p sensor (S8) operated at 1000 V (top left), at 750 V (top right), at 500 V (bottom left) and at 250 V (bottom right).

close to the electrodes, they have higher chance to undergo multiplication. In contrast, most of the charges liberated deeper in the bulk will experience trapping before reaching the high field region. A small rise in the apparent MPV is also observed for charges close to the threshold, at a depth that varies as a function of applied voltage. This rise can be attributed to a threshold effect, an investigation into which is documented in appendix C. Avalanche multiplication is observed in both Hamamatsu n-on-p and Micron n-on-p sensors at 1000 V, while the Micron n-on-n sensor does not present any observable effect even at the highest voltage tested. The charge multiplication effect is not observed for uniformly neutron irradiated sensors, even when operated at 1000 V. This can be attributed to the different nature of irradiation leading to different damage in the silicon [31].

In addition to the absence of the charge multiplication effect, n-on-n sensors present a lower degradation as a function of the fluence, as can be seen from figure 14. The charge collected at a
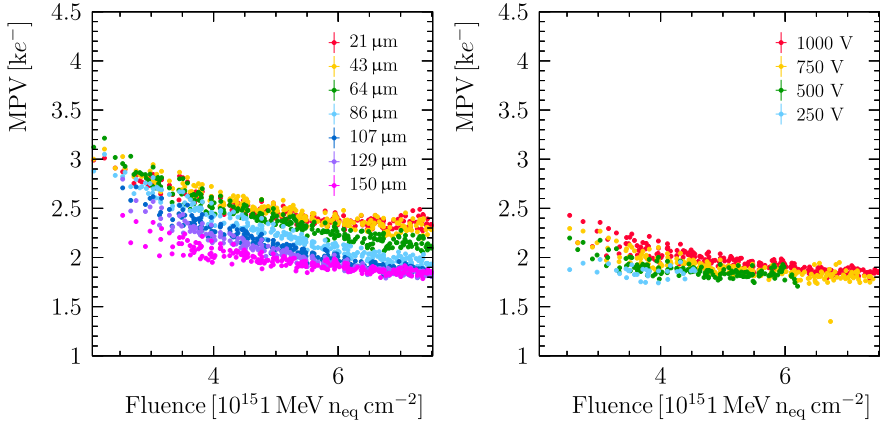
Figure 14. Charge collected as a function of fluence from different depths for a sensor operated at 1000 V (left) and charge collected as a function of fluence for charges liberated at 150 μm depths at different operation voltages (right). The sensor is a 150 μm Micron n-on-n sensor (S30).

depth of 150 μm is examined as a function of fluence for different operation voltages in figure 14 (right). It can be seen that the charge collected never falls below the threshold value of $1000\,e^-$ and thus is collected up to the full thickness even at 400 V, showing that Micron n-on-n has a larger active depth compared to the other types of sensors.

5 Conclusions

The timing properties of a range of prototype sensors are presented in this paper. Several assemblies are studied perpendicular to the incident beam in order to investigate the sensor resolution and time-to-threshold as a function of bias voltage and fluence. Before irradiation the temporal resolution saturates at about 0.8 ns slightly before reaching full depletion. After uniform irradiation up to a fluence of $8 \times 10^{15}\,1\,\text{MeV}\,n_{eq}\,\text{cm}^{-2}$, the temporal resolution does not saturate up to at least 1000 V. Assemblies irradiated with a non-uniform irradiation profile show that the temporal resolution degrades with increasing fluence. It is also observed that with the onset of charge multiplication, the temporal resolution does not improve.

The grazing angle technique proves to be a powerful method to study charge collection and time-to-threshold properties of charges generated at different depths in the bulk of the sensors. For nonirradiated sensors the most probable value of collected charge is constant as a function of depth once full depletion is reached and higher than $3500\,e^-$. The time-to-threshold is therefore barely affected by timewalk. The time-to-threshold is extended by the time needed for the charge to migrate from the nondepleted volume. For sensors uniformly irradiated to the full fluence it is observed that most of the charge collected originates close to the pixel electrode. Due to radiation damage there is a reduction of the charge collected, leading to an increase in timewalk. Otherwise, the temporal collection properties of the sensor are only marginally affected by radiation damage.

Nonuniformly irradiated sensors allowed the study of charge collection and time-to-threshold variations as a function of fluence. In particular there is a clear enhancement of charge collected from depths up to 80 µm at an operating voltage of 1000 V due to charge multiplication for fluences higher than 6×10^{15} 1 MeV n_{eq} cm^{-2}. The charge multiplication effect has been observed for proton but not neutron irradiated sensors.

Acknowledgments

A   List of assemblies

The details of the assemblies tested are summarised in table 4.

Table 4. Assemblies tested.

ID	Vendor	Thickness [µm]	Type	Edge width [µm]	Implant [µm]	Irradiation facility	Peak fluence [10^{15} 1 MeV n_{eq} cm^{-2}]
S6	HPK	200	n-on-p	450	39	JSI	8
S8	HPK	200	n-on-p	450	35	IRRAD	8
S11	HPK	200	n-on-p	450	39	IRRAD	8
S17	HPK	200	n-on-p	450	39	JSI	8
S22	HPK	200	n-on-p	450	35	JSI	8
S23	Micron	200	n-on-p	450	36	JSI	8
S24	Micron	200	n-on-p	450	36	JSI	8
S25	Micron	200	n-on-p	450	36	IRRAD	8
S27	Micron	150	n-on-n	450	36	JSI	8
S29	Micron	150	n-on-n	450	36	JSI	8
S30	Micron	150	n-on-n	450	36	IRRAD	8
S33	Micron	150	n-on-n	250	36	—	—
S34	Micron	150	n-on-n	250	36	—	—

B   Timewalk correction

With the grazing angle method, the timewalk curve can be determined directly from the testbeam data by selecting only charges liberated at small depth, up to about 25 μm from the pixel electrodes. The timewalk curve obtained is validated for some assemblies by comparing it to the timewalk curve determined by injecting a test pulse with known charge in the pixel front-end, as shown in figure 15. The shape variation of the timewalk curve is negligible, leading to the conclusion that the profile obtained is sufficiently representative of a pure electronics effect. The horizontal bar on the hit charge of the test pulse curve is due to the binning and it is not representative of the charge uncertainty.
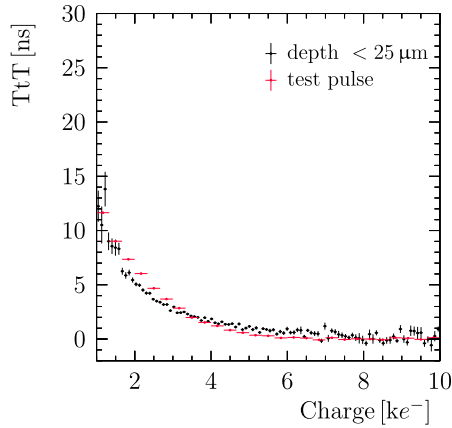
Figure 15. Comparison between timewalk curve from test pulse data and from test beam data with charges liberated close to the electrode. The sensor is a 200 μm thick nonuniformly irradiated HPK n-on-p sensor at 1000 V bias voltage.

For assemblies irradiated at full fluence, the contribution of timewalk becomes significant, since the charge collected is lower than $3000\,e^-$. The timewalk effect broadens the time-to-threshold distribution, leading to an asymmetric uncertainty on the single measurement that varies from 3 ns up to 15 ns depending on the depth. In the left plot of figure 16 the time-to-threshold profile for a HPK n-on-p sensor at 1000 V is compared to the profile obtained by applying the timewalk correction described in section 2.3. The timewalk curve is fitted and a correction to the time-to-threshold of each hit is applied as a function of charge. The magnitude of the correction increases as the charge decreases, hence with depth, leading to a smaller mean value and narrower distribution compared to the uncorrected case. The corrected time-to-threshold spread results in less than 3 ns along the whole sensor depth and the uncertainty spans from ∼ 1.5 ns at small depth up to ∼ 4 ns at the border of the active region. In the right plot of figure 16 the corrected profiles at the highest (1000 V) and lowest (250 V) voltage tested are compared to the time-to-threshold profile for the same type of sensor before irradiation and fully depleted. The profiles agree within
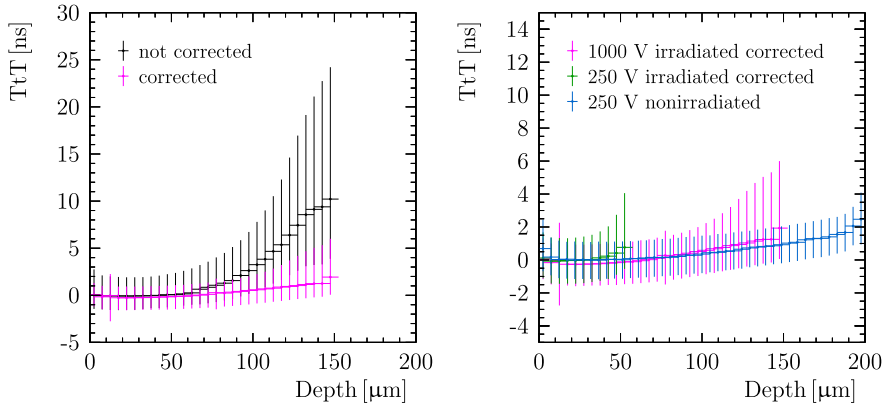
Figure 16. Comparison between time-to-threshold profiles before and after timewalk correction (left) and comparison between time-to-threshold profiles for a nonirradiated sensor operated at 250 V and for a uniformly irradiated sensor operated at 250 V and 1000 V (right). The sensors are 200 µm thick HPK n-on-p sensors. The uncertainty is assigned as uncertainty on the single measurement.

the uncertainties. The main difference with respect to the nonirradiated case is represented by the larger uncertainty on the single measurement: close to the electrodes the uncertainty is comparable, while at the border of the active region is almost double, due to possible residual timewalk.

C   Rise in MPV close to threshold

A small rise in the measured MPV as a function of fluence is observed in the grazing angle setup close to the threshold at some depths, as shown in figure 12. The MPV in some cases should be below the threshold from a naive extrapolation from lower fluences, and thus the expected charge distribution in such cases is investigated using pseudoexperiments. The distribution of charges is generated using parameters typical of the real data, and the threshold emulated by selecting only charges above $1000 \pm 100\,e^-$, where the variation is assumed to be Gaussian in nature. Both the true charge distribution and that with the emulated threshold are shown in figure 17 for an MPV of $800\,e^-$. The charge distribution can still be described by a Landau function after the threshold has been applied, albeit with a significantly larger MPV and width. Due to the wide tail of the Landau distribution, the measured MPV increases as the true MPV decreases, up to a few times the threshold dispersion.

This model is compared to the data set where the effect appears most pronounced, at a depth of 114 µm and an applied voltage of 750 V. The true MPV is estimated by assuming a linear decrease as a function of fluence, with slopes of: $-0.2, -0.35, -0.5\,\mathrm{ke^-}/10^{15}\,1\,\mathrm{MeV}\,n_{eq}\,\mathrm{cm^{-2}}$ considered. The MPV obtained by performing a fit to the simulated data sets are compared with real data in figure 17, where the observed rise in MPV is largest when the true MPV is furthest below threshold. There is qualitatively a good agreement between the data and the model, and thus this effect can account for the artificial rise in MPV at very high fluences and close to the threshold.
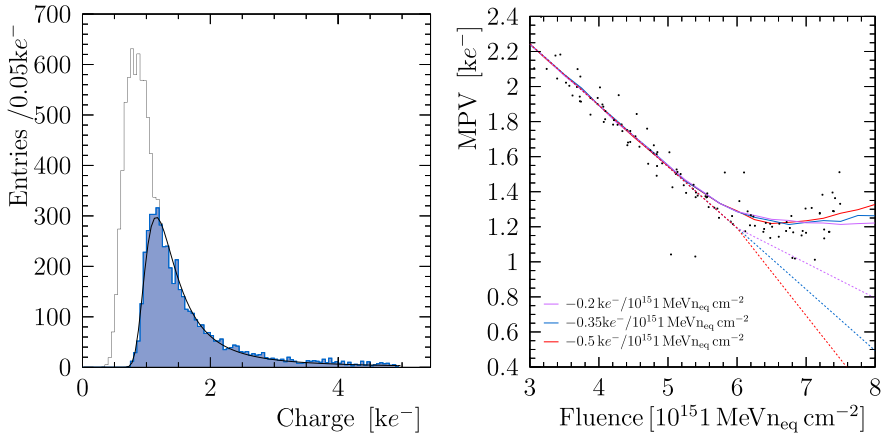
Figure 17. Left: distribution of simulated of charges for an MPV of $800\,e^-$, demonstrating the effect of the threshold on the shape, with the filled histogram indicating the charges that pass the threshold. Right: comparison with trend observed in a $200\,\mu m$ HPK n-on-p sensor operated at $750\,V$ at a depth of $114\,\mu m$, assuming different linear dependence on the true MPV with fluence.

References

[1] LHCb collaboration, *LHCb VELO upgrade technical design report, Tech. Rep. CERN-LHCC-2013-021,* CERN, Geneva (2013).

[2] V. Chiochia et al., *Simulation of the CMS prototype silicon pixel sensors and comparison with test beam measurements, IEEE Trans. Nucl. Sci.* **52** (2005) 1067.

[3] S. Meroli, D. Passeri and L. Servoli, *Measurement of charge collection efficiency profiles of CMOS active pixel sensors,* 2012 *JINST* **7** P09011.

[4] B. Henrich, W. Bertl, K. Gabathuler and R. Horisberger, *Depth profile of signal charge collected in heavily irradiated silicon pixels, Tech. Rep. CMS-NOTE-1997-021,* CERN, Geneva (1997).

[5] E.J. Schioppa et al., *Study of charge diffusion in a silicon detector using an energy sensitive pixel readout chip, IEEE Trans. Nucl. Sci.* **62** (2015) 2349.

[6] L. Servoli, S. Meroli, D. Passeri and P. Tucceri, *Measurement of submicrometric intrinsic spatial resolution for active pixel sensors,* 2013 *JINST* **8** P11007.

[7] V. Eremin, N. Strokan, E. Verbitskaya and Z. Li, *Development of transient current and charge techniques for the measurement of effective net concentration of ionized charges (N_{eff}) in the space charge region of p-n junction detectors, Nucl. Instrum. Meth.* A **372** (1996) 388.

[8] G. Kramberger et al., *Investigation of irradiated silicon detectors by edge-TCT, IEEE Trans. Nucl. Sci.* **57** (2010) 2294.

[9] M.F. García et al., *On the determination of the substrate effective doping concentration of irradiated HV-CMOS sensors using an edge-TCT technique based on the two-photon-absorption process,* 2017 *JINST* **12** C01038.

[10] T. Poikela et al., *Timepix3: a 65k channel hybrid pixel readout chip with simultaneous ToA/ToT and sparse readout,* 2014 *JINST* **9** C05013.

6

[11] J. Visser et al., *SPIDR: a read-out system for Medipix3 & Timepix3,* 2015 *JINST* **10** C12028.

[12] K. Akiba et al., *LHCb VELO Timepix3 telescope,* (2019) arXiv:1902.09755.

[13] P. Allport et al., *Experimental determination of proton hardness factors at several irradiation facilities,* 2019 *JINST* **14** P12004.

[14] G. Kramberger, *Signal development in irradiated silicon detectors,* Ph.D. Thesis, University of Ljubljana, Ljubljana, Slovenia (2001).

[15] M. Moll, *Displacement damage in silicon detectors for high energy physics, IEEE Trans. Nucl. Sci.* **65** (2018) 1561.

[16] E. Dall'Occo, *Search for heavy neutrinos and characterisation of silicon sensors for the VELO upgrade,* Ph.D. Thesis, Vrije Universiteit Amsterdam, Amsterdam, The Netherlands (2020).

[17] BABAR collaboration, *Study of $B \to X\gamma$ decays and determination of $|V_{td}/V_{ts}|$, Phys. Rev.* D **82** (2010) 051101 [arXiv:1005.4087].

[18] N. Cartiglia et al., *Performance of ultra-fast silicon detectors,* 2014 *JINST* **9** C02001.

[19] K. Heijhoff et al., *Timing performance of the LHCb VELO Timepix3 telescope,* 2020 *JINST* **15** P09035.

[20] E. Borchi and M. Bruzzi, *Radiation damage in silicon detectors, Riv. Nuovo Cim.* **17** (1994) 1.

[21] C. Leroy and P-G. Rancoita, *Particle interaction and displacement damage in silicon devices operated in radiation environments, Rep. Prog. Phys.* **70** (2007) 493.

[22] R. Geertsema et al., *Charge collection properties of prototype sensors for the LHCb VELO upgrade,* 2021 *JINST* **16** P02029 [arXiv:2010.10147].

[23] M. Vicente Barreto Pinto, *Caracterização do TimePix3 e de sensores resistentes à radiação para upgrade do VELO,* Master Thesis, Universidade Federal do Rio de Janeiro, Rio de Janeiro, Brazil (2016).

[24] N. Croitoru, P.G. Rancoita and A. Seidman, *Charge migration contribution to the sensitive layer of a silicon detector, Nucl. Instrum. Meth.* A **234** (1985) 443.

[25] P. Tsopelas, *A silicon pixel detector for LHCb,* Ph.D. Thesis, Vrije Universiteit Amsterdam, Amsterdam, The Netherlands (2016).

[26] V. Eremin, E. Verbitskaya and Z. Li, *The origin of double peak electric field distribution in heavily irradiated silicon detectors, Nucl. Instrum. Meth.* A **476** (2002) 556.

[27] A. Ducourthial et al., *Performance of thin planar n-on-p silicon pixels after HL-LHC radiation fluences,* (2018) arXiv:1810.07279.

[28] M. Mikuž, V. Cindro, G. Kramberger, I. Mandic and M. Zavrtanik, *Study of anomalous charge collection efficiency in heavily irradiated silicon strip detectors, Nucl. Instrum. Meth.* A **636** (2011) S50.

[29] G. Casse, A. Affolder, P.P. Allport, H. Brown, I. McLeod and M. Wormald, *Evidence of enhanced signal response at high bias voltages in planar silicon detectors irradiated up to 2.2×10^{16} n_{eq} cm^{-2}, Nucl. Instrum. Meth.* A **636** (2011) S56.

[30] J. Lange et al., *Charge multiplication properties in highly irradiated epitaxial silicon detectors, PoS* **VERTEX2010** (2010) 025.

[31] A. Junkes, *Status of defect investigations, PoS* **VERTEX2011** (2011) 035.

CHAPTER 7

❧

TWO-PHOTON ABSORPTION

Optical beams in the (near-)optical spectrum have been already employed for many decades as characterisation tools for silicon sensors. This method has gained popularity since the invention of the laser (light amplification by stimulated emission of radiation) since they can be easily controlled, especially compared to particle beams. This gain in popularity, especially in high energy physics, was due to the ability to emulate a traversing charged particle with a laser. However, historically lasers have a slow injection of charge in the silicon bulk (nanoseconds), while for a charged particle the charge carriers are liberated in around a picosecond.

The application of lasers in the characterisation of silicon uses photons to excite electron-hole pairs. If the energy of the photons is higher than the bandgap energy of silicon, and a single photon can achieve such an excitation, this technique is called *Single-Photon Absorption* (SPA), and is used extensively to characterise silicon sensors through for example *Transient Current Technique* (TCT), in which the signal produced at the pixel implant is amplified by a dedicated high power amplifier and digitised, by for example an oscilloscope. However, the SPA technique is limited due to its direct absorption in silicon, since photons can excite electron-hole pairs as soon as they are in the silicon volume. Therefore, the absorption of photons, and thus the creation of electron-hole pairs, is limited to this exponential decay function. When SPA with a wavelength corresponding to red (660 nm) is used, the photons are absorbed within the first couple of micrometres in silicon. If an inactive volume is present before the detection volume the generated electron-hole pairs even cannot be detected. When a wavelength closer to the bandgap energy of silicon is used, such as 1060 nm, the absorption occurs over several millimetres, and the optical beam can be reflected multiple times within the silicon sensor due to internal reflection. The application of SPA is thus limited in silicon sensors as a tool to characterise the silicon bulk.
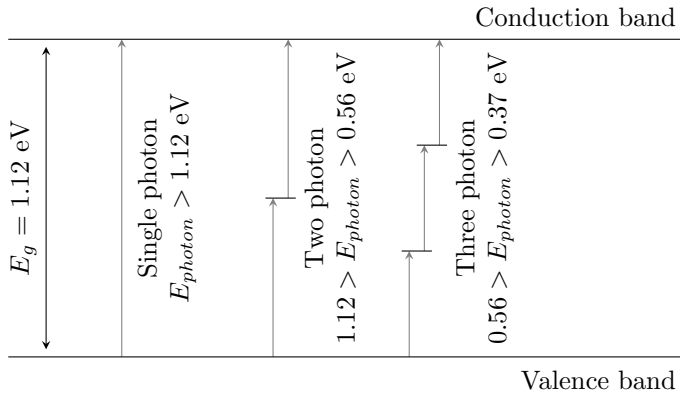
Figure 7.1: A schematic overview of the excitation of an electron from the valence to the conduction band in silicon, aided by either one (left), two (middle), or three (right) photons.

Two-Photon Absorption (TPA) is an interesting non-linear phenomenon that gives a new insight when characterising silicon sensors. While an excitation would normally not be possible for energies smaller than the bandgap energy, electrons excited by these lower energy photons can temporarily occupy a virtual state within the bandgap, and be further excited by a second photon (which gives rise to the name *two-photon* absorption). Higher-order excitations can also occur with lower energy photons, however, in practice three-photon absorption is commonly the highest order. This process with different numbers of photons is illustrated in fig. 7.1. In the past few years, dedicated tabletop two-photon absorption systems have been developed specifically for the characterisation of silicon sensors in high energy physics.

Two-photon absorption of an atom was predicted by Maria Goeppert-Mayer in 1931 [95] and only first measured in 1961, after the development of lasers with sufficient peak intensities, in europium-doped crystals (CaF_2:Eu^{2+}) [96]. Only in 1964, the first evidence of TPA was measured in a semiconductor (CdS) [97]. Since then, the application of TPA has grown into different fields of science, such as in biology for imaging [98], as well as applications outside of science such as 3D optical storage devices [99, 100] and 3D photopolymerization [101].

Contrary to the previously discussed beam telescopes (chapter 5), SPA and TPA systems can liberate charge carriers at the same position in a controlled way. This enables systematic studies of individual pixels. Such measurements have been previously performed with SPA systems, where the energy of the photons is above the bandgap energy of silicon. In contrast, TPA systems use a photon energy just above half of the bandgap energy.

Silicon is transparent for wavelengths below the bandgap energy and therefore the photons can penetrate deep into the bulk. Two-photon absorption can only be achieved when the photon density is sufficient. Since TPA is generally achieved with a focussed Gaussian beam, the TPA region is ellipsoidal in shape and can be placed anywhere in the bulk. This precise control of the volume where charge carriers are generated provides an excellent tool for understanding their behaviour in silicon sensors.

A two-photon absorption system has been developed at Nikhef, based on a 1550 nm pulsed laser system (LFC1500X) [102] from Fyla[1] with a FHWM between 380 fs and 540 fs. Details about this system can be found in section 7.1.

The commissioning of the Nikhef TPA system is described in section 7.1. We have employed the TPA system to measure the temporal characteristics of planar silicon sensors bonded to Timepix3 and Timepix4 ASICs. The results of these measurements can be found in section 7.1 and section 7.2.

---

[1]FYLA, Ronda Guglielmo Marconi 14, Parque Tecnológico 46980 Paterna, Valencia, Spain.

7.1   CHARGE AND TEMPORAL CHARACTERISATION OF SILICON SENSORS USING A TWO-PHOTON ABSORPTION LASER

This section contains a paper describing the commissioning results of the TPA system at Nikhef, as well as results from the temporal characterisation of planar sensors on Timepix3 ASICs.

This paper titled *"Charge and temporal characterisation of silicon sensors using a two-photon absorption laser"* is published in JINST [103].

Charge and temporal characterisation of silicon sensors using a two-photon absorption laser

R. Geertsema,[a,b,*] **K. Akiba,**[a] **M. van Beuzekom,**[a] **T. Bischoff,**[a] **K. Heijhoff**[a] **and H. Snoek**[a,c]

[a]*Nikhef,*
Amsterdam, the Netherlands
[b]*Universiteit Maastricht,*
Maastricht, the Netherlands
[c]*Universiteit van Amsterdam,*
Amsterdam, the Netherlands

E-mail: r.geertsema@nikhef.nl

ABSTRACT: First measurements are presented from a newly commissioned two-photon absorption (TPA) setup at Nikhef. The characterisation of the various components of the system is discussed. Two planar silicon sensors, one being electron collecting and one hole collecting, are characterised with detailed measurements of the charge collection and time resolution. The TPA spot is determined to have a radius of 0.975(11) µm and length of 23 µm in silicon. The trigger time resolution of the system is shown to be maximally 30.4 ps. For both sensors, uniform charge collection is observed over the pixels, and the pixel side metallisation is imaged directly using the TPA technique. The best time resolution for a single pixel is found to be 600 ps and 560 ps for the electron and hole collecting sensors respectively, and is dominated by ASIC contributions. Further scans at different depths in the sensor and positions within the pixels have been performed and show a uniform response. It is concluded that the TPA setup is a powerful tool to investigate the charge collection and temporal properties of silicon sensors.

---

*Corresponding author.

Contents

1 Introduction

Single-photon absorption (SPA) techniques have been extensively used to characterise silicon sensors, as reported in [1]. These techniques are however limited due to the nature of photon interactions in silicon at the wavelengths typically used, resulting in small absorption depths and thus most charge is liberated close to the surface and not deep into the bulk. In contrast two-photon absorption (TPA) can access regions deeper into the bulk of sensors by using photons with energies below the silicon bandgap energy. Recently TPA techniques have seen an increase in their application for the characterisation of silicon detectors in high-energy particle physics [2, 3], and initial spatial measurements indicate that TPA can be used to probe the silicon bulk with high resolving power [2].

To achieve the intensities required for TPA to occur without damaging the material, the optical pulses need to have a very short time duration. These pulses therefore also provide the possibility of sub-picosecond time resolution, since all charge carriers are typically liberated in a time window of hundreds of femtoseconds. Because of the short pulses, TPA systems can also be employed to study the time resolution of silicon detectors with high temporal precision. In this paper an overview of the TPA setup commissioned at Nikhef is outlined, and the time resolution of the system is determined. The system has been used to characterise the charge collection spatially as well as the time resolution of planar silicon sensors bump bonded to Timepix3 application-specific integrated circuits (ASIC) [4].

The paper is organised as follows: the TPA system is outlined in section 2 along with the characterisation studies of this system that have been performed. The detectors that have been used to perform the first characterisations are discussed in section 3. The charge collection and temporal measurements are described in section 4, followed by the conclusions in section 5.

2   Two-photon absorption laser system

Typically, low energy ($\sim O\left(1\right)$ eV) photons propagating in a semiconductor are absorbed via a single interaction with an electron. The energy of the photon may excite an electron from the valence band of the semiconductor to the conduction band. This excitation can only occur if the initial photon energy is larger than the bandgap energy of the semiconductor. This excitation can also be achieved by a simultaneous interaction of multiple photons, if their combined energy is high enough to bridge the bandgap and if the interaction of the later photon(s) occurs within the de-excitation time of the electron. This process is called multi-photon absorption, and more specifically, the excitation that requires two photons is called two-photon absorption (TPA). The multi-photon process requires a high density of photons to achieve a significant probability of multiple photons interacting simultaneously. As described in [5], the optical absorption in silicon is given as a function of depth z along the beam propagation direction:

$$\frac{\mathrm{d}I}{\mathrm{d}z} = -\alpha I - \sigma_{\mathrm{ex}} N I - \beta_2 I^2 + O\left(I^3\right), \tag{2.1}$$

where I is the intensity, α and β_2 are the SPA and TPA absorption coefficients, respectively, σ_{ex} is the cross section for free-carrier absorption and N the number of free charge carriers. From eq. 2.1 it can be seen that the number of charge carriers created using SPA scales linearly with the intensity and quadratically for TPA.

For a focused Gaussian beam, the intensity required for TPA to occur is only achieved close to the focal point (or by a very large beam power), thereby effectively constraining the TPA in space. The focused beam creates an ellipsoidal volume (voxel — see figure 1) in which the liberation of charge carriers occurs. It is straightforward to scan the detector volume by moving it with respect to this voxel, making it possible to study the sensors in all three dimensions. The axis system that is used is indicated in figure 2.
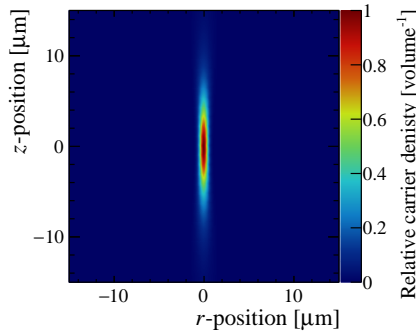
Figure 1. The relative charge carrier density that is liberated along the beam path. This profile shows the intensity squared from eq. 2.2.

The system presented in this paper consists of a fiber based 1550 nm pulsed laser system (LFC1500X) from Fyla.[1] For all measurements it is operated at a repetition rate of 15.92 kHz, and

[1]FYLA, Ronda Guglielmo Marconi 14, Parque Tecnológico 46980 Paterna, Valencia, Spain.
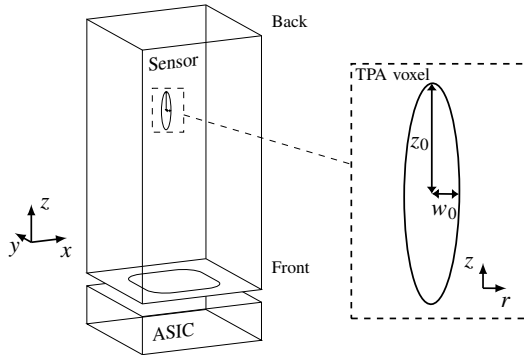
Figure 2. Schematic overview of the sensor in which the TPA voxel is positioned. The definition of the coordinate system is indicated for both the sensor and the TPA voxel. The Timepix3 ASIC is also indicated.
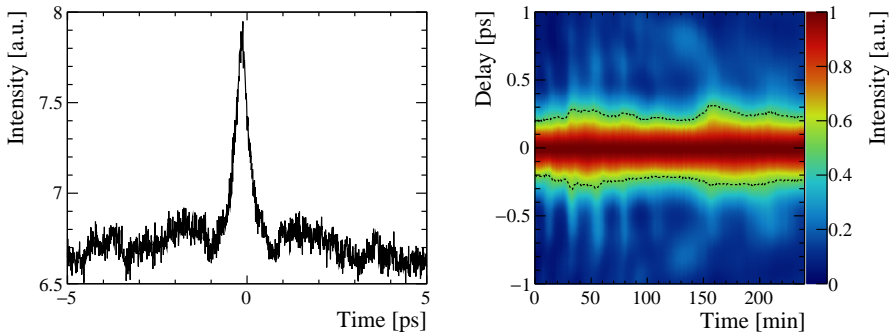
Figure 3. Left: a typical auto-correlation trace for a pulse length of 380 fs. Right: the pulse shape monitored using an autocorrelator over a time span of four hours. The dashed line indicates the FWHM of the pulses.

a variable Neutral Density (ND) filter is used to tune the pulse energy. The Full Width at Half Maximum (FWHM) pulse width is measured with an APE Carpe autocorrelator [6] and varies between 380 fs and 540 fs throughout the measurements. A typical auto-correlation trace can be seen in figure 3 (left). The FWHM can be tuned to larger values by changing the group delay dispersion (GDD) using a D-Scan 1.5 system.[2] A schematic overview of the system is shown in figure 4. The laser system is controlled via a dedicated computer that can communicate with the computer (DAQ) that acquires the data of the Timepix3 ASIC.

The pulse width is observed to vary over time for a constant dispersion compensation. To characterise these fluctuations, the pulse width is monitored over four hours, showing a peak-to-peak variation of 150 fs. This data can be seen in figure 3 (right). Along with a small (< 1%) variation of the output power of the laser, this results in an undesired variation of the number of charge carriers liberated in the semiconductor per laser pulse over time. To correct for this variation offline, a

---

[2]Sphere Ultrafast Photonics, Rua do Campo Alegre, n.º 1021, Edifício FC6 4169-007 Porto, Portugal.
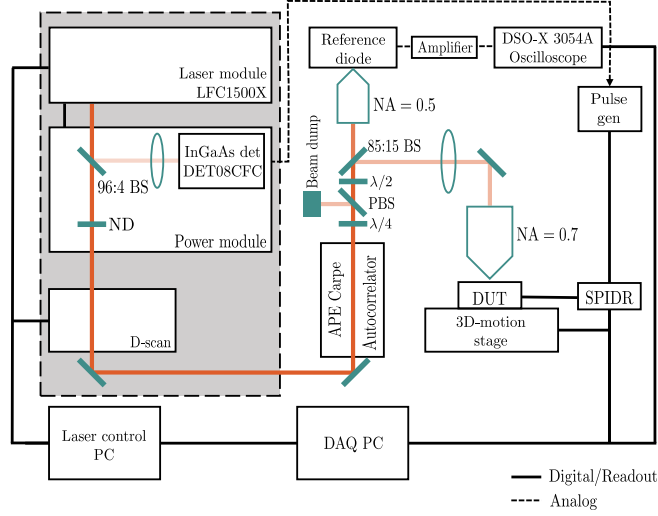
Figure 4. Schematic overview of the TPA setup. The grey area indicates the section of the setup manufactured by Fyla. The orange line indicates the path of the laser beam, the dashed blue lines indicate all analogue connections, and the black lines all digital connections. The green components represent the optical components.

fraction of the beam is diverted to a silicon diode. The same material, silicon, is chosen to have a direct correspondence to TPA effects since it is inherently nonlinear. At the present time the calibration fraction is about 85% of the total laser power as it also serves to decrease the incident power onto the Detectors Under Test (DUT). The output of this reference diode is first amplified with a Cividec C2-TCT amplifier [7]. This amplified signal is monitored using an oscilloscope (DSO-X 3054A) which integrates the signal of each pulse. A quarter-wave and half-wave plate combined with a polarising beam splitter are placed after the autocorrelator to ensure constant polarisation at both the reference diode and the DUT. The half-wave plate is used to rotate the polarisation such that the maximum transmission at the air-silicon interface is achieved. The resulting signal fluctuation after this correction is 1.6% (standard deviation) of the signal; the data are shown in figure 5.

To minimise the voxel size, the laser beam is focused using a microscope objective. As described in [8], the temporal and spatial evolution of a Gaussian beam with a temporal width τ that is focused to a beam waist w_0 is given by [8]:

$$I(r, z, t) = \frac{E_p}{\tau} \frac{4\sqrt{\ln 2}}{\pi^{3/2} w^2(z)} \exp\left(-\frac{2r^2}{w^2(z)}\right) \exp\left(-4\ln 2 \frac{t^2}{\tau^2}\right), \tag{2.2}$$

where E_p is the pulse energy. The two-sigma beam radius $w(z)$ of the electric field along the beam propagation direction is given by

$$w(z) = w_0 \sqrt{1 + \left(\frac{\lambda z}{\pi w_0^2 n}\right)^2} = w_0 \sqrt{1 + \left(\frac{z}{z_0}\right)^2}, \tag{2.3}$$
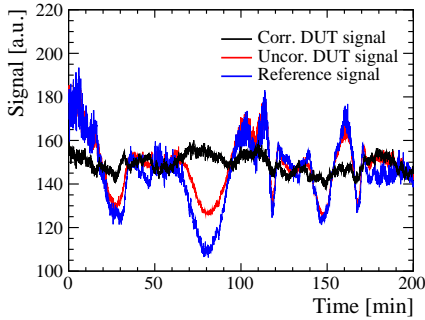
Figure 5. The uncorrected TPA signal of the DUT (red), the scaled TPA signal measured at the reference diode (blue) and the corrected TPA signal of the DUT (black). After correction a standard deviation of 1.6% is achieved.
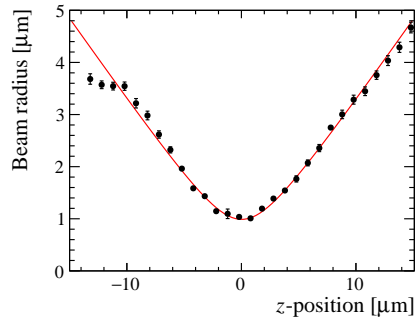
Figure 6. The beam radius of the laser pulses as a function of height around the focal point. The black dots indicate the measured data and the red line indicates the fit. The first three data points are excluded from the fit.

where n is the refractive index of the material, λ the wavelength, and z_0 the Rayleigh length ($z_0 = \pi w_0^2 n / \lambda$). Since the Rayleigh length is related to the beam waist size, the dimensions of the voxel are proportional to w_0. The voxel dimensions and axis system are shown in figure 2. Since a small voxel is desired, an objective with a high magnification needs to be used. The objective chosen is a 100x Mitutoyo[3] Plan Apo NIR HR Infinity Corrected (NA = 0.7) for tests of the thin sensors and a 100x Mitutoyo Plan Apo NIR Infinity Corrected (NA = 0.5) for tests of the thicker sensors. The lower NA is required for thicker sensors since the increased spherical aberration for the higher NA objective causes a TPA intensity loss that increases linearly with depth [9]. The beam radius of the 1550 nm beam around the focal point has been measured using a knife-edge method, and the results are shown in figure 6. Fitting eq. 2.3 to the data yields a value of 0.975(11) µm for the minimum beam radius and a value of 3.01(5) µm for the Rayleigh length in air. For this fit the first three data points (from -14 to -10 µm) are excluded. These points deviate from the expected curve, however an explanation for this behaviour is not yet found.

The voxel becomes effectively longer in silicon due to the change in refractive index at the air-silicon interface, as described in [5]. Therefore, the effective position z' within the silicon is given by

$$z' = z \sqrt{\frac{z_0 \pi n^3}{z_0 \pi n - \lambda n^2 + \lambda}}. \tag{2.4}$$

This effect results in a larger Rayleigh length in silicon, and yields $z_{0,\text{Si}} = 11.9$ µm. The width of the voxel, is however not affected by the refractive index, and thus remains the same as in air. This correction is applied to determine the actual position of the focal point within the silicon detector during the measurements.

---

[3]Mitutoyo Corporation, 20-1, Sakado 1-Chome, Takatsu-ku, Kawasaki-shi, Kanagawa 213-8533, Japan.

2.1 Trigger system

A trigger signal is created in the laser power module using a 5 GHz InGaAs detector (Thorlabs DET08CFC [10]) with a rise time of 70 ps. A beam splitter is used to redirect 4% of the beam to this detector. The time resolution of this detector has been determined by measuring the remaining 96% of the beam with a Thorlabs PDA05CF2 [11], which has a rise time of 2.3 ns. The time difference between the rising edge of the signals (using a threshold of 50% of the peak height) of the two detectors was determined using an oscilloscope. The standard deviation of the time difference is taken as the resolution of the two detectors combined. With a statistical sample of 150k measurements, the combined resolution is 43 ps. Lower time resolutions are measured with shorter intervals due to intensity fluctuations described earlier in this section. Assuming that both detectors contribute equally, the trigger resolution is $43/\sqrt{2} = 30.4$ ps. However, based on bandwidth considerations it is expected that the trigger time resolution is much better than that of the reference detector. Nevertheless, a time resolution of 30.4 ps is sufficiently small not to influence the measurements presented in this paper. In order to use the signal of the InGaAs detector, the level of the signal needs to be adapted to match that of the input of the TDC on the readout board (SPIDR - see section 3.1). A pulse generator was used to adapt the level of the trigger signal.

3 Sensor and Timepix3 ASIC

The studies presented in this paper are obtained with hybrid pixel detectors, with sensors bump-bonded to Timepix3 ASICs [4], read out by a SPIDR [12] readout system. In this section, the Timepix3 ASIC along with SPIDR is briefly discussed, after which the sensors characterised in this study are described.

3.1 Timepix3 ASIC and SPIDR readout system

The Timepix3 ASIC is developed by the Medipix3 [13] collaboration. It has a matrix of $55 \times 55\,\mu m^2$ structures each with a charge sensitive amplifier as a first stage and a discriminating circuit capable of measuring both the Time-of-Arrival (ToA) and the Time-over-Threshold (ToT) simultaneously for every signal. The time-to-digital converter (TDC) digitises the ToA using a 640 MHz clock, giving a bin size of 1.56 ns (corresponding to a time resolution of 451 ps). The time resolution of the analogue front-end of Timepix3 has been determined to be approximately 240 ps [14] for a typical signal amplitude and planar sensor. Variations in the clock distribution and in the manufacturing process contribute to a larger time resolution obtained for all pixels on average [15], even excluding the contributions arising from the sensors. For all measurements in this paper, the Timepix3 is operated at a threshold of 1000 e$^-$, corresponding to approximately 5% of the typical signal amplitude of a Minimum Ionising particle (MIP). The ToT information can be converted into units of electrons via a charge calibration process, as described in [16].

Lower charge hits suffer from a lower induced current and thus cross the threshold level with a larger delay. The resulting delay (also known as timewalk) can be corrected for using the ToT information of each hit. The timewalk curve is parameterised as

$$t(q) = \frac{A}{q - q_0} + C,$$ (3.1)

151

where t is the timewalk, q the charge, q_0 the charge corresponding to the onset of the asymptote, A the slope, and C the offset. A typical timewalk curve in shown in figure 7 (left). In this figure the black points indicate the measured data, and the line indicates the fit with eq. 3.1. To parametrise the timewalk curve, the TPA voxel is positioned at the centre of the sensor implant, and the intensity of the laser is varied by rotating the variable ND filter. Using this method, the Time-to-Threshold (TtT) can be determined for a range of ToT (charge) values. The measured curve obtained from a fit to this data is used to correct for timewalk in the offline analysis. This parameterisation has been performed for every pixel individually. An example of the corrected TtT as a function of ToT is shown in figure 7 (right). A systematic under- and over-correction can be observed in the corrected TtT curve for low ToT values.
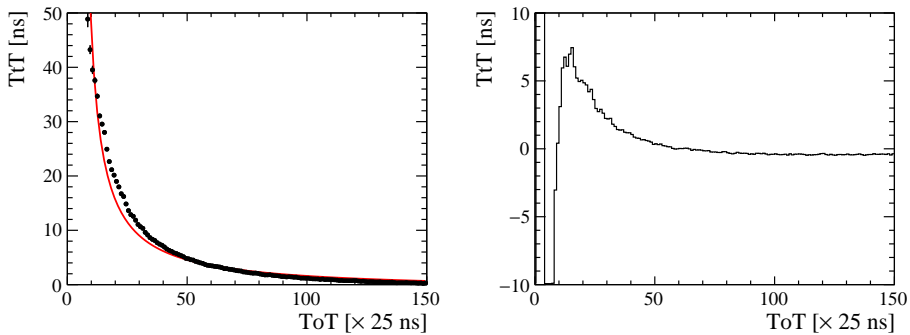
Figure 7. Left: a typical timewalk curve indicated in black, and the resulting parametrised correction is shown in red. Right: the TtT after applying the parametrised correction, for low ToT a systematic under- and over-correction can be observed.

The Timepix3 is read out using a SPIDR readout system [12]. The SPIDR also has an on-board TDC with 260 ps bins based on a 320 MHz clock generated using the 40 MHz clock of the Timepix3. This TDC is used to register the trigger. In practise a non-uniformity on the TDC bin size is observed and the overall standard deviation of time measurements is 77 ps, instead of $260/\sqrt{12} = 75$ ps for the ideal case.

In combination with the SPIDR TDC, the Timepix3 has a time resolution of $451 \oplus 240 \oplus 77 = 516$ ps (adding the separate contributions listed above in quadrature). This time resolution is insufficient for precise temporal measurements of the silicon sensor, but it may be used for the investigation of rough temporal characteristics of these sensors.

3.2 Silicon sensors

Two planar silicon pixel sensors are characterised for this paper. A 200 μm electron collecting n-on-p sensor,[4] used in the prototyping phase of the LHCb VELO Upgrade R&D, and a 300 μm hole-collecting p-on-n sensor.[5] These sensors have already been studied in detail in the past and therefore are ideal to test the TPA setup. From here on the side of the sensors with the segmented

---

[4]Hamamatsu Photonics K. K., 325-6, Sunayama-cho, Naka-ku, Hamamatsu City, Shizuoka, 430-8587, Japan.
[5]Canberra Semiconductors N.V., Lammerdries 25, 2259 Olen, Belgium.

electrodes (to which the ASIC is connected) will be referred to as the front side. The other side with the common contact is referred to as the back side (see figure 2).

The time resolution of these assemblies (sensor and ASIC combined) can be approximated by a quadratic sum of three terms [17]:

$$\sigma_t^2 = \left(\left[\frac{t_r V_{\text{th}}}{S}\right]_{\text{RMS}}\right)^2 + \left(\frac{t_r}{S/N}\right)^2 + \left(\frac{\text{TDC}_{\text{bin}}}{\sqrt{12}}\right)^2, \tag{3.2}$$

where the terms make explicit the independent contributions from timewalk, jitter and TDC binning, respectively. Here t_r is the rise time of the signal at the output of the amplifier, V_{th} is the threshold of the discriminator, S is the amplitude of the signal, N is the noise of the front-end, and TDC_{bin} is the TDC bin width.

Since both an electron and a hole collecting device are studied, the charge collection times of the two are expected to be different. The Shockley-Ramo mechanism [18] contributes to the effective time resolution of the sensors since the drift velocity of holes in silicon is lower than that of electrons. The weighting field also slightly differs between the two sensors due to the difference in thickness and the small differences in the geometry of the pixel implants. Since these two effects will result in a difference in the induced current on the implants for the two sensors, the rise time (of the integrated current) of the electron collecting device is expected to be faster than that of the hole collecting device. These contributions, however, are small compared to ASIC contributions that have been discussed earlier. Therefore, the difference in time resolution of the two sensors that can be observed will be dominated by ASIC contributions and not by the difference in sensor type and thickness.

4 Measurements and results

4.1 Charge collection studies

To study the charge collection properties of the sensors, the laser intensity is kept constant at a signal amplitude corresponding to a MIP, while the position of the TPA voxel is positioned at different places in the sensors. A single pixel of the n-on-p sensor has been scanned at different depths in its bulk. These pixel scans are shown in figure 8 for three different depths: back side (upper left plot), middle (upper right), and at the front side (lower). These scans extend 27.5 μm into the neighbouring pixels (these pixels are not read out). Small fluctuations of the TPA intensity can be observed as vertical stripes in these scans, because the data were collected via a vertical raster scan. Therefore the time difference between two vertical lines is larger than between two neighbouring points at the same x-position (one single vertical line typically takes 10 minutes to measure, while a single point typically takes a few seconds). In all plots the boundary of the pixel is indicated by the dashed white lines.

The scans of the back and middle of the sensor show uniform charge collection. The main difference between these two scans is the increased width of the transition region at the edge of the pixel. Charge generated at the back side of the sensor travels longer before being collected, and therefore also has larger lateral diffusion. The front-side measurement shows a structure due to the front-side metallisation. Owing to the strong reflection at the silicon-metal interface at the front of the sensor, the intensity of the laser in the silicon close to the interface is larger than without this reflection. This localised increased laser intensity results in an increase of TPA and thus in a larger deposited
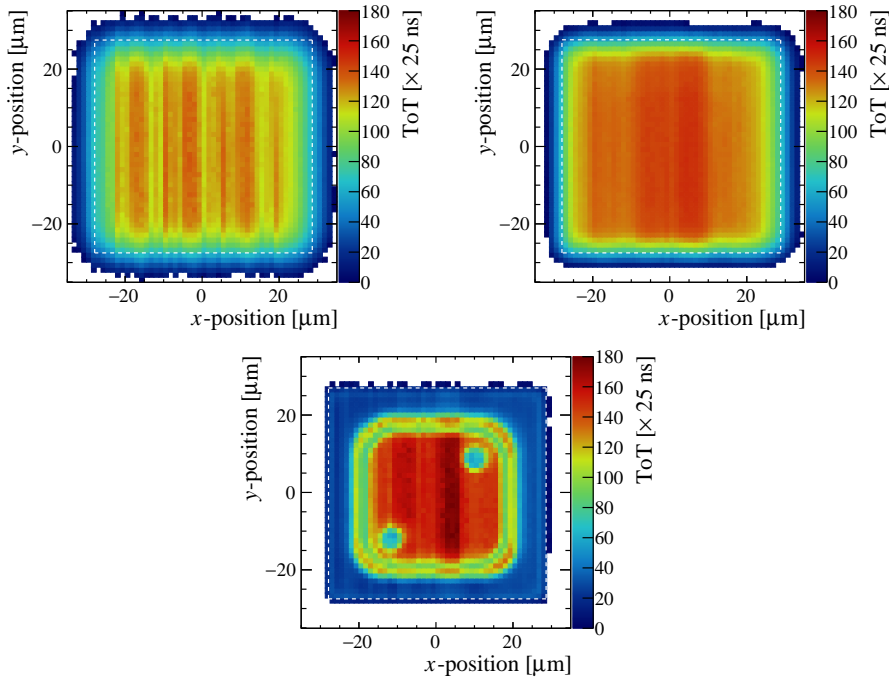
Figure 8. Time-over-Threshold (ToT) scans of a pixel in the n-on-p sensor, the dashed line indicates the area of the pixel. Top left: back side of sensor. Top right: middle of the sensor. Bottom: front side of the sensor.

charge near the silicon-metal interface. This structure is a direct observation of the front-side metallisation as well as the angle of the metallisation with respect to the normal of the sensor. The position of two vias present in the pixel is observed, visible as two circles with lower ToT. A small increase in the ToT is observed at the implant border, indicating a feature on the front side which is unknown to us. It should be noted that the intensity correction implemented, is not able to fully correct the fluctuations near the metallisation since the reflected beam no longer is linearly proportional to the TPA signal in the reference diode. Since the thickness of the silicon part of the sensor is slightly larger at the pixel implant, and the alignment of the z-axis is performed at the pixel implant as well, the beam waist is outside of the bulk in the corners of the pixel. Therefore, relatively little charge is liberated at these positions compared to the implant. The same study was also performed for the p-on-n sensor. Besides a different front side metallisation, the results are similar and therefore not included here.

The pixel width along the x-coordinate is determined with pixel scans to be 55 μm without any additional calibration of the stage, however the width along y is measured to be approximately 2.4 μm smaller. After a calibration of the y-stage, this discrepancy has disappeared and the pixel widths along y are also 55 μm.

Because the longitudinal TPA voxel length is larger than its transversal width, the spatial resolution that can be achieved perpendicular to the normal of the bulk is better. Nonetheless the

resolution of the voxel is good enough to also resolve structures along the longitudinal direction. A scan along the longitudinal direction is shown in figure 9 (left: 200 µm n-on-p, right: 300 µm p-on-n). The 0.7 NA objective was used for the 200 µm n-on-p sensor and the 0.5 NA objective was used for the 300 µm p-on-n sensor. This figure shows the ToT as a function of position along the beam direction (z-axis corrected for the length scaling in silicon), for different bias voltages. The different height of the ToT plateaus is due to a different starting phase of the TPA fluctuations, resulting in a different scale factor between the two scans. In figure 9 the 0 µm position corresponds to the back of the sensor and the 200 µm position (or 315 µm) corresponds to the front of the sensor. The number of charge carriers liberated in the sensor for different z-positions, assuming negligible reflection at the silicon-air interface, is given by eq. 4.1 [5], where d is the thickness of the sensor.

$$N_{\text{tpa}}(z) = \frac{E_p^2 n \beta_2 \sqrt{\ln 4}}{4 c \hbar \pi^{3/2} \tau} \left[\arctan\left(\frac{d-z}{z_0}\right) + \arctan\left(\frac{z}{z_0}\right) \right]. \tag{4.1}$$

Since for hybrid sensors the reflection at the front of the sensor is not negligible due to the presence of the metallisation, only the left side of these scans (below 185 µm) are fitted using eq. 4.1 to retrieve the effective position of the back side, while the position of the front side is assumed to be at the centre of the peak (caused by reflection) and is approximated by a Gaussian distribution. From this, the effective thickness of the n-on-p (p-on-n) sensor is determined to be 201(1) µm (315(1) µm), where the quoted uncertainties are conservative estimates, expected to be dominated by contributions from the motion stages. These values are consistent with the thicknesses stated by the manufacturers.

The z-scans at different bias voltages also show the depletion depth growing with higher bias voltages. Around 100 V is needed to collect all charge from the back side of the 200 µm n-on-p sensor, which is not consistent with the depletion voltage of 120 V determined using charge collection efficiency [19] and grazing angle [20] data. For the 300 µm p-on-n sensor, a bias voltage of around 75 V is needed to completely deplete the sensor. The lower depletion voltage found using the TPA setup is due to the collection of charge from the non-depleted region by means of diffusion, which in the charge collection and grazing angle analysis was not (or only partially) possible because of charge being liberated along the entire thickness of the sensor (line-like) instead of a point-like volume. In those analyses the random time interval between hits in some cases is smaller than the time it takes a single hit to cross the threshold. Therefore it is not possible to precisely assign a hit with a large drift time to a trigger.

4.2 Time resolution studies

The fast nature of the optical pulses of the TPA setup makes it possible to study the temporal characteristics of the sensors as a function of the 3D position within the sensor. In this section the time resolution as well as the Time-to-Threshold (TtT) of the two sensors under study are discussed.

Each hit is assigned to a corresponding trigger from the SPIDR TDC within a time window of 1 µs. Since the laser pulses are spaced by 126 µs, this windows leaves sufficient time not to associate triggers from different pulses. This selection ensures that the hits are generated by laser pulses, and not by noise or background radiation. The TtT is determined after this selection, and is defined as the time difference between the trigger and the hit. The time resolution (σ_t) is defined as the RMS of this TtT distribution. The RMS is determined for each position by fitting the TtT distribution with a Gaussian function.
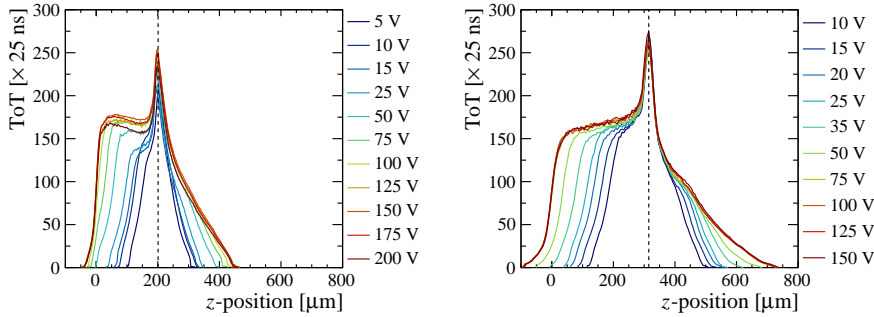
7

Figure 9. Time-over-Threshold (ToT) as a function of the voxel z-position for different bias voltages for the 200 μm n-on-p sensor (left) and the 300 μm p-on-n sensor (right). The ToT is proportional to the amount of charge collected. If the bias voltage is below the depletion voltage the effective thickness of the sensor decreases. The vertical dashed line indicates the physical thickness of the sensor.

The standard deviation and the average of the TtT distributions for the area scan in the middle of the bulk of the pixel are presented in figure 10 (same data set as figure 8). The white dashed line in these figures indicates the outline of the pixel. The TtT (left) shows a uniform behaviour over the complete pixel. Slight variations in the TtT can be observed near the centre of the pixel. These, however, are due to intensity fluctuations in combination with the residual timewalk because of the imperfect timewalk correction. For low ToT values the TtT is consistently below (or above) the parameterisation, which causes these ToT values to be systematically under (over) corrected. Therefore a variation in ToT results in a TtT spread, which can be observed as vertical bands in figure 10 (left). However, the differences at the corners and the pixel edges are sensor effects. Towards the corner of the pixel it can be seen that the TtT becomes longer. This is also observed when the TPA voxel is outside of the pixel under test. This is due to an increased travel time of the charge carriers to reach the implant, leading to an increased lateral diffusion, and subsequently to more charge sharing. As mentioned before, for low ToT hits the timewalk correction (section 3.1) performance is less optimal which results in the systematic under- or over-correction of the TtT. An improved timewalk calibration is currently planned, and requires additional work on the Timepix3 data which is not the main scope of this paper.

The time resolution, shown in figure 10 (right), shows similar behaviour as the TtT. The resolution is uniform over almost the entire pixel, with the exception of the four corners, where the charge is shared among four pixels. This is similar to the uniform behaviour that is observed using a charged particle beam [20], although the time resolution found in this paper is significantly better than that observed with the beam data. The difference is attributed to two main effects. Firstly, the time resolution measured using lasers is expected to be better due to smaller charge fluctuations compared to the energy loss straggling of a charged particle. Secondly, the measurements presented in [20] combines data of all pixels together and this convolutes the matrix fluctuations and clock distribution effects. This degrades the time resolution compared to that of a single pixel, see [15].

The TPA voxel can also be moved throughout the depth (z-direction) of the sensor by moving the z-stage. During these scans, the TPA voxel is positioned in the centre of the pixel. Figure 11
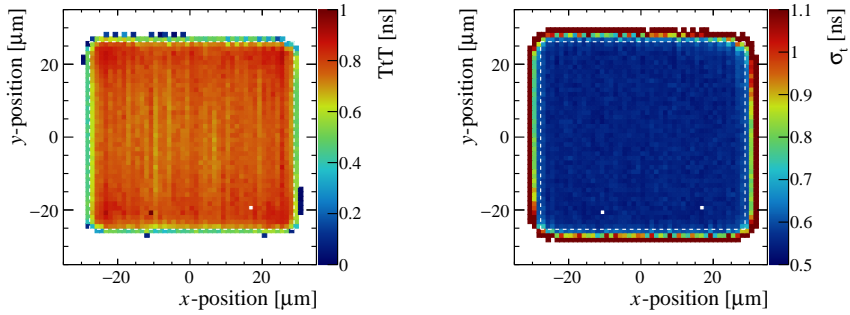
Figure 10. Time-to-Threshold, (TtT), (left) and time resolution (right) for different positions in and around a single pixel in the n-on-p sensor. The dashed white lines indicate the outline of the pixel. The one (two) white dot(s) that are visible in the left (right) plot indicate positions where the fit did not converge.

shows the TtT and the time resolution as a function of the depth in the bulk for the 200 μm n-on-p sensor (top), and the 300 μm p-on-n sensor (bottom). The z-position for these scans is corrected for the difference in refractive index as discussed in section 2. Below, the 200 μm n-on-p sensor will mainly be discussed since most observations are consistent between the two sensors. As mentioned in section 4.1, the 200 μm n-on-p sensor is actually measured to be 201 μm thick. However, in figure 11 the depth is scanned from approximately the back of the sensor, to about 250 μm beyond the front of the sensor (0 μm to 450 μm in the plot). The signal observed from 200 μm to 450 μm is due to internal reflection of the laser light at the front and back interfaces.

Figure 11 (left) shows the TtT as a function of the voxel depth in the bulk, where different colored curves denote different bias voltages. The figure contains error bars indicating the statistical uncertainty of the fit. However, for most data points the error bars are too small to distinguish in the figure. The TtT is, as expected, larger for positions far away from the implant, and low for positions close to the implant. The bias voltage also influences the TtT significantly, since the magnitude of the induced current and hence the slope of the integrated current, is lower for low drift velocities due to the lower electric field at low bias voltages. The small increase in time resolution present when the TPA voxel is first reflected (around 215 μm) is not yet understood. Also a small decrease in the TtT around 0 μm and 450 μm is observed which is due to a systematic under- or over-correction of the timewalk as discussed in section 3.1.

The time resolution throughout the depth of the sensor for different bias voltages is shown on the right side of figure 11. For the highest bias voltage (200 V), the resolution remains constant at about 600 ps (560 ps for the 300 μm sensor at 150 V) for almost all positions probed within the sensor. The resolution degrades when the voxel is placed at the back side of the sensor (low z-values) caused by a loss in signal magnitude due to a partial depletion for lower bias voltages, and thus of the TPA voxel is outside of the depleted region. The resolution is also observed to be approximately constant for the different bias voltages, with degradations mainly caused by the loss in signal magnitude. This is observed when the signal decreases after internal reflection between 200 μm and 450 μm. The main difference between the time resolution of the two assemblies is caused by pixel-to-pixel variations giving the ASIC contribution of the two different pixels slightly different time resolutions, and not
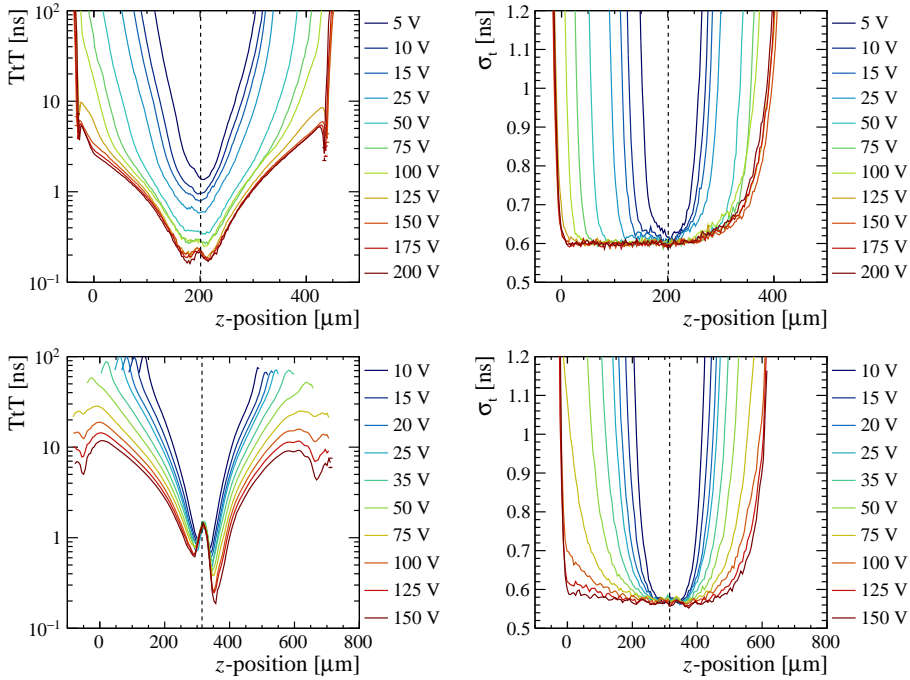
7

157

Figure 11. Time-to-Threshold, (TtT), (left) and time resolution (right) as a function of depth within the sensors at different bias voltages. The top (bottom) row shows the results of the 200 μm n-on-p sensor (300 μm p-on-n sensor). All plots have error bars indicating the statistical uncertainties from the fit, however most are too small to see.

by the resolution of the sensors itself. Since the resolution of the sensors is significantly smaller than of the ASIC, a small difference in the sensor contributions is not expected to be observed.

As discussed in section 3.2, the measured time resolution is the effective results of the Timepix3 TDC, time resolution of the analogue front-end of Timepix3, SPIDR TDC, and the time resolution of the silicon sensor. These components, excluding the sensor resolution, combine to a time resolution of 516 ps. Therefore, from the overall resolution of 600 ps (560 ps), about 306 ps (218 ps) is attributed to the sensor for the n-on-p (p-on-n) type. The resolution found for these two sensors is still significantly higher compared to resolutions found for similar planar sensors. For a planar 200 μm sensor a resolution of 127.1 ps (including ASIC contributions) is reported previously [21]. This may indicate that the time resolution of the characterised sensors is better, and that currently we are limited by the pixel-to-pixel variations in the ASIC which dominates the fluctuations on the time resolution.

5 Conclusion and outlook

TPA techniques provide a method that enables the characterisation of the complete detector volume, which is in contrast to using SPA techniques. The strong optical focusing needed for TPA also leads

to small voxel sizes where charge is liberated, leading to a good spatial resolution with which the detectors can be studied.

An initial investigation of the capabilities of the newly commissioned TPA setup at Nikhef is presented. Characterisation studies of this system show an output power variation below 1%. However, the TPA signal presents an instability measured to be about 1.6%, which is found to be linked to a variation of the temporal width of the pulse over time. This instability is corrected offline using a TPA reference signal generated on a silicon diode with 85% of the beam power. The system is equipped with a precise timing trigger which is shown to have a resolution better than 30.4 ps. This resolution is dominated by its reference detector, and therefore is, most likely, significantly better.

Two sensors connected to Timepix3 ASICs have been tested with the TPA system. The charge collection and temporal behaviour were presented. The charge collection is found to be uniform over the pixel, and scans along the beam direction indicate a thickness of the sensor that is in agreement with the thickness stated by the manufacturer. Light is reflected by the metallisation at the front side of the sensor, yielding a small region with increased intensity and thus a larger charge collection. This effect proved useful in imaging the shape and height differences of the front side metallisation.

The combined time resolution of the sensor and the ASIC is found to be dominated by the ASIC contributions, and is measured to be 600 ps and 560 ps for the 200 µm n-on-p and 300 µm p-on-n sensors, respectively. An overall degradation of the time resolution and the TtT is observed at lower bias voltages due to lower charge collection and lower drift velocities. Studies with sensors and ASICs with better timing resolution are expected to be performed soon and will utilise the full potential of this TPA system in space and time.

Acknowledgments

References

[1] V. Eremin, N. Strokan, E. Verbitskaya and Z. Li, *Development of transient current and charge techniques for the measurement of effective net concentration of ionized charges (N(eff in the space charge region of p-n junction detectors*, *Nucl. Instrum. Meth. A* **372** (1996) 388.

[2] M.F. García, R.J. Echeverría, M. Moll, R.M. Santos, R. Palomo Pinto, I. Vila et al., *High resolution* 3*D characterization of silicon detectors using a Two Photon Absorption Transient Current Technique*, *Nucl. Instrum. Meth. A* **958** (2020) 162865.

[3] S.O. Ugobono, M. Centis Vignali, M. Fernandez Garcia, C. Gallrapp, S. Hidalgo Villena, I. Mateu et al., *Multiplication onset and electric field properties of proton irradiated LGADs*, *PoS* **Vertex2017** (2018) 041.

[4] T. Poikela et al., *Timepix3: a 65k channel hybrid pixel readout chip with simultaneous ToA/ToT and sparse readout*, 2014 *JINST* **9** C05013.

7

[5] M. Wiehe, M. Fernandez Garcia, M. Moll, R. Montero, F.R. Palomo, I. Vila et al., *Development of a Tabletop Setup for the Transient Current Technique Using Two-Photon Absorption in Silicon Particle Detectors*, *IEEE Trans. Nucl. Sci.* **68** (2020) 220.

[6] Carpe — Microscopy Autocorrelator to Measure Pulse Duration at Sample Location, https://www.ape-berlin.de/en/autocorrelator/carpe/.

[7] C2-TCT, TCT amplifier, 10 kHz–2 GHz, 40 dB, https://cividec.at/electronics-C2-TCT.html.

[8] O. Svelto and D.C. Hanna, *Principles of lasers*, Springer (1998).

[9] M. Gu, *Advanced optical imaging theory*, Springer Science & Business Media, 2000.

[10] Thorlabs DET08CFC — 5 GHz InGaAs FC/PC-Coupled Photodetector, 800–1700 nm, https://www.thorlabs.com/drawings/a99628e220ead7eb-7E413078-B193-0008-889A9AA4DDF58878/DET08CFC-Manual.pdf.

[11] Thorlabs PDA05CF2 — InGaAs Fixed Gain Amplified Detector, 800–1700 nm, 150 MHz BW, 0.2 mm^2, https://www.thorlabs.com/drawings/a99628e220ead7eb-7E413078-B193-0008-889A9AA4DDF58878/PDA05CF2-Manual.pdf.

[12] J. Visser, M.v. Beuzekom, H. Boterenbrood, B.v.d. Heijden, J.I. Muñoz, S. Kulis et al., *SPIDR: a read-out system for Medipix3 & Timepix3*, 2015 *JINST* **10** C12028.

[13] R. Ballabriga, M. Campbell and X. Llopart, *Asic developments for radiation imaging applications: The medipix and timepix family*, *Nucl. Instrum. Meth. A* **878** (2018) 10.

[14] L. Hendrikx, *Characterisation of the analogue front-end of the Timepix3*, MSc. thesis, University of Twente (2021).

[15] K. Heijhoff et al., *Timing performance of the LHCb VELO Timepix3 Telescope*, 2020 *JINST* **15** P09035 [arXiv:2008.04801].

[16] K. Akiba et al., *LHCb VELO Timepix3 Telescope*, 2019 *JINST* **14** P05026 [arXiv:1902.09755].

[17] N. Cartiglia et al., *Performance of Ultra-Fast Silicon Detectors*, 2014 *JINST* **9** C02001 [arXiv:1312.1080].

[18] W. Shockley, *Currents to conductors induced by a moving point charge*, *J. Appl. Phys.* **9** (1938) 635.

[19] R. Geertsema et al., *Charge collection properties of prototype sensors for the LHCb VELO upgrade*, 2021 *JINST* **16** P02029 [arXiv:2010.10147].

[20] E. Dall'Occo et al., *Temporal characterisation of silicon sensors on Timepix3 ASICs*, 2021 *JINST* **16** P07035 [arXiv:2102.06088].

[21] G. Aglieri Rinella et al., *The NA62 GigaTracKer: a low mass high intensity beam 4D tracker with 65 ps time resolution on tracks*, 2019 *JINST* **14** P07010 [arXiv:1904.12837].

7

7.2 Results with Timepix4

The time resolution achieved with Timepix3 is dominated by its TDC resolution (451 ps), as is discussed in section 7.1. This is not sufficient to measure the temporal behaviour of fast-timing sensors. Therefore, to measure the intrinsic contribution of silicon sensors it is necessary to study them assembled to an ASIC with a better resolution, both in terms of the analogue front-end and the TDC. Alternatively, one can use a laser to study sensors through the transient current technique (TCT), in which the signal produced at the pixel implant is amplified by a dedicated high-power amplifier and digitised. The time resolution of Timepix4 is sufficiently good to study planar sensors directly. Hence, a Timepix4 ASIC in combination with the TPA system has been used to study the performance of planar sensors, complementary to the Timepix4 telescope discussed in section 5.2.

This section presents the first results of temporal characterisation studies of a silicon sensor assembly with a Timepix4v2 ASIC obtained with the TPA system. The Timepix4 ASIC is bump-bonded to a planar 100 μm n-on-p sensor. A single pixel of the assembly is tested and characterised, where a digital pixel is used to timestamp the trigger provided by the TPA system. The analogue trigger signal has a resolution of at least 30.4 ps, and the time measurement of the digital pixel is not corrected for fluctuations in the fToA and ufToA bin sizes.

7.2.1 Time bin and timewalk corrections

To obtain the optimal temporal performance of the Timepix4 [81], we correct the data for non-uniform behaviour of the finest timing bins (fToA_rise and the ufToA_stop) and for timewalk effects. To perform the time bin corrections we first determine both the fToA_rise and the ufToA_stop bin sizes for each fToA bin separately. The fToA_rise distribution is shown in fig. 7.2 (left) and the ufToA_stop distribution for three different fToA_rise bins is shown in fig. 7.2 (right). The ufToA_start size is not characterised, since this value is always zero (cluster size is one). The first fToA bin is only half the size (only four ufToA bins) by design, and the last fToA bin (17$^{\text{th}}$ bin) can be partially occupied due to fluctuations in the VCO frequency. By applying these two corrections, a contribution of 64.7 ps to the overall resolution is subtracted.

After the time bin corrections are applied to the data, a timewalk calibration is applied. Timewalk is characterised as a function of Time-over-Threshold (ToT - which is an analogue for the charge) by varying the laser intensity while the TPA voxel is positioned close to the implant. The resulting timewalk curve is shown in fig. 7.3, where the black dots/line indicate the average delay per ToT value, which is used as the correction. This is used as the correction and is applied on a per-event basis. Due to a problem in the ASIC, the coarse ToA is sometimes not incremented properly. This problem was found to be (partially) fixed by increasing the supply voltage from 1.2 V to 1.3 V. However, during these preliminary measurements

7
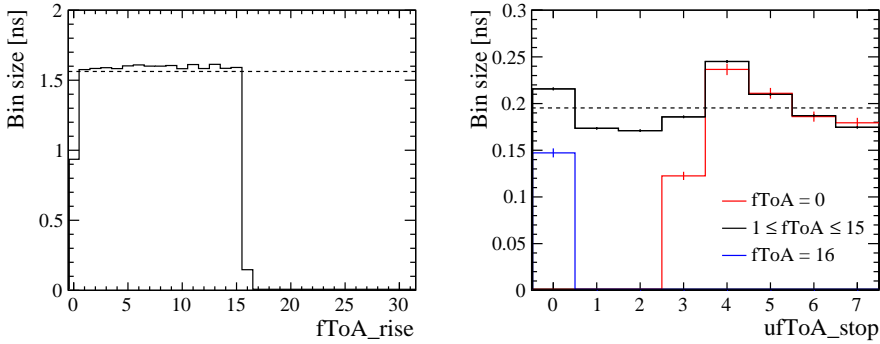
Figure 7.2: The measured sizes of the different fToA_rise (left) and ufToA_stop bins in the pixel studied with the TPA system. The ufToA_stop distribution is shown for the first fToA_rise bin (red), the last fToA_rise bin (blue) and the fToA_rise bins in between (black). The dashed lines indicate the theoretical bin sizes, 1.56 ns for fToA_rise and 195 ps for ufToA_stop.

this issue was partially mitigated but unfortunately not completely solved by the increased supply voltage. Therefore, a second band is visible in the timewalk curve that is offset by 25 ns, corresponding to a ToA counter that was not incremented. This results in the correction being skewed below a ToT of around 20 to lower values due to the overlapping bands. To partially account for this, the timewalk curve above ToT of 20 is parametrised according to

$$\mathrm{TtT}\,(\mathrm{ToT}) = \frac{A}{\mathrm{ToT} - \mathrm{ToT}_0} + B, \tag{7.1}$$

where TtT is the Time-to-Threshold, and A, B, ToT_0 are variables in the fit. This parametrised curve is extrapolated to lower ToT values and used as the timewalk correction for hits with a ToT of 20 or lower. This curve is shown in fig. 7.3 as the black line for low ToT values. Another effect is a binning artefact at a TtT of 0 and 8.4 ns. This artefact slightly affects the correction value but does not dominate the corrected time resolution.

7.2.2   Temporal characterisation - first results

In this section, we present the first results of the temporal characterisation of a thin planar sensor bonded to a Timepix4. These studies are presented as a demonstration of the abilities of the Timepix4 assemblies in the TPA system. We present, similar to the results in section 7.1, the Time-over-Threshold (ToT), Time-to-Threshold (TtT) and time resolution (σ_t) are studied as a function of the depth (z) in the sensor (perpendicular to the surface of the detector). These results for a range of voltages are shown in fig. 7.4. The ToT, in contrast to the results discussed in section 7.1, is not corrected for fluctuations in TPA intensity due to a
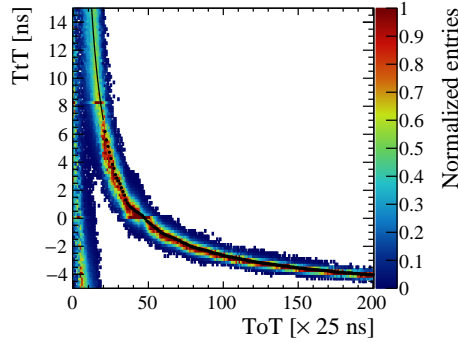
Figure 7.3: Timewalk of a single pixel of Timepix4 measured with the TPA system. The black points indicate the average TtT for each ToT value, which is used as the timewalk correction. For ToT ≤ 20, the timewalk correction is indicated by the black line, which is an extrapolation from higher ToT values.

problem with the digitisation of the reference signal. The intensity was tuned such that a ToT of around $100 \times 25\,$ns corresponds to a MIP-like signal in a $100\,\mu$m silicon sensor (8 ke⁻). The ToT distributions for all voltages are similar, except for the lowest voltage due to a slightly larger TPA signal fluctuation. However, even for the lowest voltage, all the charge is collected throughout the sensor, indicating that the device is already fully depleted at the lowest voltage.

The temporal characteristics are overall similar to the results on Timepix3, however, the temporal performance is significantly better, reaching at best a resolution of $147.4\pm1.1\,$ps at the implant, where the charge is approximately similar to the magnitude of two MIP-like signals in a silicon sensor (16 ke⁻). For this result, as well as the results shown in fig. 7.4, the contribution of the theoretical size of the trigger TDC bins is subtracted in quadrature ($195/\sqrt{12}\,$ps). The resolution improves, as expected, with increasing bias voltages since the induced current has a shorter risetime. When the TPA voxel is reflected back onto itself at the metallisation surface within the silicon volume, the resolution has a local minimum due to the higher number of liberated charge carriers. As discussed in [81], the resolution of the analogue front-end for similar settings and an injected charge of 8 ke⁻ is approximately 90 ps and 16 ke⁻ is approximately 65 ps.

A similar dip as was noticed in the results with Timepix3, is visible in the TtT around a position of 0 and $250\,\mu$m. This dip originates from a small difference between the actual timewalk effect and the parametrised/extrapolated curve. Therefore, these artefacts of the timewalk calibration should not be interpreted as physical effects. Besides these local minima, the TtT behaves as expected. We can observe three effects, the first is the decreasing drift distance that leads to a smaller TtT when the charge is collected closer to the implant. The second effect
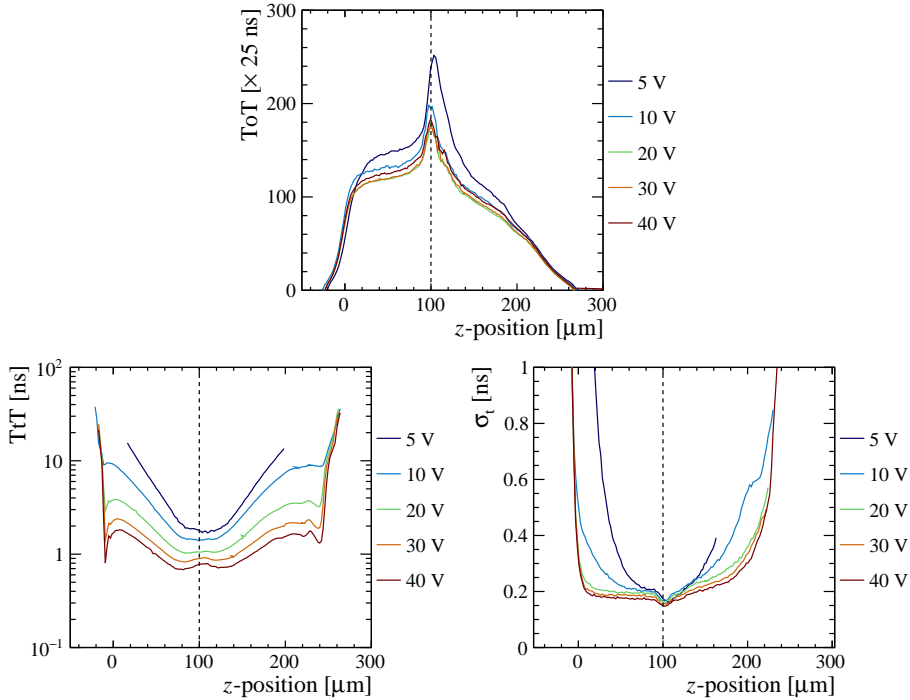
Figure 7.4: The ToT (top), TtT (bottom left) and time resolution (bottom right) as a function of height in a 100 μm sensor bump-bonded to a Timepix4 ASIC. The best measured time resolution is achieved when charge carriers are liberated close to the implant and is 147.4 ± 1.1 ps at around 16 ke⁻.

is the increase of the drift velocity when the bias voltage is increased, resulting in an overall smaller TtT. Lastly, the local increase of the TtT at the front of the sensor (at $z = 100\,\mu$m) is due to the increased contribution of the holes when the charge carriers are liberated close to the implant [104]. Since the mobility of holes is smaller compared to electrons, and the holes start dominating the induced signal, and thus the TtT is increased.

The temporal information from the active Timepix4 pixel is corrected according to the measured bin sizes of both the fToA_rise and the ufToA_stop. Unfortunately, these corrections could not be applied for the bin sizes of the digital pixel that digitised the trigger signal. Therefore, the contribution of the TDC binning of the trigger signal, in reality, is larger than the ideal $195/\sqrt{12}\,\text{ps} = 56\,\text{ps}$. The impact of the non-uniform TDC binning is studied using the distributions measured in the normal pixel (fig. 7.2), and is determined to result in a resolution of 154 ps. A similar study found an average resolution over the top and bottom super-pixel row of 111 ps [81]. Therefore, a significant contribution of the TDC binning of

the trigger signal is still present in the measured time resolution. Future studies can incorporate similar corrections for the TDC bins of the trigger signal, as well as different operating conditions, and can most likely further improve upon these results. However, these first studies into the time resolution of a single pixel have shown that a resolution close to the theoretical limit of Timepix4 is possible.

7.3   SUMMARY

In this chapter, we discussed how the two-photon absorption technique enables detailed and controlled characterisation studies of (novel) silicon sensors, utilising its unique ability to locally generate electron-hole pairs deep in the silicon bulk. With the two-photon absorption technique both the spatial and temporal characteristics of silicon sensors can be studied in detail. The TPA system built and commissioned at Nikhef is discussed, as well as the first results of the stability of the system. Results from a single pixel on multiple types of silicon planar sensors bonded to Timepix3 ASICs have been discussed. It was concluded that the TDC and analogue front-end of Timepix3 dominate the time resolution. The resolution of Timepix3 with a planar silicon sensor was measured to be just below 600 ps. Similar studies have been performed with a Timepix4 ASIC bonded to a planar silicon sensor, where temporal characteristics have also been studied as a function of height in the sensor. Similar results to the studies with Timepix3 have been found, however, the time resolution, as expected, has been improved significantly, and a resolution of 147.4 ± 1.1 ps was found for a planar $100 \, \mu$m n-on-p sensor bump bonded to a Timepix4 ASIC.

7

CHAPTER 8

❦

CONCLUSION AND PROSPECTS

The RESEARCH presented in this dissertation covers the aspect of temporal information measurements in current and future silicon particle detectors. It was with great joy and curiosity that I experienced the development in this field throughout the years of pursuing it. After presenting this work, I believe it is important to take a step back and reflect on what has been accomplished, and more importantly, what can be further achieved. This chapter aims to provide, with a hint of prejudice, an overview of the results presented in this dissertation and the opportunities that await this technology.

The impact of the addition of temporal information on important parameters for physics analysis within LHCb and the time resolution of small-pitch silicon sensors and detectors are studied. These simulations indicate the time resolution required for the VELO and provide a goal for the development in the coming years of fast-timing silicon pixel detectors. In the next sections, we will discuss the results and the prospects of these two main topics.

PROSPECTS FOR THE ADDITION OF TEMPORAL INFORMATION IN TRACKING DETECTORS

In chapter 2 we discussed how incorporating temporal information is crucial for the VELO detector to minimize the negative effects of higher pile-up. As LHCb aims to broaden the physics potential beyond what the current detector can accommodate, the instantaneous luminosity is required to increase and in the LHC this is achieved through a higher pile-up: a higher number of visible proton-proton collisions in a single bunch crossing. For this reason, the VELO needs to incorporate this increase in pile-up. Hence, we focus on determining the impact of implementing temporal information, with various time resolutions, on commonly used parameters in analyses.

Simulations presented in this dissertation, as well as in [13], indicate that a per-hit time resolution of 50 ps will provide a similar performance of the VELO in this higher pile-up scenario as the current detector provided under low pile-up conditions. Although the final design of the detector may still evolve over the coming years, the added value of temporal information became evident from these simulations. The first practical example of the value of temporal information will be seen from the ATLAS and CMS experiments, where dedicated timing detectors will be installed during the 2026-2028 shutdown of LHC, after which the LHCb experiment will install fast-timing detectors in the subsequent shutdown in 2033.

For the application of temporal information in the VELO, the 50 ps is taken as a strict requirement. However, the time resolution of current, large-scale applicable, pixelated silicon detectors, falls short of this requirement. As it stands, planar silicon sensors, which are studied in this dissertation, will most likely not provide a resolution sufficient enough for this goal. For this reason, 3D silicon sensors currently seem the best solution for the VELO Upgrade 2 [13].

The experience gained from the development of tracking systems at LHC experiments that use temporal information will most likely lead to significant progress in the application of pixelated silicon based detectors using accurate measurements of the time-of-arrival. This progress will be especially valuable for large-scale applications, such as we have already seen with the ASICs developed by the Medipix collaborations.

PROSPECTS FOR NOVEL SILICON SENSORS AIMED AT SPATIAL AND TEMPORAL MEASUREMENTS

The working principle of silicon sensors and their accompanying readout, more specifically Timepix3 and Timepix4 ASICs are discussed throughout this dissertation. Silicon sensors techniques that achieve a time resolution below 50 ps currently exists, however, none of them are universally applicable. Under certain compromises, one can find silicon sensors with a good time resolution that are applicable in experiments. Some of these sensor techniques sacrifice radiation hardness or fill factor to achieve a good time resolution. Hence, there is currently no clear solution to fulfil all requirements. For the VELO specifically, the specific sensor technique to be used in Upgrade 2 is yet to be determined. The 3D sensor technologies seem to be the most promising solution laid out in [13]. The downsides of this technology are mostly limited to the production phases, such as lower production yields and higher prices, but are mitigated by the relatively small detection area needed by the VELO. Applying monolithic sensors within the VELO, with the current requirements, seems too optimistic since these monolithic devices are lacking the

time resolution that is required. However, in the long term, these devices show promise due to their low material budget and show progress on improving the time resolution. This however also implies that hybrid detectors will be used in the VELO Upgrade 2.

In addition to an overview of the different sensor techniques given in chapter 3, two different characterisation approaches have been discussed: beam telescopes (chapter 5), in which highly energetic particles are tracked and used to evaluate the performance of a Device-Under-Test (DUT), and a Two-Photon Absorption (TPA) system (chapter 7) which employs 1550 nm wavelength photons to evaluate the spatial and temporal characteristics as well as charge collection of silicon sensors. Using a beam telescope, the intra-pixel time resolution and charge collection properties of planar 200 μm sensors are studied on Timepix3 ASICs in view of Upgrade 1 of the VELO. With Timepix3, the time resolution was found to be sufficient for Upgade 1, but insufficient for Upgrade 2 due to the limited resolution of the ASIC. The time resolution of 100 μm n-on-p silicon sensors on Timepix4 is also studied using a fully Timepix4 based beam telescope. The first results indicate a single hit resolution of 420 ± 10 ps averaged over the pixel matrix. However, it was noted this time resolution will be improved with the later iterations of the Timepix4 ASIC where we aim to achieve a resolution below 150 ps for a full ASIC and well below 100 ps for an eight plane Timepix4 based beam telescope.

Using the two-photon absorption system, planar silicon sensors are studied on both Timepix3 and Timepix4 ASICs. Timepix3 obtained a time resolution of just below 600 ps, mostly dominated by the TDC and analogue front-end of Timepix3. With Timepix4, a resolution of 147.4 ± 1.1 ps is achieved for measurements with a single pixel, which is significantly better than the results with Timepix3. This also indicates that the current resolution obtained for the full ASIC during the characterisation of the Timepix4 telescope has a large contribution from pixel-to-pixel variations resulting in a worse overall time resolution. These single pixel results obtained with the TPA system are expected to improve further with improved processing of the trigger signal. However, it is expected that when the resolution of the TDC and analogue front-end is further improved and improved corrections for per-pixel offsets and timewalk are applied, the limiting factor will be the silicon sensor. This will enable the study of different sensor technologies that can be directly bump-bonded to a full ASIC.

The two characterisation tools developed in this dissertation, the Timepix4 ASIC based beam telescope and the two-photon absorption system, are expected to play crucial roles in the next few years in developing the next generation of fast-timing silicon pixel detectors for high energy physics. These silicon pixel detectors will serve in future detectors to reduce the complexity of the analyses of high pile-up environments.

The time resolutions determined in this dissertation are still quite far away from 50 ps that is required for the VELO Upgrade 2. However, with improvements in sensor techniques and a switch away from planar sensors, to for example 3D technologies which currently achieve a resolution below 30 ps, the contribution of the sensor to the total time resolution can be lowered to a great extent. If in the meantime new techniques can be utilized to improve the TDC in ASICs as well as to improve pixel-to-pixel variations, I am hopeful that in the next few years a detector can be achieved that can reach a 50 ps time resolution in a single plane over the full detector area.

❧ BIBLIOGRAPHY ❧

[1] B. Hyams et al., *A silicon counter telescope to study short-lived particles in high-energy hadronic interactions*, Nuclear Instruments and Methods in Physics Research **205** (1983) 99.

[2] R. Bailey et al., *A silicon strip detector telescope for the measurement of production and decay of charmed particles*, Nuclear Instruments and Methods in Physics Research Section A: Accelerators, Spectrometers, Detectors and Associated Equipment **226** (1984) 56.

[3] B. Knudsen, *Presentation of the WA97 experiment at CERN*, Czechoslovak Journal of Physics **47** (1997) 925.

[4] P. Chochula et al., *The DELPHI Silicon Tracker at LEP2: The DELPHI Silicon Tracker Group*, Nuclear Instruments and Methods in Physics Research Section A: Accelerators, Spectrometers, Detectors and Associated Equipment **412** (1998) 304.

[5] W. Röntgen, *Ueber eine neue Art von Strahlen*, Sitzungsberichte der Würzburger Physikalischen-Medicinischen Gesellschaft (1895) 1.

[6] J. Thomson, *Cathode rays*, The London, Edinburgh, and Dublin Philosophical Magazine and Journal of Science **44** (1897) 293.

[7] A. Sessler and E. Wilson, *Engines of Discovery*. World Scientific, revised and expanded ed., 2014, 10.1142/8552.

[8] R. Varian, U.S. Patent No. 2.242.275 (Applied for, October 11, 1937).

[9] LHCb Collaboration, *LHCb Tracker Upgrade Technical Design Report*, tech. rep., CERN, Geneva, 2014.

[10] LHCb Collaboration, *Letter of Intent for the LHCb Upgrade*, tech. rep., CERN, Geneva, 2011.

[11] LHCb collaboration, *Physics case for an LHCb Upgrade II - Opportunities in flavour physics, and beyond, in the HL-LHC era*, tech. rep., CERN, Geneva, 2016.

[12] LHCb Collaboration, *Framework TDR for the LHCb upgrade II: Opportunities in flavour physics, and beyond, in the HL-LHC era*, tech. rep., CERN, Geneva, 2022.

[13] LHCb VELO Group, *Considerations for the VELO detector at the LHCb Upgrade II*, tech. rep., CERN, Geneva, 2022.

[14] LHCb Collaboration, *LHCb VELO Upgrade Technical Design Report*, tech. rep., CERN, Geneva, 2013.

[15] N. van Bakel and M. Ferro-Luzzi, *Shielding of the VELO detectors from the LHC beam high-frequency fiels: preliminary considerations*, tech. rep., CERN, Geneva, 2001.

[16] F. Sanders. Personal communication.

[17] A. Papadelis, *Characterisation and commissioning of the LHCb VELO detector*, Ph.D. thesis, NIKHEF, Amsterdam, 2009.

[18] J. Albrecht et al., *Luminosity scenarios for LHCb Upgrade II*, tech. rep., CERN, Geneva, 2019.

[19] I. Belyaev et al., *Handling of the generation of primary events in Gauss, the LHCb simulation framework*, Journal of Physics: Conference Series **331** (2011) 032047.

[20] S. Agostinelli et al., *Geant4 — a simulation toolkit*, Nuclear Instruments and Methods in Physics Research Section A: Accelerators, Spectrometers, Detectors and Associated Equipment **506** (2003) 250.

[21] M. Clemencic et al., *The LHCb Simulation Application, Gauss: Design, Evolution and Experience*, Journal of Physics: Conference Series **331** (2011) 032023.

[22] J. Hook and H. Hall, *Solid State Physics*, Manchester Physics Series. Wiley, 2013.

[23] W. Pauli, *Über den Zusammenhang des Abschlusses der Elektronengruppen im Atom mit der Komplexstruktur der Spektren*, Zeitschrift für Physik A Hadrons and Nuclei **31** (1925) 765.

[24] P. Dirac, *On the theory of quantum mechanics*, Proceedings of the Royal Society of London. Series A, Containing Papers of a Mathematical and Physical Character **112** (1926) 661.

[25] D. Hynds, *Resolution studies and performance evaluation of the LHCb VELO upgrade*, Ph.D. thesis, Glasgow University, 2015.

[26] C. Hu, *Modern Semiconductor Devices for Integrated Circuits*. Prentice Hall, 2010.

[27] J. Chelikowsky and M. Cohen, *Electronic structure of silicon*, *Physical Review B* **10** (1974) 5095.

[28] S. Watanabe et al., *CdTe stacked detectors for gamma-ray detection*, *2001 IEEE Nuclear Science Symposium Conference Record* **4** (2001) 2434.

[29] M. Veale et al., *Chromium compensated gallium arsenide detectors for X-ray and γ-ray spectroscopic imaging*, *Nuclear Instruments and Methods in Physics Research Section A: Accelerators, Spectrometers, Detectors and Associated Equipment* **752** (2014) 6.

[30] H. Spieler, *Semiconductor detector systems*, vol. 12. Oxford University Press, 2005.

[31] G. Pellegrini et al., *Technology developments and first measurements of Low Gain Avalanche Detectors (LGAD) for high energy physics applications*, *Nuclear Instruments and Methods in Physics Research Section A: Accelerators, Spectrometers, Detectors and Associated Equipment* **765** (2014) 12.

[32] C. Kenney et al., *Silicon detectors with 3-D electrode arrays: fabrication and initial test results*, *IEEE Transactions on Nuclear Science* **46** (1999) 1224.

[33] A. Poruba et al., *Temperature dependence of the optical absorption coefficient of microcrystalline silicon*, *Journal of non-crystalline solids* **338** (2004) 222.

[34] D. Groom and S. Klein, *Passage of particles through matter*, *The European Physical Journal C - Particles and Fields* **15** (2000) 163.

[35] M. Berger et al., *Main Tables: Stopping Powers, Ranges, and Radiation Yields*, *Journal of the International Commission on Radiation Units and Measurements* **os-19** (1984) .

[36] D. Groom, N. Mokhov and S. Striganov, *Muon stopping power and range tables 10 MeV–100 TeV*, *Atomic Data and Nuclear Data Tables* **78** (2001) 183.

[37] M. Berger et al., *Main Proton Tables*, *Journal of the International Commission on Radiation Units and Measurements* **os-25** (1993) 107.

[38] M. Berger et al., *Main Alpha Particle Tables*, *Journal of the International Commission on Radiation Units and Measurements* **os-25** (1993) 183.

[39] P. Vavilov, *Ionization losses of high-energy heavy particles*, *Soviet Physics JETP* **5** (1957) 749.

[40] L. Landau, *On the energy loss of fast particles by ionization*, *Journal of Physics* **8** (1944) 201.

[41] H. Bichsel, *Straggling in thin silicon detectors*, *Reviews of Modern Physics* **60** (1988) 663.

[42] W. Shockley, *Currents to conductors induced by a moving point charge*, *Journal of applied physics* **9** (1938) 635.

[43] W. Riegler and G. Rinella, *Point charge potential and weighting field of a pixel or pad in a plane condenser*, *Nuclear Instruments and Methods in Physics Research Section A: Accelerators, Spectrometers, Detectors and Associated Equipment* **767** (2014) 267.

[44] G. Cavalleri et al., *Extension of Ramo's theorem as applied to induced charge in semiconductor detectors*, *Nuclear Instruments and Methods* **92** (1971) 137.

[45] G. Cavalleri et al., *On the induced charge in semiconductor detectors*, *Nuclear Instruments and Methods* **21** (1963) 177.

[46] S. Reggiani et al., *Electron and hole mobility in silicon at large operating temperatures — Part I: Bulk mobility*, *IEEE Transactions on Electron devices* **49** (2002) 490.

[47] N. Cartiglia et al., *Performance of ultra-fast silicon detectors*, *Journal of Instrumentation* **9** (2014) C02001.

[48] J. Xanthakis, *Electronic Conduction: Classical and Quantum Theory to Nanoelectronic Devices*. CRC Press, 2020, 10.1201/9780429506444.

[49] C. Leroy and P. Rancoita, *Particle interaction and displacement damage in silicon devices operated in radiation environments*, *Reports on Progress in Physics* **70** (2007) 493.

[50] C. Canali, G. Ottaviani and A. Quaranta, *Drift velocity of electrons and holes and associated anisotropic effects in silicon*, *Journal of Physics and Chemistry of Solids* **32** (1971) 1707.

[51] S. Li and W. Thurber, *The dopant density and temperature dependence of electron mobility and resistivity in n-type silicon*, *Solid-State Electronics* **20** (1977) 609.

[52] C. Jacoboni et al., *A review of some charge transport properties of silicon*, *Solid-State Electronics* **20** (1977) 77.

[53] G. Kramberger et al., *Radiation effects in Low Gain Avalanche Detectors after hadron irradiations*, Journal of Instrumentation **10** (2015) P07006.

[54] M. Moll, *Displacement damage in silicon detectors for high energy physics*, IEEE Transactions on Nuclear Science **65** (2018) 1561.

[55] V. Van Lint, *Mechanisms of radiation effects in electronic materials*, vol. 1. Wiley-Interscience, New York, NY, 1980.

[56] M. Huhtinen, *Simulation of non-ionising energy loss and defect formation in silicon*, Nuclear Instruments and Methods in Physics Research Section A: Accelerators, Spectrometers, Detectors and Associated Equipment **491** (2002) 194.

[57] M. Arratia Munoz, *Studies of radiation damage in silicon sensors and a measurement of the inelastic proton-proton cross-section at 13 TeV*, Ph.D. thesis, Cambridge University, 2016.

[58] *Standard Practice for Characterizing Neutron Fluences Spectra in Terms of an Equivalent Monoenergetic Neutron Fluence for Radiation- Hardness Testing of Electronics*, standard, Revision 1993.

[59] M. Moll, *Radiation damage in silicon particle detectors: Microscopic defects and macroscopic properties*, Ph.D. thesis, 1999.

[60] M. Moll et al., *Investigation on the improved radiation hardness of silicon detectors with high oxygen concentration*, Nuclear Instruments and Methods in Physics Research Section A: Accelerators, Spectrometers, Detectors and Associated Equipment **439** (2000) 282.

[61] N. Johnson, *Neutralization of donor dopants and formation of hydrogen-induced defects in n-type silicon*, Semiconductors and Semimetals **34** (1991) 113.

[62] M. Li et al., *Effects of shallow carbon and deep N^{++} layer on the radiation hardness of IHEP-IME LGAD sensors*, IEEE Transactions on Nuclear Science **69** (2022) 1098.

[63] G. Lutz, *Semiconductors as Detectors*, in *Semiconductor Radiation Detectors*, pp. 79–93, Springer, (2007).

[64] G. Kramberger et al., *Effective trapping time of electrons and holes in different silicon materials irradiated with neutrons, protons and pions*, Nuclear Instruments and Methods in Physics Research Section A: Accelerators, Spectrometers, Detectors and Associated Equipment **481** (2002) 297.

[65] G. Lindström, *Radiation damage in silicon detectors*, *Nuclear Instruments and Methods in Physics Research Section A: Accelerators, Spectrometers, Detectors and Associated Equipment* **512** (2003) 30.

[66] V. Chiochia et al., *A double junction model of irradiated silicon pixel sensors for LHC*, *Nuclear Instruments and Methods in Physics Research Section A: Accelerators, Spectrometers, Detectors and Associated Equipment* **568** (2006) 51.

[67] G. Kramberger et al., *Investigation of irradiated silicon detectors by edge-TCT*, *IEEE Transactions on Nuclear Science* **57** (2010) 2294.

[68] R. Ballabriga et al., *The Timepix4 analog front-end design: Lessons learnt on fundamental limits to noise and time resolution in highly segmented hybrid pixel detectors*, *Nuclear Instruments and Methods in Physics Research Section A: Accelerators, Spectrometers, Detectors and Associated Equipment* **1045** (2023) 167489.

[69] ATLAS Collaboration, *Technical Design Report: A High-Granularity Timing Detector for the ATLAS Phase-II Upgrade*, tech. rep., CERN, Geneva, 2020.

[70] CMS Collaboration, *A MIP Timing Detector for the CMS Phase-2 Upgrade*, tech. rep., CERN, Geneva, 2019.

[71] ATLAS Collaboration, *ATLAS insertable B-layer technical design report*, tech. rep., CERN, Geneva, 2010.

[72] F. Krummenacher, *Pixel detectors with local intelligence: an IC designer point of view*, *Nuclear Instruments and Methods in Physics Research Section A: Accelerators, Spectrometers, Detectors and Associated Equipment* **305** (1991) 527.

[73] R. Ballabriga, M. Campbell and X. Llopart, *An introduction to the Medipix family ASICs*, *Radiation Measurements* **136** (2020) 106271.

[74] P. Delpierre, *A history of hybrid pixel detectors, from high energy physics to medical imaging*, *Journal of Instrumentation* **9** (2014) C05059.

[75] M. Campbell et al., *A readout chip for a 64×64 pixel matrix with 15-bit single photon counting*, *IEEE Transactions on Nuclear Science* **45** (1998) 751.

[76] X. Llopart, *Design and characterization of 64k pixels chips working in single photon processing mode*, Ph.D. thesis, Mid Sweden University, Sundsvall, 2007.

[77] X. Llopart et al., *Timepix, a 65k programmable pixel readout chip for arrival time, energy and/or photon counting measurements*, Nuclear Instruments and Methods in Physics Research Section A: Accelerators, Spectrometers, Detectors and Associated Equipment **581** (2007) 485.

[78] R. Ballabriga et al., *Medipix3: A 64k pixel detector readout chip working in single photon counting mode with improved spectrometric performance*, Nuclear Instruments and Methods in Physics Research Section A: Accelerators, Spectrometers, Detectors and Associated Equipment **633** (2011) S15.

[79] T. Poikela et al., *Timepix3: A 65k channel hybrid pixel readout chip with simultaneous ToA/ToT and sparse readout*, Journal of Instrumentation **9** (2014) C05013.

[80] X. Llopart et al., *Timepix4, a large area pixel detector readout chip which can be tiled on 4 sides providing sub-200 ps timestamp binning*, Journal of Instrumentation **17** (2022) C01044.

[81] K. Heijhoff et al., *Timing performance of the Timepix4 front-end*, Journal of Instrumentation **17** (2022) P07006.

[82] M. Morris Mano, *Digital Design*. Prentice Hall, 2013.

[83] B. van Der Heijden et al., *SPIDR, a general-purpose readout system for pixel ASICs*, Journal of Instrumentation **12** (2017) C02040.

[84] J. Visser et al., *SPIDR: a read-out system for Medipix3 & Timepix3*, Journal of Instrumentation **10** (2015) C12028.

[85] K. Akiba et al., *LHCb VELO timepix3 telescope*, Journal of Instrumentation **14** (2019) P05026.

[86] K. Heijhoff et al., *Timing performance of the LHCb VELO Timepix3 telescope*, Journal of Instrumentation **15** (2020) P09035.

[87] E. Buchanan, *Spatial Resolution Studies for the LHCb VELO Upgrade*, Ph.D. thesis, University of Bristol, 2019.

[88] E. Dall'Occo, *Search for heavy neutrinos and characterisation of silicon sensors for the VELO upgrade*, Ph.D. thesis, Vrije Universiteit Amsterdam, 2020.

[89] T. Poikela et al., *The VeloPix ASIC*, Journal of Instrumentation **12** (2017) C01070.

[90] M. Clemencic et al., *Recent developments in the LHCb software framework Gaudi*, Journal of Physics: Conference Series **219** (2010) 042006.

[91] K. Akiba et al., *Reconstruction of charged tracks with Timepix4 ASICs*, *Journal of Instrumentation* **18** (2023) P02011.

[92] R. Geertsema et al., *Charge collection properties of prototype sensors for the LHCb VELO upgrade*, *Journal of Instrumentation* **16** (2021) P02029.

[93] E. Buchanan et al., *Spatial resolution and efficiency of prototype sensors for the LHCb VELO Upgrade*, *Journal of Instrumentation* **17** (2022) P06038.

[94] E. Dall'Occo et al., *Temporal characterisation of silicon sensors on Timepix3 ASICs*, *Journal of Instrumentation* **16** (2021) P07035.

[95] M. Göppert-Mayer, *Über elementarakte mit zwei quantensprüngen*, *Annalen der Physik* **401** (1931) 273.

[96] W. Kaiser and C. Garrett, *Two-Photon Excitation in CaF_2:Eu^{2+}*, *Physical Review Letters* **7** (1961) 229.

[97] R. Braunstein and N. Ockman, *Optical Double-Photon Absorption in CdS*, *Physical Review* **134** (1964) A499.

[98] W. Denk, J. Strickler and W. Webb, *Two-photon laser scanning fluorescence microscopy*, *Science* **248** (1990) 73.

[99] D. Parthenopoulos and P. Rentzepis, *Three-Dimensional Optical Storage Memory*, *Science* **245** (1989) 843.

[100] S. Kawata and Y. Kawata, *Three-dimensional optical data storage using photochromic materials*, *Chemical reviews* **100** (2000) 1777.

[101] N. Fatkullin et al., *Two-photon photopolymerization and 3D lithographic microfabrication*, *NMR 3D Analysis Photopolymerization* (2004) 169.

[102] A. Almagro-Ruiz et al., *Fiber laser system of 1550 nm femtosecond pulses with configurable properties for the two-photon excitation of transient currents in semiconductor detectors*, *Applied Optics* **61** (2022) 9386.

[103] R. Geertsema et al., *Charge and temporal characterisation of silicon sensors using a two-photon absorption laser*, *Journal of Instrumentation* **17** (2022) P02023.

[104] K. Heijhoff et al., *Timing measurements with a 3D silicon sensor on Timepix3 in a 180 GeV/c hadron beam*, *Journal of Instrumentation* **16** (2021) P08009.

[105] McCoy Wynne photography partnership. Personal communication.

Summary

The research presented in this dissertation aims to develop temporal information for high energy physics experiments at the European Organization for Nuclear Research (CERN). These experiments are designed to investigate the fundamental building blocks of nature, described by the Standard Model. They utilise a particle accelerator complex that accelerates particles, protons most of the time, to near the speed of light and smash them together at dedicated interaction points. The resulting collisions produce new particles that are studied by the experiments.

Substantial progress in the understanding of these fundamental building blocks of nature has been made since the first discovery of elementary particles, starting with the discovery of the electron by Joseph Thomson [6] using particle accelerators. Ever since, different designs of particle accelerators have emerged, and their development led to the Large Hadron Collider (LHC) which started operation in 2008. The LHC is a circular accelerator and contains two beam pipes next to each other to guide two beams in opposite directions, one beam per pipe, around a circle with a length of 27 km. The two beams contain so-called *bunches*, a cloud which contains a large number of protons: around 1.15×10^{11}. At four dedicated *interaction points* the two beams are crossed in such a way that protons from the two different beams can collide every 25 ns. Such a collision is called a *bunch crossing*, in which the individual proton-proton collisions occur spread over around 200 ps due to the spatial characteristics of the bunches. The energy frontier of the LHC has been pushed tremendously after the start of the LHC. When the LHC started the energy contained within a single collision was 7 TeV and has been increased in steps to the current energy of 13.6 TeV. The statistical frontier of the LHC has been developed alongside the energy frontier of the LHC. The increase in the proton-proton collision rate also directly increases the statistics of the physical processes to be studied. These physical processes of interest can often contain novel hints towards the validity and understanding of the Standard Model and thus are of prime interest for particle physicists.
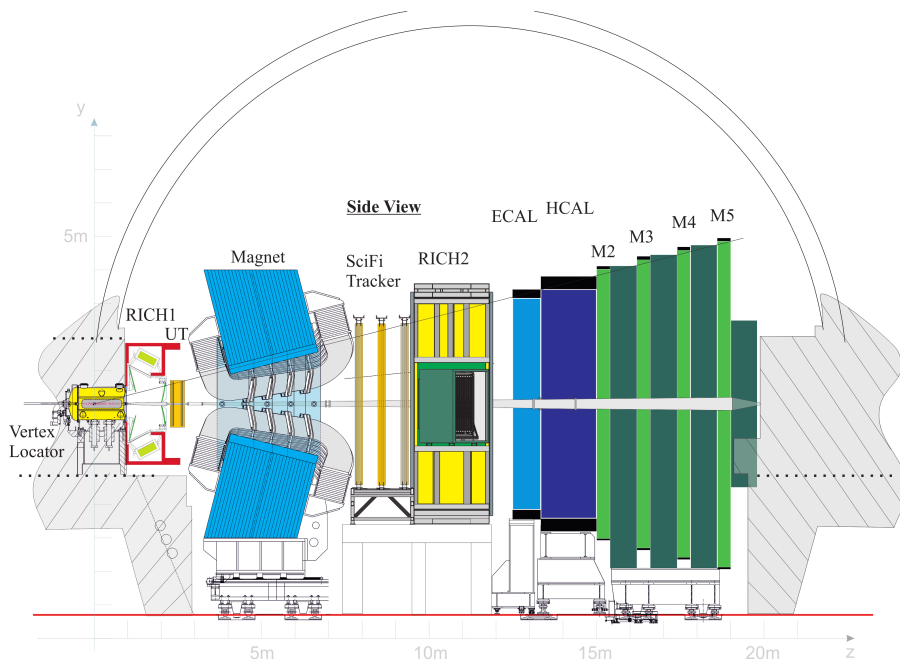
Figure 1: An illustration of the LHCb detector after its first upgrade (2022). The different subdetectors are indicated in various colours, as well as the outline of the cavern (grey lines and striped grey area) and the magnet (blue). The proton-proton interactions take place in the VELO, around $z = 0$. Figure taken from [9].

LHCb's Upgrade 2

One of the experiments operating around an interaction point at the LHC is LHCb (LHC beauty - shown in fig. 1), which is a so-called *forward single-arm spectrometer*, in other words, it focuses its detection at low azimuthal angles with respect to the beamline. Similarly to the other experiments operating at the LHC, it is planning to increase the proton-proton collision rate at the experiment currently planned to start in 2035 and referred to as Upgrade 2. This rate increase is required such that more interactions can be measured over its lifetime. Such a drastic change also requires a complete redesign and upgrade of the various subdetectors in the experiment in order to cope with the increase in rate, radiation damage, data volume and much more. The aim is to increase the average number of visible collisions each 25 ns, in other words, 40 million times per second, from 7 to 42 after the upgrade, resulting in an increased pile-up (the number of collisions occurring within the same event). This increase in pile-up allows LHCb to extend its physics potential beyond what is currently possible.
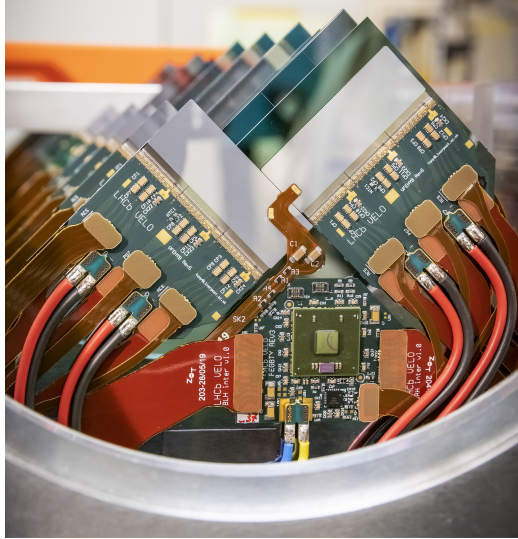
Figure 2: Picture of one side of the VELO detector. The first detector plane is visible along with multiple planes behind it. Picture by [105].

The tracking system of the LHCb detector, needed to reconstruct the trajectories of the various particles emerging from the proton-proton collisions (also called primary vertices), consists of various subdetectors. The subdetector that surrounds the proton-proton collisions, and is the closest to these collisions, is the *VErtex LOcator* (VELO - partially shown in fig. 2). This detector is based on multiple layers of silicon pixel detectors and serves the purpose of tracking the particles emerging from the proton-proton collisions, as well as the reconstruction of the position of these collisions. With the increase in collision rate, the VELO will lose discriminating power in the parameters it provides to the physics analyses, which makes it impossible to perform these analyses. Therefore, temporal information will be included in the VELO, which is information about the time-of-arrival of particles in each pixel detector. This information will be included in its reconstruction to regain the loss in performance. This addition of temporal information enables disentangling overlapping physics processes and collisions.

Since the proton-proton collisions taking place during a bunch crossing are not instantaneous, the timestamp of the collisions and their products can be utilised in the reconstruction. This dissertation investigates how this addition can aid in improving the performance of the VELO. Therefore the impact of this temporal information to two different parameters used in the VELO is studied. Using simulation, the impact of a time resolution of 50 ps per hit is studied. In fig. 3 the impact of temporal information on a typical bunch crossing is shown. The lower plot shows a typical bunch crossing at LHCb during Upgrade 2 with around 42
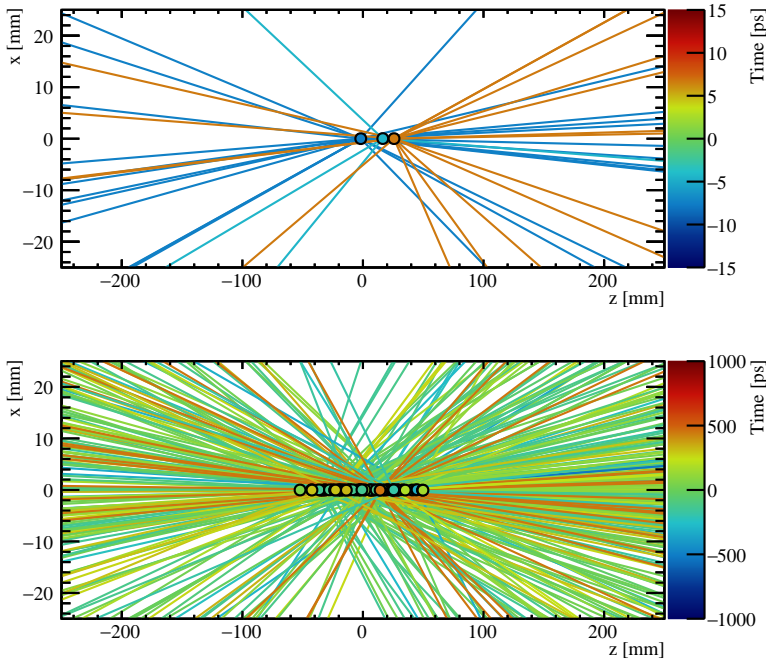
Figure 3: Two figures that indicate the impact of temporal information on pile-up suppression for the VELO. The circles visible in the figures are the proton-proton collisions (primary vertices) and the lines indicate the particle trajectories originating from these primary vertices. The colours indicate the timestamp associated with the vertices and tracks. A typical bunch crossing for Upgrade 2 is shown in each figure, with on average 42 visible collisions. By including temporal information, and selecting a smaller window in time, the effective pile-up is artificially reduced, visible by a reduction of vertices and tracks. The bottom figure shows the full bunch crossing and the top figure shows one of the time slices of 30 ps.

visible proton-proton collisions. The circles in these figures indicate the position of the vertices (the individual proton-proton collisions) and the lines indicate the trajectories of the particles that are created during these collisions. The colours are associated with the individual collisions and the lines indicate the relative time at which they are created. This creation time, referred to as timestamp, enables associating tracks to collisions and depending on the timestamp precision, even without spatial information. One can see that within a time window of around 2 ns, the individual vertices and the particles that emerged from them are difficult, if not impossible, to distinguish. However, when the timestamp of the collisions and particles is considered, a smaller window in time can be selected. Since the individual collisions are spread out in time, the smaller window selected contains

fewer collisions and therefore the individual collisions can easily be identified. This is indicated in the top figure in fig. 3, where a 30 ps window is shown out of the full bunch crossing. The colours, or timestamps, can also be used to relate the created particles to their respective collisions, as visible in this top figure.

These simulations indicate that with a per-hit time resolution of 50 ps the adverse effects of higher pile-up are suppressed. These simulations, therefore, sets a stringent goal for the time resolution of silicon pixel sensors that needs to be achieved in the coming years.

Development of silicon pixel detectors and dedicated characterisation systems

At this moment, all existing detectors do not achieve the requirements set for the VELO Upgrade 2. However, extensive R&D programs are ongoing that explore a wide range of possible novel technologies for both the silicon sensor and the electronics. As part of this program, we develop new measurement techniques and equipment to characterise these novel techniques and equipment.

To measure, and more importantly, characterise the temporal performance of novel silicon sensors and detectors that are developed in view of the VELO Upgrade 2, dedicated characterisation systems are developed. In this dissertation, two separate systems are developed. This first system is a beam telescope that uses charged particle beams to study the sensor response. The second system is a laser-based two-photon absorption system that uses photons to induce signals to study the sensor response.

The beam telescope consists of eight planes of silicon detectors, equipped with Timepix4 *Application-Specific Integrated Circuits* (ASICs), and tracks these particles as they traverse the system. Such a system is often called a telescope, and in this specific case is called the Timepix4 telescope. The Timepix4 telescope is developed to provide both precise position tracking and a precise time resolution of the tracked particles. This system in turn allows to compare the reconstructed information of the particles traversing the telescope to the measurements of the particles by an external detector, which enables the characterisation of the different detectors by comparing the measured signals.

The Timepix4 telescope is built in stages and therefore different versions of the Timepix4 telescope have existed. The temporal performance of the four plane system with two thin silicon sensors and two thick silicon sensors (half of the envisioned telescope) and based on the first version of the Timepix4 ASIC is determined at different bias voltages and threshold values. A summary of the results of the time resolution for bias scans (left) and threshold scans (right) of the telescope planes are shown in fig. 4 and are used to find the optimal operating conditions. The best time resolution of this four plane telescope is determined to be 340 ± 5 ps.

However, it was also noted that this resolution will be improved significantly when the final version of the Timepix4 ASIC is implemented in the system as well as adding a further four planes. The resolution will also further improve when the so-called timewalk calibration and clock synchronisation have been further optimised. A time resolution below 100 ps is expected to be achieved by the complete telescope. This resolution will be enough to test the first generation of novel ASICs but is not sufficient to test silicon sensors themselves to their limit. The telescope, however, can also provide a more precise timestamp at a lower rate using a dedicated timing system to timestamp the tracks to a precision of below 20 ps which is sufficient to test the performance of the novel sensors.
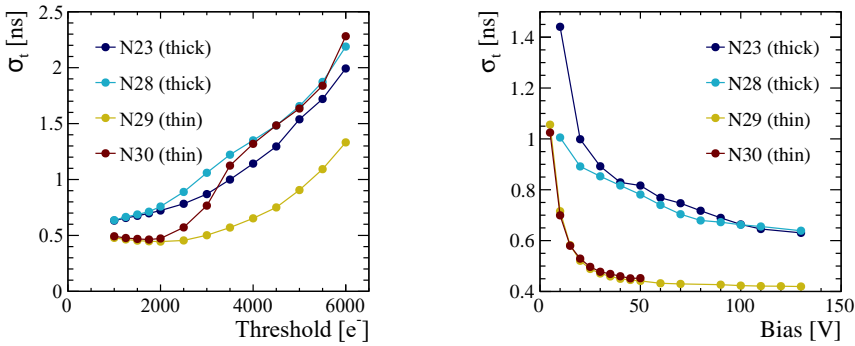

Figure 4: Left: the time resolution of the four telescope planes for a variety of threshold values. Right: the time resolution of the four telescope planes as a function of the bias voltage. Two of the planes reach their best resolution at a threshold of around 2000 e⁻, and the time resolution improves for higher bias voltages for all planes. Figures adapted from [91].

Employing the predecessor of the Timepix4 telescope, the Timepix3 ASIC based telescope called the Timepix3 telescope, the charge collection and temporal characteristics have been measured for a variety of sensor designs in view of the first upgrade of the VELO that is currently installed. These studies provided information on the impact of radiation damage which sensors need to handle with close to the interaction point. In these studies, it was concluded that the radiation damage that the VELO will have received at the end of its lifetime will reduce the collected charge from 16 ke⁻ to 6 ke⁻, which is sufficiently high to achieve the required performance. A small amount of charge multiplication has been discovered in a subset of sensors that received the highest amount of radiation damage, which slightly increased the collected charge. The time resolution was also studied as a function of radiation damage and has been found to degrade with increasing damage. No improvement in the time resolution was found when charge multiplication occurred. These studies however were performed with the Timepix3 ASIC, which has an intrinsic time resolution of at least 451 ps and thus

dominates the time resolution. Therefore, small changes in the time resolution, due to for example charge multiplication, might not have been identified.

Besides the telescope, the development of a laser-based system is also described in this dissertation. This system consists of a fibre-based 1550 nm laser that can create signals in silicon sensors through the *Two-Photon Absorption* (TPA) effect. This process relies on the fact that two photons are absorbed in the silicon sensor within a short period of time at the same position. This technique therefore enables the localised characterisation of charge collection within the silicon bulk. Since the duration of the laser pulses is short, between 380 to 540 fs, this allows to create a precise time reference signal, which is estimated to have a jitter of less than 30 ps, limited by the device that was used to verify the time resolution. This makes the TPA system ideal to characterise the spatial, charge collection and temporal performance of silicon sensors and detectors in a controlled way.
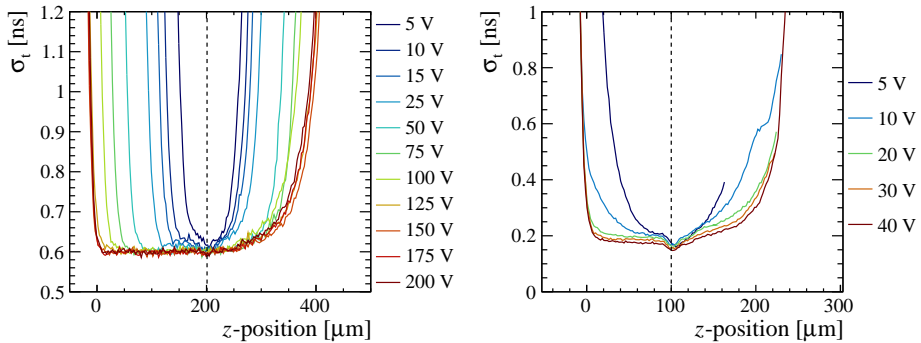

Figure 5: Left (Right): the time resolution of a 200 μm (100 μm) silicon sensor connected to a Timepix3 (Timepix4) ASICx as a function of the height within the sensor for different bias voltages indicated by the different colours. The dashed line indicates the front of the sensor and the 0-point on the horizontal axis indicates the back of the sensor. Left figure taken from [103].

The two-photon absorption system constructed at Nikhef has been commissioned and the results are discussed in this dissertation. Initial measurements indicate a variation in the TPA signal intensity due to fluctuations in the temporal width of the laser pulses over a timescale of several minutes. These fluctuations can partially be corrected offline using a separate silicon sensor as an intensity reference. Using this system, both planar sensors on Timepix3 and Timepix4 ASICs have been investigated. Two planar sensors have been investigated on Timepix3 ASICs and it is concluded that the time resolution is dominated by the contributions from the ASIC and not the sensor, in line with the findings from the Timepix3 telescope. Nonetheless, a resolution of around 600 ps is achieved. For the initial results with the Timepix4 ASIC, a resolution of 147.4 ± 1.1 ps has been achieved,

which is substantially better compared to the results with Timepix3 ASICs. This improvement can be attributed to the improved analogue front-end and digital time measurement of the Timepix4 ASIC. Small improvements are envisioned to be implemented that can improve this time resolution further. Two measurements, left with Timepix3 and right with Timepix4 ASIC, are shown in fig. 5. These measurements show the time resolution of the sensors as a function of depth within the sensor volume. The dashed line indicates the front side of the sensor and the 0-point indicates the back side. Both show similar response curves independent of their different thickness, however, the time resolution scale is significantly different with the Timepix3 ASIC reaching a saturation at around 600 ps compared to the Timepix4 ASIC at just below 200 ps.

These initial measurements with the TPA system indicate that the characterisation of novel silicon detectors can be performed and that this system is a valuable tool and testbed for developing fast-timing silicon detectors in the coming years. We have seen that the current limiting factor for fast silicon sensors is the analogue front-end and digitisation (TDC). However, with the current trend of improvements over the past few years, this limiting factor will most likely disappear in the near future. Novel silicon sensor techniques have already proven that a time resolution below 30 ps is achievable, however full-scale implementation of them in the VELO are still under study. At this moment, it seems that the sensor will not be the limiting factor of these development in the near future.

The time resolution of the detectors that have been covered in this dissertation is far away from the required 50 ps for the VELO. However, as can be seen from the transition of the Timepix3 ASIC to the Timepix4 ASIC, significant steps are already achieved. This trend needs to continue in the coming years to achieve the goal of a per-hit time resolution of 50 ps. The two characterisation systems discussed in this dissertation will become crucial tools in the development of silicon based fast-timing detectors.

Samenvatting

Het onderzoek gepresenteerd in deze dissertatie is gericht op de ontwikkeling en gebruik van tijdsinformatie in hoge energy fysica experimenten op CERN (de Europese organisatie voor kernonderzoek). Deze experimenten zijn gericht op het onderzoeken van de fundamentele bouwstenen van de natuur, welke omschreven zijn door het Standaard Model. Deze experimenten gebruiken een uitgebreid versneller complex welke deeltjes, protonen voor het grootste gedeelte van het jaar, versnelt naar bijna de lichtsnelheid. Deze deeltjes worden op elkaar geschoten en de resulterende botsingen die plaatsvinden produceren nieuwe deeltjes welke bestudeerd worden door de experimenten.

Sinds de eerste ontdekking van elementaire deeltjes, welke de ontdekking van het elektron was door Joseph Thomson [6] met behulp van een deeltjesversneller, is er aanzienlijke vooruitgang geboekt in het begrip van deze fundamentele bouwstenen van de natuur. Sindsdien zijn er verschillende ontwerpen versnellers gemaakt om deze bouwstenen verder te kunnen bestuderen. Deze ontwikkelingen hebben geleid tot het ontwerp en constructie van de Grote Hadron Botser (LHC), die in 2008 in werking is genomen. De LHC is een circulaire versneller met een lengte van 27 km en heeft twee bundelpijpen, welke groepjes protonen - bundels genoemd - in tegengestelde richting begeleiden. Deze twee bundels bestaan uit zogenoemde *bosjes* die elk uit een heel groot aantal protonen bestaan: ongeveer 1.15×10^{11}. Op vier punten rondom de LHC worden deze twee bundels gekruist zodat elke 25 ns de protonen van de twee bundels op elkaar kunnen botsen. Zo een kruising wordt een *groepskruising* genoemd, in welke de individuele proton-proton botsingen over ongeveer 200 ps uitgespreid zijn. De energiegrens van de LHC is enorm verlegd sinds de opening. Toen de LHC begon, was de energie van elke botsing 7 TeV en is stapsgewijs opgevoerd naar 13.6 TeV. De statistische grens van de LHC is samen met de energiegrens ontwikkeld door de tijd heen. De toename van de proton-proton botsingsfrequentie die over de afgelopen jaren mogelijk is gemaakt, verhoogt direct de statistiek van de te bestuderen fysische processen,

welke lineair afhankelijk zijn van het aantal botsingen. Deze processen bevatten vaak nieuwe aanwijzingen voor het begrip en geldigheid van het Standaard Model en zijn daarom van groot belang voor deeltjesfysici.
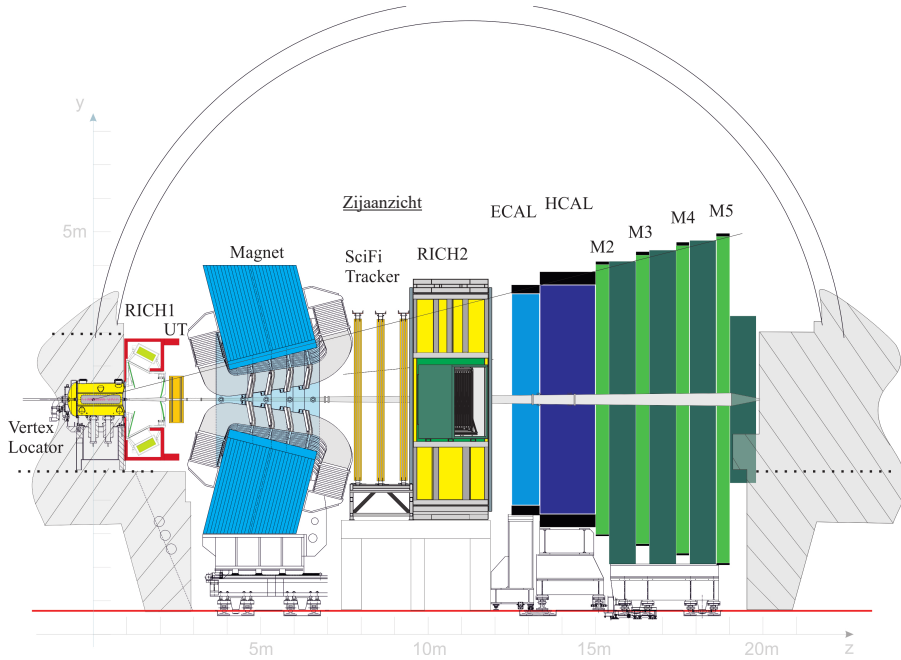

Figuur 1: Een illustratie van de LHCb detector na zijn eerste upgrade (2022). De verschillende subdetectoren zijn aangegeven door middel van verschillende kleuren alsmede de magneet in het blauw. De grot waarin LHCb gebouwd is, is aangegeven door middel van de grijze lijnen en de grijze vlakken. De proton-proton botsingen vinden plaats in de VELO op $z = 0$. Dit figuur is overgenomen uit [9].

LHCB'S UPGRADE 2

Een van de experimenten die meet aan de botsingen van de LHC is LHCb (LHC beauty - te zien in fig. 1). Dit is experiment focust zich in de voorwaartse richting, dicht rondom de bundelpijp. Net als bij de andere experimenten rondom LHC, is er een plan om de botsingsfrequentie verder te verhogen vanaf 2035. Dit betekend dat een geheel verbeterde detector nodig zal zijn, die de Upgrade 2 detector genoemd wordt. Deze verhoging van de frequentie is nodig om tijdens de levensduur van het experiment een groter aantal proton-proton botsingen te kunnen meten. Echter vereist zo een drastische verandering in de frequentie ook een compleet herontwerp en upgrade van de verschillende subdetectoren van LHCb zodat deze overweg kunnen met de gevolgen van deze hogere botsingsfrequentie: snelheid, stralingsschade, data volume en nog veel meer. Het doel is om het gemiddelde aantal zichtbare proton-proton botsingen per groepskruising te verhogen van 7

naar 42. Dit aantal botsingen per groepskruising word ook wel de pile-up genoemd. Door deze toename in aantal botsingen die gemeten wordt, kan LHCb zijn fysicapotentieel verder uitbreiden tot voorbij wat momenteel haalbaar is.
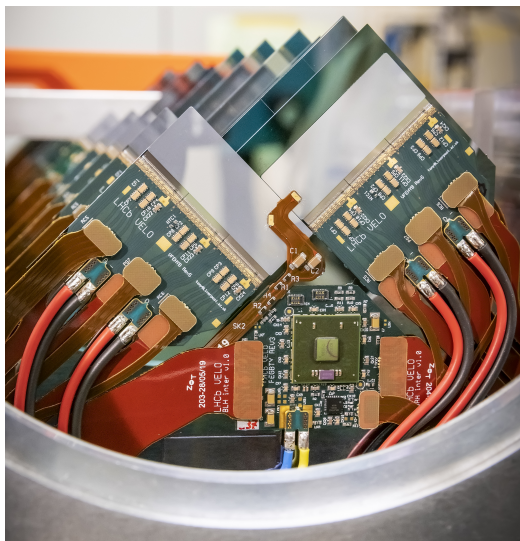
Figuur 2: Foto van de helft van de VELO detector. Het eerste detector vlak is geheel zichtbaar, met daarachter een paar andere vlakken. Foto gemaakt door [105].

Het tracking systeem van de LHCb detector, welke het pad van de deeltjes die uit de proton-proton botsingen ontstaan kan reconstrueren, bestaat uit verschillende subdetectoren. De subdetector die de botsingen omringt, en het dichtste bij deze botsingen staat, is de VELO (VErtex LOcator - zichtbaar in fig. 2). Deze detector bestaat uit meerdere lagen van silicium pixeldetectoren en heeft als doel, naast het reconstrueren van de paden, het reconstrueren van de positie van de proton-proton botsingen. Met de toename van de pile-up zal de VELO aan discriminerend vermogen verliezen in parameters die het de fysica analyses aanlevert. Hierdoor wordt het onmogelijk om deze analyses uit te voeren. Daarom zal in de VELO tijdsinformatie worden toegevoegd aan elke meting, welke bestaat uit informatie over de aankomsttijd van de deeltjes in elke detector (ook wel de tijdsstempel genoemd). Deze toevoeging maakt het mogelijk om overlappende botsingen te ontwarren en weer aan discriminerend vermogen te winnen.

Omdat de proton-proton botsingen tijdens een groepskruising niet gelijktijdig plaatsvinden kan de tijdsstempel van de botsingen en de producten hiervan gebruikt worden in de reconstructie. In dit proefschrift wordt de invloed van de toevoeging van tijdsinformatie in de VELO voor twee verschillende parameters onderzocht en wordt er gekeken naar hoe deze toevoeging van tijdsinformatie kan
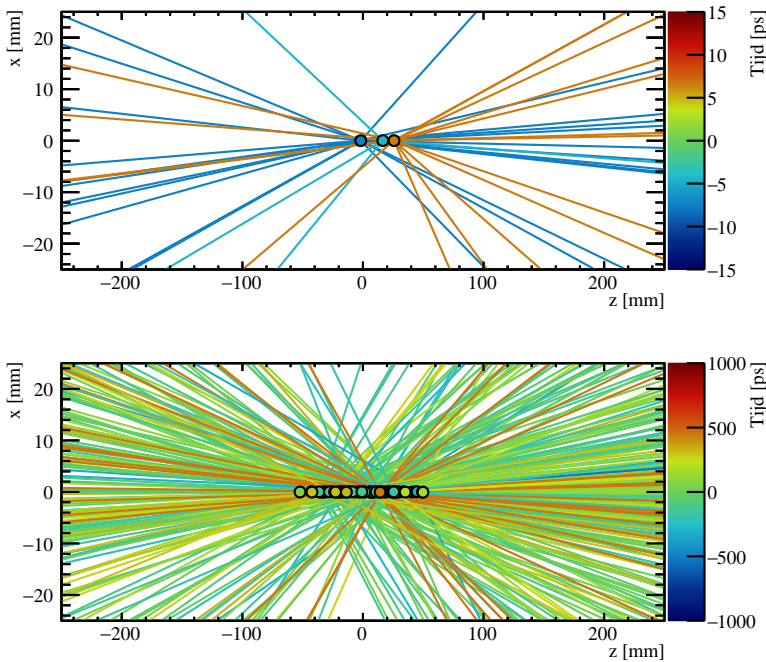
Figuur 3: Twee figuren die aangeven hoe tijdsinformatie kan helpen in het onderdrukken van pile-up. De cirkels zijn de proton-proton botsingen en de lijnen geven het pad van deeltjes aan die ontstaan zijn uit deze botsingen. De kleur geeft de tijd van de botsingen en de paden aan. Een typische groepskruising voor Upgrade 2 is getoond in elk figuur, met gemiddeld 42 botsingen. Door tijdsinformatie op te nemen en een klein stukje in tijd te selecteren, wordt de pile-up artificieel gereduceerd, wat zichtbaar is als een vermindering in het zichtbaar aantal botsingen en paden. Het onderste figuur toont de volledige groepskruising en het bovenste figuur toont tijd selectie van slechts 30 ps.

helpen in het verbeteren van de prestatie van de VELO. Met behulp van simulatie wordt de invloed van een tijdsresolutie per meting van 50 ps bestudeerd. In fig. 3 wordt de invloed van de additie van tijdsinformatie op een typische groepskruising getoond. De onderste plot toont een typische groepskruising tijdens Upgrade 2 van LHCb met ongeveer 42 zichtbare proton-proton botsingen. De cirkels in dit figuur geven de positie van deze botsingen aan en de lijnen geven de banen aan van de deeltjes die tijdens deze botsingen zijn ontstaan. De kleuren geven de relatieve tijd aan van zowel de botsingen als de paden. Deze tijd, ook wel hun tijdsstempel genoemd, maakt het mogelijk om sporen te koppelen aan botsingen op basis van hun tijdsstempel. Men kan zien dat binnen een tijdsvenster van 2 ns de individuele botsingen en de door hun gecreëerde deeltjes niet van andere botsingen te

onderscheiden zijn. Wanneer echter de tijdsstempel van botsingen en gecreëerde deeltjes wordt gebruikt, kan een kleiner tijdsvenster worden geselecteerd. Omdat de botsingen verspreid zijn in de tijd, bevat het kleinere tijdsvenster minder botsingen en kunnen de individuele botsingen en de gerelateerde deeltjes gemakkelijk worden geïdentificeerd. Dit wordt aangegeven in het bovenste figuur van fig. 3, waar een venster van slechts 30 ps wordt getoond uit de volledige groepskruising. De tijdsstempel, oftewel de kleur, kan ook worden gebruikt om gecreëerde deeltjes te relateren aan de botsingen, zoals zichtbaar is in het bovenste figuur.

De simulaties die zijn uitgevoerd om de invloed van de toevoeging van tijdsinformatie in de VELO te onderzoeken, geven aan dat met een per-hit tijdsresolutie van 50 ps de negatieve effecten van hogere pile-up kunnen worden opgelost. Deze simulaties stellen daarom een doel voor de tijdsresolutie die de komende jaren moet worden bereikt voor silicium pixel detectoren om de VELO werkend te houden tijdens Upgrade 2.

Ontwikkeling van silicium pixel detectoren en karakteriseringssystemen

Op dit moment bestaat er nog geen silicium pixel detector die voldoet aan de eisen voor de VELO tijdens Upgrade 2. Er zijn echter uitgebreide R&D programma's gaande die een breed scala aan mogelijk technologieën onderzoeken voor zowel het silicium detector materiaal en de uitleeselektronica. Als onderdeel van dit programma ontwikkelen wij nieuwe meettechnieken en apparatuur.

Om de temporele prestaties te kunnen meten, en nog belangrijker, te karakteriseren, van silicium sensoren en detectoren die ontwikkeld zijn voor de VELO worden speciale karakteriseringssystemen ontwikkeld. In dit proefschrift worden twee systemen ontwikkeld voor dit doel. Het eerste systeem is een *telescoop*, een systeem dat een deeltjesbundel gebruikt, en het tweede systeem is gebaseerd op het twee-foton absorptie fenomeen waarbij fotonen worden gebruikt om signalen op te wekken in de silicium sensor.

De telescoop bestaat uit acht Timepix4 ASICs (Application-Specific Integrated Circuits) met ieder een silicium sensor, en reconstrueert het pad van deeltjes die door deze acht lagen heen vliegen. Deze telescoop word de Timepix4 telescoop genoemd, omdat hij bestaat uit Timepix4 ASICs. Deze telescoop is ontwikkeld om zowel de positie en de tijdsresolutie van gereconstrueerde deeltjes zeer nauwkeuring te kunnen bepalen. Deze informatie kan dan vergeleken worden met de meting van een externe detector, die naast of tussen de telescoop geplaats kan worden, waardoor deze externe detector gekarakteriseerd kan worden. Dit maakt het mogelijk om nieuwe sensor en detector technologieën te kunnen testen met deze deeltjesbundel.

De Timepix4 telescoop is in fases opgebouwd waardoor er verschillende versies van deze telescoop zijn geweest. De temporele prestaties van de telescoop toen deze uit slechts vier lagen bestond, twee dunne en twee dikke silicium sensoren (de helft van de uiteindelijke telescoop), en die gebruikt maakt van de eerste versie van de Timepix4 ASIC, zijn bepaald voor verschillende operationele condities. De tijdsresolutie van een bias scan (links) en een threshold scan (rechts) voor de vier verschillende telescoop vlakken is getoond in fig. 4. Deze resultaten zijn gebruikt om de optimale condities voor de telescoop te kunnen bepalen, met als doel het behalen van de beste tijdsresolutie. Deze beste tijdsresolutie van deze versie van de telescoop is vastgesteld op $340 \pm 5\,\text{ps}$. Echter, is ook vastgesteld dat deze tijdsresolutie aanzienlijk zal worden verbeterd wanneer de nieuwste versie van de Timepix4 ASIC gebruikt zal worden, samen met het toevoegen van de laatste vier vlakken. De resolutie zal ook nog verder kunnen worden verbeterd als de zogenoemde tijdskalibratie en verbeterde kloksynchronisatie zijn geïmplementeerd. Er word verwacht dat de uiteindelijke versie van de telescoop een tijdsresolutie van beter dan $100\,\text{ps}$ kan behalen. Deze resolutie is voldoende om de eerste generatie nieuwe ASICs te kunnen testen, maar is echter nog niet voldoende om de huidige snelste silicium sensoren tot het uiterste te kunnen testen. De telescoop kan ook een meer nauwkeurige tijdsmeting geven, echter wel met een lagere frequentie, door gebruik te maken van een speciaal tijdsreferentie systeem. Dit systeem kan een resolutie van beter dan $20\,\text{ps}$ geven, welke voldoende is om deze sensoren te kunnen testen.
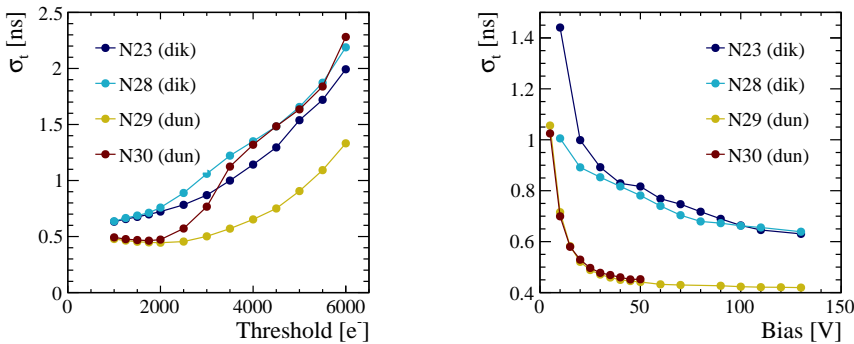

Figuur 4: Links: tijdsresolutie van de vier telescoopvlakken voor verschillende threshold waardes. Rechts: de tijdsresolutie van de vier telescoopvlakken als functie van de bias spanning. Twee van de vlakken bereiken hun beste resolutie rond een threshold van 2000 e⁻. De tijdsresolutie word voor alle vlakken beter voor hogere bias voltages. Figuren zijn aangepast van [91].

Met behulp van de voorganger van de Timepix4 telescoop, de Timepix3 telescoop - volledig gebaseerd op de Timepix3 ASIC - zijn de ladingcollectie en de temporele kenmerken gemeten voor verschillende sensorontwerpen met het oog op de eerste upgrade van de VELO (Upgrade 1). Deze studies leverde informatie over de impact van stralingsschade waarmee de sensoren dicht bij de proton-proton botsingen te maken krijgen. Met deze studies is geconcludeerd dat de stralingsschade die de VELO sensoren aan het einde van hun levensduur zullen hebben opgelopen resulteert in een vermindering van de verzamelde lading per deeltje van 16 ke⁻ naar 6 ke⁻. Deze lading is hoog genoeg om te voldoen aan de vereiste voor de VELO. Tijdens deze studies is een kleine hoeveelheid ladingsvermenigvuldiging ontdekt in een klein deel van de sensoren. De tijdsresolutie is onderzocht als een functie van de hoeveelheid stralingsschade en bleek, als verwacht, slechter te worden voor hogere hoeveelheden stralingsschade. Er werd geen verbetering in de tijdsresolutie gevonden wanneer er ladingsvermenigvuldiging optrad. Deze studies werden uitgevoerd met de Timepix3 ASIC die een intrinsieke resolutie van 451 ps heeft. Daarom domineerde deze ASIC de tijdsresolutie die gemeten was. Kleine veranderingen in de totale resolutie, door bijvoorbeeld ladingsvermenigvuldiging, zijn daarom mogelijk niet opgemerkt.

Naast de telescoop wordt in dit proefschrift ook de ontwikkeling van een lasersysteem besproken. Dit systeem bestaat uit een 1550 nm gepulseerde laser die in staat is signalen te creëren in silicium door middel van het TPA (two-foton absorptie) fenomeen. Dit proces maakt gebruik van het feit dat twee fotonen binnen een korte tijd op dezelfde plaats in het silicium kunnen worden geabsorbeerd. Deze techniek maakt het daarmee mogelijk om gelokaliseerde karakterisatie van de ladingsverzameling in silicium uit te voeren. Omdat de lengte van de laser pulsen kort is, tussen de 380 fs tot 540 fs, kan een nauwkeurige tijdreferentie worden gemaakt, die gebruikt kan worden om te vergelijken met de tijdsmeting van de sensor of detector. Deze referentie heeft een resolutie van beter dan 30 ps, welke geheel gelimiteerd was door de meetmethode van deze resolutie, waardoor deze waarschijnlijk zelfs nog preciezer is. Dit maakt het TPA systeem ideaal om de ruimtelijke, ladingscollectie en temporele prestaties van silicium sensoren en detectoren op een gecontroleerde manier te karakteriseren.

Het twee-foton absorptie systeem dat op Nikhef is gebouwd, is gekarakteriseerd en de resultaten zijn in dit proefschrift besproken. De eerste metingen wijzen op een variatie in de intensiteit van het TPA-signaal door fluctuaties in de lengte van de laserpulsen. Deze variaties vinden plaats over de tijdschaal van enkele minuten en kunnen gedeeltelijk offline gecorrigeerd worden met behulp van een tweede silicium sensor als referentie. Met dit TPA systeem zijn zowel *planar* silicium sensor op de Timepix3 en Timepix4 ASIC onderzocht. De twee onderzochte sensoren op de Timepix3 ASICs geven aan dat de tijdsresolutie wordt gedomineerd door de bijdrages van de ASIC en niet die van de sensoren. Desondanks wordt een resolutie
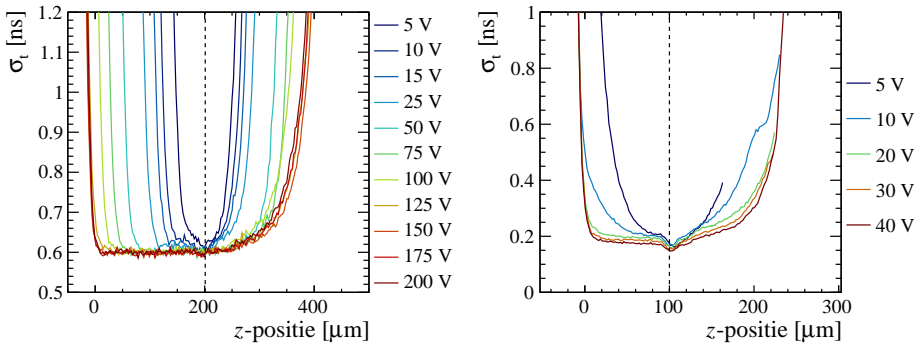
Figuur 5: Links (Rechts): de tijdsresolutie van een 200 μm (100 μm) silicium sensor, aangesloten op een Timepix3 (Timepix4) ASIC, als functie van de hoogte en voor verschillende bias voltages aangegeven door de verschillende kleuren. De gestippelde lijn geeft weer waar de voorkant van de sensor is en het 0-punt op de horizontale as geeft de achterkant van de sensor aan. Het linker figuur is overgenomen uit [103].

van ongeveer 600 ps bereikt. Voor de eerste resultaten met de Timepix4 ASIC met hetzelfde type sensor is een resolutie van 147.4 ± 1.1 ps bereikt, welke aanzienlijk beter is. Deze verbetering kan worden geweid aan de verbeterde analoge front-end en de digitale tijdsmeting van de Timepix4. De volgende stap is het verbeteren van kleine systematische fouten van de Timepix4 tijdens metingen, waardoor de tijdsresolutie verbeterd kan worden. Twee metingen, link met de Timepix3 en rechts met de Timepix4, worden getoond in fig. 5. Deze metingen laten de tijdsresolutie zien als een functie van de diepte van de sensoren. De stippellijn geeft de voorkant van de sensor aan en het 0-punt op de horizontale as geeft de achterkant van de sensor aan. Beide metingen laten een vergelijkbare trend zien, onafhankelijk van hun verschillende diktes, maar de schaal van de tijdsresolutie is significant verschillend. Waar de Timepix3 een resolutie van ongeveer 600 ps behaald, haalt de Timepix4 een resolutie van iets beter dan 200 ps.

Deze eerste metingen met het TPA system hebben laten zien dat de karakterisatie van de nieuwste sensor technologieën kan worden uitgevoerd met dit systeem. Daarnaast blijkt dat het een waardevol systeem is om te helpen met de ontwikkeling van silicium detectoren gericht op snelle tijdsmetingen. Wij hebben ook gezien dat de huidige beperkende factor voor silicium detectoren de analoge front-end en digitalisering (TDC) zijn. Met de huidige trend van ontwikkelingen zouden deze beperkende factoren echter in de nabije toekomst opgelost moeten kunnen worden. De nieuwste silicium sensoren hebben al bewezen dat een tijdsresolutie van minder dan 30 ps haalbaar is, maar een volledige implementatie in de VELO met deze resolutie wordt momenteel nog bestudeerd. Het lijkt er op dit moment op

dat de silicium sensor niet de beperkende factor zal zijn, maar dat dit de ASIC zal zijn.

De tijdsresolutie van de detectoren die in dit proefschrift beschreven zijn, is ver verwijderd van de vereiste 50 ps resolutie voor de VELO. Echter, zoals te zien is in de ontwikkelingstap van de Timepix3 naar de Timepix4 ASIC, worden er grote stappen gemaakt. Deze trend moet zich in de komende jaren voortzetten om de vereiste resolutie te kunnen behalen. De karakteriseringssystemen die besproken zijn in dit proefschrift zullen cruciaal zijn voor ontwikkelingen van silicium pixel detectoren gericht op snelle tijdsmetingen.

Impact paragraph

<center>❧</center>

In the current age of high energy physics, silicon tracking detectors have become a central component of many high energy physics experiments. The drive to improve and develop new detectors, as well as almost all instrumentation used at European Organization for Nuclear Research (CERN), leads to inventions that are applied in a wide range of fields outside of high energy physics. Perhaps the most well-known of these inventions to come from CERN is the world wide web, but other inventions such as Gas Electron Multiplier (GEM) detectors for radiotherapy have also seen dedicated use outside of high energy physics.

By adding temporal information to imaging techniques like Positron Emission Tomography (PET), or improving the time resolution of time-of-flight systems, the quality and accuracy of results from these systems can be substantially enhanced. By performing research and constructing systems to characterize, in the case of this dissertation, hybrid pixel detectors, the temporal performance of such detectors can be improved. The results obtained, and lessons learned from improving the temporal performance of hybrid pixel detectors, can aid significantly in the design of novel detectors. Another benefit is having developed dedicated systems that can test the temporal performance of such devices, enables the possibility to test detectors from outside of high energy physics.

The work presented in this dissertation focuses on the characterisation and development of planar silicon sensors, as well as Timepix3 and Timepix4 readout chips. A new characterisation system is commissioned at Nikhef, which gives researchers a tool to investigate novel silicon sensors with precise time resolution. Besides this, a new beam telescope is constructed and commissioned that allows researchers to test novel sensors, as well as candidate detector systems for the upgrade of the LHCb VErtex LOcator (VELO) in a beam environment. Besides these two systems, the temporal characteristics of planar (thin) silicon sensors have been investigated. The results of planar sensors attached to Timepix3 readout chips have been limited by the time resolution of these readout chips, and therefore

can also not be applied in demanding systems in the industry. The result of a thin planar sensor attached to a Timepix4 readout chip, however, is promising, reaching a resolution of $147.4 \pm 1.1\,$ps.

These systems are accessible for researchers within Nikhef and other institutes and collaborations and allow for the development and characterisation of next-generation sensors and ASICs. Ultimately, these developments can lead to the creation of next-generation detector systems that can be applied in for example time-of-flight measurements in mass spectrometry. Besides this, developments in characterisation systems can more easily lead to new systems that can be applied to different kinds of detectors that for example are applied in PET. Therefore, the experience gained by constructing and utilizing these systems can lead to a shortened development time for different detector systems.

To implement these detectors in the next-generation experiments at CERN, a time resolution of 50 ps is required. Therefore, the time resolution achieved with Timepix4 readout chips is not yet sufficient to be directly applied in these experiments. However, efforts are ongoing to improve both the sensor (by applying different geometries) and the readout chip. A lot of effort however still needs to be given in order to achieve the desired resolution of 50 ps in the coming years. This work, however, lays a basis to develop and characterise these sensors in the coming years.

Acknowledgments

Now that the formalities are behind us and the world of physics and silicon sensors has concluded its discourse, I want to take this moment to express my gratitude to all those who have accompanied me on this unforgettable journey during my PhD.

First and foremost, I want to extend my appreciation and gratitude to my supervisors and promoter. Hella, it has been a delight to work together with you. I am grateful you managed to persuade me to embark on this PhD adventure! Your out-of-the-box ideas, like the polarization problem with the TPA system, have always been amazing. Moreover, your invaluable assistance and guidance throughout my writing process have been instrumental in finishing my dissertation. Kazu, thank you for all the laughter and bad jokes. Working with you has been a pleasure. I have enjoyed your unique approach to debugging electronics problems tremendously. Hopefully, now with my dissertation in hand, you can see I was not stressed at all. Marcel, your openness and honesty have always been remarkable. The leadership, guidance and enthusiasm you give to the bfys group has been extraordinary. I am grateful for all the advice and freedom you have given my research endeavors during my PhD.

During my time, I had the privilege of being part of the detector R&D group at Nikhef and collaborating with all the amazing people that comprised this group throughout my PhD years. I would like to express my gratitude to Daan, Douwe, Jory, Kevin, Mariia, Marjolein, Martin, Navrit, Niels, Roberto, Timesh, Tjip, Uwe and last but certainly not least Martin. Although you were not my official supervisor, I cannot thank you enough for the invaluable discussions and the help you provided me throughout the years. Without you, many problems would have taken a lot more time to solve.

I was also fortunate to be part of the bfys group, which comprises many more amazing people whom I cherished countless coffee breaks, cookie meetings, outings and Friday meetings: Alice, Aleksandra, Andrii, Antonio, Brían, Carolina, Chris, Cristina, Davide, Daniel of Scotland, Daniel of Sweden, Efrén, Emmy, Ganrong, Gerhard, Jacco, Jan, Jordy, Keri, Kristoff, Lex, Maarten, Mara, Mark, MD, Michele, Mick, Miriam, Maxime, Niels, Patrick, Igor, Suzanne and Wouter.

Of course, I also had the pleasure, be it in some cases online, to work together with the amazing telescope and endgame gang! It was tremendously fun working together and therefore I would like to thank all of you: Edgar, Elena, Emma, Heinrich, Paula, Raphael, Tim, Tommaso, Victor and Vinicius.

During my time at Nikhef, I was lucky enough to have met and been supported by people from the mechanical and electronic groups that more than deserve a thank you: Gino, Krista and Oscar.

Dit dankwoord zou natuurlijk niet compleet zijn zonder het benoemen van mijn familie. Pa en ma, ik kan jullie niet genoeg bedanken voor alle steun die jullie mij hebben gegeven. Van klein tot groot, jullie zijn er altijd voor mij. An(nemarie), jammer dat je bent overgelopen naar de wiskunde kant. Desondanks ben ik ontzettend blij dat jij mijn kleine zusje bent. Opa en oma, de tripjes naar jullie in Andijk zijn herinneringen die ik altijd zal blijven koesteren. Bedankt voor alle mooie momenten samen en verhalen die jullie vertellen. Oma Flits, bedankt voor alle leuke (flits)bezoekjes, gezelligheid en etentjes. Familie Overmeer, ik ben blij dat ik al zoveel jaren uitmaak van de familie en ik hoop dat jullie kunnen genieten van dit boekwerk (er staan mooie plaatjes in!). Bedankt voor de skilessen (eindelijk hupjes vrij) en gezelligheid. Danique, ik ben super blij dat wij elkaar (al dik) negen jaar geleden hebben ontmoet. De tijd die wij samen hebben doorgebracht zijn de leukste van mijn leven en daar zullen nog tallozen jaren bijkomen! Bedankt voor alle steun die je mij hebt gegeven gedurende mijn PhD. Mijn proefschrift is er nu eindelijk en we kunnen met veel plezier terugkijken. Op naar het volgende avontuur!

About the author

"Alles is mogelijk, behalve wanneer het niet mogelijk is."

– Marten Toonder, *De Kwinkslagen*

Robbert Geertsema was born in 1996 in Purmerend, the Netherlands. He completed secondary school in 2014. From 2014 to 2019 he attended the Universiteit van Amsterdam and Vrije Universiteit Amsterdam, where he obtained his Bachelor's degree in Physics and Astronomy in 2017 and Master's degree in Physics and Astronomy in 2019. Robbert's master's degree thesis focussed on the characterisation of hybrid pixel detectors and the development of a single-photon system for the characterisation of silicon sensors.

In 2019 he started his PhD in experimental particle physics in the R&D and LHCb group at Nikhef, associated with Universiteit Maastricht. As part of his PhD, he presented his work at different high-profile conferences and workshops within the field of detector R&D and took tutor roles in several courses at both Bachelor and Master levels at both the Universiteit van Amsterdam and Universiteit Maastricht.

"But wherever they go, and whatever happens to them on the way, in that enchanted place on the top of the Forest a little boy and his Bear will always be playing."

– A.A. Milne, *The House at Pooh Corner*